Measurement of differential cross-sections of the $t\bar{t}\gamma$ process with the ATLAS detector

DISSERTATION
zur Erlangung des Grades eines Doktors
der Naturwissenschaften

vorgelegt von
Buddhadeb Mondal

Eingereicht bei der Naturwissenschaftlich-Technischen Fakultät
der Universität Siegen

2024

Measurement of differential cross-sections of the $t\bar{t}\gamma$ process with the ATLAS detector

DISSERTATION
zur Erlangung des Grades eines Doktors
der Naturwissenschaften

vorgelegt von
Buddhadeb Mondal

Eingereicht bei der Naturwissenschaftlich-Technischen Fakultät
der Universität Siegen

2024

Betreuerin und erste Gutachterin:
PD. Dr. Carmen Diez Pardos, Universität Siegen

Zweiter Gutachter:
Prof. Dr. Ivor Fleck, Universität Siegen

Mitglieder der Promotionskommission:
Prof. Dr. Guido Bell, Universität Siegen
Prof. Dr. Markus Risse, Universität Siegen

Tag der mündlichen Prüfung:
04.07.2024

Abstract

This thesis presents a measurement of the differential cross-sections of the associated production of a top quark pair and a photon ($t\bar{t}\gamma$) in proton-proton collisions at a center-of-mass energy of 13 TeV. The data were collected with the ATLAS detector at the Large Hadron Collider during Run 2 operation, corresponding to an integrated luminosity of 140.1 fb^{-1}. The analysis is performed in the single-lepton and dilepton top quark pair decay channels, focusing on events where the photon is radiated from the initial-state parton or one of the top quarks. Additionally, cross-sections are measured for the inclusive $t\bar{t}\gamma$ process, including events where the photon is radiated from the decay products of the top quarks.

The measurement is performed at particle level within a fiducial phase space volume designed to closely mimic the detector acceptance. Detector effects are corrected using a profile likelihood unfolding method. The absolute and normalized differential cross-sections are measured as functions of various observables characterizing the photon, lepton, and jet kinematics as well as variables related to the angular separation between these objects. The results are compared to state-of-the-art Monte Carlo simulations, finding good overall agreement.

Zusammenfassung

Diese Dissertation präsentiert eine Messung der differentiellen Wirkungsquerschnitte der assoziierten Produktion eines Top-Quark-Paares und eines Photons ($t\bar{t}\gamma$) in Proton-Proton-Kollisionen bei einer Schwerpunktsenergie von 13 TeV. Die Daten wurden mit dem ATLAS-Detektor am Large Hadron Collider während des Run-2 aufgezeichnet und entsprechen einer integrierten Luminosität von 140,1 fb^{-1}. Die Analyse wird in den Zerfallskanälen des Top-Quark-Paares mit einem Lepton und mit zwei Leptonen durchgeführt, wobei der Fokus auf Ereignissen liegt, bei denen das Photon von einem Parton des Anfangszustands oder von einem der Top-Quarks abgestrahlt wird. Zusätzlich werden Wirkungsquerschnitte für den inklusiven $t\bar{t}\gamma$-Prozess gemessen, einschließlich Ereignissen, bei denen das Photon von den Zerfallsprodukten der Top-Quarks abgestrahlt wird.

Die Messung wird auf Teilchenebene innerhalb eines eingeschränkten Phasenraums durchgeführt, der so konzipiert ist, dass er die Detektorakzeptanz genau widerspiegelt. Detektoreffekte werden mithilfe einer Profile-Likelihood-Entfaltungsmethode korrigiert. Die Messung der absoluten und der normierten differentiellen Wirkungsquerschnitte erfolgt in Abhängigkeit verschiedener Observablen, welche die Kinematik der Photonen, Leptonen und Jets sowie deren Winkelabstände zueinander beschreiben. Die Ergebnisse werden mit aktuellen Monte-Carlo-Simulationen verglichen, wobei insgesamt eine gute Übereinstimmung festgestellt wird.

Contents

1 Introduction

The Standard Model (SM) of particle physics stands as a monumental achievement in our quest to understand the fundamental building blocks of the universe and the forces that govern their interactions. It elegantly describes a diverse array of phenomena, from the behavior of atoms to the interactions of particles at the highest energies achieved in colliders. The predictions of the SM have been confirmed by numerous experiments, including those conducted at the Large Hadron Collider (LHC). The discovery of the Higgs boson in 2012 provided crucial validation of the SM. The model yet remains incomplete and leaves many questions unanswered such as it does not account for gravity, dark matter, dark energy, neutrino masses, among other open questions. These open questions compel us to push the boundaries of our understanding, seeking new physics phenomena beyond the SM.

Among the fundamental particles within the SM, the top quark occupies a special place. As the heaviest known elementary particle, with a mass of approximately 173 GeV, it plays a unique role in shaping the structure of the SM. Its large mass leads to a strong coupling with the Higgs boson, making it a crucial probe of the electroweak symmetry breaking mechanism. Moreover, its short lifetime, decaying before hadronization, allows us to study the properties of a bare quark, providing a window into the dynamics of the strong interaction.

This thesis focuses on the measurement of the production of a top quark-antiquark pair in association with a photon ($t\bar{t}\gamma$ process). By studying this process, we can directly probe the coupling between the top quark and the photon and test the predictions of the SM. Precise measurements of this coupling can reveal subtle deviations from SM predictions, potentially signaling the presence of new physics.

This thesis utilizes proton-proton collision data at a center-of-mass energy of 13 TeV collected by the ATLAS experiment during the Run 2 operation (2015-2018). The large dataset collected by ATLAS, corresponding to an integrated luminosity of 140.1 fb^{-1}, provides an unprecedented opportunity to study the $t\bar{t}\gamma$ process with high precision. This analysis delves into measuring the production rate differentially as a function of various

kinematic observables, which can provide insights into the underlying dynamics of the process.

This thesis is structured as follows: Chapter 2 provides a theoretical background on the Standard Model, focusing on the top quark and its interactions. Chapter 3 describes the LHC and the ATLAS experiment, highlighting the key components used in this analysis. Chapter 4 discusses the development of a dedicated software framework for raw data analysis of the ATLAS pixel detector. Chapter 5 delves into the simulation techniques used in high-energy physics to model particle collisions and the response of detectors. Chapter 6 details the data and Monte Carlo samples used in this analysis. Chapter 7 describes the event selection criteria employed to isolate the $t\bar{t}\gamma$ process. Chapter 8 presents the data-driven methods used to estimate several background contributions. Chapter 9 describes the various sources of systematic uncertainties that affect the measurement. Chapter 10 presents the measurement strategy. Chapter 11 presents the measurement of the $t\bar{t}\gamma$ cross-sections, both absolute and normalized, compares the results to theoretical predictions and previous measurements, and discusses the results in the context of effective field theory (EFT). Finally, Chapter 12 summarizes the key findings of this research and outlines potential avenues for future investigations.

This thesis aims to advance our understanding of the top quark and its significance in the fundamental structure of the universe. Through precise measurements of the $t\bar{t}\gamma$ process, we endeavor to test the predictions of the Standard Model and unveil any subtle hints of new physics that may lie beyond our current theoretical framework.

2 The Standard Model and the top quark

The Standard Model (SM) of particle physics is the most successful theory to date in explaining the fundamental particles of our universe and the interactions among them. These fundamental particles include six types of quarks (up, down, charm, strange, top, and bottom), each of which comes in three color quantum numbers (red, green, and blue), making them fundamental in nature. Additionally, there are six leptons (electron, muon, tau, and their corresponding neutrinos: electron neutrino, muon neutrino, and tau neutrino), along with three force carriers responsible for the electromagnetic, weak, and strong forces. The theory of SM does not include the gravitational force.

The particles in the SM are divided into two categories: fermions and bosons. Fermions, which are spin-$\frac{1}{2}$ particles, include quarks and leptons. They are the fundamental building blocks of matter and obey the Pauli exclusion principle, meaning no two fermions can occupy the same quantum state simultaneously. Bosons, on the other hand, do not follow the Pauli exclusion principle. Vector bosons (spin-1 particle) act as force carriers mediating the fundamental forces of nature. There are four vector bosons in the SM: the photon, the W and Z bosons, and the gluon. The photon mediates the electromagnetic force, the W and Z bosons mediate the weak force, and the gluon mediates the strong force. Additionally, the Higgs boson (spin-0 particle), a scalar boson, is related to the mechanism that generates masses to the fundamental particles. Figure 2.1 illustrates the elementary particles and force carriers of the SM along with their properties.

The quarks and leptons are grouped into three generations with the same properties but different masses. Quarks and leptons have a property called electric charge, and particles with electric charge participate in electromagnetic interactions. A difference between quarks and leptons is that quarks have fractional electric charges, whereas leptons have integer electric charges. Both quarks and leptons participate in weak interactions because they carry weak isospin, a quantum number that is conserved in weak interactions. Quarks have a special property called color charge, as mentioned above, which causes them to participate in strong interactions, while leptons do not have this property. The theory of the SM and the interactions among particles and forces are discussed in detail in Section 2.1.

The properties, production, and decay of the top quark are briefly discussed in Section 2.2. Lastly, the coupling between the top quark and the photon is described in Section 2.3.

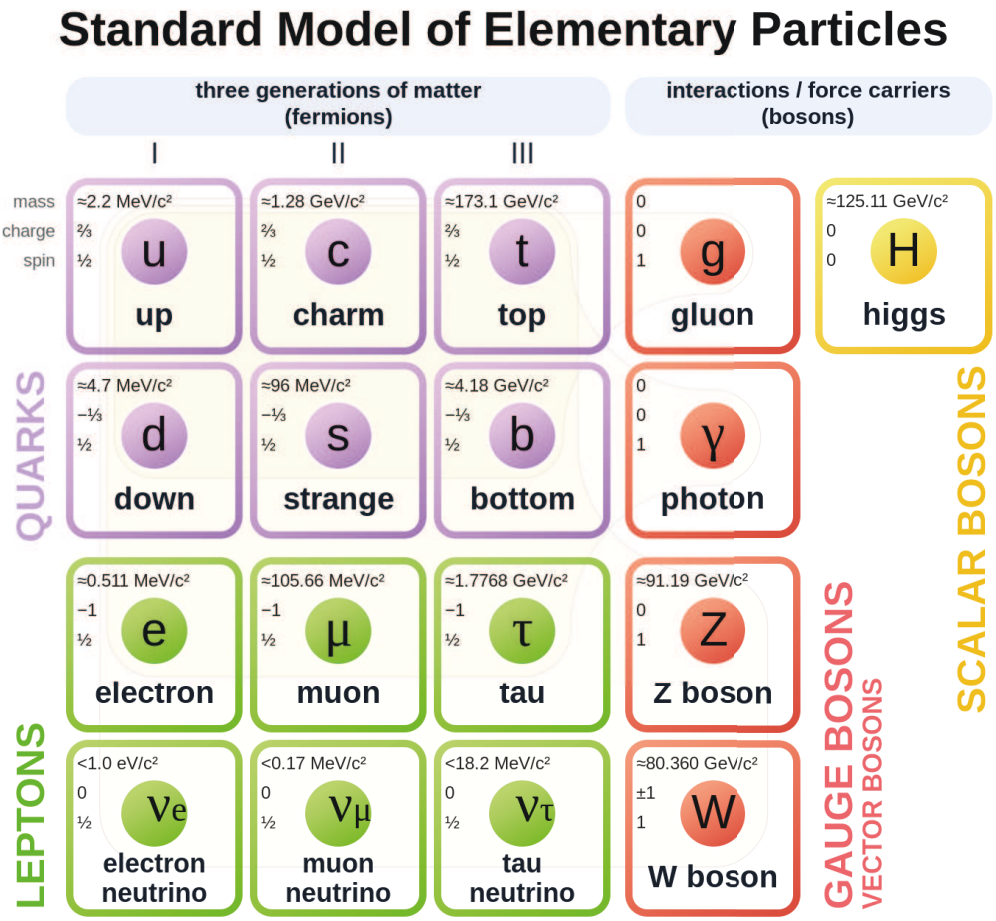

Figure 2.1: Elementary particles and force carriers of the Standard Model [1].

2.1 The Standard Model

The SM is a gauge theory based on the symmetry group $SU(3)_C \times SU(2)_L \times U(1)_Y$. The $SU(3)_C$ is the symmetry group of the strong force, governing the interactions between quarks and mediated by gluons. The $SU(2)_L$ is the symmetry group of the weak force, which only acts on left-handed particles and right-handed antiparticles. The $U(1)_Y$ is the symmetry group of the weak hypercharge. The electromagnetic interactions are described by the $U(1)_{EM}$ symmetry, which emerges from a combination of the $SU(2)_L$ and $U(1)_Y$ symmetries after the spontaneous symmetry breaking mediated by the Higgs mechanism.

In the SM, the fundamental particles are formulated as fluctuations of quantum fields, meaning for every fundamental particle there exists a fundamental quantum field. The quantum field theory (QFT) which has the formalisms of the quantum fields is a theoretical framework that combines quantum mechanics and the effect of special relativity. QFT is based on the principle of quantization of fields, meaning that the classical fields (for example, the electric field) are now described by operators that satisfy the commutation relations of quantum mechanics.

The gauge theory is a type of field theory in which the Lagrangian, which describes the dynamics of the fields, does not change under certain transformations of the fields. These transformations are known as gauge transformations. The invariance of the Lagrangian implies that the physical observables are unchanged by these gauge transformations. These transformations are considered symmetry transformations because they do not alter the Lagrangian, thus leaving the physical dynamics unchanged. This concept is analogous to symmetry operations in physical space, such as rotating a sphere around its axis, which returns it to an indistinguishable state. The mathematical transformation corresponding to rotation would be analogous to gauge transformation. However, gauge symmetries often involve transformations in more abstract internal spaces associated with the fields. These gauge transformations form the mathematical group known as a Lie group, which requires that the field is smooth and continuous transformation is possible across all points in space-time. The generators of the Lie groups are associated with gauge fields that act as force carriers. These force carriers, such as photons, gluons, W, and Z bosons, mediate the interactions between particles.

Symmetry plays a fundamental role in particle physics, and Emmy Noether's theorem [2] provides a profound insight linking the symmetries and conservation laws. According to Emmy Noether's theorem, every continuous symmetry (differentiable symmetry) of the action of a physical system corresponds to a conservation law. For example, translational symmetry in space leads to the conservation of momentum, rotational symmetry leads to the conservation of angular momentum, and translation symmetry in time leads to the conservation of energy. Additionally, gauge transformations of the field, which are another type of symmetry, lead to the conservation of specific charges, for example, electric charge in quantum electrodynamics (QED) and color charge in quantum chromodynamics (QCD).

2.1.1 Local gauge invariance and emergence of gauge bosons

This section explores the role of the local phase invariance in particle physics. Similar to translational symmetry, the physics should not depend on the local phase of the field. To

make the Lagrangian invariant under local phase transformations of the field, it requires the introduction of a gauge field. This is the key idea behind the gauge theory. As this thesis focuses on the top quark and photon coupling, it is important to understand how the photon couples to the fields with electric charge. The following discussion focuses on the coupling of the photon with the electron field; however, the same principles apply to the top quark field and photon coupling.

An electron is described by a complex filed $\psi(x)$ and a Lagrangian describing the dynamics of the electron is given by

$$\mathcal{L} = \bar{\psi}(i\gamma^\mu \partial_\mu - m)\psi, \tag{2.1}$$

where $\bar{\psi} = \psi^\dagger \gamma^0$ is the Dirac adjoint of the electron field, γ^μ are the Dirac matrices, ∂_μ is the derivative operator, and m is the mass of the electron. The Lagrangian is invariant under global phase transformation $\psi \to e^{i\alpha}\psi$ where α is a real constant. The family of phase transformations given by $U(\alpha) \equiv e^{i\alpha}$ forms a unitary Abelian group known as U(1). As shown below, the Lagrangian remains invariant under global phase transformation.

$$\bar{\psi} \to e^{-i\alpha}\bar{\psi}, \tag{2.2}$$

$$\mathcal{L} = \bar{\psi}(i\gamma^\mu \partial_\mu - m)\psi = \bar{\psi}e^{i\alpha}(i\gamma^\mu \partial_\mu - m)e^{-i\alpha}\psi = \bar{\psi}(i\gamma^\mu \partial_\mu - m)\psi. \tag{2.3}$$

However, the Lagrangian is not invariant under the local phase transformation $\psi \to e^{i\alpha(x)}\psi$ where $\alpha(x)$, the phase depends on space-time points (thus local). The last term of $\mathcal{L}$ remains invariant while the derivative term $\partial_\mu \alpha(x)$ breaks the invariance.

$$\partial_\mu \psi \to e^{i\alpha(x)}\partial_\mu \psi + ie^{i\alpha(x)}\psi \partial_\mu \alpha. \tag{2.4}$$

In order to make the Lagrangian invariant under a local phase transformation, a modified derivative operator is introduced, which transforms the field covariantly under local phase transformation. The modified derivative operator is given by

$$D_\mu = \partial_\mu - ieA_\mu. \tag{2.5}$$

The Lagrangian becomes invariant under local phase transformation:

$$D_\mu \psi \to e^{i\alpha(x)} D_\mu \psi. \tag{2.6}$$

To form the covariant derivative, the gauge field A_μ is introduced. The gauge field A_μ is a vector field that transforms under local phase transformation as

$$A_\mu \to A_\mu + \frac{1}{e}\partial_\mu \alpha(x). \tag{2.7}$$

Hence, by demanding local phase invariance of the Lagrangian, the gauge field A_μ emerges. The gauge field A_μ is the mediator of the electromagnetic force and it couples to the electron field. This leads to the Lagrangian of QED:

$$\mathcal{L}_{\text{QED}} = \bar{\psi}(i\gamma^\mu D_\mu - m)\psi + e\bar{\psi}\gamma^\mu A_\mu \psi - \frac{1}{4}F_{\mu\nu}F^{\mu\nu}, \tag{2.8}$$

where $F_{\mu\nu} = \partial_\mu A_\nu - \partial_\nu A_\mu$ is the field strength tensor of the gauge field A_μ corresponding to the kinetic energy of the gauge field. The second term in the Lagrangian is the interaction term between the electron field and the gauge field.

Quantum Chromodynamics (QCD) describes the strong force, which arises from the color charge of quarks. The transformations from one color to another form a $SU(3)_C$ group. In this case, making the Lagrangian local phase invariant under $SU(3)_C$ transformations (or making $SU(3)_C$ transformations gauge invariant way) leads to the conservation of color charge and the introduction of the gluon fields. The gluon fields are the mediators of the strong force. The Lagrangian of QCD is given by:

$$\mathcal{L}_{\text{QCD}} = \bar{\psi}(i\gamma^\mu D_\mu - m)\psi - \frac{1}{4}G_{\mu\nu}G^{\mu\nu}. \tag{2.9}$$

Here, the covariant derivative is defined as:

$$D_\mu = \partial_\mu - ig_S\frac{\lambda^a}{2}G^a_\mu, \tag{2.10}$$

where g_S is the coupling constant of the strong force, λ^a are the Gell-Mann matrices representing the generators of the $SU(3)_C$ group, and G^a_μ are the gluon fields. Each gluon field corresponds to one of the eight generators of $SU(3)_C$. The field strength tensor $G_{\mu\nu}$ is defined by:

$$G^a_{\mu\nu} = \partial_\mu G^a_\nu - \partial_\nu G^a_\mu + g_S f^{abc} G^b_\mu G^c_\nu, \tag{2.11}$$

where f^{abc} are the structure constants of $SU(3)_C$, representing the non-commutative interactions between gluons. This term contributes to the self-interaction properties of gluons that are unique to the strong force. This structure of the Lagrangian ensures that

under local $SU(3)_C$ transformations, not only does the quark field transform covariantly, but the gluon fields themselves also adjust in a way that maintains overall gauge invariance.

To preserve the local gauge invariance of the Lagrangian, the gauge bosons must be massless. In QED and QCD, the photon and gluons are massless. However, the weak force is mediated by the W and Z bosons, which are massive. This contradiction is resolved by the Higgs mechanism, which introduces a scalar field called the Higgs field. The Higgs field acquires a non-zero vacuum expectation value, leading to the spontaneous breaking of the electroweak symmetry and generating masses for the gauge bosons and fermions.

2.1.2 The SM Lagrangian

The SM Lagrangian is given by

$$\mathcal{L}_{\text{SM}} = \mathcal{L}_{\text{Gauge}} + \mathcal{L}_{\text{Matter}} + \mathcal{L}_{\text{Yukawa}} + \mathcal{L}_{\text{Higgs}}. \tag{2.12}$$

The first term corresponds to the pure gauge terms [3]:

$$\mathcal{L}_{\text{Gauge}} = -\frac{1}{2g_S^2}\text{Tr}G_{\mu\nu}G^{\mu\nu} - \frac{1}{2g^2}\text{Tr}W_{\mu\nu}W^{\mu\nu} - \frac{1}{4g'^2}\text{Tr}B_{\mu\nu}B^{\mu\nu}, \tag{2.13}$$

where $G_{\mu\nu}$, $W_{\mu\nu}$, and $B_{\mu\nu}$ are the field strength tensors of the gauge fields (representing the kinetic energy or the gauge field) corresponding to the strong, weak, and electromagnetic forces respectively. The g_S, g, and g' are the coupling constants of the strong, weak, and electromagnetic forces respectively.

The second term in the Lagrangian represents the matter Lagrangian which describes the interaction of the fermions and the gauge fields which is contained in the covariant derivative. It is given by [3]

$$\mathcal{L}_{\text{Matter}} = i\bar{Q}_L^i D_\mu Q_L^i + i\bar{u}_R^i D_\mu u_R^i + i\bar{d}_R^i D_\mu d_R^i + i\bar{L}_L^i D_\mu L_L^i + i\bar{e}_R^i D_\mu e_R^i, \tag{2.14}$$

where Q_L^i, u_R^i, d_R^i, L_L^i, and e_R^i are the left-handed quark doublets, right-handed up quark, right-handed down quark, left-handed lepton doublet, and right-handed electron respectively. The index i represents the generation of the fermion.

The covariant derivative is given by

$$D_\mu = \partial_\mu - ig_S\frac{\lambda^a}{2}G_\mu^a - ig\frac{\sigma^i}{2}W_\mu^i - ig'\frac{Y}{2}B_\mu, \tag{2.15}$$

where λ^a, σ^i, and Y are the generators of the $SU(3)_C$, $SU(2)_L$, and $U(1)_Y$ respectively.

The third term of the Lagrangian is the Yukawa interaction of the Higgs field with the fermion fields. This Yukawa interaction gives the mass to the fermion. The Yukawa Lagrangian is given by [3]

$$\mathcal{L}_{\text{Yukawa}} = -y^u_{ij}\bar{Q}^i_L\tilde{\phi}u^j_R - y^d_{ij}\bar{Q}^i_L\phi d^j_R - y^e_{ij}\bar{L}^i_L\phi e^j_R + \text{h.c.}, \tag{2.16}$$

where $\tilde{\phi} = i\sigma^2\phi^*$ is the conjugate of the Higgs field ϕ, y^u_{ij}, y^d_{ij}, and y^e_{ij} are the Yukawa couplings of the up-type quarks, down-type quarks, and charged leptons respectively. The i and j are the generation indices.

The final part of the SM Lagrangian is the Higgs Lagrangian which describes the kinetic and potential energy of the Higgs field. The Higgs Lagrangian is given by

$$\mathcal{L}_{\text{Higgs}} = (D_\mu\phi)^\dagger(D^\mu\phi) - V(\phi), \tag{2.17}$$

where the potential energy of the Higgs field is given by

$$V(\phi) = -\mu^2\phi^\dagger\phi + \lambda(\phi^\dagger\phi)^2 \tag{2.18}$$

The λ is the self-coupling constant of the Higgs field. The coefficient of the quadratic term μ^2 is the only dimensionful parameter in the SM. The sign of the μ^2 was chosen to be negative which gives the Higgs field a non-zero vacuum expectation value. This non-zero value leads to the spontaneous breaking of electroweak symmetry, thereby generating masses for W, Z bosons and fermions [3].

$$M_W = \frac{1}{2}vg, \quad M_Z = \frac{1}{2}v\sqrt{g^2+g'^2}, \quad m_f = \frac{y_f}{\sqrt{2}}v, \tag{2.19}$$

where y_f is the Yukawa coupling of the fermion f, and $v = \sqrt{-\mu^2/\lambda}$ is the vacuum expectation value of the Higgs field.

Shortcomings of the SM Although the SM is a huge success in explaining the fundamental particles and their interactions as proved by the excellent agreement with a plethora of experimental results, it fails to explain several phenomena observed in nature. Some of the shortcomings of the SM are listed below which indicate that the SM is not the ultimate theory of nature and there is a need for a more comprehensive theory that can explain these phenomena.

Gravity The SM explains three out of four fundamental forces known to us, namely the electromagnetic, weak, and strong forces. However, it cannot explain the gravitational interaction. The theory of general relativity explains the gravitational force with great accuracy but doesn't have a quantum description and does not fit into the SM. Many theories like string theory and loop quantum gravity have been proposed to unify the gravitational force with the other fundamental forces but none of them tested with experiments yet.

Dark matter and dark energy From the astrophysical observations such as rotation curves of galaxies, and gravitational lensing, it is known that the visible matter accounts for approximately 5% of the universe. The rest of the universe is made up of dark energy (approximately 68%) and dark matter (approximately 27%). The SM does not explain the dark matter and dark energy.

Neutrino In the SM the neutrinos do not have mass. However, the experimental observations from the neutrino oscillation experiments have shown that neutrinos have mass.

There are several other phenomena like matter-antimatter asymmetry, hierarchy problem, strong charge-parity (CP) problem, etc. which are not explained by the SM [4–6].

2.2 The top quark

In SM, the top quark is the most massive (≈ 173 GeV) of all observed elementary particles with a very short lifetime ($\approx 5 \times 10^{-25}$ s). It gets its mass from the coupling with the Higgs field. The top quark is a spin-$\frac{1}{2}$ fermion like all other quarks and leptons. It carries an electric charge of $+\frac{2}{3}e$ and is a color triplet. It forms a weak isospin doublet with the bottom quark. The top quark participates in strong, weak, and electromagnetic interactions. The lifetime of the top quark is about a twentieth of the timescale for the strong interaction, and therefore it decays before it forms hadrons with other quarks. This gives a unique opportunity to study the bare quark itself. The top quark decays almost exclusively to a W boson and a b quark. The branching ratio of the top quark decay to a W boson and a b quark is $\approx 99\%$.

2.2.1 Top quark mass

The top quark gets its mass from interacting with the Higgs field. The Yukawa coupling of the top quark to the Higgs field is the largest among all the fermions and it is close

to unity, that is why the top quark is the heaviest among all elementary particles. The Yukawa coupling in the SM has the following form:

$$\mathcal{L} = -y_t \bar{\psi}_t \phi \psi_t, \tag{2.20}$$

where y_t is the Yukawa coupling of the top quark, ψ_t is the top quark field, ϕ is the Higgs field. The mass of the top quark is given by:

$$m_t = \frac{y_t v}{\sqrt{2}}, \tag{2.21}$$

where v is the vacuum expectation value of the Higgs field.

The most precise result of the top quark mass measurement comes from the CMS and ATLAS experiments is $m_t = 172.52 \pm 0.33$ GeV [7], which is obtained by combining several measurements.

2.2.2 Top quark production

The top quark is very massive, and a significant amount of energy is needed to produce one. This amount of energy is only available in cosmic rays and high-energy particle colliders. After the Tevatron experiment in Fermilab, the LHC is the only collider with sufficient beam energy to produce top quarks. There are various processes through which top quarks can be produced, which can be divided into two categories: single top quark production and top quark pair production.

Top quark pair production At the LHC the most common process for top quark production is the pair production of top quark and top antiquark. Top quark pairs can be produced through the following processes:

- **Quark-antiquark annihilation:** A top quark and a top antiquark are produced by the annihilation of a quark and an antiquark. An example Feynman diagram at leading order (LO) for this process is shown in Figure 2.2 (a).
- **Gluon-gluon fusion:** A top quark and top antiquark are produced by the fusion of two gluons. The Feynman diagram for this process is shown in Figure 2.2 (b).
- **t-channel:** A top quark pair can also be produced via the t-channel process in which two gluons interact, resulting in the exchange of a virtual top quark and the production of a top and a top antiquark, which is illustrated in Figure 2.2 (c).

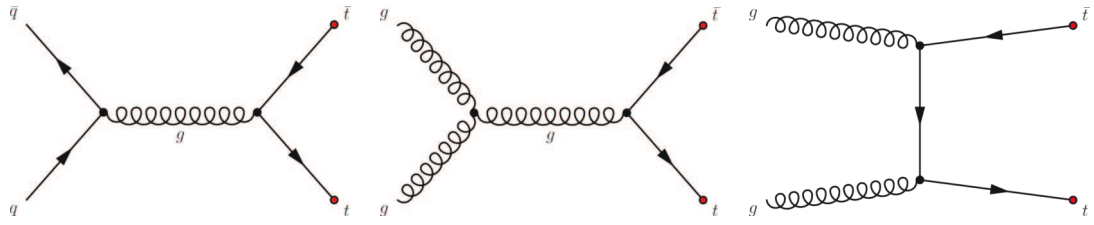

(a) **(b)** **(c)**

Figure 2.2: Examples of LO Feynman diagrams for top quark pair production through (a) quark-antiquark annihilation, (b) gluon-gluon fusion, and (c) t-channel production.

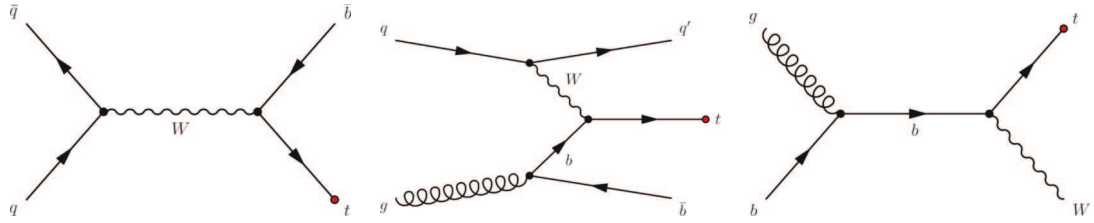

(a) **(b)** **(c)**

Figure 2.3: Examples of LO Feynman diagrams for single top quark production through (a) s-channel, (b) t-channel, and (c) tW-channel.

Single top quark production Top quarks can be produced singly through the following processes:

- **s-channel:** A top quark is produced by the annihilation of a quark and an antiquark to produce a virtual W boson, which then decays into a top quark and a b quark. A LO Feynman diagram for this process is shown in Figure 2.3 (a).
- **t-channel:** In the t-channel single top quark production, a quark exchanges a virtual W boson with a bottom quark coming from gluon splitting, resulting in the production of a top quark. A LO Feynman diagram is shown in Figure 2.3 (b).
- **tW-channel:** In the tW-channel production, a gluon interacts with a bottom quark to produce a top quark and a W boson. A LO Feynman diagram is shown in Figure 2.3 (c).

2.2.3 Top quark decay

The top quark decays via the electroweak charged-current process $t \to W^+q$, where q is a down type quark. The top quark decays almost exclusively to a W boson and a b quark via weak interaction in the SM. The expected branching ratio of the top quark decay to

a W boson and a b quark $\mathrm{BR}(t \to Wb) = \Gamma(t \to Wb)/\sum_{d,s,b}\Gamma(t \to Wq) = 0.998$ for a unitary Cabibo-Kobayashi-Maskawa (CKM) matrix [8].

The top quark decay is described in the SM Lagrangian in following way:

$$\mathcal{L}_{Wtb} = -\frac{g}{\sqrt{2}}\bar{q}\gamma^{\mu}V_{tq}\frac{1}{2}(1-\gamma_5)tW_{\mu}^{-} + h.c., \tag{2.22}$$

where g is the electroweak coupling constant, V_{tq} is the element of the CKM matrix. The total decay width of the top quark at LO is given by:

$$\Gamma_b^{\mathrm{LO}} = \frac{G_F}{8\pi\sqrt{2}}m_t^3\left(1-\frac{m_W^2}{m_t^2}\right)^2\left(1+2\frac{m_W^2}{m_t^2}\right) \approx 1.5 \text{ GeV}, \tag{2.23}$$

where m_t and m_W are the masses of the top quark and W boson, respectively, $G_F = \sqrt{2}g^2/8m_W^2$ is the Fermi constant.

2.3 Top quark pair production in association with a photon

In the SM, the coupling between the top quark and photon is described by the interaction vertex:

$$\mathcal{L}_{t\gamma} = -\alpha_{\mathrm{em}}Q_t\bar{\psi}_t\gamma^{\mu}\psi_t A_{\mu}, \tag{2.24}$$

where α_{em} is the fine-structure constant, Q_t is the electric charge of the top quark, ψ_t is the top quark field, and A_{μ} is the photon field.

For quarks other than the top quark, this fermion-photon vertex can be studied directly through processes like $e^+e^- \to q\bar{q}$ production in electron-positron colliders. However, electron-positron colliders have not reached the center-of-mass energy required to produce top quarks. At the LHC, the coupling between the top quark and photon can be studied through the processes of top quark pair production in association with a photon ($t\bar{t}\gamma$) and single top quark production in association with a W boson and a photon. Many new physics models predict modifications to the top quark-photon vertex. For example, some models change the electric charge of the top quark to $Q_t = 4/3$ [9; 10], which has been ruled out by LHC experiments [11; 12]. Other models predict anomalous magnetic and electric dipole moments of the top quark [13; 14], which can be constrained by precisely measuring the $t\bar{t}\gamma$ production cross-section. The Lagrangian describing the coupling of the top quark and photon in these models can be written as:

$$\mathcal{L}_{t\bar{t}\gamma} = e\bar{\psi}_t\left[Q_t\gamma^{\mu} + \frac{i\sigma^{\mu\nu}}{2m_t}\left(C_{2,V}^{\gamma} + iC_{2,A}^{\gamma}\gamma_5\right)q_{\nu}\right]\psi_t A_{\mu}, \tag{2.25}$$

where e is the electric charge, Q_t is the electric charge of the top quark, m_t is the mass of the top quark, $\sigma_{\mu\nu} = \frac{i}{2}[\gamma_\mu, \gamma_\nu]$, and $C^{\gamma}_{2,V}$ and $C^{\gamma}_{2,A}$ are the magnetic and electric dipole moments of the top quark, respectively. The values of $C^{\gamma}_{2,V}$ and $C^{\gamma}_{2,A}$ are zero in the SM at tree level but acquire very small values when higher-order corrections are considered.

These parameters can be expressed in terms of effective field theory (EFT) operators as follows [15]:

$$C^{\gamma}_{2,V} = \Re(C_{tW} + C_{tB})\frac{2m_t m_Z}{\Lambda^2}, \qquad C^{\gamma}_{2,A} = \Im(C_{tW} + C_{tB})\frac{2m_t m_Z}{\Lambda^2}, \tag{2.26}$$

where C_{tW} and C_{tB} are the Wilson coefficients of the dimension-six operators, m_Z is the mass of the Z boson, and Λ is the energy scale of the new physics. By precisely measuring the $t\bar{t}\gamma$ cross-section, the values of C_{tW} and C_{tB} can be constrained.

Experimental status Although top quark pairs can be easily produced at the LHC, the top quark pair production in association with a photon ($t\bar{t}\gamma$) has a smaller cross-section in proton-proton collisions. The first evidence of the $t\bar{t}\gamma$ production was reported by the CDF collaboration [16] at the Tevatron. The first observation was reported by the ATLAS collaboration with the proton-proton collision data at a center-of-mass energy $\sqrt{s} = 7$ TeV with a significance of 5.3σ [17]. After that ATLAS and CMS performed further measurements using proton-proton collision data at $\sqrt{s} = 8$ and 13 TeV [18–24]. Also, for the first time, a measurement of the top quark charge asymmetry in $t\bar{t}\gamma$ production was performed by the ATLAS collaboration [25].

$t\bar{t}\gamma$ production The $t\bar{t}\gamma$ process can be produced through quark-antiquark annihilation and gluon-gluon fusion. Example LO Feynman diagrams are shown in Figure 2.4. In Figure 2.4, the photon is radiated during the production of the top quark pair, either from an off-shell top quark or from one of the initial quarks. These are collectively referred to as the radiative production process. In Figure 2.5, the photon is radiated either from an on-shell top quark, or any of the decay product of the top quark, referred to as the radiative decay process.

Theoretical calculations First calculations of the $t\bar{t}\gamma$ process ($pp \to t\bar{t}\gamma$) at next-to-leading order (NLO) in QCD were performed for on-shell top quarks, as presented in Ref. [26; 27]. The NLO electroweak (EW) corrections for the $t\bar{t}\gamma$ process were calculated in Ref. [28]. In all these calculations, the top quark was considered to be on-shell. Also, these calculations do not take into account the decay of the top quark. In Ref. [29] the NLO

QCD correction is matched with parton shower (PS) calculation. The top quark decay was included in the PS approximation omitting $t\bar{t}$ spin correlations and photon emission in the parton shower evolution. Fully realistic predictions for the $t\bar{t}\gamma$ process at NLO QCD with top quark decay taking into account the spin correlations and photon emission from the top quark decay were calculated using narrow-width approximation (NWA) in Ref. [30]. In Ref. [31] a complete description of $t\bar{t}\gamma$ in the dilepton top quark decay channel was presented which includes all resonant and non-resonant contributions, interference effects, and off-shell effects of the top quark and the W boson. It is based on the matrix element for $e^{+}\nu_{e}\mu^{-1}\nu_{\mu}b\bar{b}\gamma$. In Ref. [32] it is shown that for integrated cross-section the finite top quark width effects are small and of the order of $\mathcal{O}(\Gamma_t/m_t)$, where Γ_t is the top quark decay width, and NWA is a good approximation. Finally, approximate next-to-next-to-leading-order (NNLO) QCD corrections with second-order soft-gluon resummation for the $t\bar{t}\gamma$ process were calculated in Ref. [33].

In the NWA, the $t\bar{t}\gamma$ production can be factorized into two parts depending on whether the photon emission happens in the production part of the process (referred to as $t\bar{t}\gamma$ production) or the photon emission arises in the decay part of the process (referred to as $t\bar{t}\gamma$ decay). The former is sensitive to the top quark and photon coupling. In this thesis, the main focus is on measuring the $t\bar{t}\gamma$ production process, where the $t\bar{t}\gamma$ decay is treated as a background. Additionally, the total $t\bar{t}\gamma$ process, where photon emission from both the production and decay stages is considered as signal, is also measured.

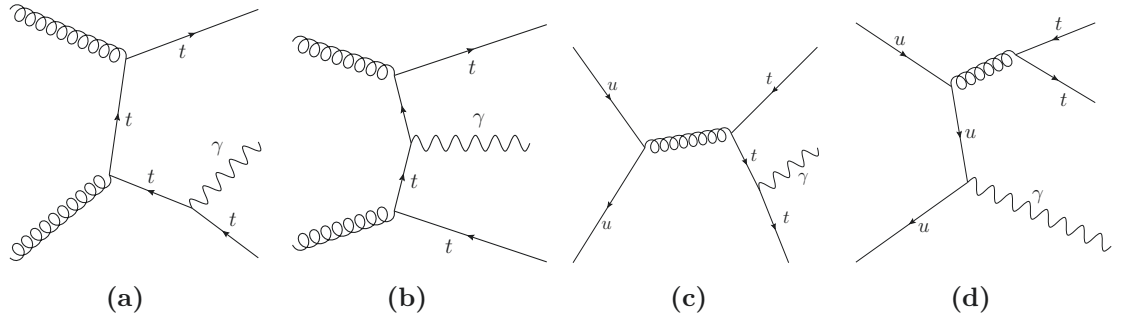

Figure 2.4: Feynman diagrams of $t\bar{t}\gamma$ production where the photon is radiated during production (a, b, c) and radiated from initial partons (d).

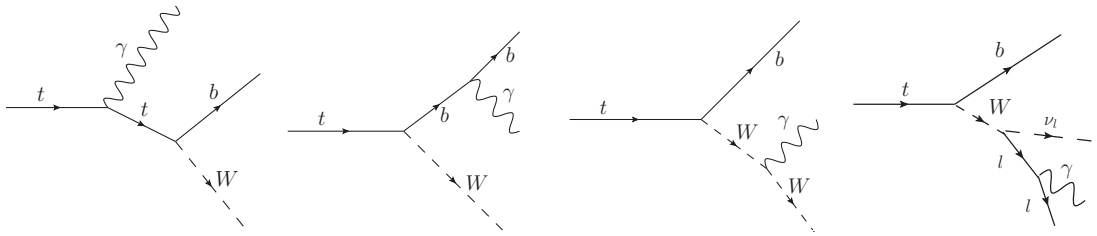

(a) **(b)** **(c)** **(d)**

Figure 2.5: Feynman diagrams illustrating the radiative decay of the top quark.

3 The LHC and ATLAS experiment

This chapter details the experimental setup used for the measurement of the $t\bar{t}\gamma$ process. The LHC produces proton-proton collision events, which are then recorded by the ATLAS experiment. The LHC has four interaction points where the proton-proton collisions take place. The ATLAS experiment is one of the four main experiments at the LHC. It is a general-purpose detector designed to explore a wide range of physics topics. This thesis focuses on analyzing the data collected by the ATLAS detector to measure the cross-section of the $t\bar{t}\gamma$ process. The chapter provides an overview of the LHC, describes the components and capabilities of the ATLAS detector, and outlines the algorithms employed to reconstruct different physics objects from the collision data.

3.1 The Large Hadron Collider

The LHC [34] is the world's largest and most powerful particle accelerator. It is located at the European Organization for Nuclear Research (CERN), on the border between France and Switzerland. The LHC is a circular accelerator with a circumference of 26.7 kilometers situated in an underground (approximately 100 m) tunnel. The tunnel was initially built and used by the Large Electron-Positron collider (LEP). The LHC is designed to accelerate protons and heavy ions to high energies and then collide them at four interaction points, where the four main experiments ATLAS, ALICE, CMS, and LHCb are located. Other smaller experiments are also located around the LHC ring. The LHC was built to explore a wide range of physics topics, including the search for the Higgs boson, extra dimensions, and particles that could make up dark matter. The LHC started operation in 2008 and has been running successfully since then, producing a large amount of data that has led to many important discoveries and precise measurements in particle physics. One of the most important discoveries was the discovery of the Higgs boson in 2012 observed by the ATLAS and the CMS detector.

The LHC is a two-ring-superconducting-hadron accelerator, with two beams of particles circulating in opposite directions. Each beam contains a maximum of 2800 bunches

of protons, with each bunch containing approximately 10^{11} protons. The bunches are accelerated by radio frequency (RF) cavities and focused by superconducting magnets. The RF cavities are designed to oscillate at a specific frequency and provide an electric field to accelerate the particles. The superconducting magnets are designed to provide a very strong magnetic field to keep the particles on track and focused. The superconducting magnets are made of niobium-titanium and niobium-tin, and they are cooled to a temperature of 1.9 K using liquid helium. To prevent collisions with gas molecules, the beams are confined within a vacuum pipe. A system of collimators ensures precise beam control, and at the end of the acceleration cycle, the beams are safely directed into a beam dump.

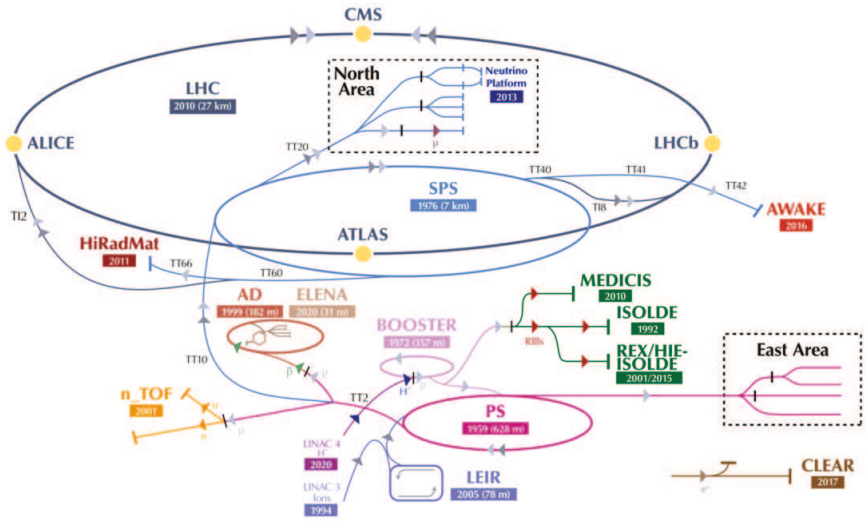

Figure 3.1: The CERN accelerator complex where proton beams are accelerated in different stages before being injected into the LHC. The LHC is the last stage of the accelerator complex.[Image credit: CERN]

Before the proton bunches are injected into the LHC, they undergo a series of pre-accelerations using various accelerators. The process begins with the extraction of protons from ionized hydrogen gas, forming bunches containing approximately 10^{11} protons each. These protons are first accelerated in a linear accelerator (LINAC2), which is about 80 meters long and employs RF cavities to boost the protons to a maximum energy of 50 MeV.

Next, the proton bunches are injected into the Proton Synchrotron Booster (PSB), a circular accelerator that increases their energy to about 1.4 GeV. The accelerated protons are then transferred to the Proton Synchrotron (PS), a larger circular accelerator that further boosts their energy to approximately 25 GeV. Subsequently, the protons enter the Super Proton Synchrotron (SPS), another circular accelerator, where their energy is

elevated to about 450 GeV. Both the PS and SPS utilize dipole and quadrupole magnets to steer and focus the proton beams. Finally, the protons are injected into the two separate rings of the LHC, where they are accelerated in opposite directions and made to collide at four designated interaction points.

The design luminosity of the LHC is 10^{34} $\text{cm}^{-2}\text{s}^{-1}$ for proton-proton collisions, with a design center-of-mass energy of 14 TeV [34]. For heavy ion (Pb) collisions, the design energy is 2.8 TeV per nucleon, with a peak luminosity of 10^{27} $\text{cm}^{-2}\text{s}^{-1}$ [34]. The LHC operated at a center-of-mass energy of 7 TeV in 2010 and 2011, and at 8 TeV in 2012 for proton-proton collisions. After a two-year shutdown for upgrades and maintenance, the LHC restarted in 2015 at a center-of-mass energy of 13 TeV. A long shutdown occurred from 2019 to 2021 for further upgrades and maintenance, and the LHC resumed operations in 2022 at a center-of-mass energy of 13.6 TeV.

3.2 The ATLAS experiment

The ATLAS detector has a cylindrical shape with an onion-like structure, measuring 44 meters in length and 25 meters in diameter. Its various components are arranged in concentric layers around the beam pipe. The detector is composed of three main sections: the inner detector, the calorimeter, and the muon spectrometer. A computer-generated cut-away view of the ATLAS detector is shown in Figure 3.2.

The inner detector measures the direction, momentum, and charge of electrically charged particles. It consists of three sub-detectors: the pixel detector, silicon microstrip trackers, and the transition radiation tracker, all immersed in a 2 T magnetic field parallel to the beam axis, provided by the central solenoid.

The calorimeter measures the energy of particles by stopping them and quantifying the energy deposited in its cells. It is divided into two primary parts: the tile calorimeter and the LAr (Liquid Argon) calorimeter. The tile calorimeter measures the energy of hadrons, electrons, and photons, while the LAr calorimeter specifically measures the energy of electrons and photons.

The muon spectrometer measures the momentum of muons by accurately tracking their paths. It operates within a strong magnetic field generated by the toroid magnet.

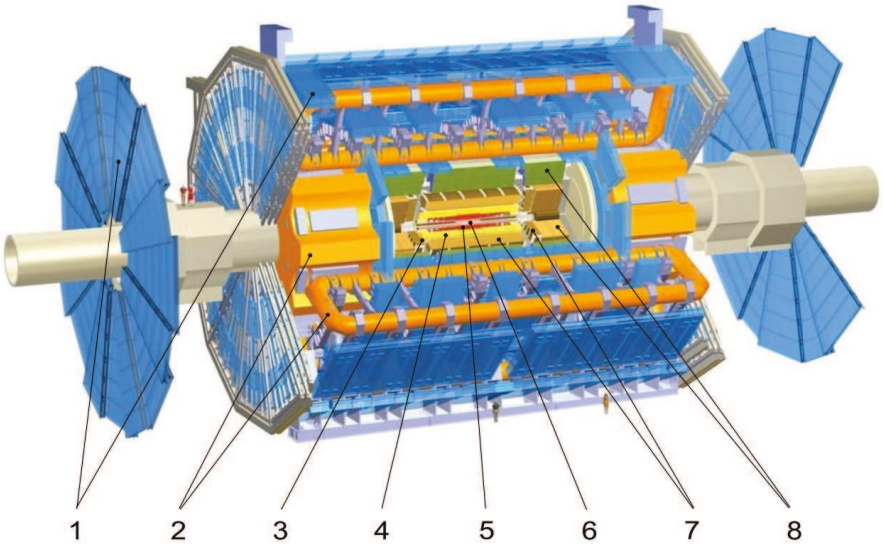

Figure 3.2: Computer generated cut-away view of the ATLAS detector at the LHC. The various components of the detector are (1) Muon spectrometer in forward and barrel region (2) Toroid magnet in froward and barrel region (3) Solenoid magnet (4) Transition radion tracker (5) Semi-conductor tracker (6) Pixel detector (7) Liquid Argon calorimeter (8) Tile calorimeter

3.2.1 The ATLAS coordinate system

The ATLAS detector has a cylindrical shape with a beam pipe along the z-axis. The x-y plane is perpendicular to the beam axis. The x-axis points towards the center of the LHC ring, the y-axis points upwards. ATLAS uses a slightly modified version of the cylindrical coordinate system, where the polar angle θ is replaced by the pseudorapidity η defined as

$$\eta = -\ln\left(\tan\left(\frac{\theta}{2}\right)\right). \tag{3.1}$$

The azimuthal angle ϕ remains unchanged. Quantities in the x-y plane with x and y components are replaced by a single transverse component. The transverse component stays invariant under Lorentz boost along the z-axis. For example, the momentum of a particle is replaced by the transverse momentum p_{T} defined as

$$p_{\mathrm{T}} = \sqrt{p_x^2 + p_y^2}. \tag{3.2}$$

The angular distance between two particles can be expressed as $\Delta R = \sqrt{(\Delta\eta)^2 + (\Delta\phi)^2}$, where $\Delta\eta$ and $\Delta\phi$ are the differences in pseudorapidity and azimuthal angle between the two particles.

3.2.2 The inner detector

The pixel detector The pixel detector is the innermost part of the ATLAS detector. It is used to measure the tracks of charged particles with high precision. There are four layers (IBL, B-layer, L0, L1) of pixel sensors arranged in a concentric cylinder around the beam pipe and there are three disks with pixel sensors in each endcap side of the detector. The first layer IBL is as close as 3.3 cm from the LHC beam pipe. The pixel detector is made up of silicon pixels with each pixel having a size of $50 \times 400\mu\text{m}^2$ for the external layers and $50 \times 250\mu\text{m}^2$ for the innermost IBL layer. The pixel detector has a resolution of 10 μm in the η-ϕ plane. The pixel detector has around 92 million pixels and all of them are read out every 25 ns. The particles coming out of the collision point will pass through the pixel detector and leave a charge in the pixels. These signals are read out to determine the position of the particles. The pixel detector can measure tracks up to $|\eta| < 2.5$ [35].

The semiconductor tracker The semiconductor tracker (SCT) surrounds the pixel detector and is used to detect and reconstruct the tracks of the charged particles produced during collision. The SCT is composed of silicon microstrip sensors. The SCT has eight layers of silicon sensors in the barrel region and nine disks in the endcap region. The mean pitch of the sensors is 80 μm. There are a total 4000 modules and 6.3 million readout channels in the SCT. The SCT also cover the same η range as the pixel detector, $|\eta| < 2.5$ [35].

The transition radiation tracker The transition radiation tracker (TRT) is a straw tube detector, with the tubes placed parallel to the beam pipe in the barrel region and perpendicular to the beam pipe in the endcap region. The hits in the TRT detector are used for tracking. In addition, the TRT is used to identify the particle, the transition radiation characteristic is different for different particles, this is used to identify light, ultra-relativistic electrons, and to distinguish them from pions or other hadrons. The TRT has a coverage of $|\eta| < 2.0$ [35].

3.2.3 The calorimeter system

Calorimeters are used to measure the energy of particles produced in collisions. When particles enter the calorimeter, they initiate a shower of secondary particles. The energy of

the original particles is determined by measuring the energy of these secondary particles. The ATLAS calorimeter is a sampling calorimeter, meaning it alternates layers of passive material (to absorb particles) and active material (to generate and read out signals). There are two primary calorimeter systems in the ATLAS detector: the electromagnetic calorimeter (EM) and the hadronic calorimeter (HCAL). While the EM calorimeter is primarily designed to measures the energy of electrons and photons, hadrons can also deposit a fraction of their energy in the EM calorimeter. The HCAL is specifically designed to fully absorb the hadronic shower and measures the energy of hadrons.

The calorimeter system covers a wide range up to $|\eta| < 4.9$. Within the region covered by the inner detector, the calorimeter has finer granularity for precision measurements. In other regions, the granularity is coarser but sufficient for jet reconstruction and $E_{\mathrm{T}}^{\mathrm{miss}}$ measurements. A good calorimeter must provide effective containment of particle showers and limit the punch-through of particles to the muon spectrometer. The total thickness of the EM calorimeter is greater than 20 radiation lengths in the barrel region and greater than 24 radiation lengths in the endcap region. The EM calorimeter is divided into barrel ($|\eta| < 1.475$) and endcap ($1.375 < |\eta| < 3.2$) sections. It is a lead-LAr sampling calorimeter, where lead acts as the passive absorber and liquid argon (LAr) serves as the active medium.

The HCAL is also divided into barrel and endcap regions, positioned outside the EM calorimeter. The HCAL consists of three parts: the tile calorimeter in the barrel region, the LAr hadronic calorimeter in the endcap region, and the LAr forward calorimeter in the forward region. The HCAL is a sampling calorimeter as well. In the tile calorimeter, steel is the passive material and scintillating tiles are the active medium, with the signals read out using photomultiplier tubes. The barrel part of the HCAL covers $|\eta| < 1.0$. The extended barrel part covers $0.8 < |\eta| < 1.7$. The endcap part covers $1.5 < |\eta| < 3.2$. The forward part covers $3.1 < |\eta| < 4.9$.

3.2.4 The muon spectrometer

The muon spectrometer (MS) is the outermost part of the ATLAS detector. It is used to measure the momentum of muons based on the deflection of their tracks in the magnetic field. The muon spectrometer consists of four different types of detectors: the Monitored Drift Tubes (MDT), the Cathode Strip Chambers (CSC), the Resistive Plate Chambers (RPC), and the Thin Gap Chambers (TGC). The muon spectrometer is immersed in a 4 T magnetic field provided by the superconducting air-core toroid magnets in both the barrel and endcap regions. In the range $|\eta| < 1.4$, the magnetic field is provided by the barrel toroid magnet. In the range $1.6 < |\eta| < 2.7$, the magnetic field is provided by the endcap

toroid magnet. The region $1.4 < |\eta| < 1.6$ is known as the transition region, where both the barrel and endcap toroid magnets contribute to the magnetic field.

3.2.5 The trigger system

At the center of the ATLAS detector, proton-proton collisions occur at a maximum rate of 40 MHz. However, not all collision events are of interest, and reading out and storing data at this rate poses significant challenges, requiring vast amounts of storage. The trigger system is used to reduce the event rate to a manageable level by selecting only the interesting events. The ATLAS trigger system is divided into two levels: the Level-1 (L1) trigger and the High-Level Trigger (HLT).

The Level-1 trigger is a hardware-based system that reduces the event rate from 40 MHz to 100 kHz. The L1 trigger decision is made by the Central Trigger Processor (CTP), which uses information from the calorimeter and the muon spectrometer. Additionally, the CTP is responsible for applying preventive dead-time between two consecutive L1 trigger accepts to avoid overlapping readout windows and for restricting the number of L1 accepts in a given number of bunch crossings to prevent buffer overflow in the front-end electronics.

After the L1 trigger decision, the event is passed to the HLT. The HLT is a software-based trigger system that further reduces the event rate from 100 kHz to 1 kHz. The HLT also receives information about regions of interest (RoI) from the L1 trigger, which can be used for reconstruction in the HLT software. The events that pass the HLT are saved to disk for further analysis.

3.3 Physics object reconstruction in ATLAS

At the heart of the ATLAS detector, proton-proton collisions occur at a rate of 40 MHz. We are interested in probing the hard interaction physics. The particles produced in the hard interaction are not directly observed; they undergo a series of decays to lighter particles before they reach the detector.

Electrons and muons have longer lifetimes, allowing high-momentum electrons and muons to reach the EM calorimeter (or the muon spectrometer for muons) after leaving tracks in the ID. The tau lepton, however, has a very short lifetime (approximately 10^{-13} seconds) and decays before reaching the detector. Quarks hadronize before they reach the detector, forming hadrons that can further decay until they become stable enough to travel through

the detector, ultimately being stopped by the HCAL. Below, different methods for the reconstruction of various physics objects in ATLAS are discussed.

3.3.1 Reconstruction of electrons and photons

High-energy electrons and photons travel through the detector until they are stopped by the EM calorimeter, where they lose energy through cascades of electromagnetic interactions. By measuring the energy of these showers, the energy of the original particle can be determined with high precision. Additionally, an electron, being charged, ionizes or excites the atoms in the detector material as it passes through the inner detector (ID). By measuring this ionization, the electron's path can be traced. Photons, being neutral, do not leave any track in the ID. However, sometimes a photon can decay into an electron-positron pair before reaching the EM calorimeter. In such cases, the conversion vertex, track information, and cluster energy can be used to reconstruct the photon. This type of photon is referred to as a *converted photon*, while a photon that directly interacts with the EM calorimeter is referred to as an *unconverted photon*.

The following briefly discusses the reconstruction of electron and photon objects (detailed in Ref. [36]). The first step in electron and photon reconstruction involves creating topological clusters (topo-clusters) from the energy deposits in the calorimeter cells [37]. After applying certain selections on the topo-clusters, the selected clusters define a region of interest (ROI) for track searches. Within these ROIs, standard track pattern recognition [38] is performed. If a seed track fails the pattern recognition, other pattern recognition methods with looser requirements are employed (Kalman filter formalism [39], global χ^2 fitter [40], Gaussian sum filter [41]). These tracks are then matched to EM clusters with tight $\eta - \phi$ requirements. Loosely matched tracks are used for conversion vertex reconstruction.

After track matching and vertex reconstruction, supercluster reconstruction is performed starting from a topo-cluster as the seed cluster. During this stage, nearby satellite clusters, which may result from bremsstrahlung radiation or topo-cluster splitting, are identified. These satellite clusters are merged with the seed cluster if they meet certain criteria, thus forming a supercluster. For photons, the supercluster is built from the seed topo-cluster without track requirements. The reconstruction algorithm flow is shown in Figure 3.3 [36]. The electron and photon superclusters are built independently, and there is a chance that the same energy deposit can be reconstructed as both an electron and a photon. An ambiguity resolution is performed to reduce the overlap [36]. Some overlap remains to maintain better object reconstruction efficiency, which is addressed at the analysis level. Finally, the energies of the resulting electron and photon objects are calibrated.

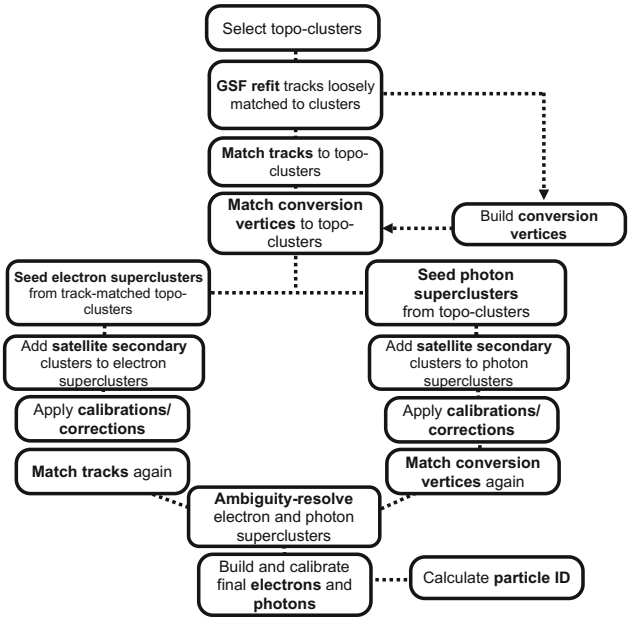

Figure 3.3: Flow-chart involving different stages for reconstruction of electron and photon in ATLAS [36].

3.3.2 Reconstruction of muons

A muon, being 200 times heavier than an electron, produces minimal bremsstrahlung radiation. Instead, it passes through the calorimeter with relatively little energy loss and minimal electromagnetic shower production. Muons can be measured using tracks in the MS. The strong toroidal magnetic field bends the path of the muon, allowing its momentum to be measured with very high precision. Additionally, muons deposit very little energy in the calorimeter, which can be useful for tracking. Tracks from the ID, calorimeter, and MS are combined for improved muon reconstruction. In ATLAS, muon track reconstruction is performed in two ways: (1) using only MS hits, and (2) using complete detector information.

The reconstruction of muon tracks using only MS hits is performed as follows (detailed in Ref. [42]). First, short-line local segments are identified using the Hough transform [43] from different MS stations. These segments are then combined to form preliminary track candidates by applying a loose pointing constraint based on the interaction point (IP) and a parabolic trajectory that represents the first-order approximation of muon bending in the magnetic field. A global χ^2 fit is then performed on the segments using the trajectory, taking into account possible misalignment of different chambers and other material effects.

Outlier hits are removed from the fitted track, and previously excluded hits along the track are added. A χ^2 fit is performed with the updated hit information, removing many ambiguities. Finally, the track is refitted with the full track information, a loose constraint on the IP, and considering energy loss in the calorimeter. The reconstruction of muon tracks using complete detector information is performed as detailed in Ref. [42].

3.3.3 Reconstruction of jets

In ATLAS, two different types of jets are reconstructed: small-radius jets and large-radius jets. Small-radius jets are primarily used in major physics analyses. Anti-k_t algorithm [44] with a radius parameter of 0.4, as implemented in the FastJet package [45] is used for jet clustering. The four-momentum of the particles, charged particle tracks, and calorimeter energy deposits are used as input. ATLAS employs particle-flow techniques [46] in jet reconstruction, which utilize both the calorimeter energy deposits and track information. In this technique, topological clusters are built from the calorimeter energy deposits and then matched with the primary vertex. Subsequently, the calorimeter energy deposit is replaced by the momentum measured by the track. This method significantly improves energy and angular resolution, reconstruction efficiency, and pileup stability. The jet energy and direction calibration are done in several steps, detailed in Ref. [47].

b-quark jet tagging b-tagging is used to identify jets originating from bottom quarks. Numerous algorithms have been developed in ATLAS over time. This analysis uses the DL1r tagger [48]. The DL1r tagger is a neural network-based tagger that uses information from the tracks and secondary vertices in the jet. The output is a multidimensional probability distribution corresponding to the identification probabilities of b-jets, c-jets, and light-flavor jets.

3.3.4 Reconstruction of missing transverse energy

The missing transverse energy ($E_{\mathrm{T}}^{\mathrm{miss}}$) estimates the amount of missing transverse momentum in an event. It is calculated using calibrated detector signals corresponding to muons, electrons, photons, hadronically decaying τ-leptons, and jets. The $E_{\mathrm{T}}^{\mathrm{miss}}$ is computed from the components along the x and y directions as follows:

$$E_{\mathrm{x(y)}}^{\mathrm{miss}} = E_{\mathrm{x(y)}}^{\mathrm{miss},\mu} + E_{\mathrm{x(y)}}^{\mathrm{miss},e} + E_{\mathrm{x(y)}}^{\mathrm{miss},\gamma} + E_{\mathrm{x(y)}}^{\mathrm{miss},\tau} + E_{\mathrm{x(y)}}^{\mathrm{miss,jet}} + E_{\mathrm{x(y)}}^{\mathrm{miss,soft}}, \tag{3.3}$$

where each term is calculated as the negative vectorial sum of the transverse momenta of the corresponding objects. More details can be found in Ref. [49]. The soft term, $E_{\mathrm{x(y)}}^{\mathrm{miss,soft}}$, is calculated using the calorimeter energy deposits not associated with any reconstructed object.

3.3.5 Overlap removal between objects

Different objects are reconstructed from the detector signatures independently of each other. This can lead to the same energy deposit being reconstructed as different objects. For example, a photon might be reconstructed as an electron, or a jet might be reconstructed as a photon. To avoid double counting energy deposits, an overlap removal procedure is performed. The overlap removal is carried out sequentially following the recommended procedure:

- If a muon candidate uses calorimeter information during reconstruction and it shares a track with electron candidate, the electron candidate is removed.
- Jets reconstructed within a cone of $\Delta R = 0.2$ around an electron are removed.
- Electrons reconstructed within a cone of $\Delta R = 0.4$ around the remaining jets are removed.
- If there are a muon and a jet close to each other, the jet is removed if it has no more than two associated tracks and is within $\Delta R < 0.2$ of the muon. Otherwise, the muon is removed if it is within $\Delta R < 0.4$ of the jet.
- Photons reconstructed within a cone of $\Delta R = 0.4$ around a remaining electron or muon are removed.
- Jets reconstructed within a cone of $\Delta R = 0.4$ around a remaining photon are removed.

4 Pixel RawDataAnalysis framework

This chapter introduces the RawDataAnalysis software framework, used by the ATLAS pixel detector group for analyzing raw data to help debug the data acquisition process. Data acquisition in the ATLAS pixel detector is a complex process that involves multiple steps: reading signals from the pixel sensor, converting them into digital data and then storing the data on disk. It is important to validate the data acquisition process not only at the hardware level but also by examining the data.

This tool was designed for commissioning the IBL(Insertable B-layer) detector for LHC Run 2. Its main goal is to provide a way to analyze raw data and to help debug and validate the data acquisition process.

In this chapter, the data acquisition system of the ATLAS pixel detector is described, followed by a discussion of the data format used in the ATLAS event data. The RawDataAnalysis framework is then introduced, along with its working principle and the structure of the decoded data. Finally, some example analyses using the framework are presented.

The work presented focuses on several significant developments and improvements to the framework. The decoded raw data structure in ROOT `TTree` [50] format was redesigned to store information more effectively and the compilation processes was optimized using CMake [51]. The framework now supports grid and Condor submissions, facilitating distributed processing and analysis. Additionally, the codebase was cleaned up and restructured for better readability. The validation of the package was conducted by comparing its output with that of the official ATLAS software, specifically the ByteStreamCnv package [52]. These improvements contribute to a more efficient and reliable data analysis process, supporting the broader goals of the ATLAS experiment.

4.1 Data acquisition system in ATLAS pixel detector

The fundamental building blocks of the pixel detector are modules that contain sensors and front-end (FE) electronics. The FE electronics are responsible for amplifying the signal, shaping it, providing a threshold discriminator, and generating a Time over Threshold

output [53]. During Run 2, the IBL was introduced, using the FE-I4 chip, whereas the other modules use the FE-I3 chip. The FE-I4 chip can read 26,880 pixels, while the FE-I3 chip can read 2,880 pixels. An IBL module has 2 FEs, whereas other pixel modules have 16 FEs in a single module.

In the IBL, the FEs are directly connected to the Optoboard [53], which is mounted near the detector. In contrast, for other layers and discs, the FEs are connected to Module Controller Chips (MCCs), which are then connected to the Optoboard. The Optoboard converts electrical signals to optical signals for faster data transmission from the detector to the read-out electronics, referred to as DAQ crates. These crates consist of a Single Board Computer (SBC) containing a BOC (Back of Crate) and ROD (Read-Out Driver) pair. The optical signal from the Optoboard is transmitted to the Rx plug-in mounted in the BOC. The BOC converts the optical signal into an electrical signal and de-multiplexes the data into 40 Mbit/s streams. The ROD then de-serializes and formats the bit streams, combining the formatted data with trigger information to form event fragments. The ROD is equipped with four Digital Signal Processors (DSPs), each with 256 MB of memory to sample and process the event data.

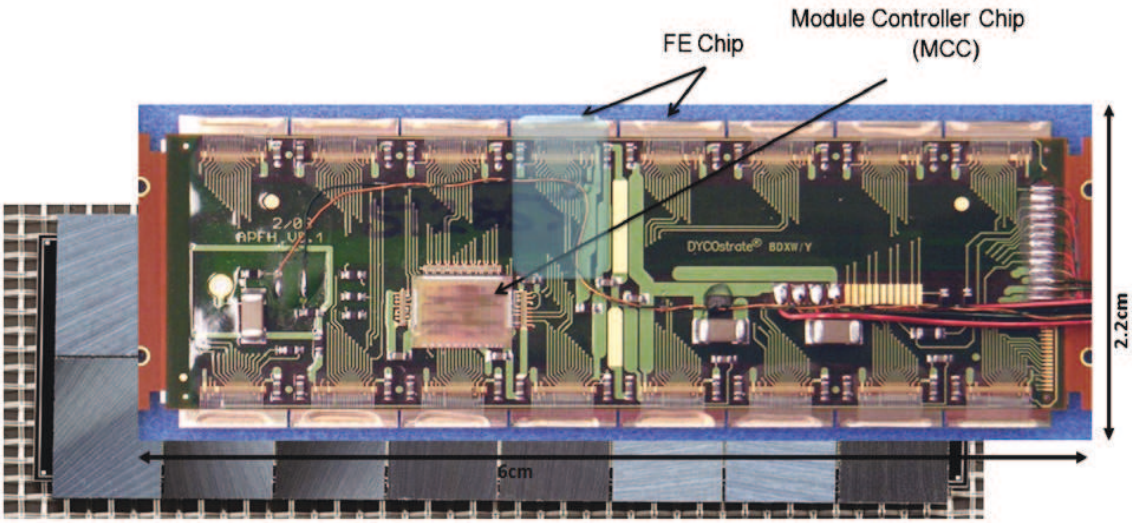

Figure 4.1: Image of a pixel module showing the pixel sensors and front-end electronics [53].

If the event is selected by the trigger system, the ROD sends the formatted data to the higher-level Read-Out System (ROS) by BOC via fast S-Links. The ROS is responsible for assembling the data from different RODs and organizing it into events. The ROS also performs data integrity checks and error corrections to ensure the reliability of the acquired data. The ROS sends the organized event data to the Event Builder (EB) system, where

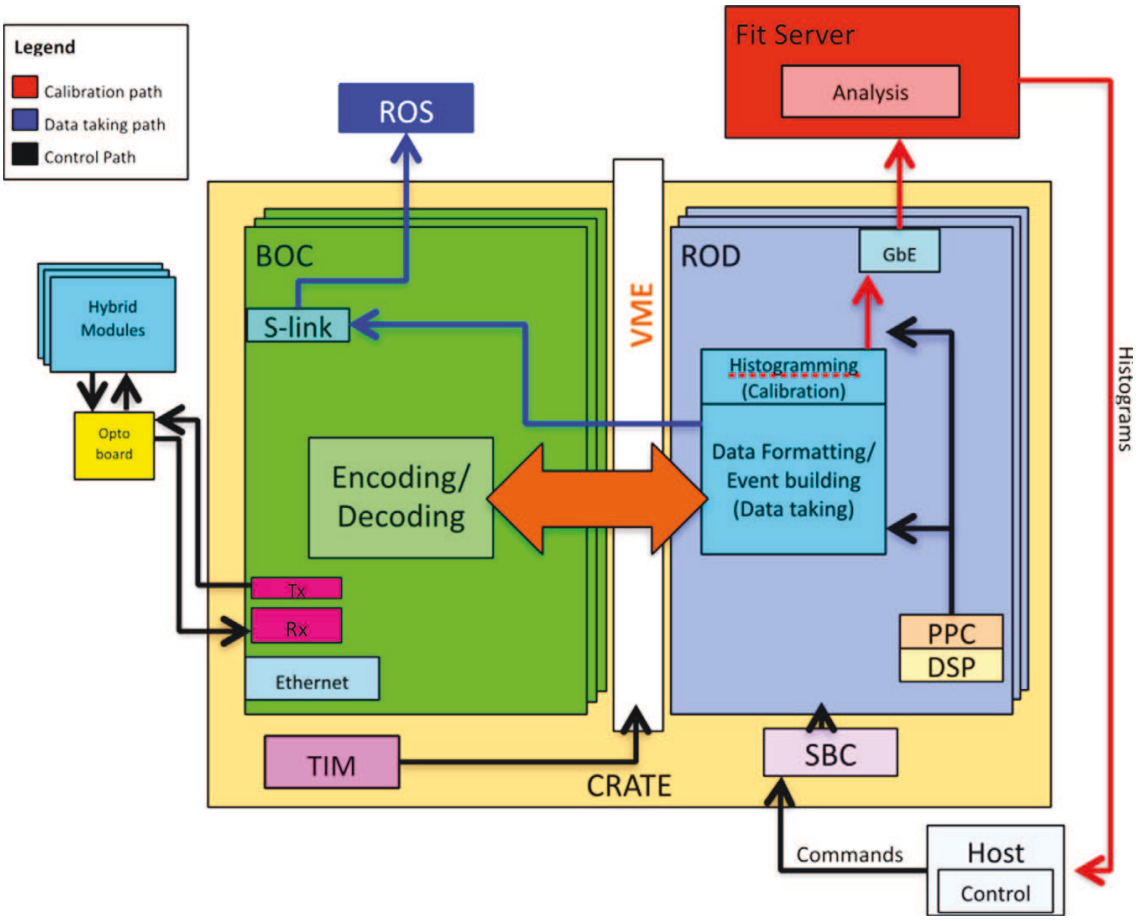

Figure 4.2: Flow chart showing the data acquisition system of the ATLAS pixel detector. The raw data from the pixel sensors is processed by the front-end electronics, transmitted to the RODs, and then organized into events by ROS and the EB systems [54].

the data from various sub-detectors are combined to form a complete event. The assembled events are then forwarded to the HLT system.

The HLT system, which is a software-based trigger, performs more sophisticated event selection than the hardware-based L1 trigger. It uses advanced algorithms and full event information to decide whether an event should be recorded for offline analysis or discarded. This decision is based on predefined physics criteria aimed at selecting events of interest for the ATLAS physics program.

4.2 Pixel data fragments on ATLAS event data

The general structure of a full event in ATLAS is shown in Figure 4.3. A full event consists of ROB fragments from different subdetectors, such as the pixel detector, the SCT, the TRT, and others. A Fragment is the formatted data from different stages of DAQ. The formatted data from the ROD is referred to as ROD fragments, and similarly from the ROS is referred to as ROB fragments. Each ROB fragment maps onto a single ROD fragment. The class diagram of the event format is shown in Figure 4.4. Except for the ROD fragment type, the other fragment types have a header that contains all the event formatting information. In general, every fragment has a header, data and trailer structure. The structure of the header is shown in Figure 4.5. The header has a generic part and a specific part. The specific part is a generalization of different types of fragments and can be different depending on the type of fragment and the sub-detectors. The structure of the ROD fragment is shown in Figure 4.6.

As mentioned earlier, for IBL one ROD reads out all FE-I4 chips of one stave which corresponds to 32 FE-I4 chips. For other layers, 16 FE-I3 chips connect to one MCC which is processed by a single ROD. The individual hit information from the module is stored in the data element part of the ROD fragment. The structure of the data element is a header, hit, FE-flag, and trailer, each of which is 32 bits. The time-over-threshold (ToT), row and column of pixel hit are encoded in the 32-bit hit word. As an example, the structure of the IBL module is shown in Figure 4.8, where the corrupted data is identified using the decoded information from the header or trailer.

4.3 The RawDataAnalysis framework

The goal of the RawDataAnalysis framework is to decode the full information from the raw data and store it in a format that is suitable for further analysis but it does not provide any

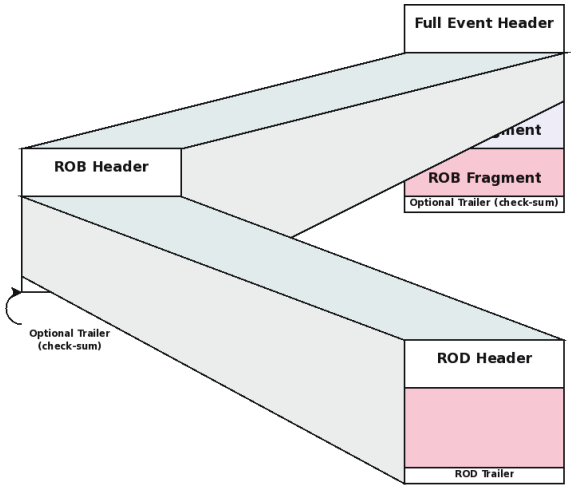

Figure 4.3: Structure of a full event in ATLAS. The event data is organized into fragments, which are the basic units of data transfer and storage. Each fragment contains a header and a payload. The payload contains the actual data from the detector, such as the pixel data from the pixel detector [55].

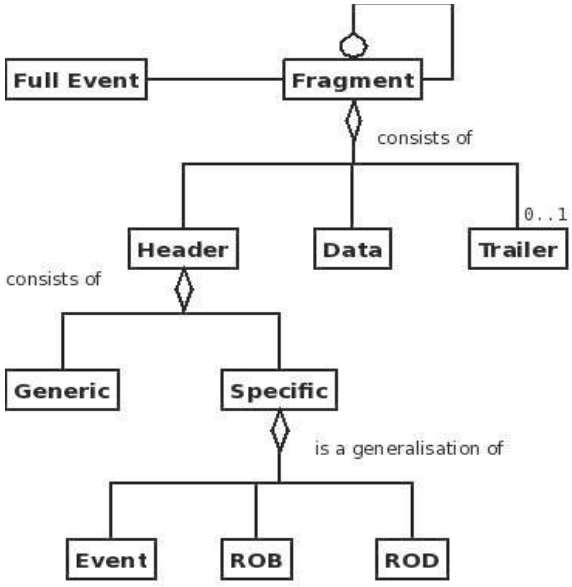

Figure 4.4: Class diagram of the event format. The event data is organized into fragments, which are the basic units of data transfer and storage. Each fragment contains a header, data and trailer. The header has generic and specific parts. The specific part is a generalization of different types of fragments [55].

Start of Header Marker	Generic
Total Fragment Size	
Total Header Size	
Format Version Number	
Source Identifier	
Number of Status Elements (N)	
Status Element[0]	
...	
Status Element[N-1]	
Check Sum Type	
Specific Header[0]	Specific
...	
Specific Header[M]	

Figure 4.5: Structure of the header [55].

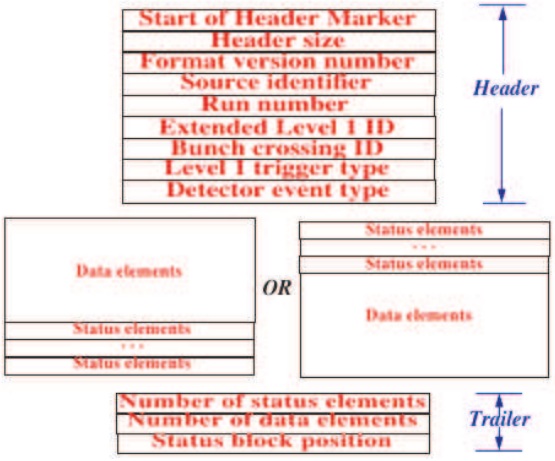

Figure 4.6: Structure of ROD fragment [55].

high-level reconstruction information. The framework helps to validate low-level DAQ logic and data formatting. In addition, it can be used to perform ROD/Module error analyses, hit-level occupancy counting, ToT measurement, timing information at pixel level and so on.

There are two main components of the framework: the decoder and the analysis framework. While the core functionality of these components was already available, this thesis focuses on further development and enhancements. The decoder is responsible for decoding the raw data and storing it in a format that is suitable for further analysis. The analysis framework is responsible for analyzing the decoded data and providing the results. The decoder processes the raw data and saves in root tuple format.

Working principle RAW data are stored using a 32-bit word format. The structure of the byte stream is shown in Figure 4.7. A header marker is used to identify the header of different types of fragments [56]. The decoder first looks for the full event starting marker "0xaa1234aa" and then reads the event header metadata information. Since the main interest is in decoding the byte stream from the IBL and pixel, the decoder looks for the ROB fragments by identifying the ROB marker "0xee1234ee" and then identifies the source using the source identifier information in the ROB header. The following identifier values are used for the barrel, disk, b-layer, and IBL, respectively: 0x11, 0x12, 0x13, 0x14 [56]. The ROD fragments can be found by identifying the ROD marker "0xdd1234dd". Once the ROB/ROD fragments are found, the decoder reads the header and trailer of the fragment, following the structure of the header and trailer mentioned in the previous section. In the case of the ROD fragment, the decoder finds the data elements that contain the module hit information and FE flag information, which are surrounded by the module header and module trailer as shown in Figure 4.8. This way, the pixel module and the corresponding hit information can be decoded. From the 32-bit word, the individual bit information is extracted using bit masking and bit shifting.

The decoded information is then stored in a tuple format using the `TTree` class of the ROOT library [50]; the structure is shown in Figure 4.9. The event metadata is stored for every event in `atlas_event_header`. The `module_hit_array` is an array structure that contains the information for every ROD fragment, meaning it includes the information of 16 FE-I3 or 32 FE-I4 chips. The hits processed by a single ROD from those modules are further stored inside `hit_array`, which is also an array structure. The `hit_array` contains the hit information for every hit in the pixel detector.

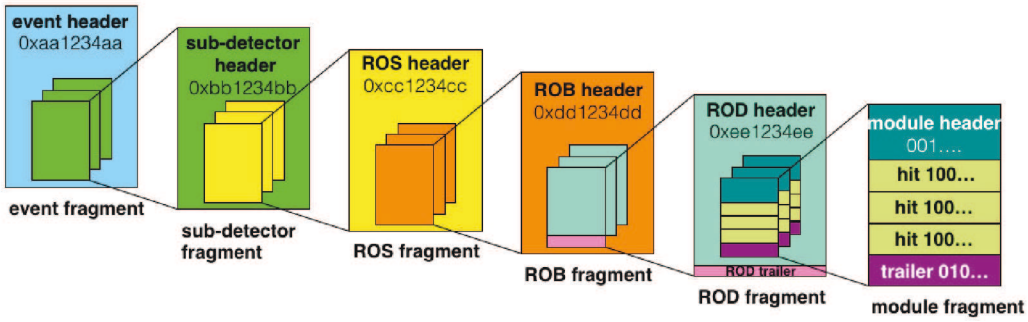

Figure 4.7: ATLAS raw data byte stream format [57].

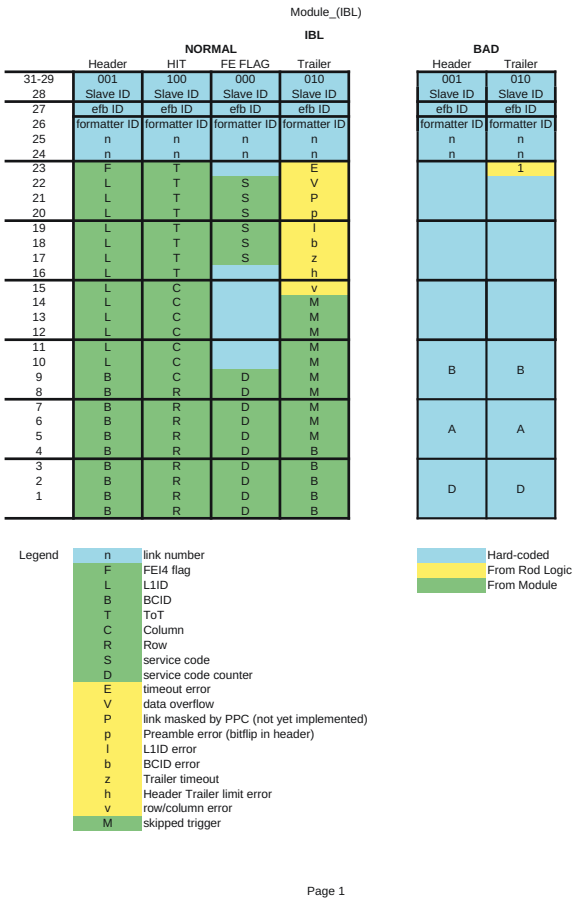

Figure 4.8: Each hit's information is stored in the data element part of the ROD fragment. The structure of the data element consists of a header, hit, FE-flag, and trailer, each 32 bits. The ToT, row, and column of a pixel hit are encoded in the 32-bit hit word. Corrupted data can be identified using the decoded information from the header or trailer, indicated by the "BAD" keyword.

Figure 4.9: Structure of the output in ROOT TTree format. A class structure is defined to store the decoded information, which is saved as a tuple using the ROOT::TTree library. Event metadata is stored for each event in `atlas_event_header`. The `module_hit_array` is an array structure containing information for each ROD fragment. Hits processed by a single ROD are stored within `hit_array`, another array structure. The `hit_array` includes detailed hit information for every hit in the pixel detector.

4.4 Example analyses using the framework

Hit occupancy One of the interesting analyses that can be done using the decoded information is to look into the hit occupancy in different layers of the pixel detector. The hit occupancy is the number of hits that can be counted per module (or per FEs) per layer. The distribution of the hit occupancy collected from the real collision events can be used to simulate the detector response and validate the DAQ logic and also test the performance in a high occupancy environment. An example of the the hit occupancy distribution for proton-proton collision data and heavy-ion collision data is shown in Figure 4.10. Figure 4.10 presents an example of hit occupancy distributions for a subset of the 2018 proton-proton collision data at $\sqrt{s} = 13$ TeV and the 2018 heavy-ion collision data at $\sqrt{s} = 5.02$ TeV. The hit occupancy is calculated by counting the number of hits in each module. As seen in the figures the hit occupancy has a similar distribution for modules for the b-layer and the barrel but has a different distribution for modules in the disc.

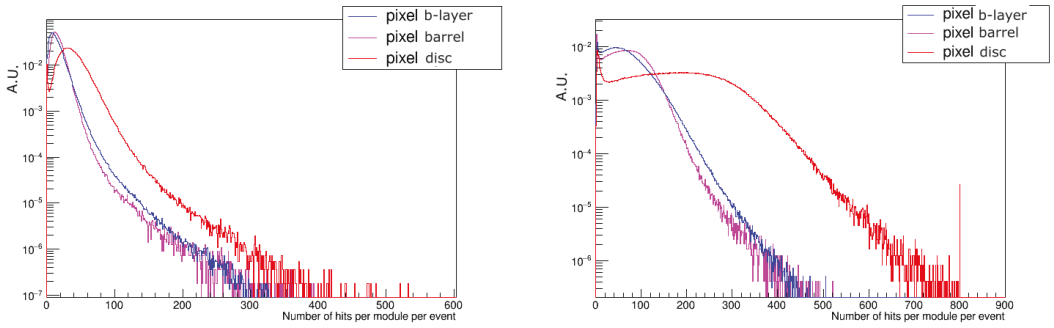

Figure 4.10: Hit occupancy per module in different layers of the pixel detector. The left plot shows the hit occupancy for proton-proton collision data at $\sqrt{s} = 13$ TeV, while the right plot shows the hit occupancy for heavy-ion collision data at $\sqrt{s} = 5.02$ TeV. The distributions are normalized to have the area under the curve equal to 1.

5 Simulation of events

This chapter gives a brief overview of some of the crucial parts involved in simulating collider events. The event generators are used to simulate the events in the collider. An event is the outcome of a collision between two incoming particles, the goal of the event generators is to simulate the event as precisely as possible close to the real collision event in the collider. Because of the randomness of quantum mechanics, the number of outgoing particles in the event and the kinematic properties vary from event to event. The goal of the experiments is to measure the underlying probability distribution of a quantity by studying an ensemble of events in data. On the opposite side, given a set of theoretically calculated (or modeled) probability distributions, it is possible to generate an ensemble of simulated events that can be compared to data. Simulations have many applications in experimental analysis, for example, comparing the measured result with the theoretical prediction, understanding the detector response, optimizing the analysis strategy, studying different phenomenological models.

To generate a full event, the event generator needs to simulate the physics effects at different energy scales accessible to experiments in as much detail as possible. The event generators generally order the physics effects in terms of the energy scale. The hard-scattering process is the fundamental interaction at the high-energy scale, and the parton-showering process describes the emission and splitting of partons as they evolve from the hard-scattering scale to the hadronization scale. The hadronization process describes the formation of color-neutral hadrons from the partons due to the confinement nature of the strong force at the hadronization scale, and the underlying event describes the additional scattering and radiation in the event that is not associated with the hard-scattering process. A simplified schematic of the structure of a $pp \to t\bar{t}$ event modeled by Pythia is shown in Figure 5.1.

The event generators use Monte Carlo (MC) methods to simulate the events. The MC methods are based on the random sampling of probability distributions. This random sampling is important because it allows the generators to model the inherent stochasticity of quantum mechanical processes.

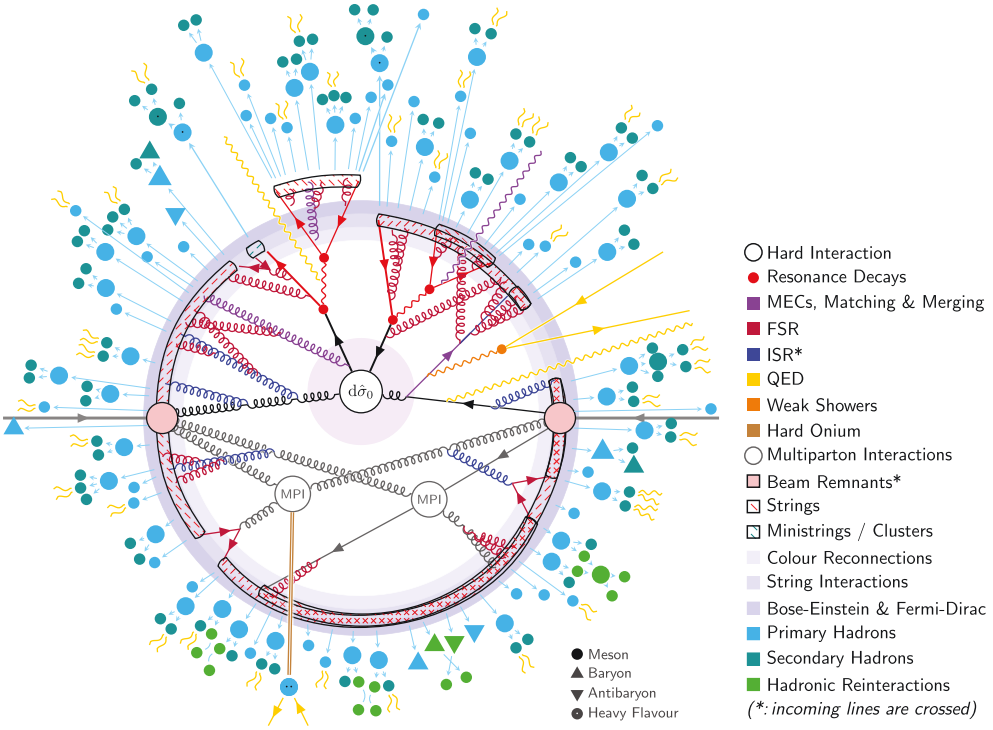

Figure 5.1: Schematic of the structure of a $pp \to t\bar{t}$ event modeled by PYTHIA [58]. In PYTHIA, the event is simulated in order of energy scale. The hard interaction is the fundamental high-energy collision between partons. Resonance decays involve the decay of intermediate resonant particles produced in the hard interaction. Final State Radiation (FSR) refers to the radiation emitted by outgoing partons after the hard interaction. Initial State Radiation (ISR) describes the radiation emitted by incoming partons before the hard interaction. The weak shower involves emissions and decays involving weak force carriers (W and Z bosons). Multiple Parton Interactions (MPI) account for additional parton-parton interactions occurring within the same proton-proton collision. Beam remnants are the leftover parts of the protons after the hard interaction. Strings represent the color field between partons, which fragment into hadrons. Color reconnection refers to the rearrangement of color connections between partons before hadronization. Bose-Einstein and Fermi-Dirac statistics describe the quantum statistical behavior of bosons and fermions, respectively, affecting particle production. Primary hadrons are the first hadrons formed after hadronization. Hadronic reconnection involves further rearrangement of hadronic matter.

5.1 Hard scattering

At the heart of the event simulation is the fundamental interaction that happens at the high-energy scale meaning physics at a very short distance scale. This is called the hard-scattering part of the event generation. The cross-section is defined as the probability of the interaction happening. The hard-scattering cross-section can be computed perturbatively order by order using perturbation theory based on Feynman-diagram rules. For the electroweak interaction, the couplings are sufficiently small and the higher-order corrections become smaller with increasing orders. The exception is enhanced emission of soft or collinear photons or gluons, which are resummed to all orders. For the strong interaction, the coupling constant is large, hence the higher-order corrections are large. The perturbative calculation is still possible for large momentum transfer interactions. However, for low momentum transfer interactions, α_s is large (asymptotic freedom) and the perturbative calculation breaks down. Therefore, the interactions at the low energy scales are described in terms of phenomenological modeling.

Considering the hard-scattering process generation, for the process $a+b \to f_n$, where a and b are the incoming particles and f_n are the final state particles, the differential cross-section is given by

$$d\sigma = \frac{1}{2s}|M|^2 d\Phi_n, \tag{5.1}$$

where s is the center of mass energy, M is the matrix element for the process, and $d\Phi_n$ is the phase space element for the final state particles. The matrix element M is calculated using the Feynman rules. The phase space element $d\Phi_n$ is given by

$$d\Phi_n(P; p_1, p_2, ..., p_n) = (2\pi)^4 \delta^{(4)}(P - \sum_{i=1}^{n} p_i) \prod_{i=1}^{n} \frac{d^3 p_i}{(2\pi)^3 2E_i}, \tag{5.2}$$

where P is the total four-momentum, and p_i and E_i are the momentum and energy of the final state particles. Generally, the phase space is defined with Lorentz invariant variables.

At the LHC, proton beams are collided instead of individual quarks. To describe the parton content of the proton, parton distribution functions (PDFs) are used. PDFs represent the probability distribution of finding a parton with a fraction x of the proton's momentum. These PDFs are determined from global fits to experimental data [59]. If the PDF of the incoming protons A and B are $f_a^A(x, Q^2)$ and $f_b^B(x, Q^2)$, the differential cross-section for the process $a + b \to f_n$ is given by

$$\sigma = \int dx_a f_a^A(x_a, Q^2) \int dx_b f_b^B(x_b, Q^2) \int \frac{d\sigma(\hat{s}, Q^2)}{d\Phi_n} d\Phi_n \tag{5.3}$$

where $\hat{s} = x_a x_b s$ with $s = (p_A + p_B)^2$, and Q^2 is the momentum transfer scale (factorization scale). The PDFs are evaluated at the scale Q^2.

$2 \to 2$ process For the $2 \to 2$ process, $a(p_1) + b(p_2) \to c(p_3) + d(p_4)$, it is conventional to write the phase space element in terms of the Mandelstam variables, $\hat{s} = (p_1 + p_2)^2$, $\hat{t} = (p_1 - p_3)^2$, and $\hat{u} = (p_1 - p_4)^2$. The cross-section for the process can be written as [58]

$$\sigma = \int\int\int \frac{d\tau}{\tau} dy d\hat{t} x_a f_a^A(x_a, Q^2) x_b f_b^B(x_b, Q^2) \frac{d\hat{\sigma}(\hat{s}, \hat{t}, Q^2)}{d\hat{t}}, \tag{5.4}$$

where $\tau = x_a x_b = \hat{s}/s$, and the pseudo rapidity $y = 1/2 \ln(x_a/x_b)$.

The phase space points are generated for $[\tau, y, \hat{t}]$ using the sampling method. For example, in Pythia [58] multichannel phase space sampling is used to generate the phase space points. Once the phase space points are generated, the energy and momentum of the final state particles are calculated using the phase space points and the matrix element.

5.2 Parton showering

Parton showering is a process in which initial-state radiation (ISR) and final-state radiation (FSR) occur. It is intuitive to think about the showering of the final state partons, but the showering of initial state partons is also done at this stage because as mentioned before the simulation of physics effects is ordered in terms of energy scale. This radiation is predominantly in the form of gluons, but can also include photons. Parton showering is an important aspect of the event generation as it accounts for the emission and splitting of partons, leading to the formation of jets and the overall structure of the final state particles.

During parton showering, a quark can emit a gluon ($q \to qg$), a gluon can split into quarks ($g \to qq$), and any charged fermion can emit a photon ($q \to q\gamma$). These emissions and splittings continue until the partons reach the hadronization scale, where the strong force coupling becomes very strong and color reconnection occurs.

Calculating all possible emissions and splittings using matrix element calculations can be computationally expensive. Instead, parton showering is modeled using a probabilistic approach. The DGLAP (Dokshitzer-Gribov-Lipatov-Altarelli-Parisi) evolution equations are used to describe the probability of parton emission at different time/energy scales.

The parton showering process is typically implemented in event generators using MC methods. The showering algorithm generates a sequence of parton emissions and splittings, taking into account the kinematics and probabilities associated with each emission. The generated partons are then used as input for the subsequent steps of the event generation, such as hadronization and the underlying event.

Final state radiation For example, consider the process $q\bar{q} \to Z \to q\bar{q}$. Either of the two quark in the initial state can emit a gluon, e.g. $q \to qg$, this produces qqg final state. After this either of the three parton can branch, and so on. The differential probability of a parton to branch is given by

$$d\mathcal{P}_a(z, Q^2) = \frac{dQ^2}{Q^2} \frac{\alpha_s(Q^2)}{2\pi} \sum_{b,c} P_{a\to bc}(z) dz, \tag{5.5}$$

where a is the parent parton, b and c are the daughter partons, z is the fraction of energy carried by the daughter parton, Q^2 is the momentum transfer scale, and $P_{a\to bc}(z)$ is the splitting function. The splitting function is calculated using the DGLAP evolution equations.

Initial state radiation The ISR is the process in which the incoming partons radiate before the hard-scattering process. The ISR description starts from the evolution of the PDFs of the incoming protons

$$\begin{aligned} df_b(x, Q^2) &= \frac{dQ^2}{Q^2} \frac{\alpha_s(Q^2)}{2\pi} \sum_a \int f_a(x', Q^2) dx' \int P_{b/a}(z) dz \delta(x - x'z) \\ &= \frac{dQ^2}{Q^2} \frac{\alpha_s(Q^2)}{2\pi} \sum_a \int \frac{dz}{z} f_a(x' = x/z, Q^2) P_{b/a}(z), \end{aligned} \tag{5.6}$$

where $f_i(x', Q^2)$ is the probability of finding a parton i inside a hadron carrying a fraction x of the full hadron momentum if the hadron is probed at a scale Q^2. $P_{b/a}(z)$ is the splitting function. The PDFs are evaluated at the scale Q^2.

A very common parton shower package is PYTHIA. More details can be found in the manual [58].

Matching and merging The collider event covers physics at a wide range of energy scales. To simulate the whole process, it is not feasible to do perturbative calculations for

all possible branching of the parton as they evolve from hard-scattering. That is why the hard-scattering is calculated using fixed-order perturbative calculations using Feynman rules which give a more accurate result in high-energy and low multiplicity regime, while the evolution of parton is calculated using the parton showering algorithm. The matching and merging techniques are used to combine these two different calculations in a consistent way without double counting the emissions [58].

Hadronization Hadronization is the process in which the partons produced in the hard-scattering process combine to form color-neutral hadrons. This happens because of the colour reconnection. The hadronization energy scale is around 1 GeV. The hadronization process is non-perturbative and cannot be calculated using perturbation theory. Instead, hadronization is modeled using phenomenological models based on the principles of QCD.

The most commonly used hadronization models are the Lund string model and the cluster model. In the Lund string model, the partons are connected by color strings, which stretch and break to form hadrons [58]. In the cluster model, the partons are grouped into color-neutral clusters, which then decay into hadrons. The hadronization models are implemented in event generators to simulate the formation of hadrons from partons.

Underlying event The underlying event is the additional activity in the event that is not associated with the hard-scattering process. This activity is due to the multiple parton interactions and the remnants of the colliding protons. The underlying event is an important background in collider experiments, as it can affect the measurement of the hard-scattering process and the reconstruction of the final state particles.

The underlying event is modeled in event generators using phenomenological models based on the principles of QCD. The models include the multiple parton interactions, the beam remnants, and the soft radiation from the initial and final state partons.

Event generators There are several event generators available for simulating collision events at the LHC. Each one is tailored for different purposes. For instance, MadGraph5_aMC@NLO [60], Powheg [61], and Sherpa [62] are known for their automatic generation of matrix elements for a wide range of processes. Pythia [63] and Herwig [64] are well-known for their sophisticated parton shower algorithms, hadronization models, and underlying event handling.

6 Data and MC simulations

6.1 Data set

The data set used in this measurement was collected in proton-proton collisions at LHC at center-of-mass energy of 13 TeV, recorded by the ATLAS detector during Run 2 operation (2015-2018). In total, ATLAS recorded 140.1 fb^{-1} [65] of data which can be used for physics analysis [66]. The mean number of interactions per bunch crossing in this data-taking period are shown in Figure 6.1.

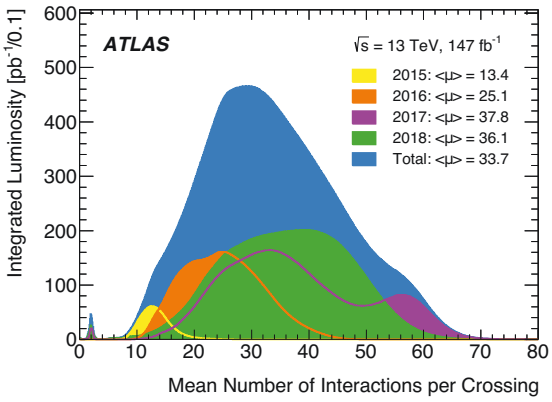

Figure 6.1: The distribution of the average number of interactions per bunch crossing in the data-taking period during LHC Run2 operation [65].

6.2 Simulation of signal and background processes

The MC simulated events are used in different parts of the analysis. For example, for modeling signal and background events, measuring the detector response from particle level to reconstruction level, finding signal-enriched regions, training neural networks, quantifying different sources of uncertainties. Different event generators used to simulate the signal and background process are discussed in the following.

MC simulations are performed using the ATLAS simulation infrastructure [67], where the detector simulation is done using GEANT4 [68]. As full detector simulation is computationally expensive, for some of the MC samples, the fast-simulation package ATLFAST-II [67] is used, which speeds up the detector simulation. Additional proton-proton interactions (pileup interactions) from the same bunch crossing are simulated as minimum-bias interactions using PYTHIA8 [69] using the set of tuned parameters called A3 [70] and the NNPDF2.3LO PDF set [71]. These events are then superimposed on the hard-scattering events. Simulation is done separately for each data-taking period to match the varying conditions of the ATLAS detector. Three different sub-campaigns, *mc16a, mc16d* and *mc16e* are defined to reflect the data-taking conditions in the years 2015-16, 2017, and 2018 respectively.

This analysis utilizes MC simulated samples where photon emission is handled in two ways: either directly at the matrix-element level or through parton shower algorithms. Matrix-element calculations offer greater precision for photon emission and are used for $t\bar{t}\gamma$ production and $V\gamma$ ($V = W, Z$) processes. For other processes, the photon emission is modeled within the parton shower. To prevent double-counting of events between these approaches, a phase space overlap removal procedure is implemented, as detailed in Section 6.3.

$t\bar{t}\gamma$ production

The $t\bar{t}\gamma$ production process is simulated using MADGRAPH5_AMC@NLO v.2.7.3 [60] as a $2 \to 3$ process at NLO QCD precision. In the matrix-element calculation, the NNPDF3.0NLO set of PDFs [72] is used. The simulated hard scattering events are interfaced with PYTHIA 8.240 [63] using the *A14* set of tune parameters [73] and the NNPDF2.3LO PDF set to model parton shower, hadronization, fragmentation, and underlying event. The decay of top quarks is done at LO using MADSPIN [74; 75] to preserve spin correlations. The decays of bottom and charm hadrons are simulated using the EVTGEN 1.6.0 program [76]. The renormalization and factorization scales are dynamic and correspond to half of H_{T}, defined as

$$\mu_R = \mu_F = \frac{H_{\mathrm{T}}}{2}, \quad H_{\mathrm{T}} = \sum_f \sqrt{m_f^2 + p_{\mathrm{T},f}^2}, \tag{6.1}$$

where f runs over all final-state particles, and m_f and $p_{\mathrm{T},f}$ are the rest mass and the transverse momentum of particle f, respectively. Some phase space cuts are applied on the matrix-element level to avoid infrared and collinear singularities due to the photon

radiation. Also, leptons and quarks at the matrix-element level are required to have a minimum p_{T} of 20 GeV and 1 GeV, respectively. Photons are required to have a minimum p_{T} of 15 GeV and to be isolated according to a smooth-cone isolation (Frixione isolation [77]) criterion with $\delta_0 = 0.1$, $\epsilon_\gamma = 0.1$ and $n = 2$. The $t\bar{t}\gamma$ production sample is normalized to the NLO cross-section given by the MC simulation. This sample is used as signal in $t\bar{t}\gamma$ production measurement, presented in Section 11.1.

$t\bar{t}\gamma$ decay The $t\bar{t}\gamma$ decay is simulated using MadGraph5_aMC@NLO 2.7.3 [60] as a $2 \to 2$ LO $t\bar{t}$ production followed by the decay of the top quarks at LO where either of the top decays with a photon. The ME calculation uses the NNPDF3.0nlo set of PDFs [72]. The hard scattering simulation is interfaced with Pythia 8.240 [63] using the *A14* set of tune parameters [73] and the NNPDF2.3LO PDF set to model parton shower, hadronization, fragmentation, and underlying event. The decays of bottom and charm hadrons are simulated using the EvtGen 1.6.0 program [76]. The renormalization and factorization scales are set at $H_{\mathrm{T}}/2$, see Eq. 6.1. The phase-space cut and isolation criteria at the matrix-element level are the same as for $t\bar{t}\gamma$ production. Since this is a LO sample, an inclusive K-factor ($\sigma_{\mathrm{NLO}}/\sigma_{\mathrm{LO}}$) is calculated to correct the normalization of the sample. A K-factor of 1.50592 was estimated by comparing the normalizations of the sum of the NLO $t\bar{t}\gamma$ production sample and the LO $t\bar{t}\gamma$ decay sample with the normalization of a LO inclusive $2 \to 7$ $t\bar{t}\gamma$ sample corrected with the K-factor obtained in Ref. [78] using the calculation described in Ref. [79].

$$K_{\mathrm{LO}}^{2\to7} \times \sigma_{\mathrm{LO}}^{2\to7} = \sigma_{\mathrm{NLO}}^{\mathrm{production}} + K_{\mathrm{LO}}^{\mathrm{decay}} \times \sigma_{\mathrm{LO}}^{\mathrm{decay}}. \tag{6.2}$$

This sample is used as background in $t\bar{t}\gamma$ production measurement and used as signal in total $t\bar{t}\gamma$ production and decay measurement presented in Section 11.3.

$tW\gamma$ production Two $tW\gamma$ samples are simulated, one with the photon emitted from the production process and the other with the photon emitted from the decay process. The $tW\gamma$ process is simulated using MadGraph5_aMC@NLO 2.7.3 [60] at LO with the 5-flavor scheme of partons. To model the parton shower, hadronization, fragmentation, and underlying event, the generated events are interfaced with Pythia 8.240 [63] using the *A14* set of tune parameters [73] and the NNPDF2.3LO PDF set. The decays of bottom and charm hadrons are simulated using the EvtGen 1.6.0 program [76]. The renormalization and factorization scales are set at $H_{\mathrm{T}}/2$ (Eq. 6.1). This sample is used for background modeling.

Wγ/Zγ + jets $W\gamma$ and $Z\gamma$ events are simulated in dedicated samples. Both processes are simulated using SHERPA 2.2.8 [80; 81] at NLO in QCD using the NNPDF3.0NNLO PDF set. The parton showering is done using the SHERPA-internal parton showering based on Catani-Seymour dipoles [82; 83] using the MEPS@NLO prescription [84–86]. Virtual corrections for the NLO accuracy in QCD in the matrix-element are provided by the OpenLoops library [87; 88]. This sample is used for background modeling.

Top quark pair production ($t\bar{t}$) The $t\bar{t}$ process is simulated at NLO in QCD using POWHEG-BOX [2] [61; 89; 90] at the matrix-element level and interfaced with PYTHIA 8.230 [63] for parton showering, hadronization, fragmentation, and underlying event with the *A14* tune in conjunction with the NNPDF2.3LO PDF set. The matrix-element calculation uses the NNPDF3.0NLO PDF set [72] with the top quark mass fixed to 172.5 GeV . The heavy-flavor decays are modeled with EVTGEN 1.6.0. The internal POWHEG parameter, h_{damp}, which regulates the high-p_{T} radiation spectrum, is set to 1.5 times the top quark mass. The cross-section is normalized to the NLO in perturbative QCD including soft-gluon resummation to next-to-next-to-leading-log (NNLO) using the TOP++2.0 program [91].

Single top quark production The single-top quark production is simulated for the three channels s, t, and tW using POWHEG-BOX at NLO in QCD. The matrix-element calculation uses the NNPDF2.3LO PDF set [72]. The hard scattering events are interfaced with PYTHIA 8.230 [63] using the *A14* tune [73] and the NNPDF2.3LO PDF set to model parton showering, hadronization, fragmentation, and underlying event. The decays of bottom and charm hadrons are simulated using the EVTGEN 1.6.0 program [76]. The cross-section is normalized to the NLO in perturbative QCD using K-factors [92–94].

W/Z+jets Events with W and Z bosons in association with additional jets are simulated with SHERPA 2.2.1 at NLO in QCD. The samples are normalized to the NLO cross-section in QCD [95].

Diboson Events with two vector bosons, that is WW, WZ and ZZ, are generated with SHERPA versions 2.2.2 (purely leptonic decays) and 2.2.1 at NLO in QCD. The samples are normalized to NLO cross-sections in QCD [96].

$t\bar{t}$ +W/Z $t\bar{t}$ pair production in association with a W or Z boson ($t\bar{t}V$) is simulated at NLO in QCD on the matrix-element level with MADGRAPH5_aMC@NLO using the

NNPDF3.0NLO PDF set. The matrix-element generator is interfaced to PYTHIA 8.210, for which the *A14* tune is used in conjunction with the NNPDF2.3LO PDF set. The samples are normalized to NLO in both QCD and electroweak theory [97].

6.3 Sample-overlap removal procedure

For some processes, two types of MC samples are simulated where photon emission is handled in two different ways: either directly at the matrix-element level (referred to as dedicated samples) or through parton shower algorithms (referred to as inclusive samples). To avoid double-counting between these approaches, a phase space overlap removal procedure is implemented. The following processes have very small contributions in the signal region, so only the parton shower photon emission is considered: single top quark production, diboson, and $t\bar{t}V$. The overlap removal is applied between $t\bar{t}\gamma$ and $t\bar{t}$ samples, W/Z+jets and $W/Z\gamma$ samples, and single top tW and $tW\gamma$ samples.

The procedure for overlap removal is as follows:

1. Accept all events from the dedicated samples, since the photon radiation simulated at the matrix-element level has higher accuracy than the radiation accounted for in the showering algorithm. The dedicated samples cover a smaller phase space than the inclusive samples. 2. Remove events from the inclusive samples if they overlap with the dedicated simulation. The overlap region is defined by the set of cuts applied to the dedicated samples at the matrix-element level. The cuts are:

1. $p_{\mathrm{T}}(\gamma) > 15\,\mathrm{GeV}$, and
2. $\Delta R(\ell, \gamma) > 0.2$, where $\Delta R = \sqrt{\Delta\phi^2 + \Delta\eta^2}$.

The overlap-removal procedure starts by listing all photons and leptons generated at the matrix-element level. The candidates are matched using their PDG ID to identify photons and leptons. These candidates must not originate from interactions with the detector interactions or hadronic activity but must come from the primary vertex (verified with their *barcode* and *truth origin*). It is ensured that the candidates are stable (or considered before their decay in the case of muons and τ-leptons). For example, τ-leptons decaying leptonically are considered as such their decay products are vetoed from the candidates list. After compiling the candidate lists, all photon candidates are checked against the criteria mentioned above. The photon candidate is discarded if it fails any of the criteria. If any photon candidate remains, the event is considered to fall in the overlap region and is vetoed from the inclusive samples ($t\bar{t}$, W/Z+jets, single top Wt samples).

6.4 Categorisation of photons

The primary focus of this analysis is to measure processes where a photon is emitted during the $t\bar{t}$ production, specifically from the hard scattering part of the event. Photons emitted from these hard interactions are termed 'prompt photons'. Photons can also be emitted at various other stages, such as during the evolution from the hard scattering energy scale to the hadronization scale, or from hadron decays to photons. Additionally, photons may be emitted by any lepton at any time. Mis-reconstruction of particles can also produce photon-like objects; for example, an electron might be misidentified as a photon if the track reconstruction fails. Based on the origin of the photon, the events are categorized into the following types:

- **Prompt photon:** The photon is emitted from the hard-scattering process.
- **Electron-fake photon:** An electron is mis-reconstructed as a photon, referred to as e-fake photon events.
- **Hadron-fake photon:** Non-prompt photons originating from hadron decays, for example, $\pi^0 \to \gamma\gamma$, a jet signature in the calorimeter can be mis-reconstructed as a photon. All these are grouped into one category and referred to as h-fake photon events.

The origin of the photons is identified in the reconstructed MC simulated events using a matching procedure between the objects at reconstruction level and at generator (truth) level, referred to as "MC-truth matching" procedure. However, this information is unavailable for data events. The modeling of e-fake photon and h-fake photon events is further explored in Sections 8.1 and 8.2.

The MC truth matching procedure: The origin of the reconstructed photon candidates is determined using the MC truth records as follows. The reconstructed photon is defined as γ^{rec} and the associated truth-matched object as γ^{truth}_{cand}.

A photon candidate is classified as an e-fake photon if any of the following conditions are met:

- The PDG ID of γ^{truth}_{cand} is 11 or -11 (electron).
- $\Delta R(\gamma^{truth}_{cand}, e_{truth}) < 0.1$, where e_{truth} is a truth electron.

A photon candidate is classified as an h-fake photon if any of the following conditions are met:

- The origin of the truth-matched object is a hadron.
- The γ_{cand}^{truth} is a decay product of π^0.
- The hadronic calorimeter energy deposit does not align with any truth-matched photon.

If none of these conditions are met, the photon candidate is classified as a prompt photon.

7 Event selection

After introducing the object reconstruction from the detector signatures, this chapter focuses on further requirements applied to select the events of interest. The events are selected based on the reconstructed objects present and certain kinematic requirements. After the event selection, neural-network classifiers are used to define regions with high signal purity. The chapter is divided into several sections: Section 7.1 describes the definition of the objects with the preliminary requirements, Section 7.2 describes the reweighting of the MC events to normalize to the luminosity in data, and Section 7.3 presents the event selection criteria. Finally, the definition of the signal and control regions based on neural networks is described in Section 7.4.

7.1 Object definition

The reconstructed objects from the detector signatures are defined by certain identification and isolation criteria. This section describes the identification criteria for the objects used in the analysis.

Primary vertex Primary vertices are constructed by grouping reconstructed tracks that are spatially compatible with the interaction region. The primary vertex associated with the hard scattering is identified by selecting the vertex that has the highest sum of squared transverse momenta (Σp_{T}^2) from its associated tracks. Additionally, this vertex must have at least two associated tracks.

Electron Electrons are selected with the so-called `MediumLH` identification criteria and the `PLVLoose` isolation criteria [98]. Electrons with $p_{\mathrm{T}} > 7$ GeV and $|\eta| < 2.47$, excluding the calorimeter crack region $1.37 < |\eta| < 1.52$, are considered. The following requirements are applied to ensure that electrons are originating from the primary vertex: the longitudinal impact parameter $|d_0|/\sigma(d_0) < 5$, the distance between the PV and the track origin ($|z_0 \sin\theta| < 0.5$ mm).

Muon Muons are required to pass the `Medium` identification criteria and `PLVLoose` isolation criteria as defined in Ref. [99]. The following requirements are applied to ensure that muons are originating from the primary vertex: the longitudinal impact parameter fulfills $|d_0|/\sigma(d_0) < 3$, and the distance between the PV and the track origin $|z_0 sin\theta| < 0.5\ mm$. Calibrated muons with $p_{\mathrm{T}} > 7$ GeV and $|\eta| < 2.5$ are considered.

Photon Photons are identified with the `Tight` identification criteria and the `FixedCutTight` isolation criterion is required [100]. The calibrated photons are required to have $p_{\mathrm{T}} > 15$ GeV and $|\eta| < 2.37$, excluding the calorimeter crack region $1.37 < |\eta| < 1.52$.

Jet Jets are reconstructed using the anti-k_t algorithm with a radius parameter of 0.4 and are required to have $p_{\mathrm{T}} > 25$ GeV and $|\eta| < 2.5$. Jets are required to pass additionally the Jet Vertex Tagger (`JVT`) [101] requirement to suppress pileup jets. The `JVT` requirement is applied to jets with $p_{\mathrm{T}} < 60$ GeV and $|\eta| < 2.4$.

b-jet Jet b-tagging is done using the `DL1r` tagger, which is a neural-network-based tagger. The output is a multidimensional probability distribution of tagging the jet as a b-jet, c-jet, or light-flavor jet.

7.2 MC normalization and object scale factors

MC simulated events have associated weights that reflect the sampling techniques used by MC generators to sample the phase space and generate events. Since only a limited set of events is sampled, integrating these weights over the phase space yields an estimate of the process cross-section, but this estimate lacks precision due to the limited sample size.

To achieve greater precision, MC generators first calculate the cross-section by integrating the phase space more accurately using sophisticated integration techniques. This calculated value is known as the MC-predicted cross-section (σ^{MC}), which is more precise than the cross-section obtained directly from the generated event weights.

The generated events are then normalized by dividing each weight by the sum of all weights. This normalization gives the relative probability of each event within the sample. To determine the expected number of events for the process, these normalized weights are scaled by the more precise MC-predicted cross-section.

Thus, the weight of each event after normalization and scaling becomes:

$$w_i = \left(\frac{\text{weight\_mc}^i}{\sum_i^N \text{weight\_mc}^i} \times \sigma^{\text{MC}} \right), \tag{7.1}$$

where w_i is the weight of the i-th event and N is the total number of events generated. σ^{MC} is the MC predicted cross-section and weight_mc^i is the MC generator weight of the i-th event.

To calculate expected number of events for the same luminosity of the data set, the MC events are further scaled by the following formula:

$$w_i = \frac{\sigma^{\text{MC}} \times \text{weight\_mc}^i \times \text{Luminosity}}{\sum_i^N \text{weight\_mc}^i}. \tag{7.2}$$

Events are reweighted to account for the exact pileup distribution in the data in the following way:

$$w_i = \frac{\sigma^{\text{MC}} \times \text{weight\_mc}^i \times \text{Luminosity} \times \text{weight\_pileup}}{\sum_i^N \text{weight\_mc}^i}. \tag{7.3}$$

Additionally, the reconstruction level events are corrected by scale factors (SFs) related to object identification efficiency, isolation efficiencies, trigger efficiencies, JVT efficiency, and b-tagging efficiency. These SFs are calculated as the ratio of the efficiencies in data and in MC and are applied to MC events to correct discrepancies in the simulated events. Including all the scale factors, the event weight for reconstruction level event becomes:

$$w_i = \frac{\sigma^{\text{MC}} \times \text{weight\_mc}^i \times \text{Luminosity} \times \text{weight\_pileup} \times \text{SF\_photon} \times \text{SF\_lepton} \times \text{SF\_JVT} \times \text{SF\_bTag}}{\sum_i^N \text{weight\_mc}^i}. \tag{7.4}$$

7.3 Event selection

The selected events must meet the primary vertex criteria and have at least one single-lepton trigger fired for both the single-lepton and dilepton channels. Trigger thresholds vary depending on the run period[102; 103]. If a lepton is trigger matched, its transverse momentum must satisfy $p_{\text{T}} > p_{\text{T}}$ threshold of trigger + 1 GeV. In the dilepton channel, the second lepton is required to have $p_{\text{T}} > 20$ GeV. In the single-lepton channel, the

selection criteria require exactly one lepton, one photon with $p_{\mathrm{T}} > 20$ GeV, at least four jets with $p_{\mathrm{T}} > 25$ GeV, and at least one b-tagged jet. The detailed kinematic variable requirements are listed in Table 7.1. In the dilepton channel, events must contain exactly two leptons, one photon, at least two jets, and at least one b-tagged jet. Events with additional isolated leptons with $p_{\mathrm{T}} > 7$ GeV are rejected in both channels. The detailed kinematic requirements are in Table 7.2. Events are reweighted according to the procedure described in Section 7.2. The categorization of events based on photon origin is discussed in Section 6.4.

The expected event yields for the single-lepton and dilepton channels are presented in Table 7.3, with breakdowns of the e-fakes and h-fakes events in Table 7.4 and Table 7.5. Distributions of the photon p_{T} and $|\eta|$, $\Delta R(\gamma, \ell)_{\mathrm{min}}$, number of jets, leading jet p_{T}, and event H_{T} in data and MC predictions are shown in Figures 7.1 and 7.2 for the single-lepton and dilepton channels, respectively.

Table 7.1: Event selection for the single-lepton channel

Selection	Channel	
	e+jets	μ+jets
1 lepton	$\|\eta\| < 1.37$ or $1.52 < \|\eta\| < 2.47$	$\|\eta\| < 2.5$
	$p_{\mathrm{T}} > p_{\mathrm{T}}$ threshold of trigger + 1 GeV	
1 photon	$p_{\mathrm{T}} > 20$ GeV $\|\eta\| < 1.37$ or $1.52 < \|\eta\| < 2.37$	
jets	$N_{\mathrm{jets}} \geq 4$ $p_{\mathrm{T}} > 25$ GeV, $\|\eta\| < 2.5$	
b-tagged jets	≥ 1 jets with DL1r at 70%	
m(e,γ) veto	|m(e,γ)-91.19 GeV |>5 GeV	–

Table 7.2: Event selection for the dilepton channel

Selection	Channel		
	ee	$\mu\mu$	eμ
2 leptons	$\|\eta\| < 1.37$ or $1.52 < \|\eta\| < 2.47$	$\|\eta\| < 2.5$	e: $\|\eta\| < 1.37$ or $1.52 < \|\eta\| < 2.47$; μ: $\|\eta\| < 2.5$
	$p_{\mathrm{T}} > p_{\mathrm{T}}$ threshold of trigger + 1 GeV, (20 GeV for second lepton)		
1 photon	$p_{\mathrm{T}} > 20$ GeV $\|\eta\| < 1.37$ or $1.52 < \|\eta\| < 2.37$		
jets	$N_{\mathrm{jets}} \geq 2$ $p_{\mathrm{T}} > 25$ GeV, $\|\eta\| < 2.5$		
b-tagged jets	≥ 1 jets with DL1r at 85%		
$m(l,l)$ veto	$\|m(l,l)$ - 91.19 GeV $\| > 5$ GeV		–
	$m(l,l) > 15$ GeV		
E_{T}^{miss}	$E_{\mathrm{T}}^{miss} > 30$ GeV		–

Table 7.3: The observed and the expected event yields for both the single-lepton and dilepton channels are shown, incorporating all data-driven corrections (c.f. Chapter 8). The $t\bar{t}\gamma$ decay sample has been scaled using the NLO K-factor. In the dilepton channel, the $W\gamma$ contribution is accounted for within the Other prompt γ category. The contribution of lepton fakes in the dilepton channel is negligible and has been included in the corresponding MC yields. The reported uncertainties represent the combined statistical and systematic uncertainties (c.f. Chapter 9). This table is taken from [24].

Process	Single-lepton channel	Dilepton channel
$t\bar{t}\gamma$ production	12450 ± 740	2400 ± 99
$t\bar{t}\gamma$ decay	13400 ± 3100	3100 ± 640
h-fake	3600 ± 1200	220 ± 82
e-fake	6900 ± 980	57.9 ± 7.0
$W\gamma$	2700 ± 1400	–
$tW\gamma$	1180 ± 580	290 ± 150
Other prompt γ	2500 ± 600	820 ± 170
Lepton fake	640 ± 110	–
Total	43900 ± 4600	6900 ± 710
Data	47767	7379

Table 7.4: Breakdown of $e \to \gamma$ fake and $h \to \gamma$ fake yields from different processes in the single-lepton channel.

Process	$e \to \gamma$	$h \to \gamma$
$t\bar{t}\gamma$ production	46	11
$t\bar{t}\gamma$ decay	35	15
$W\gamma$	0.0	2.8
$Z\gamma$	25	0.5
W + jets	0.5	68
Z + jets	490	25
$Wt\gamma$	3.7	1.3
Wt	190	110
$t\bar{t}$	6000	3280
singletop(s, t ch)	1.6	30
$t\bar{t}V$	80	17
VV	28	5.0

Table 7.5: Breakdown of $e \to \gamma$ fake and $h \to \gamma$ fake yields from different processes in the dilepton channel.

Process	$e \to \gamma$	$h \to \gamma$
$t\bar{t}\gamma$ production	5.1	0.8
$t\bar{t}\gamma$ decay	2.5	0.8
$W\gamma$	0.0	0.0
$Z\gamma$	0.0	3.3
W + jets	0.0	0.1
Z + jets	0.9	10.1
$Wt\gamma$	0.5	0.2
Wt	1.4	6.6
$t\bar{t}$	14.4	193.0
singletop(s, t ch)	0.0	0.1
$t\bar{t}V$	17.3	2.8
VV	15.1	1.1

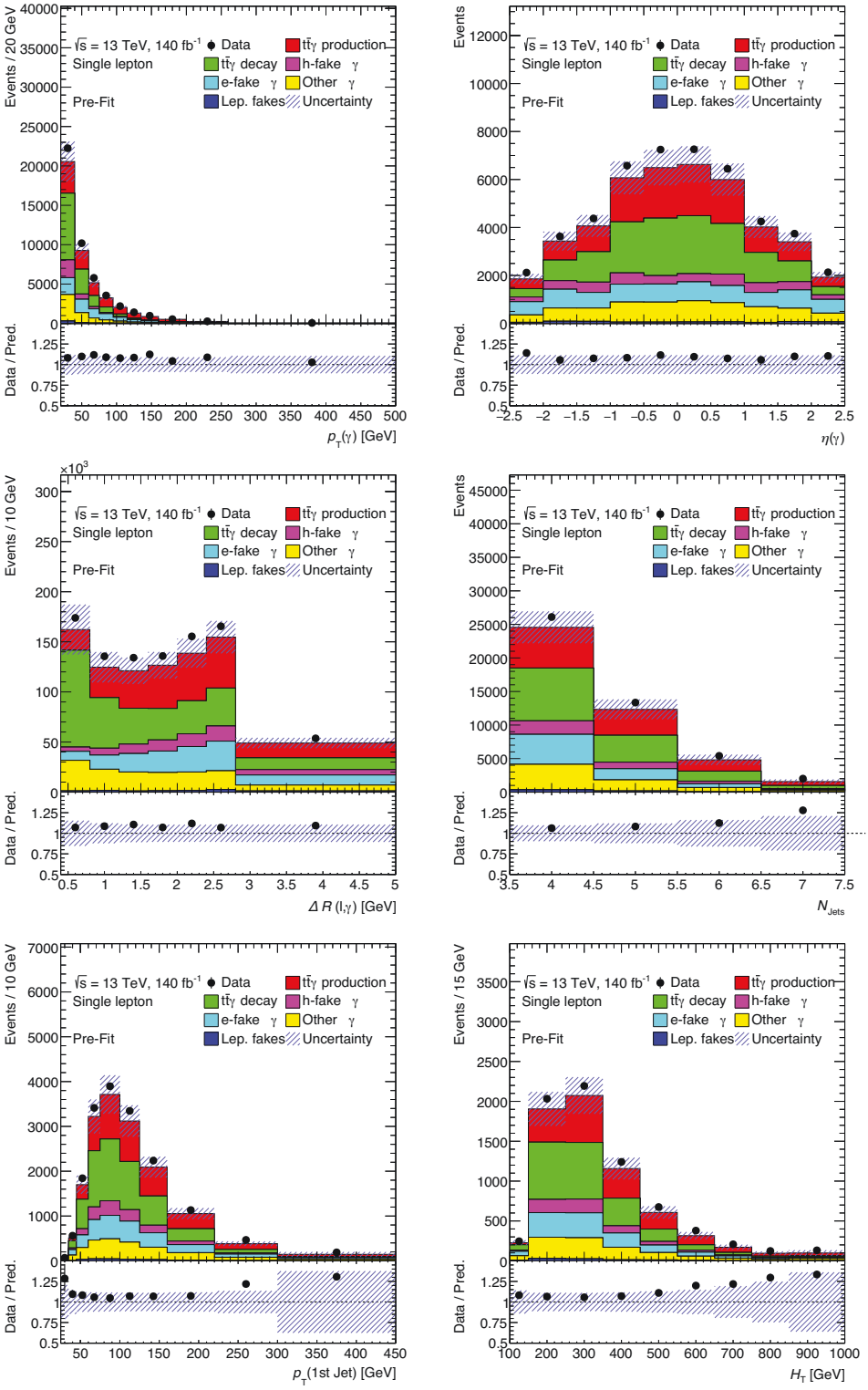

Figure 7.1: Photon p_{T} (a) and η (b), $\Delta R(\gamma,\ell)_{\mathrm{min}}$ (c), number of jets (d), leading jet p_{T} (e), and event H_{T} (f) distributions at the reconstruction level in the single-lepton channel. The expected signal and background contributions are shown based on the MC predictions. The shaded band represents the total pre-fit uncertainty. The last bin includes overflow events.

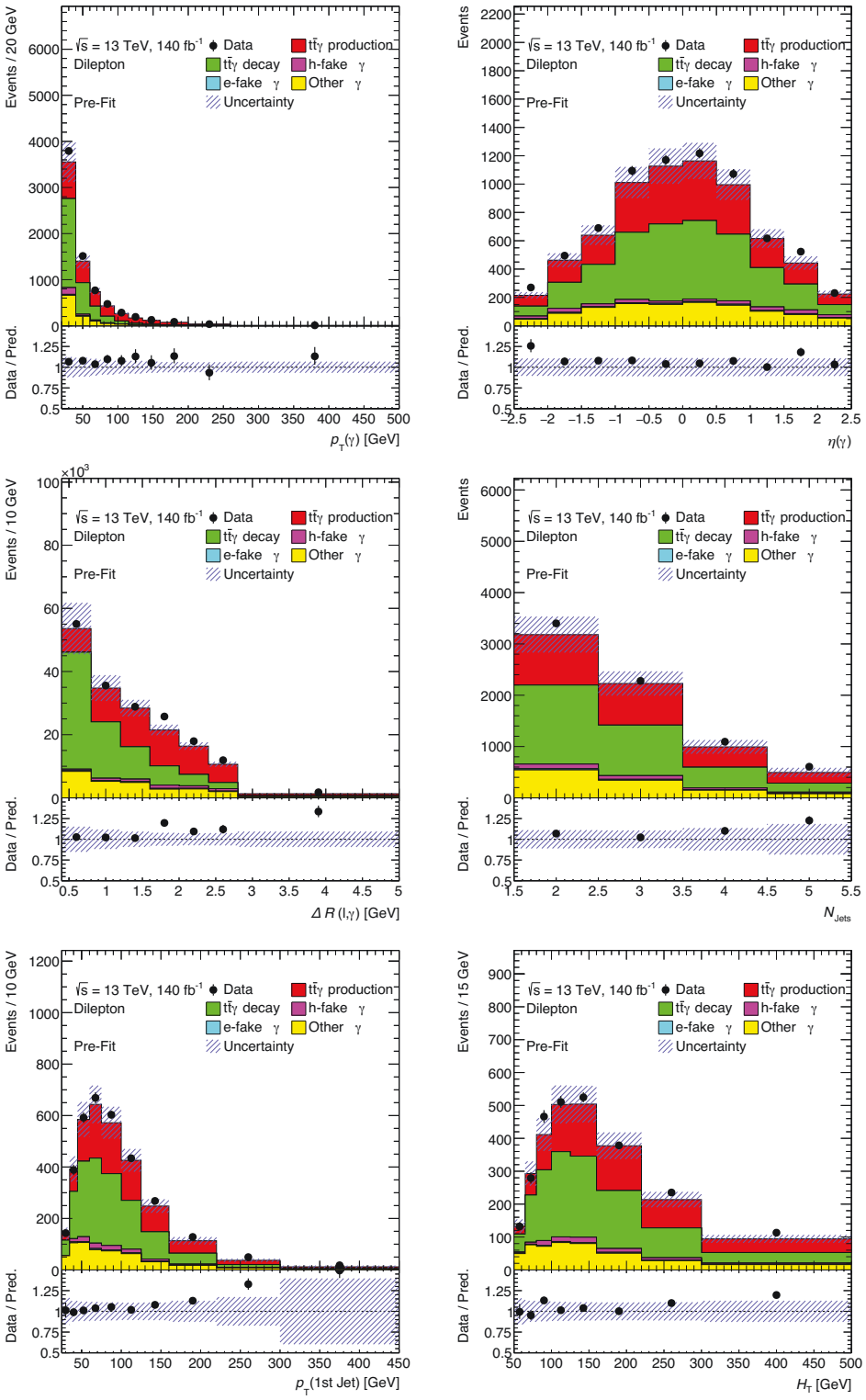

Figure 7.2: Photon p_{T} (a) and η (b), $\Delta R(\gamma,\ell)_{\mathrm{min}}$ (c), number of jets (d), leading jet p_{T} (e), and event H_{T} (f) distributions at the reconstruction level in the dilepton channel. The expected signal and background contributions are shown based on the MC predictions. The shaded band represents the total pre-fit uncertainty. The last bin includes overflow events.

7.4 Defintion of signal and control regions

The event selection is designed to enhance the fraction of signal events. However, many background events still meet these criteria and are selected. To characterize these backgrounds, both MC-simulated events and data-driven methods are employed. A good agreement between data and MC is observed within the uncertainties. To further enhance signal purity, a neural network classifier is utilized. A neural network can be thought of as a multidimensional function that takes the input features (properties of the event) and outputs a probability distribution indicating the likelihood of an event being signal. After training on numerous events, this network optimizes its parameters and learns to differentiate between signal and background. The neural network, trained on MC simulated events, is then applied to both data and MC events to classify them. By applying a cut on the output of the neural network, a region in abstract phase space dimensions is defined where the signal purity is higher.

In the single-lepton channel, a four-class fully connected feed-forward neural network architecture is employed (details in Ref. [24]). The four classes are $t\bar{t}\gamma$ production as a signal against $t\bar{t}\gamma$ decay, fake photon events (e-fake photon and h-fake photon events), and other prompt photon events as backgrounds. The output is a four-dimensional probability distribution. In the dilepton channel, where the expected fraction of background events from different processes is lower, a two-class fully connected feed-forward neural network architecture is used (details in Ref. [24]). The two classes are $t\bar{t}\gamma$ production as a signal against all background processes. The output is a one-dimensional probability distribution with the signal at higher values.

The neural network is trained using 40 variables in the single-lepton channel and 16 variables in the dilepton channel. These variables include the kinematic properties of the photon and the leptons, the kinematic and flavor properties of the jets, invariant masses, and angular distances between different objects. Additionally, in the single-lepton channel, to improve discrimination between $t\bar{t}\gamma$ production and $t\bar{t}\gamma$ decay, the full event is reconstructed using top quark reconstruction techniques. Further details on the variables and the neural network architecture can be found in Ref. [24]. In the single-lepton channel, the signal region (SR) and the control regions (CRs) are defined by the requirements on the neural network output summarized in Table 7.6.

In the dilepton channel, the signal region (SR) is defined by ($O_{\mathrm{NN}} > 0.6$) and the control region (CR) by ($O_{\mathrm{NN}} < 0.6$), where O_{NN} represents the output of a neural network-based discriminant, providing a one-dimensional probability distribution used to separate signal from background events.

Table 7.6: Summary of the criteria on neural network output classifiers to define the SR and CR in the single-lepton channel. The last column of the table corresponds to the purity of the target processes (signal or specific background processes) in the particular region (taken from Ref. [24]).

Category	$t\bar{t}\gamma$ decay classifier	fake γ classifier	other prompt γ classifier	purity
SR $t\bar{t}\gamma$ production	< 0.15	< 0.2	< 0.5	73%
CR $t\bar{t}\gamma$ decay	> 0.25	–	< 0.4	71%
CR fake γ	< 0.15	> 0.2	< 0.5	50%
CR Other γ		remaining events		26%

8 Estimation of background processes

The simulated events are classified into the following categories based on the photon origin detailed in Section 6.4: events with prompt photons, e-fake photon, and h-fake photon. Prompt photons are those that originate from the hard scattering process. Events with prompt photons can arise from the following processes and are estimated using the MC simulation: $t\bar{t}$, single-top, V+jets, $V\gamma$, VV, $t\bar{t}V$. The simulation of these processes is discussed in Section 6.2.

As discussed in Section 6.4, e-fake photon and h-fake photon events can be mis-reconstructed due to detector effects and photon reconstruction algorithms. Although the detector simulation models these effects, there are discrepancies between the data and the MC simulation. The mis-modeling of e-fake photon and h-fake photon events in MC is corrected using data-driven methods described in the following sections[1]. The results in Section 8.1 are also used in the charge asymmetry measurement in $t\bar{t}\gamma$ process [25].

There are events with non-prompt leptons in which the origin of the lepton is not hard scattering (e.g. from heavy-flavor decays, photon conversions, object misidentification). The contribution of these events is estimated using the data-driven matrix method detailed in Section 8.3.

8.1 e-fake photon background estimation

Electrons are reconstructed based on energy deposits in the electromagnetic calorimeter and the associated tracks in the inner detector, while photons are reconstructed solely from calorimeter energy deposits. The reconstruction processes for electrons and photons are similar, with the primary difference being that electrons have an associated track. Consequently, electrons may sometimes be misidentified as photons if the track is not reconstructed or poorly matched to the calorimeter cluster. These photons are referred to as $e \to \gamma$ fake photons. The reconstruction efficiency of electromagnetic clusters is nearly

[1]The h-fake estimation was not performed by the author, therefore they are discussed briefly in this chapter.

100%, and the misidentification of electrons as photons primarily results from tracking inefficiencies or poor matching between tracks and clusters.

It is an important background in the single-lepton channel. The main processes contributing to this background are $t\bar{t}$ dileptonic events (ee and $e\mu$ channels) and $Z \to ee$ events, where one electron fakes a photon. Although the detector simulation models this effect in the MC simulation, there are still some mis-modelling of the $e \to \gamma$ fakes between data and MC. This mis-modeling is corrected in the MC simulation using a data-driven method. In this method, the $e \to \gamma$ fake rate (defined in Section 8.1.3) is measured both in data and MC simulation, and the ratio of the two is used as a scale factor to correct the MC simulation. The $e \to \gamma$ fake rate is measured using the tag-and-probe method using the $Z \to ee$ process discussed in the following section.

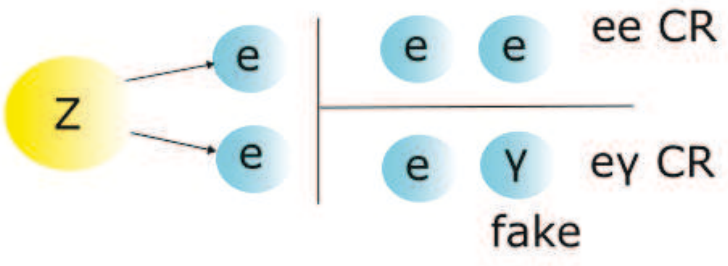

Figure 8.1: Graphical representation of the ee and $e\gamma$ control regions.

8.1.1 Tag and probe method

The so-called tag-and-probe method is a data-driven technique used for measuring the efficiency of objects. In this method, the decay of a resonance into a pair of particles is analyzed to determine the efficiency of reconstructing one of them. Specifically, this analysis uses the decay of a Z boson into an e^+e^- pair to study the fake probability of electrons. Of the two decay products, one particle is labeled as the *tag*, while the other is labeled as the *probe*. The efficiency is then measured with respect to the probe. Two control regions (CR) are defined: the ee CR and the $e\gamma$ CR. The ee CR is enriched with $Z \to ee$ events, while the $e\gamma$ CR is enriched with $Z \to ee$ events where one electron is misidentified as a photon.

The $e\gamma$ CR is created using the following requirements, where the electron is labeled *tag electron* and the photon is labeled *probe photon*:

- Exactly one electron which is trigger matched.

- At least one photon. The leading p_{T} photon is referred to as photon in the following.
- The opening angle between the electron and the photon is larger than 150 degrees. This requirement helps to reduce different background sources due to hadrons being mis-reconstructed as photons and prompt photons radiated from the electron.
- The invariant mass of the electron and the photon is within 50 GeV around the Z mass (91.188 GeV).

The ee CR is defined in exactly the same way as above, replacing the photon in the requirements with an electron with opposite charge sign with respect to the tag electron. Thus, this electron is called *probe electron* and is used as a reference to be compared with the probe photon to define the fake rate later. The complete definition of the ee and $e\gamma$ control regions is shown in the Table 8.1.

Table 8.1: Selection criteria used to define the ee and $e\gamma$ CRs.

	ee CR	$e\gamma$ CR
p_{T}	p_{T} (tag)> 25 GeV, p_{T} (probe)> 20 GeV	
$\lvert\eta\rvert$	$\lvert\eta\rvert$(tag) < 2.47, $\lvert\eta\rvert$(probe) < 2.37	
Electron identification	TightLH	TightLH
Electron isolation	FCTight	FCTight
Photon identification		Tight
Photon isolation		FCTight
	$\Delta\phi(\mathrm{tag}, \mathrm{probe}) > 150°$	
$m_{\mathrm{tag,probe}}$	$m_Z - 50$ GeV $< m_{ee} < m_Z + 50$ GeV	$m_Z - 50$ GeV $< m_{e\gamma} < m_Z + 50$ GeV
Trigger	Tag electron is trigger matched when both are trigger matched tag is chosen randomly	Tag electron is trigger matched

8.1.2 Sources of fake photons

In the $e\gamma$ CR, the origin of the probe photon can be studied using MC simulations. As previously mentioned the reconstruction level event is obtained by applying the detector simulation on the MC simulated events. The detector simulation makes it difficult to trace back the origin of the photon. The reconstructed photon is matched to the truth particle in the following way, the track of the truth particle is extrapolated to the EM calorimeter layer and the angular distance is calculated between the truth particle and the EM cluster from which the photon is reconstructed. If this angular distance (ΔR) is less than 0.3, the truth particle is considered to be the source of the photon. Based on this requirement, the photons are classified into four main categories (illustrated in Figure 8.2).

- Type (a): denoted as "mis-reco", where the photon is matched to a true electron. 87% of the selected photons belong to this class.

- Type (b): denoted as "mis-match", where the photon is matched to a true photon, but the photon's p_{T} is larger than the true photon by 10%, and at the same time there is a nearby true electron with $\Delta R < 0.1$ w.r.t photon. 1.8% of events belong to this class.

- Type (c): denoted as "non-prompt QED", where the photon matches to a true photon and there is a nearby true electron with $\Delta R < 0.1$, but the p_{T} difference between the photon and the true photon is less than 10%. 3% of the events belong to this class.

- Type (d): denoted as "prompt QED", where the photon is matched to a true photon, and there is no neighboring electron within $\Delta R < 0.1$. 8% of the selected events belong to this class.

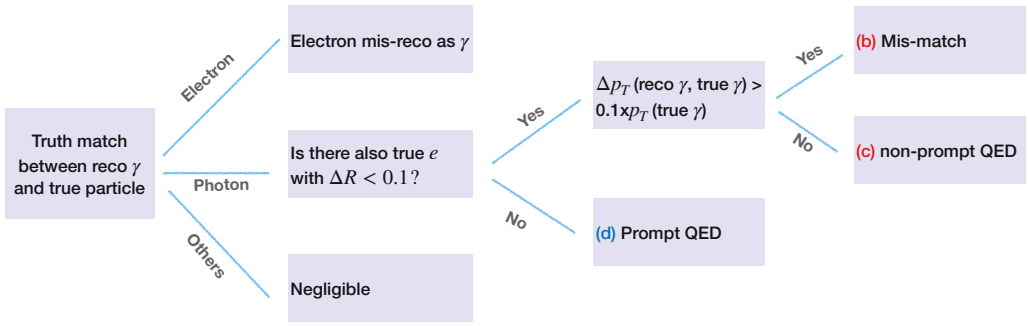

Figure 8.2: The categorisation of the selected probe photons in the $e\gamma$ CR based on the truth-particle matching.

Type (a), (b), and (c) are considered fake photons whereas type (d) is considered a genuine photon from QED emission and not considered in the MC fake rate estimation.

To better understand the four types of photons, the shape of relevant kinematic distributions is compared with the one from the probe electrons in ee CR. Figure 8.3 shows the comparison of the p_{T} spectrum between the probe e and four types of probe γ. The p_{T} spectrum of probe e matches with the three fake types (a,b,c), where type (d) has a different shape indicating that it has a different origin. In the η distribution, the type (a) and type (b) which indicate the mis-reconstruction and mis-match mostly happen in the high $|\eta|$ region. The total number of events in each category is shown in Figure 8.3 (d). The dominant contribution comes from type (a).

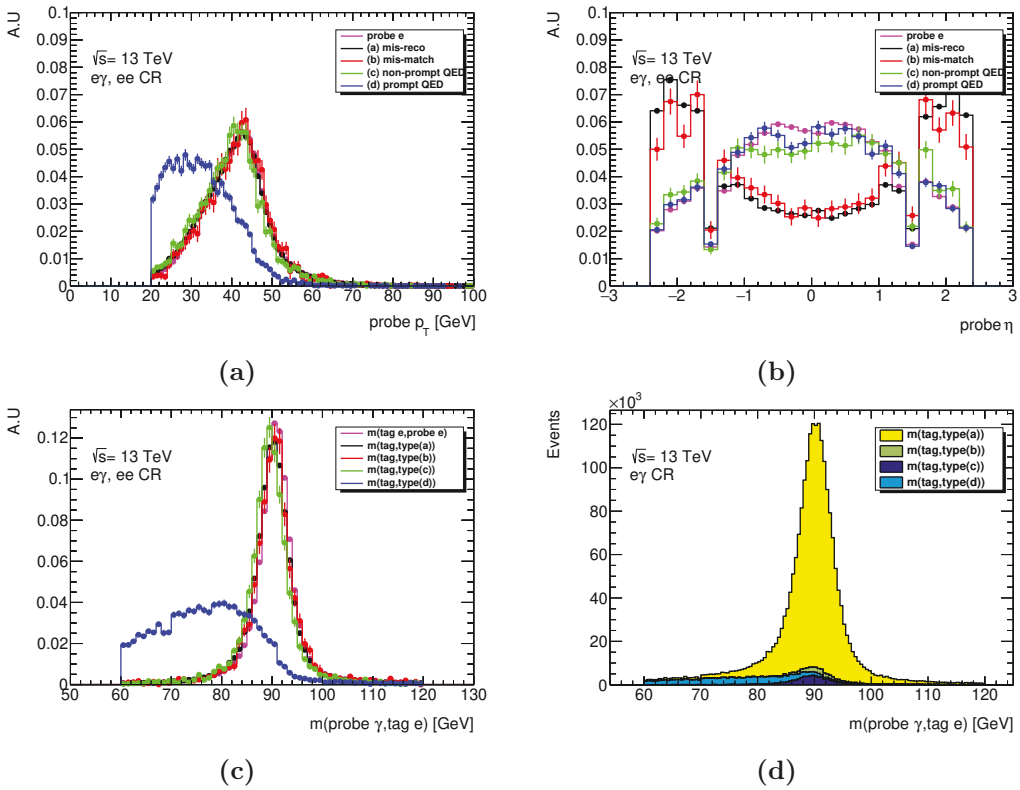

Figure 8.3: Normalized kinematic distributions are shown comparing the probe γ and probe e: p_{T} (a), η (b), and the invariant mass of the tag electron and the probe object m(probe γ, tag e) (c).

8.1.3 Fake rates

The fake rate (FR) is measured as a function of p_{T} and $|\eta|$ of the probe photon and probe electron and can be expressed as:

$$\mathrm{FR}^{i}_{e\to\gamma}(p_{\mathrm{T}},|\eta|) \equiv \frac{N^{i}_{e\gamma}(p_{\mathrm{T}},|\eta|)}{N^{i}_{ee}(p_{\mathrm{T}},|\eta|)}.$$

The number of $e\gamma$ events where the tag electron is in any bin and probe photon is in bin i ($N^{i}_{e\gamma}$) can be expressed as:

$$N^{i}_{e,\gamma} = N^{i}_{true} \times \epsilon^{reco}_{e} \times \epsilon^{\mathrm{others}}_{e} \times p^{i}_{e\to\gamma} \times \epsilon^{i}_{\gamma(F)},$$

and the number of ee events where the tag electron is in any bin and the probe electron in bin i (N^{i}_{ee})can be expressed as:

$$N^{i}_{e,e} = N^{i}_{true} \times \epsilon^{reco}_{e1} \times \epsilon^{\mathrm{others}}_{e1} \times \epsilon^{reco,i}_{e2} \times \epsilon^{\mathrm{others},i}_{e2},$$

where:

- i: bin index
- N^{i}_{true}: true number of generated $Z \to ee$ events where the probe electron is in bin i
- ϵ^{reco}_{e} and $\epsilon^{\mathrm{others}}_{e}$: reconstruction and other selection efficiencies of tag electron
- $p^{i}_{e\to\gamma}$: probability of misidentifying an electron as photon in bin i
- $\epsilon^{i}_{\gamma}(F)$: selection efficiency of the fake photon in bin i ("F" denotes the fact that it is a fake photon so that the efficiency can be different from the true photon)
- ϵ^{reco}_{e1} and $\epsilon^{\mathrm{others}}_{e1}$: reconstruction and other selection efficiencies of the tag electrons
- $\epsilon^{reco,i}_{e2}$ and $\epsilon^{\mathrm{others},i}_{e2}$: reconstruction and other selection efficiencies of the probe electrons in bin i

The $\mathrm{FR}^{i}_{e\to\gamma}$ is proportional to the $e \to \gamma$ faking probability in that bin where the proportionality constant is given by C^{i}:

$$\mathrm{FR}^{i}_{e\to\gamma} = p^{i}_{e\to\gamma} \times \frac{\epsilon^{i}_{\gamma}(F)}{\epsilon^{reco,i}_{e2} \cdot \epsilon^{\mathrm{others},i}_{e2}} = p^{i}_{e\to\gamma} \times C^{i}. \tag{8.1}$$

Fake rate in MC The FR in MC is estimated by counting the total number of fake photon events (types a, b, c) in the $e\gamma$ CR and the number of events in ee CR, and

taking the ratio of the numbers. In Figure 8.4, the p_{T} and η dependencies of the absolute differential fake rate are shown, type (d) which is not $e \to \gamma$ fake events are also shown for completeness. The fake rate changes from 0.2% to 1% for type (a) events, increasing in η. The contribution of the other categories is below 0.05% and shows a weak dependence with η.

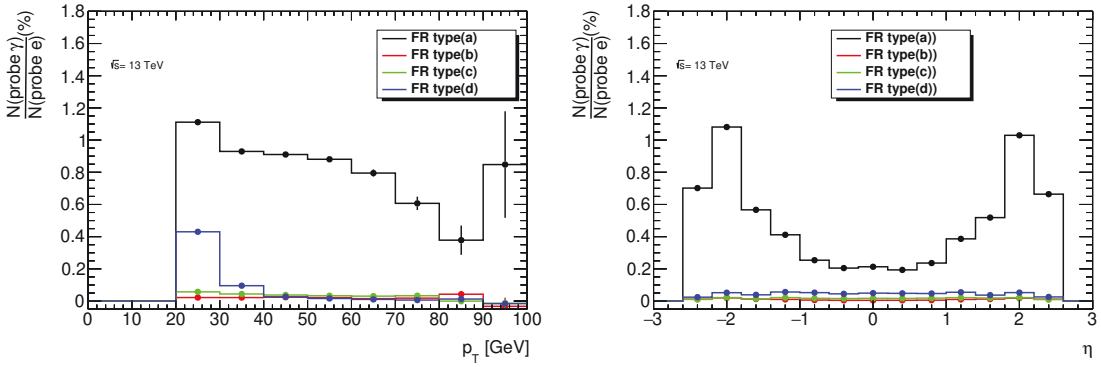

Figure 8.4: Fake rate in MC as a function of p_{T} and η. Type (d) which is not $e \to \gamma$ fake, shown here for completeness.

Fake rate in data Estimating FR in data involves more steps as the events cannot be labeled as fake photon events straightforwardly like in MC because truth particle association is not possible. Instead, a fit is performed on the invariant mass of the tag and probe to estimate the number of fake events in the $e\gamma$ and ee control regions. The number of prompt QED events, type (d), are selected in both CRs, these events are modeled using MC estimation and removed from the invariant mass histogram. Also from the MC study it is seen that the number of events from the non-Z process is negligible and therefore not subtracted.

The FR in data can be expressed as:

$$\mathrm{FR}^{i}_{dd} = \frac{N^{\mathrm{data},i}_{e,\gamma} - N^{non\text{-}Z,i}_{e,\gamma} - \text{prompt QED}}{N^{\mathrm{data},i}_{e,e} - N^{non\text{-}Z,i}_{e,e} - \text{prompt QED}}. \tag{8.2}$$

The denominator and numerator are estimated using a fit to the invariant mass distribution of tag and probe objects. In the fit, the signal is modeled using a double-sided Crystal Ball function, and the background is modeled using a Bernstein polynomial of the 4^{th} order. The fit range in the invariant mass is chosen to be 60 GeV to 120 GeV. The fit range is chosen to ensure a sufficiently pure $Z \to ee$ signal region while providing enough events in the fit to accurately model the background shape. The example of the fit in one of the bins

is shown in Figure 8.5. The signal and background functions describe the data well, and the fit is stable across different bins. A good χ^2 value is obtained for the fit, indicating that the model is a good representation of the data. The number of events are obtained by taking integral of the signal and background functions in the fit range. The FR is then calculated as the ratio of the number of events in the $e\gamma$ CR to the number of events in the ee CR.

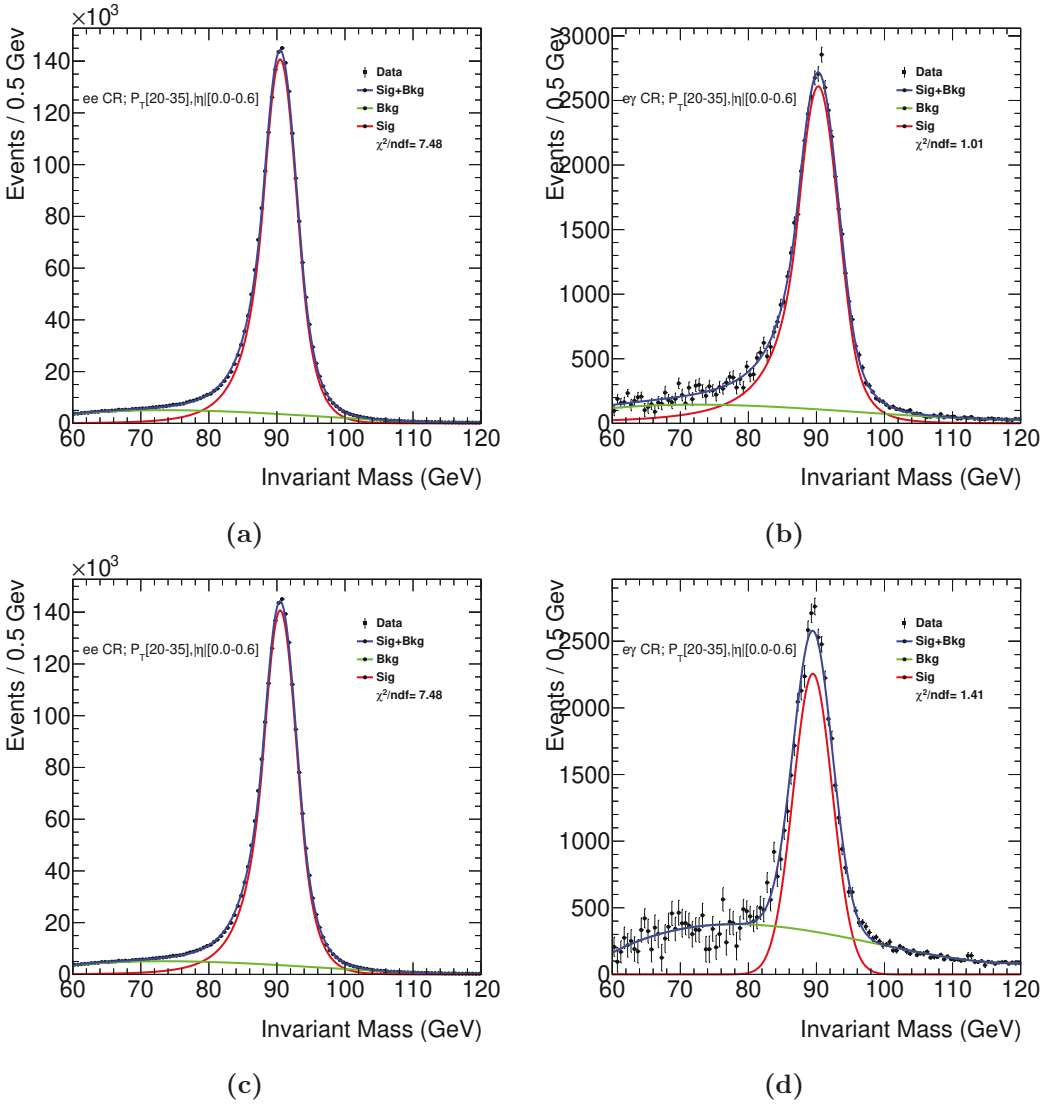

Figure 8.5: Fit to the invariant mass of the tag and probe objects in the ee and $e\gamma$ CRs. Figures (a) and (b) show the fit for converted photons for ee and $e\gamma$ CRs, respectively. Figures (c) and (d) show the fit for unconverted photons for ee and $e\gamma$ CRs, respectively. The fits are shown for the p_{T} bin [20 - 35] GeV and the $|\eta|$ bin [0 - 0.6].

Scale factor The discrepancy in the FR between data and MC is captured as a fake rate scale factor (SF):

$$\mathrm{SF}^{i}_{\mathrm{FR}} = \frac{\mathrm{FR}^{i}_{dd}}{\mathrm{FR}^{i}_{MC}}. \tag{8.3}$$

These scale factors are applied to the $e \to \gamma$ MC events as a data-driven correction.

The scale factors are derived as a function of photon p_{T} and $|\eta|$ of the fake photon. The choice of binning for p_{T} is [25, 35, 45, 1000] (in GeV) and for $|\eta|$ is [0, 0.6, 1.37] and [1.52, 1.8, 2.37]. These SFs are estimated separately for converted and unconverted photons. The SFs are shown in Figure 8.8 and Figure 8.9 for converted and unconverted photons, respectively. For converted photons, the SFs range from 0.82 to 1.45 with decreasing η, where the uncertainty ranges from 3% to 26%. For unconverted photons, the SFs range from 0.9 to 1.4 with decreasing p_{T} where the uncertainty ranges from 36% to 57%.

8.1.4 Systematic uncertainties

The uncertainties in the SF estimation are accounted for and propagated to the analysis. The following sources of systematic uncertainties are considered in estimating fake rate in data:

- The shape of the signal function has been changed from a double-sided Crystal Ball to a MC predicted template, smoothed to reduce statistical fluctuations if necessary. The results are shown in Figure 8.6a for converted photons and in Figure 8.7a for unconverted photons. For converted photons, the impact ranges from about 9% to 14% in a few bins, while for most bins, it is less than 5%. For unconverted photons, the impact is between 15% and 30% in half of the bins, and less than 10% in the other half.

- The fitting mass range has been adjusted to [65 - 115] GeV, with the results presented in Figure 8.6b for converted photons and in Figure 8.7b for unconverted photons. For converted photons, the impact is around 14% in a few bins, while for most bins it is approximately 5% or less. For unconverted photons, a couple of bins show impacts of 32% and 16%, whereas for most bins, the impact is about 10% or less.

- The shape of the background function has been changed from a Bernstein to a Gaussian, with the results shown in Figure 8.6c for converted photons and in Figure 8.7c for unconverted photons. For converted photons, the impact is about 10% or less. For unconverted photons, a couple of bins have impacts of 15% and 24%, while for most bins, the impact is about 10% or less.

The impact of different systematic variations in each $[p_{\mathrm{T}}; |\eta|]$ bin is shown in Figure 8.10 for converted photons and in Figure 8.11 for the unconverted photon case. The values show the relative impact of the systematic variations with respect to the nominal SFs in each bin. In some cases the impact is large in a few bins, but in most cases, the impact is less than 10%. The impact has no particular trend with respect to p_{T} or $|\eta|$.

The final 2D scale factors for converted and unconverted photon cases are summarized in Figure 8.8 and 8.9. The uncertainties in the scale factors represent the total uncertainty, with various sources of uncertainty combined in quadrature.

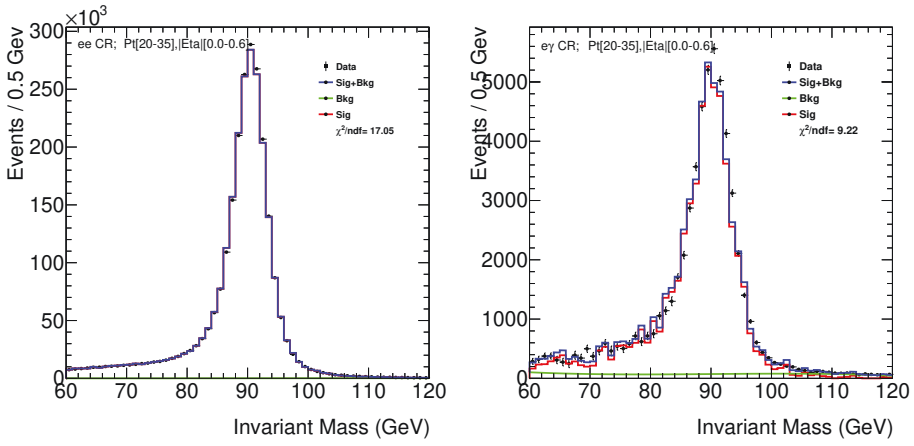

(a)

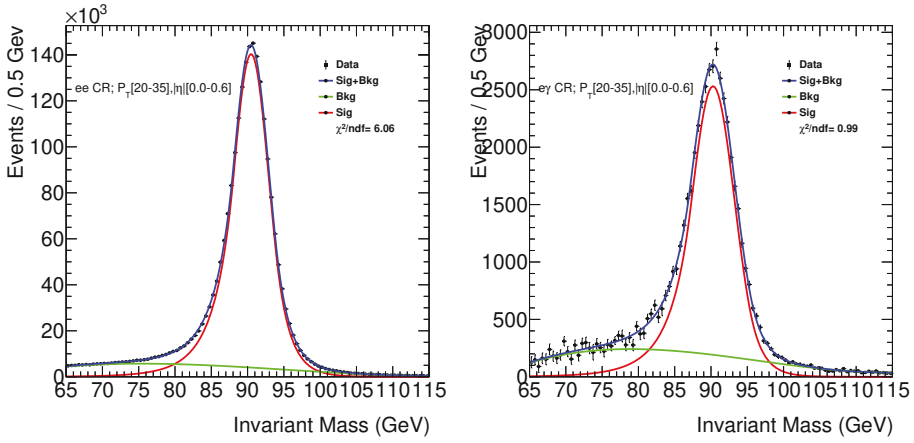

(b)

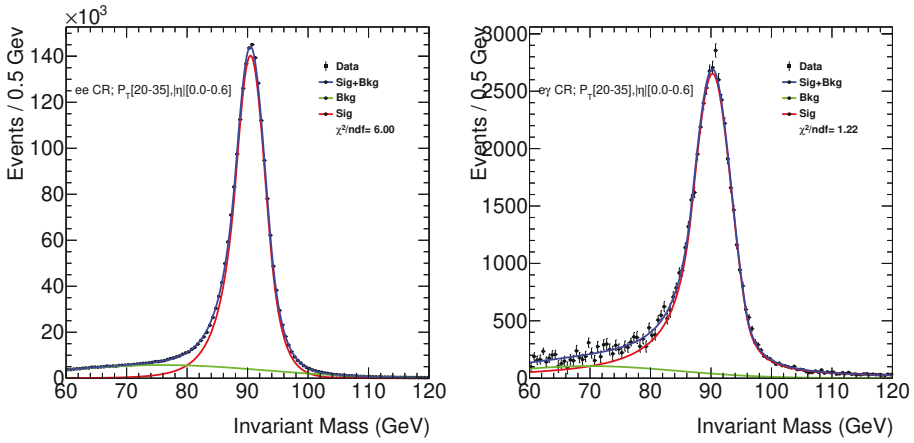

(c)

Figure 8.6: Invariant mass of the tag and probe objects in data, and fitted in the ee (left) and $e\gamma$ (right) CRs for converted photons, with different sources of systematic uncertainties: (a) the signal function modeled with MC template, (b) varying the fitting mass window on both sides by 5 GeV, and (c) the background function is replaced by a Gaussian function. The above fits are only for a particular p_{T} and $|\eta|$ bin.

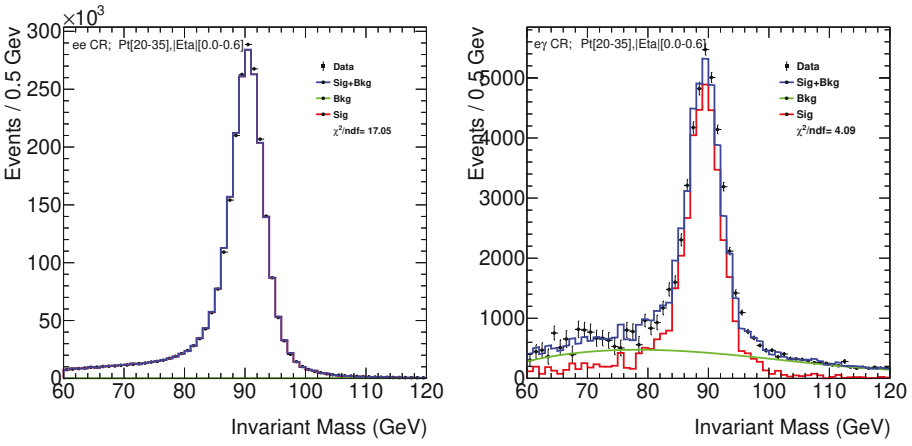

(a)

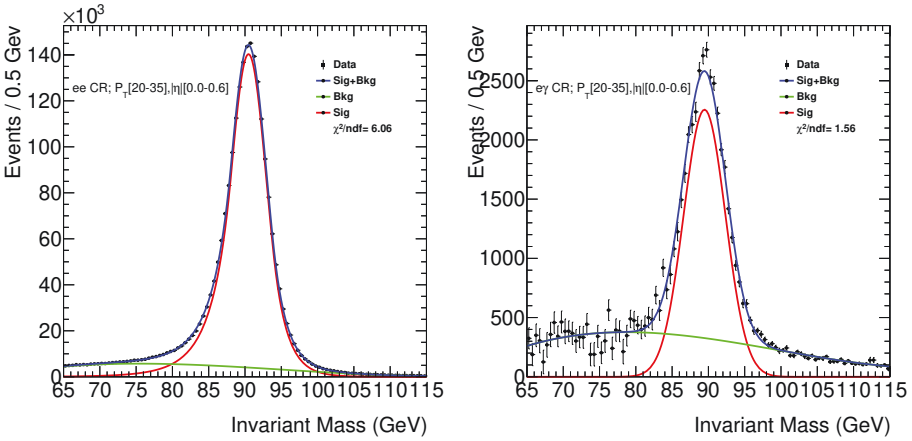

(b)

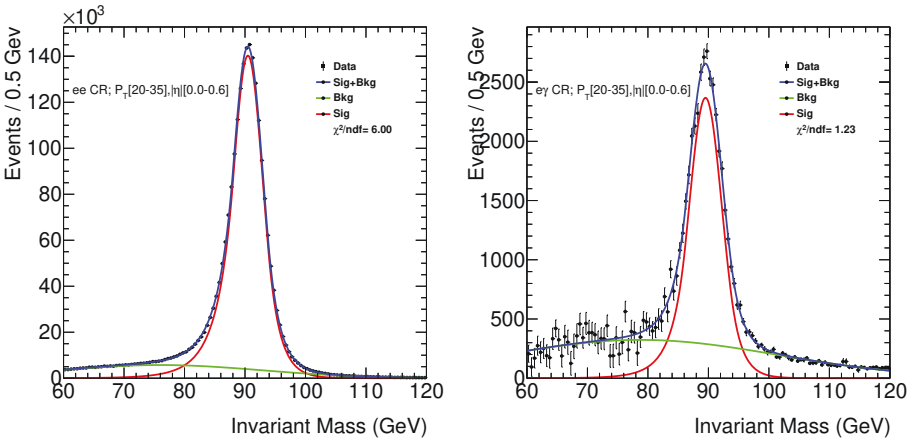

(c)

Figure 8.7: Invariant mass of the tag and probe objects in data, and fitted in the ee (left) and $e\gamma$ (right) CRs for unconverted photons, with different sources of systematic uncertainties: (a) the signal function modeled with MC template, (b) varying the fitting mass window on both sides by 5 GeV, and (c) the background function is replaced by a Gaussian function. The above fits are only for a particular p_{T} and $|\eta|$ bin.

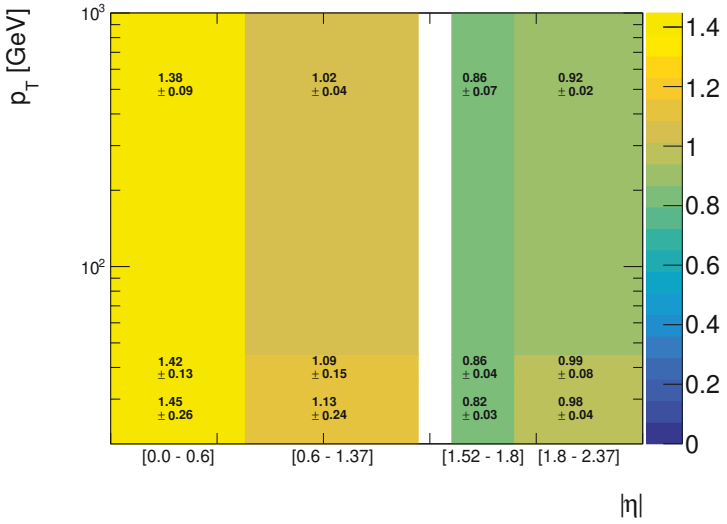

Figure 8.8: Final FR scale factors as a function of p_{T} and $|\eta|$ of the converted photon. The uncertainties correspond to the sum in quadrature of the statistical and systematic uncertainties.

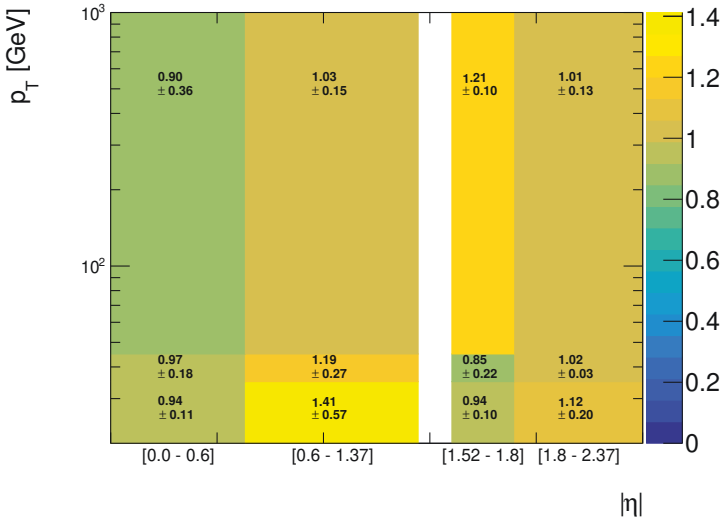

Figure 8.9: Final FR scale factors as a function of p_{T} and $|\eta|$ of the unconverted photon. The uncertainties correspond to the sum in quadrature of the statistical and systematic uncertainties.

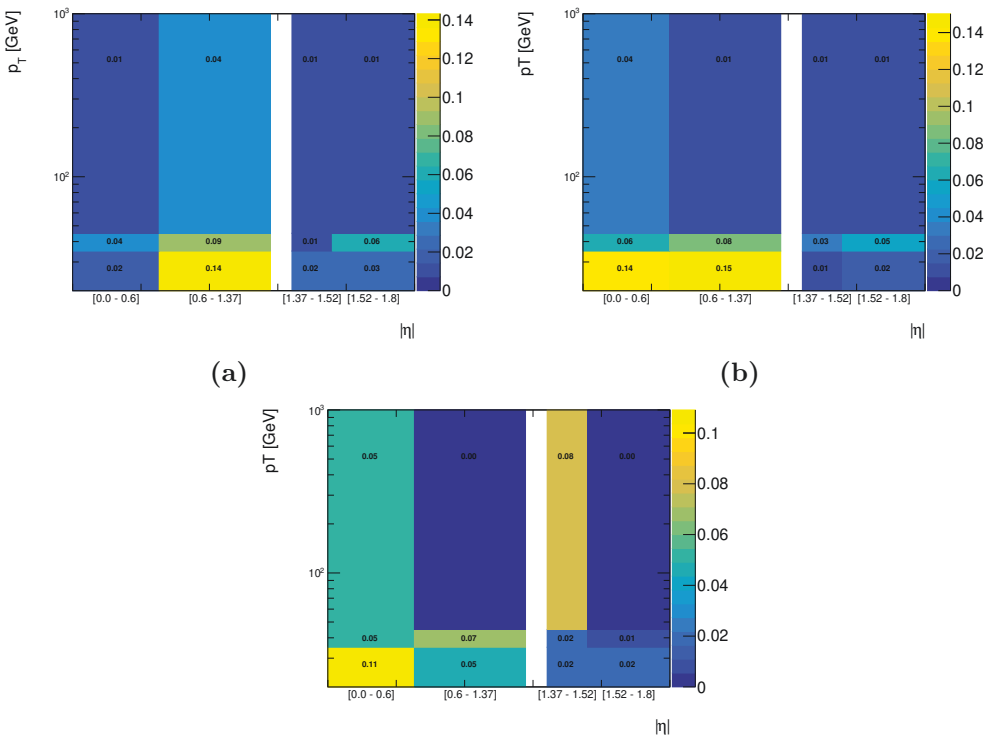

Figure 8.10: Impact of the sources of systematic uncertainties for the converted photons. The numbers show the relative uncertainty in percentage with respect to the nominal SFs in each bin. The sources of uncertainty are: (a) the signal is modeled with MC template, (b) the background function is replaced by a Gaussian function, and (c) varying the fitting mass window on both sides by 5 GeV.

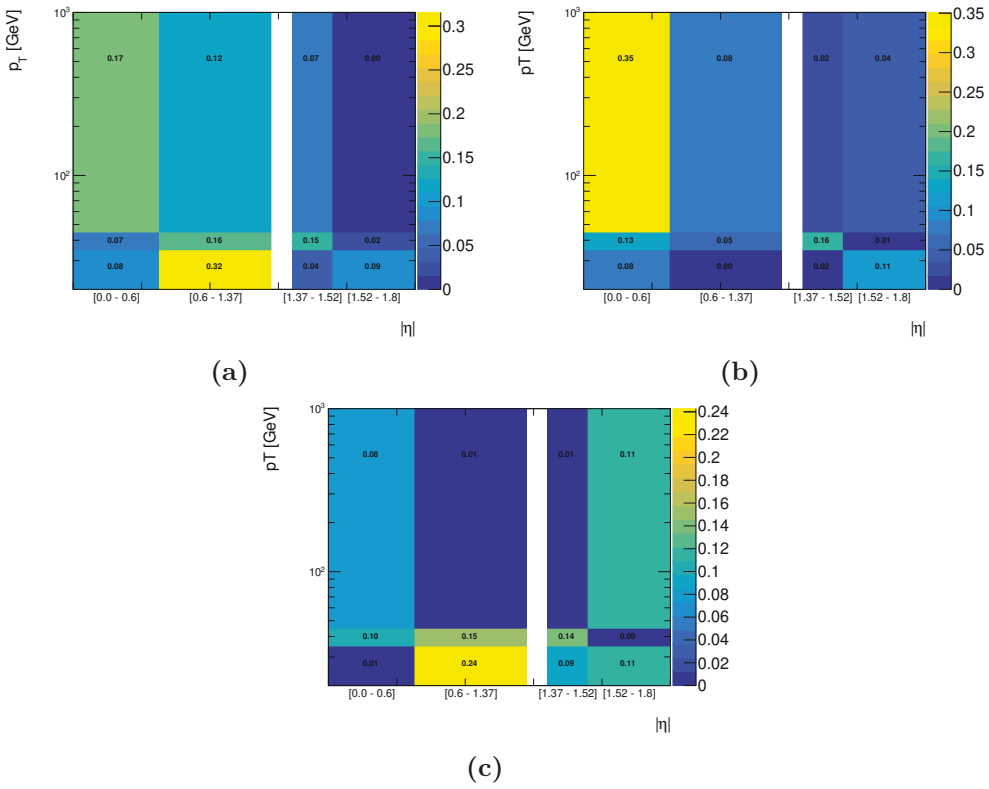

Figure 8.11: Impact of the sources of systematic uncertainties for the unconverted photons. The numbers show the relative uncertainty in percentage with respect to the nominal SFs in each bin. The sources of uncertainty are: (a) the signal is modeled with MC template, (b) the background function is replaced by a Gaussian function, and (c) varying the fitting mass window on both sides by 5 GeV.

8.2 h-fake photon background estimation

Photons are reconstructed from the EM calorimeter clusters. The improper reconstruction and identification of photons can lead to mis-reconstruction of jets as photons. Also, photons coming from hadron decays can be misidentified and these events can be selected. Mismodeling of these events is seen in MC when compared with the data. The SFs obtained by taking the ratio of the h-fake photon events in data and MC are applied to the MC events to correct for the mismodeling. The SFs are estimated[2] using the so-called data-driven ABCD method [104]. Four orthogonal regions A, B, C, and D are defined based on photon identification and isolation criteria to get different regions enriched h-fake photon photons.

[2]The h-fake estimation was not performed by the author, therefore they are discussed briefly in this section.

In addition to the event selection requirements, the following selection criteria of photons are used to define the four regions.

- **Region A:** In this region the photon must fail the "tight" requirement on photon identification. To fail the tight requirement, the photon must fulfill all the tight identification requirements except for at least two of the requirements on the shower-shape variables. The shower-shaped variables were designed to help identify the h-fake photon.

- **Region B:** Photons are required to fail the isolation requirement and fail to satisfy the Tight identification requirement.

- **Region C**: Photons are required to satisfy the tight identification requirement and be non-isolated. For this, they must fail the isolation requirement and in addition fulfill $p_{\mathrm{T}}^{\mathrm{cone20}} > 3$ GeV (This requirement helps to reduce prompt photon contamination).

- **Region D:** Photons must satisfy the same tight isolation and identification requirements used to select photons in the analysis.

Assuming no correlation between photon isolation and photon identification, the number of events in the four regions can be expressed as,

$$\frac{N_A^{\text{h-fake}}}{N_B^{\text{h-fake}}} = \frac{N_D^{\text{h-fake}}}{N_C^{\text{h-fake}}}. \tag{8.4}$$

The requirements for photon isolation and identification are chosen in such a way as to minimize any correlation between isolation and isolation. Any deviation from this assumption can be quantified by the variable θ_{MC} defined as,

$$\theta_{\mathrm{MC}} = \frac{\frac{N_{\mathrm{D,MC}}^{\text{h-fake}}}{N_{\mathrm{C,MC}}^{\text{h-fake}}}}{\frac{N_{\mathrm{A,MC}}^{\text{h-fake}}}{N_{\mathrm{B,MC}}^{\text{h-fake}}}}. \tag{8.5}$$

The variable θ_{MC} has some dependency on the photon kinematics and is estimated in MC as a function of (p_{T},$|\eta|$) for converted photons and unconverted photons [25].

Using the the relation Eq. 8.4 and taking into account the correlation between isolation and identification, the number of h-fake photons in the region D can be estimated as

$$N_{\text{est.}}^{\text{h-fake}} = \frac{N_{\mathrm{A,data}}^{\text{h-fake}} \times N_{\mathrm{C,data}}^{\text{h-fake}}}{N_{\mathrm{B,data}}^{\text{h-fake}}} \times \theta_{\mathrm{MC}}, \tag{8.6}$$

where $N^{\text{h-fake}}_{\text{i,data}}$ ($i \in$ A,B,C) is the number of h-fake photon events in data in the A, B, and C regions. The prompt photon and e-fake photon events are subtracted from these regions when estimating $N^{\text{h-fake}}_{\text{i,data}}$.

The SFs can be calculated as the ratio of the estimated number of h-fake events in data and MC as,

$$\text{SF}^{\text{h-fake}} = \frac{N^{\text{h-fake}}_{\text{est.}}}{N^{\text{h-fake}}_{\text{MC}}}. \tag{8.7}$$

The SFs are taken from Ref. [25] as a function of (p_{T},$|\eta|$) for converted and unconverted photons, and are used in the measurements presented in this thesis.

8.3 Fake-lepton background estimation

The selection on $t\bar{t}$ events requires the identification of one charged lepton in the single-lepton channel and two charged leptons in the dilepton channel. These leptons originate from W or Z boson decay for the following processes and are treated as background: $t\bar{t}$, single-top, $V\gamma$, $V+$jets, VV, $t\bar{t}V$. These leptons are referred to as "prompt" or "real" leptons. Acceptance, quality, and isolation requirements are applied to select these leptons. These processes are modeled using MC simulation. On the other hand, non-prompt leptons and non-leptonic particles may satisfy these selection criteria in the data events, giving rise to the so-called "non-prompt" or "fake" lepton background. For electrons, the contributions come from semileptonic decays of b and c quarks, photon conversions, and jets with large energy deposits in the EM calorimeter. For muons, they originate from semileptonic decays and from charged hadron decays in the tracking volume or in hadronic showers, or from punch-through particles from high energy hadronic showers.

The contribution of these events in the dilepton channel is typically from $t\bar{t}\gamma$ events or $W+$jets events in the single-lepton channel with a fake lepton in addition to a real lepton. The contribution in the dilepton channel is estimated from MC to be around 0.5%. The fake-lepton events in the single-lepton channel are typically from QCD multi-jet events with an associated photon production. This background is estimated from data using the so-called *matrix method* described in the following.

8.3.1 Matrix method

The reconstruction of electrons and muons is discussed in detail in Section 3.3. The identification and the isolation criteria mentioned in Section 7.1 make the objects referred

	electron	muon
Tight definition	MediumLH identification PLVLoose isolation	Medium identification PLVLoose isolation
Loose definition	LooseAndBLayerLH identification no isolation	Medium identification no isolation

Table 8.2: Definition of "tight" and "loose" electron and muon based on the identification and isolation criteria.

to as "tight electrons" and "tight muons". A looser isolation and identification criteria are applied to make "loose electrons" and "loose muons" objects. The "tight" and "loose" definitions are summarized in Table 8.2.

Based on two types of lepton definitions, two data samples are selected, differing only in the lepton identification and isolation requirements. The "tight" sample contains mostly events with real leptons whereas the "loose" sample is enriched in events with non-prompt and fake leptons.

The number of events in the "loose" (N^{loose}) and "tight" (N^{tight}) samples can be expressed as a linear combination of events with real and fake leptons:

$$N^{\text{loose}} = N^{\text{loose}}_{\text{real}} + N^{\text{loose}}_{\text{fake}}, \tag{8.8}$$

$$N^{\text{tight}} = N^{\text{tight}}_{\text{real}} + N^{\text{tight}}_{\text{fake}}, \tag{8.9}$$

where $N^{\text{loose}}_{\text{real}}$ and $N^{\text{tight}}_{\text{real}}$ are the number of events with real leptons in the "loose" and "tight" samples, respectively, and $N^{\text{loose}}_{\text{fake}}$ and $N^{\text{tight}}_{\text{fake}}$ are the number of events with fake leptons in the "loose" and "tight" samples, respectively. One can define ϵ_{real} as the probability of a real lepton in the loose sample to pass the tight selection and ϵ_{fake} as the probability of a fake lepton in the loose sample to pass the tight selection.

Equation 8.10 can be written as:

$$N^{\text{tight}} = \epsilon_{\text{real}} N^{\text{loose}}_{\text{real}} + \epsilon_{\text{fake}} N^{\text{loose}}_{\text{fake}}. \tag{8.10}$$

From equations Eqs. 8.8 to 8.10, the number of tight events in data with a fake lepton can be written as:

$$N^{\text{tight}}_{\text{fake}} = \frac{\epsilon_{\text{fake}}}{\epsilon_{\text{real}} - \epsilon_{\text{fake}}} (\epsilon_{\text{real}} N^{\text{loose}} - N^{\text{tight}}). \tag{8.11}$$

The number of events with fake or non-prompt leptons can be estimated from the dataset containing loose lepton events. The real and fake efficiencies are estimated from fake

enriched CRs (detailed in Section 8.3.2). Both ϵ_{real} and ϵ_{fake} have a dependency on lepton kinematics and event topology and are estimated as a function of different kinematic variables. However, using the above formula only an estimate of the total number of fake events in the tight dataset can be obtained. To obtain the number of events as a function of a particular variable, an extended matrix method is used, where a weight per event is calculated separately for each event.

If the event is present in the loose sample but not in the tight sample, a weight can be written as

$$w_i = \frac{\epsilon_{\text{fake}}\epsilon_{\text{real}}}{\epsilon_{\text{real}} - \epsilon_{\text{fake}}}. \tag{8.12}$$

If the event is present in both samples, the weight becomes

$$w_i = \frac{\epsilon_{\text{fake}}}{\epsilon_{\text{real}} - \epsilon_{\text{fake}}}(\epsilon_{\text{real}} - 1). \tag{8.13}$$

The two equations above can be written more compactly as

$$w_i = \frac{\epsilon_{\text{fake}}}{\epsilon_{\text{real}} - \epsilon_{\text{fake}}}(\epsilon_{\text{real}} - \delta_i). \tag{8.14}$$

where δ_i is unity if loose event i pass the tight selection and 0 otherwise. The loose data sample N^{loose} along with the weights can be used to estimate the fake lepton events as a function any distribution of interest in the signal region.

The efficiency estimation in the CRs is detailed in Section 8.3.2. The uncertainty on the efficiency estimation is detailed in Section 8.3.3.

8.3.2 Calculation of fake and real efficiencies

Calculation of fake efficiencies The fake efficiencies ϵ_{fake} are measured in data events dominated by non-prompt and fake lepton background events. This is done in a fake enriched CR (CR_{fake}). The criteria for selecting events for this CR_{fake} are as follows:

- number of jets between 2 and 4
- at least 1 b-tagged jet with 70% working point
- exactly one loose electron or muon
- $E_{\text{T}}^{\text{miss}} < 30$ GeV

The number of jets between 2 and 4 is chosen to create a fake enriched CR maximizing fake lepton events while minimizing contamination from real lepton events. The distributions of

$E_{\mathrm{T}}^{\mathrm{miss}}$ and the transverse mass[3] m_{T}^{W} in data and MC simulation are illustrated in Figures 8.12 and 8.13. The contamination comes dominantly from real lepton events from $t\bar{t}$, W+jets and Z+jets process. To get a sample of pure non-prompt and fake lepton events, events with real leptons are subtracted based on the MC expectation. These real leptons from the MC are matched to the truth particle, which ensures that only real lepton contribution is subtracted from the data and no fake lepton event is removed. A systematic uncertainty is assigned to this normalization of the MC predictions.

The efficiency ϵ_{fake} can be simply determined as the ratio between the number of tight and loose fake events in this region.

$$\epsilon_{\mathrm{fake}} = \left(\frac{N_{\mathrm{fake}}^{\mathrm{tight}}}{N_{\mathrm{fake}}^{\mathrm{loose}}}\right)_{CR_{\mathrm{fake}}} = \left(\frac{N^{\mathrm{tight}} - N_{\mathrm{real}}^{\mathrm{tight}}}{N^{\mathrm{loose}} - N_{\mathrm{real}}^{\mathrm{loose}}}\right)_{CR_{\mathrm{fake}}},$$

where $N_{\mathrm{real}}^{\mathrm{tight}}$ and $N_{\mathrm{real}}^{\mathrm{loose}}$ are the real lepton contributions to the tight and loose samples in the fake CR. These numbers are evaluated from MC simulation.

[3] $m_{\mathrm{T}}^{W} = \sqrt{2p_{\mathrm{T}}(l) \times E_{\mathrm{T}}^{\mathrm{miss}}(1 - \cos\phi)}$, where ϕ is the azimuthal angle between the lepton direction and the $E_{\mathrm{T}}^{\mathrm{miss}}$

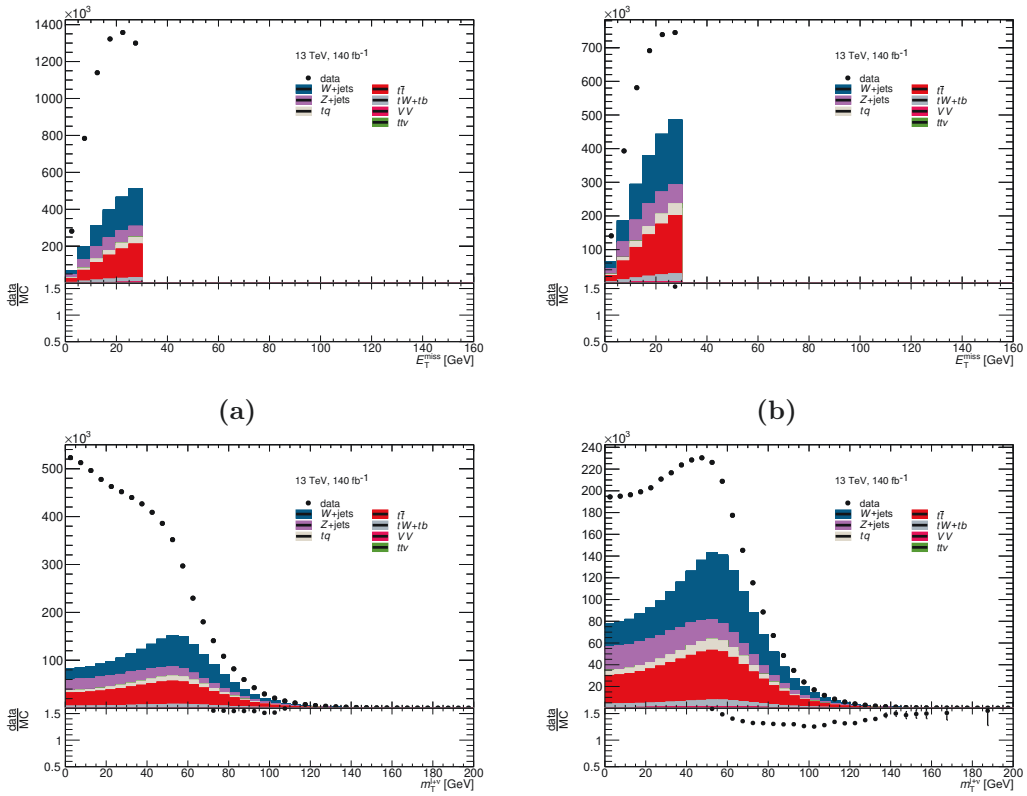

Figure 8.12: Distribution of $E_{\mathrm{T}}^{\mathrm{miss}}$ and m_{T}^{W} in a fake-enriched CR with loose (a, c) and tight (b, d) electron definitions. The expected contribution from real lepton events, based on MC simulation, is displayed. For calculating the fake efficiency, the real lepton events are subtracted from the data to isolate the fake lepton events.

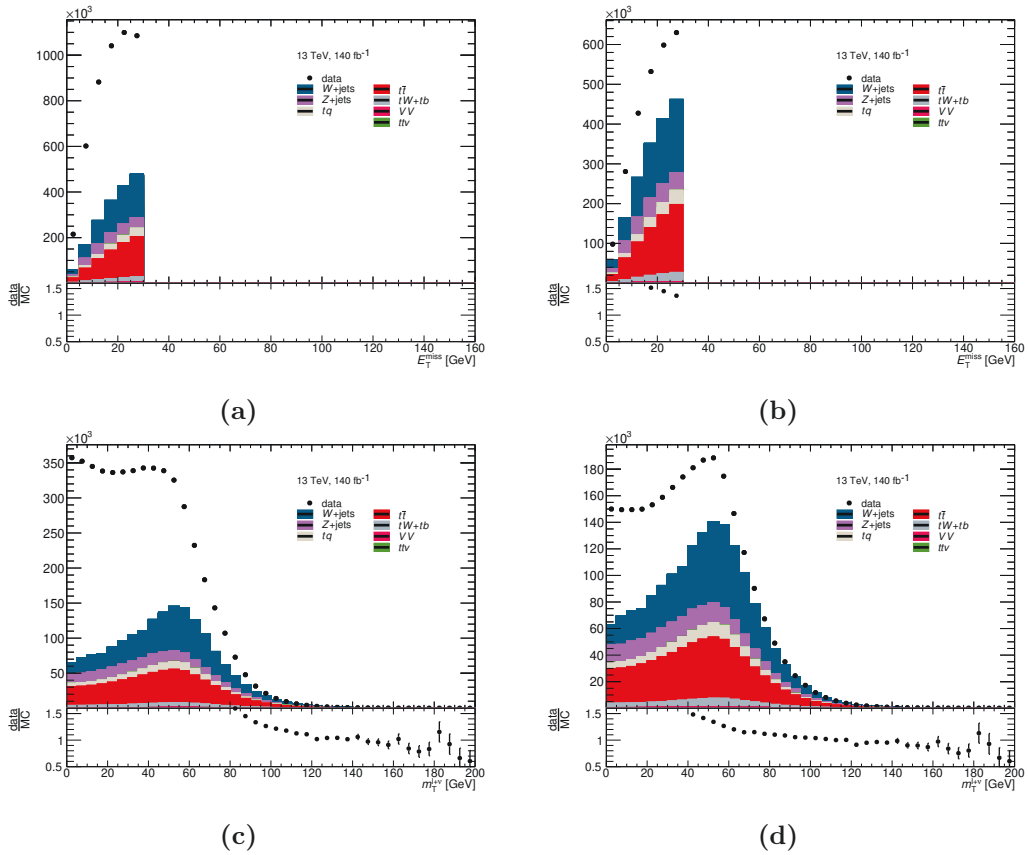

Figure 8.13: Distribution of $E_{\mathrm{T}}^{\mathrm{miss}}$ and m_{T}^{W} in a fake-enriched CR with loose (a, c) and tight (b, d) muon definitions. The expected contribution from real lepton events, based on MC simulation, is displayed. For calculating the fake efficiency, the real lepton events are subtracted from the data to isolate the fake lepton events.

Parametrization Fake and real efficiencies depend on the event topology and kinematic observables. The efficiencies are estimated as a function of the following observables.

- lepton p_{T}
- lepton $|\eta|$
- $\Delta\phi$ between the lepton and $E_{\mathrm{T}}^{\mathrm{miss}}$
- m_{T}^{W}

To accurately capture the dependence of fake and real lepton efficiencies on event kinematics, these efficiencies are measured in two-dimensional bins of (p_{T}, $|\eta|$), (p_{T}, $\Delta\phi$), and (p_{T}, m_{T}^{W}).

Calculation of real efficiencies The real efficiencies ϵ_{real} are measured with the prompt lepton events (truth matched) using the MC simulated events. The same selection is used as described in the fake efficiency calculation section.

The real efficiencies are calculated by taking the ratio of the number of events with real tight lepton over number of events with real loose leptons:

$$\epsilon_{\mathrm{real}} = \left(\frac{N_{\mathrm{real}}^{\mathrm{tight}}}{N_{\mathrm{real}}^{\mathrm{loose}}} \right)_{CR_{\mathrm{real}}}$$

The fake and real efficiencies are shown in Figure 8.14 and Figure 8.15 for the single-electron and single-muon channels, respectively. The real lepton efficiency is very high, ranging from 88% to 98% with increasing p_{T} and decreasing $|\eta|$. The fake lepton efficiency ranges from approximately 30% to 55% with increasing p_{T} and decreasing $|\eta|$, as illustrated in the figures.

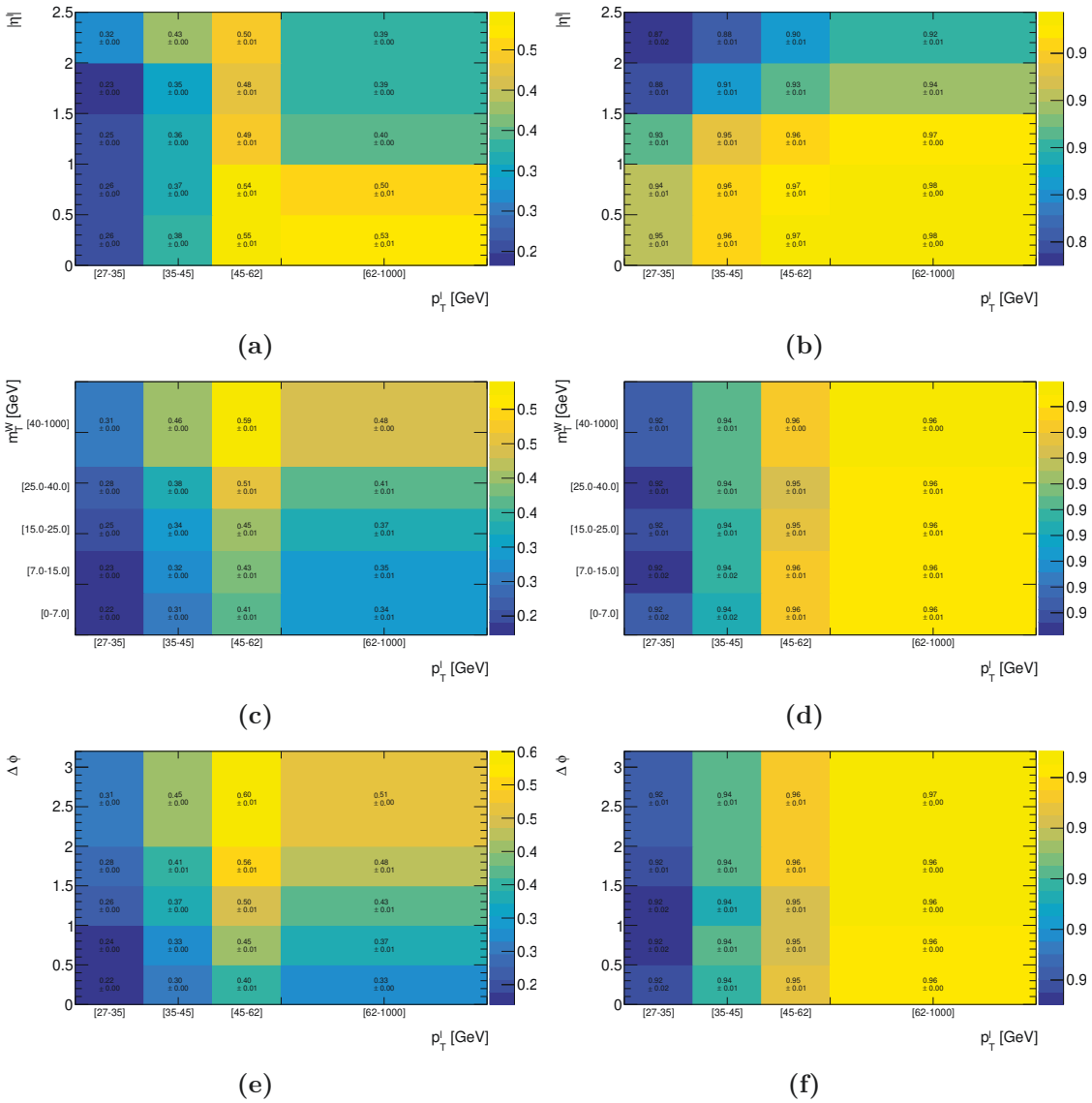

Figure 8.14: Fake (left) and real (right) efficiency in the single-electron channel in [p_{T}, $|\eta|$] (a, b), [p_{T}, m_{T}^{W}] (c, d) and [p_{T}, $\Delta\phi$] (e, f) bins. Only the statistical uncertainties are shown.

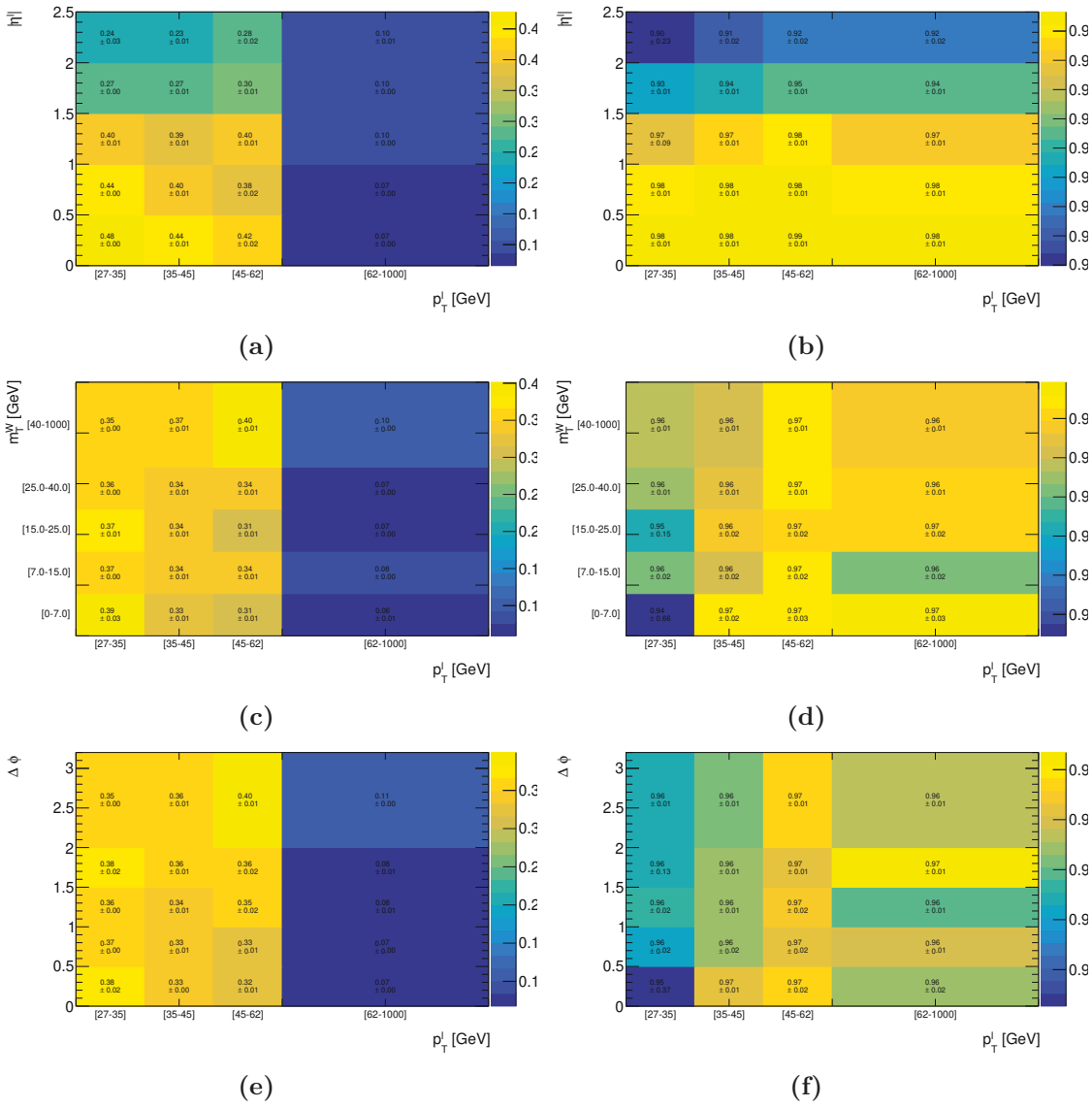

Figure 8.15: Fake (left) and real (right) efficiency in the single-muon channel in [p_{T}, $|\eta|$] (a, b), [p_{T}, m_{T}^{W}] (c, d) and [p_{T}, $\Delta\phi$] (e, f) bins. Only the statistical uncertainties are shown.

8.3.3 Uncertainty on fake lepton estimation

The sources of systematic uncertainties considered on the non-prompt and fake lepton background determination with the matrix method originate from the determination of the real efficiency, the use of MC simulation to correct the efficiency measurements, differences in the non-prompt and fake background composition in the signal regions and in the regions

used to measure the efficiencies, and the treatment of the dependence of the efficiencies on lepton and event properties.

The uncertainty on the real efficiency measurement method is assessed by measuring the efficiency in a region where the contamination from non-prompt and fake lepton events is expected to be negligible, i.e. by requiring $E_{\mathrm{T}}^{\mathrm{miss}} > 120$ GeV. The impact is found to be negligible compared to other sources of systematic uncertainty (1% level).

A source of uncertainty on the fake efficiency measurement is the uncertainty on the normalization of the MC simulated events used to subtract the real lepton contribution in the CR. The fake efficiency is measured after varying the $t\bar{t}$ cross-section by 5% and the difference with the nominal efficiency is taken as systematic uncertainty. The impact of this uncertainty on fake efficiency is shown in Figure 8.16. The fake efficiency changes by 2% or less in the single-electron channel and by 10% or less in the single-muon channel.

Real and fake efficiencies are measured in a fake enriched CR but are applied in a signal region to measure the fake lepton events. This extrapolation from the CR to the signal region is not straightforward and without uncertainty. For that reason, the efficiencies are also extracted from two different CRs and taken as systematic uncertainties. These two CRs are defined by changing the cut on the number of jets, i.e njets ≥ 1 (CR2), and the other CR is defined by varying the $E_{\mathrm{T}}^{\mathrm{miss}}$ requirement with $30 \leq E_{\mathrm{T}}^{\mathrm{miss}} \leq 50$ GeV (CR3). The impact is shown in Figures 8.17 and 8.18 for CR2 and CR3, respectively. The impact on the fake efficiency ranges approximately from 2% to 40% with increasing p_{T} and decreasing $|\eta|$ in the single-electron channel. In the single-muon channel, the impact ranges approximately from 2% to 27% with increasing p_{T}. This approach allows to partially assess the uncertainty coming from the difference in the composition of the non-prompt and fake lepton in the signal region and CRs and thus remove the possible bias in defining the CR.

Two dimensional real and fake efficiencies are measured for [p_{T}, $|\eta|$], [p_{T}, $\Delta\phi$] and [p_{T}, m_{T}^{W}] parametrisations. The [p_{T}, m_{T}^{W}] is taken as nominal parametrization and others are used as systematic variations. Using these parametrizations, the number of events with fake leptons in the signal region is estimated, shown in Figures 8.20 and 8.21 for electron and muon channels. The final real and fake efficiencies including the systematic uncertainty are shown in the Figure 8.19.

The estimation of lepton fakes was also obtained for a different identification and isolation selection and used in the charge asymmetry measurement in the $t\bar{t}\gamma$ process [25].

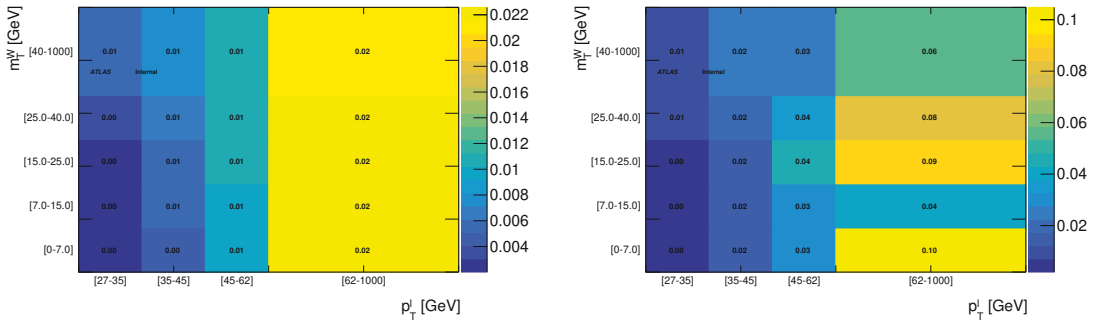

(a) **(b)**

Figure 8.16: Fake efficiencies estimated by varying the $t\bar{t}$ normalization by 5%. The 2D histograms display the impact on each bin, with the numbers representing the relative uncertainty compared to the nominal value for the electron channel (a), and for the muon channel (b).

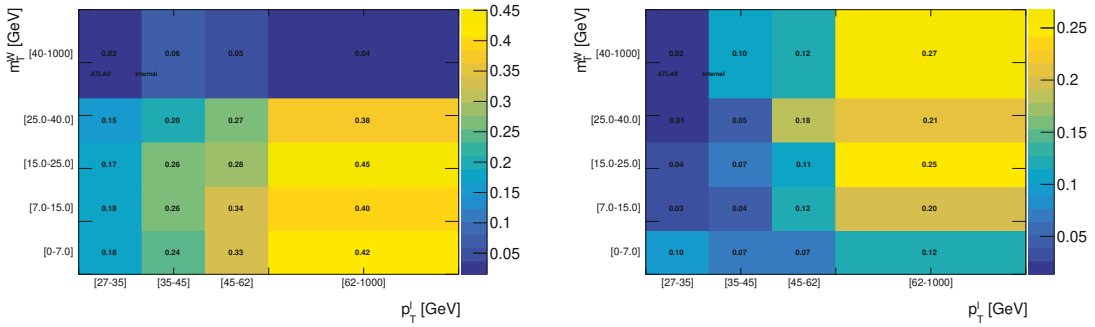

(a) **(b)**

Figure 8.17: Fake efficiencies estimated by requirement on the number of jets njets ≥ 1. The 2D histograms show the impact on each bin, with the numbers representing the relative uncertainty compared to the nominal value for the electron channel (a), and for the muon channel (b).

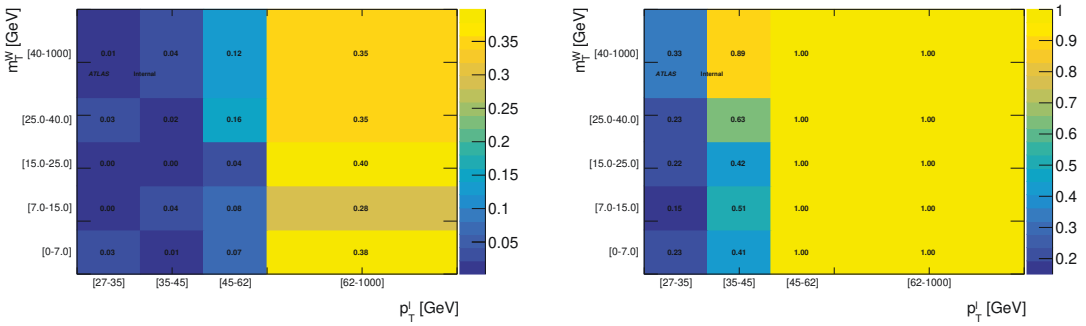

(a) **(b)**

Figure 8.18: Fake efficiencies estimated by requirement on the $E_{\mathrm{T}}^{\mathrm{miss}}$, $30 < E_{\mathrm{T}}^{\mathrm{miss}} < 50$ GeV. The 2D histograms show the impact on each bin, with the numbers representing the relative uncertainty compared to the nominal value for the electron channel (a), and for the muon channel (b).

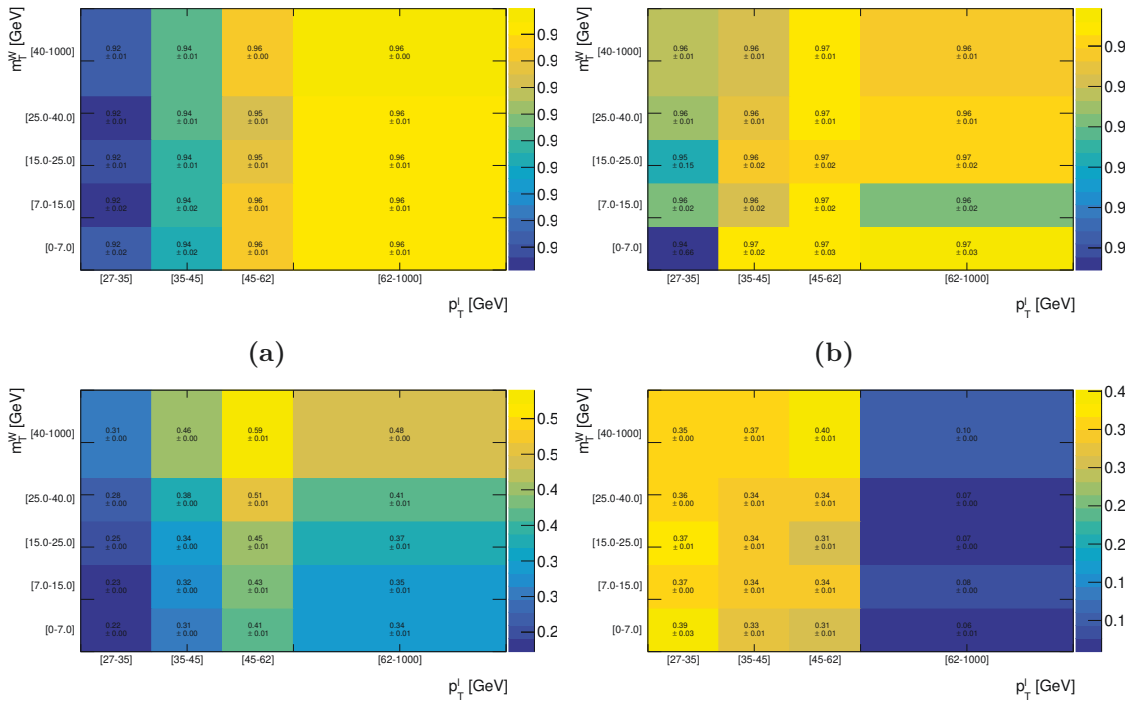

(c) **(d)**

Figure 8.19: The real and fake efficiencies, including both statistical and systematic uncertainties, are shown for the $[p_{\mathrm{T}}^{l}, m_{\mathrm{T}}^{W}]$ parametrization. The results for the electron channel are displayed in plots (a) and (c), while results for the muon channel are displayed in plots (b) and (d).

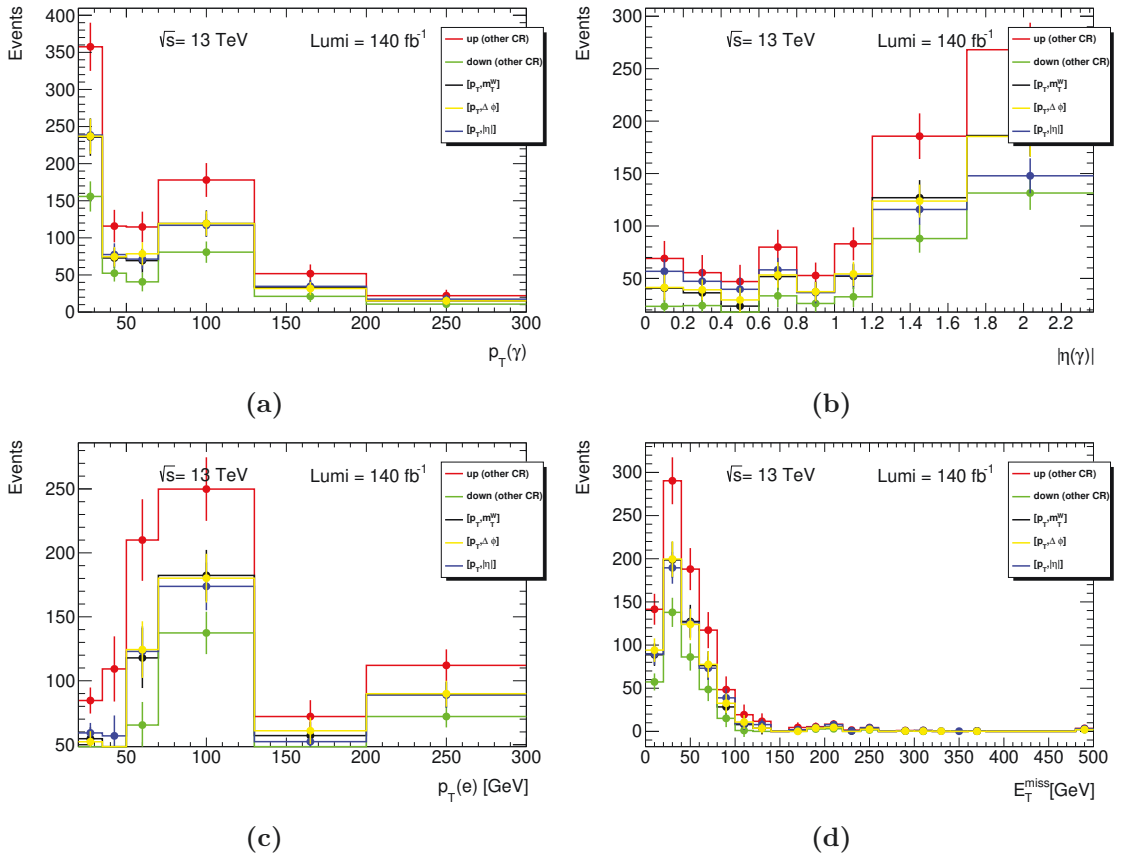

Figure 8.20: Kinematic distributions of the fake lepton contribution in the signal region in the single-electron channel obtained using three different parameterizations. The histograms "up (other CR)" and "down (other CR)" correspond to the distributions obtained by varying the real and fake efficiencies by their uncertainties (shown in Figure 8.19) using the parameterization $[p_{\mathrm{T}}^{l}{:}m_{\mathrm{T}}^{W}]$.

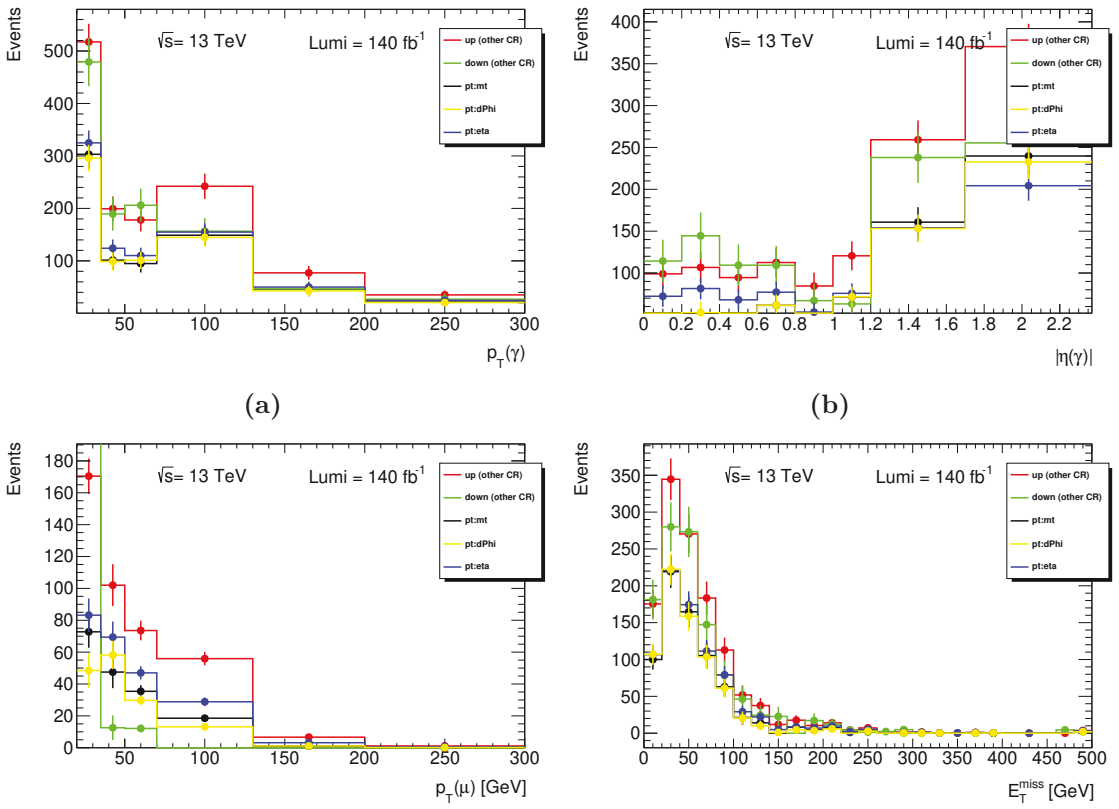

Figure 8.21: Kinematic distributions of the fake lepton contribution in the signal region in the single-muon channel obtained using three different parameterizations. The histograms "up (other CR)" and "down (other CR)" correspond to the distributions obtained by varying the real and fake efficiencies by their uncertainties (shown in Figure 8.19) using the parameterization $[p_{\mathrm{T}}^{l}$:$m_{\mathrm{T}}^{W}]$.

9 Sources of systematic uncertainties

Uncertainties are an inherent part of any measurement, and it is important to properly account for them. There are several sources of uncertainties that need to be considered. These include statistical uncertainties and systematic uncertainties. Statistical uncertainties arise from the finite size of the data and simulated samples. In collider experiments, events occur randomly with a constant probability. The number of events in a given sample is a random variable that follows a Poisson distribution. The statistical uncertainty is the standard deviation of the Poisson distribution. This can only be reduced by increasing the size of the data sample meaning more integrated luminosity.

Systematic uncertainties arise from imprecision in the experimental setup, analysis techniques, and modeling of the underlying physical processes. For example, uncertainties can come from particle reconstruction and identification, energy and momentum measurement, luminosity measurement, etc. Uncertainties in the modeling arise from the limitations of the theoretical models used to describe the data. MC event generation is used to generate events from a theoretical model. The uncertainties arise, for instance, from the choice of the PDF set, the choice of the renormalization and factorization scales, and the choice of the parton showering and hadronization models. Also, the cross-sections used to normalize the MC simulations to the data have uncertainties associated with them. Different sources of uncertainties are discussed in the following sections.

9.1 Experimental uncertainties

Experimental uncertainties arise from the reconstruction and identification of physics objects, uncertainties on the energy and momentum scales and resolutions, flavor tagging of jets, uncertainties on the integrated luminosity measurement, and uncertainties on the pile-up simulation. These affect both the signal and background modeling.

Lepton efficiencies Electrons are reconstructed from the energy deposits in the calorimeter and the inner detector tracks. Muons are reconstructed by combining the information from

the inner detector and the muon spectrometer. The simulation is corrected to describe the efficiency in the data, these include, efficiency related to the trigger, particle isolation, identification, and reconstruction. The accuracy with which the detector simulation models these effects in MC is very important. Slight mis-modelling is observed in these efficiencies between MC and in data and are corrected using data-driven approach using tag-and-probe method using $Z \to ee$ ($\mu\mu$ for muons) and $J/\psi \to ee$ ($\mu\mu$ for muons) processes [98; 99]. Multiplicative scale factors are obtained from the ratio of efficiencies in data and MC. These scale factors are obtained in the bins of kinematic observables and are applied to the MC to correct the mis-modeling. The uncertainty on the estimated scale factors is used to create systematic variation templates.

Photon efficiencies Photons are reconstructed from the energy deposits in the calorimeter. The identification of prompt photons in the hadronic environment is challenging, because of the presence of the overwhelming amount of non-prompt photons from hadron decays. Photons are identified with selection criteria on the shape and properties of the electromagnetic showers and also by requiring them to be isolated from other particles. These identification and isolation efficiencies in MC are corrected to describe the data [105; 106]. Uncertainties on these corrections are propagated to the analysis by creating varied templates.

e, μ, γ **energy and momentum calibration** Electrons and photon energy are measured from EM calorimeter clusters. The energy and momentum scale and resolution are calibrated using $Z \to ee$ decay and are validated using radiative Z boson decays [106]. The muon momentum is studied using $Z \to \mu\mu$ and $J/\psi \to \mu\mu$ events, and correction factors are derived to correct the muon momentum scale and resolution in MC to match with the data [99]. The uncertainties on the calibration are used to create systematic variation templates to propagate the uncertainties to the analysis.

Jet uncertainties Jet reconstruction is described in Section 3.3. The uncertainties come mainly from the jet energy scale, resolution and jet vertex tagging. The jets are calibrated first with a sequence of simulation-based corrections then several *in-situ* techniques to correct the differences observed between data and simulation [107]. The individual steps address various effects: origin correction adjusts the four-momentum of the jet to point to the primary vertex instead of the center of the detector; pile-up correction removes the excess energy caused by in-time and out-of-time pileup; absolute MC-based calibration aligns the jet's four-momentum with the particle-level energy scale; and global sequential

calibration reduces flavor dependence and energy leakage effects using the calorimeter, track, and other variables. A residual calibration is derived using *in-situ* measurements and is applied only to the data. The uncertainties have many sources and are reduced to fewer effective nuisance parameters through eigenvector decomposition.

The jet energy resolution (JER) is measured using energy between jets and well measured objects like photons or Z bosons [107]. There are a total of seven effective nuisance parameters associated to JER in the category reduction scheme [107], and a single source of uncertainty for the agreement between data and Monte Carlo, all of which are varied by one sigma to study their impact on the analysis.

The efficiency of the jet vertex tagging (JVT) algorithm is measured both in data and MC using the tag-and-probe method using $Z \to \mu\mu$ +jets events [108]. Scale factors are derived by taking the ratio of the efficiency in data and MC.

b-tagging uncertainties Jets coming from b-quarks have their own topological features, and b-tagging allows us to distinguish them from light-flavour jets. The uncertainty arises from the difficulty in distinguishing between b-quarks and light-flavour jets coming from the hadronization of light quarks. The b-tagging efficiency is measured using the $t\bar{t}$ events and the scale factors are derived by taking the ratio of the efficiency in data and MC [109]. For each jet category (b-, c-, light-flavor jet), the uncertainties are decomposed into several uncorrelated components using the eigenvector decomposition method [110]. As a result, there are a total of 45 uncertainties for b-jets, 20 uncertainties for for c-jets and another set of 20 uncertainties for light-flavour jets[111]. The b-jets, c-jets and light-jets are calibrated for transverse momentum below 400 GeV, 250 GeV and 300 GeV, respectively. A normalization uncertainty is assigned to the events containing at least one uncalibrated jet with higher p_{T}. A 50% normalization uncertainty is assigned to the events with uncalibrated jets. For each type of uncalibrated jet, one NP is assigned.

Missing transverse momentum The $E_{\mathrm{T}}^{\mathrm{miss}}$ is the measure of missing transverse momentum in the event. It is reconstructed from the vector sum of several terms corresponding to different types of reconstructed objects, shown in Eq. 3.3. The uncertainties in the reconstructed objects are propagated into the uncertainty of $E_{\mathrm{T}}^{\mathrm{miss}}$. An additional contribution to the systematic uncertainty of $E_{\mathrm{T}}^{\mathrm{miss}}$ comes from the soft terms $E_{x,y}^{\mathrm{Soft}}$. The uncertainty on the soft term is evaluated in [49] and the final uncertainty on the $E_{\mathrm{T}}^{\mathrm{miss}}$ is propagated to the analysis.

Pile-up uncertainties The pile-up profile in the MC is corrected to match the data using reweighting procedure. The uncertainty on the reweighting procedure is based on the disagreement between the instantaneous luminosity in data and MC. The uncertainty on the weight is used to create the systematic variation templates.

Luminosity uncertainties The integrated luminosity measured by the ATLAS experiment is 140.1 fb^{-1} with an uncertainty of 0.83% [65]. The luminosity is increased and decreased by 0.83% to estimate the impact in the measurement.

9.2 Modelling uncertainties

In the analysis the signal and background processes are modeled using MC simulations. The uncertainties in the parameter choices need to be considered, for example, the parton distribution functions, the renormalization and factorization scales, the parton shower and hadronization model, the radiation in initial state radiation (ISR) and the hard gluon emission. These choices for the signal and background processes are discussed below.

$t\bar{t}\gamma$ production, $t\bar{t}\gamma$ decay, $t\bar{t}$, and $tW\gamma$ modeling For the $t\bar{t}\gamma$ production, $t\bar{t}\gamma$ decay, $t\bar{t}$, and $tW\gamma$ simulations, the uncertainties arising from the choices of renormalization (μ_R) and factorization (μ_F) scales are estimated by varying μ_R and μ_F separately up and down by a factor of 2 with respect to the nominal value. These variations are implemented using a reweighting procedure in the MC generator to reduce the effect of statistical fluctuations.

For these simulations, the uncertainty on the parton shower and hadronization model is assessed by comparing the nominal samples with Pythia8 [63] shower to those generated with Herwig7 [64].

For $t\bar{t}\gamma$ production, $t\bar{t}\gamma$ decay, and $t\bar{t}$ simulations, the uncertainty due to initial-state radiation is estimated by comparing the nominal samples with the *A14 var3c* eigentune of Pythia8 for low and high radiation scenarios. The uncertainty on parton distribution functions (PDFs) is propagated to the analysis using the PDF4LHC15 prescription [112] for $t\bar{t}\gamma$ production and $t\bar{t}\gamma$ decay simulations. A total of 30 eigenvectors are used to estimate the PDF uncertainties.

For $t\bar{t}$ simulations, the uncertainty on the *hdamp* parameter of Powheg to control the hard gluon emission is estimated by generating an alternative set of events with Powheg + Pythia8 with the parameter set to twice its nominal value.

Additionally, for the $tW\gamma$ simulations, these uncertainties are considered uncorrelated between the $tW\gamma$ sample and the tW sample.

Cross-section uncertainties The uncertainty in cross-sections is considered for all the processes except for the signal for which the normalization is measured from the data. The measured cross-section for the $t\bar{t}$ process is known with a precision of 4.6% [113]. An uncertainty of 6% is assigned to the $t\bar{t}$ process. As discussed in Chapter 6, $t\bar{t}\gamma$ decay process is simulated at LO and a K-factor is used to scale the cross-section to NLO value. An uncertainty of 20% is assigned based on the estimated uncertainty in the NLO K-factor [20]. This source of uncertainty is only considered in the inclusive $t\bar{t}\gamma$ measurement Section 11.3 whereas for $t\bar{t}\gamma$ production measurement $t\bar{t}\gamma$ decay template is kept free floating and this source of uncertainty is not considered. For all other minor background processes contributing to the Other γ category, a conservative uncertainty of 50% is assigned for the normalisation.

10 Measurement of the $t\bar{t}\gamma$ cross-sections

In this chapter, the measurement of the $t\bar{t}\gamma$ production differential cross-sections is presented. Differential cross-sections represent the production rate of a process as a function of a certain observable. The cross-section of a process has a unique dependence on kinematical observables, thus measuring the cross-section differentially and comparing it with the theory prediction makes it possible to test the theory in a more detailed way. These comparisons help us to identify any discrepancies between the theoretical calculations and measurements which could hint at new physics. In this analysis, the cross-section is measured for both $t\bar{t}\gamma$ production and total $t\bar{t}\gamma$ production and decay processes. For the former process events with photons originating from the top quark decay products are treated as background. This makes the process more sensitive to the top quark and photon coupling compared to the total $t\bar{t}\gamma$ process, where events with photons originating from the top quark decay are also considered as signal.

The cross-section is measured as a function of transverse momentum of the photon $p_{\mathrm{T}}(\gamma)$, pseudorapidity of the photon $|\eta(\gamma)|$, angular separation between the photon and the lepton $\Delta R(\gamma, \ell)$, angular separation between the photon and the closest b-jet $\Delta R(\gamma, b)_{\mathrm{min}}$, the angular separation between the lepton and the closest jet $\Delta R(\ell, j)_{\mathrm{min}}$, and transverse momentum of the leading jet $p_{\mathrm{T}}(j_1)$. In addition, in the dilepton channel, the cross-section is measured as a function of the angular separation between the photon and the leading lepton $\Delta R(\gamma, \ell_1)$, the angular separation between the photon and the sub-leading lepton $\Delta R(\gamma, \ell_2)$, the pseudo-rapidity difference between the leptons $|\Delta\eta(\ell, \ell)|$, the azimuthal angle difference between the leptons $|\Delta\phi(\ell, \ell)|$, and the transverse momentum of the dilepton system $p_{\mathrm{T}}(\ell, \ell)$. The full list of variables used in the measurement is given in Table 10.1. The observables related to the kinetic properties of the photon are sensitive to the top quark and photon coupling, in particular the photon p_{T}. The observables related to the angular separation between the photon and the leptons give insight into the structure of this coupling. The observables related the pseudo-rapidity and azimuthal angle difference between the leptons are sensitive to the spin correlation between the top quark and the anti-top quark.

The cross-section is measured at particle level within a defined fiducial phase space volume close to the acceptance of the detector (Section 10.1). The fiducial phase space is defined at particle level, to compare the results with the theoretical predictions. It also makes it easier to compare with future calculations and among measurements from different experiments.

Any distribution at reconstruction level can be thought of as there exists an underlying "true" distribution that is convoluted with the detector effects. The distortion comes mainly because of the finite resolution of the detector, limited efficiency and acceptance of the detector. To measure the cross-section at particle level, the detector effects on the measured distribution need to be corrected, which is done using unfolding techniques. In particular, for this analysis, the profile likelihood unfolding method is used. The unfolding procedure is detailed in Section 10.2.

Ideally, a continuous functional dependence between the cross-section and the observables would be preferable. However, the finite detector resolution prevents this. Consequently, the cross-section is measured in discrete bins. The choice of binning depends on several factors, the detector resolution and the available events in that bin. The study on choosing bin width is described in Section 10.6.

Table 10.1: The differential cross sections are measured in the single-lepton channel and dilepton channel as a function of the following variables:

Variable	Definition
Both dilepton and single-lepton channels:	
$p_{\mathrm{T}}(\gamma)$	Transverse momentum of the photon
$\lvert\eta\rvert(\gamma)$	Absolute value of the pseudorapidity of the photon
$\Delta R(\gamma,\ell)_{\mathrm{min}}$	Angular separation between the photon and the closest lepton
$\Delta R(\gamma,b)_{\mathrm{min}}$	Angular separation between the photon and the closest b jet
$\Delta R(\ell,j)_{\mathrm{min}}$	Smallest angular separation between any of the selected leptons and jets
$p_{\mathrm{T}}(j_1)$	Transverse momentum of the leading jet
Additional variables for dilepton channel:	
$\Delta R(\gamma,\ell_1)$	Angular separation between the photon and the leading lepton
$\Delta R(\gamma,\ell_2)$	Angular separation between the photon and the subleading lepton
$\lvert\Delta\eta(\ell,\ell)\rvert$	Pseudorapidity difference between the two leptons
$\Delta\phi(\ell,\ell)$	Azimuthal angle difference between the two leptons
$p_{\mathrm{T}}(\ell,\ell)$	Transverse momentum of the dilepton system

Before the unfolding procedure is applied to the data various tests are performed using pseudo-data. This approach validates the unfolding procedure and avoids introducing bias. The unfolding tests are detailed in Section 10.7. After validation of the unfolding procedure, profile likelihood unfolding is performed using data to measure the cross-section. The results are discussed in Section 11.1, Section 11.3, and Section 11.2 for $t\bar{t}\gamma$ production measurement, total $t\bar{t}\gamma$ production and decay measurement, and $t\bar{t}\gamma$ production measurement in a combined single lepton and dilepton channel, respectively.

10.1 Fiducial phase space

The measurements are performed at the particle level in a fiducial phase space volume. Particle level refers to final state particles after the parton showering and hadronization but prior to any interaction with the detector apparatus. The fiducial regions in the single lepton and dilepton final states are defined to closely follow the kinematic requirements at the reconstruction level. The objects at the particle level are defined as follows:

- **Photons:** The photons should not come from the hadron decay. They must fulfill $p_{\mathrm{T}} > 20\,\mathrm{GeV}$ and $|\eta| < 2.37$. Additionally, they must be isolated, with the condition that the sum of transverse momenta of all charged particles surrounding the photon within $\Delta R \leq 0.2$ must be smaller than 5% of its own p_{T}.
- **Leptons:** Electrons and muons are "dressed" with nearby photons within a $\Delta R < 0.1$ cone around the lepton (excluding photons originating from hadron decays). Leptons are required to have $p_{\mathrm{T}} > 25$ GeV and $|\eta| < 2.5$, and not being originated from hadron decays.
- **Jets:** Jets are clustered using the anti-kt algorithm with a radius of R=0.4. They are required to have $p_{\mathrm{T}} > 25$ GeV and $|\eta| < 2.5$. Non-interacting particles and muons are not considered in the clustering.
- **b-jets:** A jet is classified as a b-jet if it is associated with a hadron (with $p_{\mathrm{T}} >$ 5 GeV) containing a b-quark. This association is done using ghost-matching [114] procedure.
- An overlap removal procedure among the objects is performed in the following order:
  - Muon-jet: If there is a muon and a jet within $\Delta R(\mu, j) \leq 0.4$, the muon is removed.
  - Electron-jet: Similarly if is are an electron and a jet within $\Delta R(e, j) \leq 0.4$, the electron is removed.
  - Photon-jet: If there is a photon and a jet within $\Delta R(j, \gamma) \leq 0.4$, the jet is removed.

The fiducial phase space in the single-lepton channel is defined by requiring exactly one photon, exactly one electron or muon, at least four jets among which at least one is a b-jet. In the case of the dilepton channels, it is defined by requiring exactly one photon, exactly two leptons (electron or muon), at least two jets among which at least one is a b-jet. In addition, the event should pass the following requirement both in single-lepton

and dilepton channels: $\Delta R(\gamma, l) > 0.4$. Events are rejected if there are additional lepton candidates with $p_{\mathrm{T}} > 7$ GeV.

10.2 Profile likelihood unfolding

The cross-section is measured from data using the so-called *template method*. This method is used to measure the contributions of different processes from observed data using histogram templates typically obtained from MC simulation, where the normalization of the template is the parameter of interest (POI), and the shape of the template remains fixed. To measure an inclusive cross-section, a single POI is assigned to the signal template. For differential cross-section measurements, the cross-section is measured for every bin, for that reason the signal template is created in such a way that each bin of the histogram template is parameterized with a normalization factor.

The reconstruction level spectrum y can be written in terms of the truth spectrum x as

$$y = Rx,$$

where R is the response matrix. The response matrix is a two-dimensional matrix that represents the detector response from particle level to reconstruction level (example distribution shown in Section 10.4). The standard unfolding procedure involves the inversion of the response matrix to obtain the truth spectrum. It becomes difficult when the matrix is not easily invertible. Instead, a different approach is followed in which a standard profile likelihood fitting is used for unfolding [115]. In this approach, the truth distribution comprising N bins is multiplied by the corresponding response matrix of size N x M, thereby transforming the truth distribution into a distribution at the reconstruction level with M bins. A normalization factor is assigned for each bin of the truth distribution, these factors are POIs. It is important to note that the normalization of these folded distributions at the reconstruction level is identical to the normalization at the particle level distribution. Therefore, by measuring the normalization factors for each bin of each folded distribution at reconstruction level, the normalization of the truth level is directly obtained, thus the cross-section is measured at the truth level. Standard profile likelihood fit is performed to obtain the POIs. A toy example to illustrate the unfolding procedure is shown in Figure 10.1.

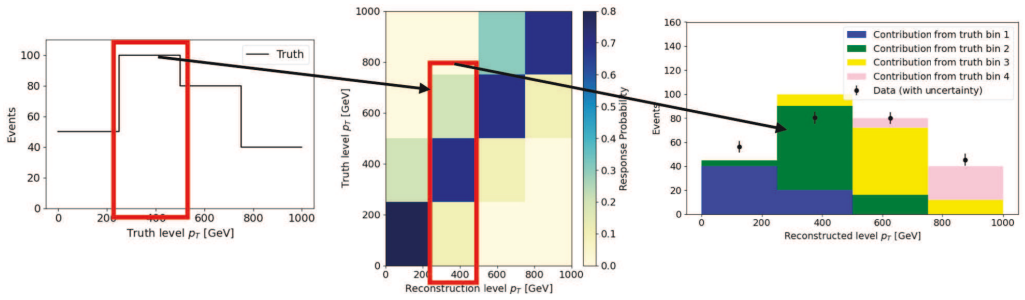

Figure 10.1: Toy example to illustrate the unfolding procedure. The truth distribution is multiplied by the response matrix to obtain the distribution at the reconstruction level. A normalization factor is assigned for each bin of the truth distribution. The profile likelihood fit is performed to the reconstruction level distribution to obtain the normalization factors. The truth distribution is directly obtained from the normalization factors.

Likelihood construction The likelihood is constructed using HISTFACTORY [116] which is used to build parameterized probability density functions in the RooFit/RooStats framework [117] using simple ROOT histograms. The likelihood is constructed (taking the product over all bins) using the truth level histogram template, the response matrix for the signal and the histogram templates at reconstruction level for backgrounds (see Eq. 10.1).

$$L(\vec{n}^{data}|\vec{\mu},\vec{\theta}) = \prod_{c\epsilon\text{Region}} \prod_{b\epsilon\text{Bins}} \text{Pois}(n_{b,c}^{\text{data}}|\nu_{b,c}(\vec{\mu},\vec{\theta})) \cdot \prod_{p} \text{Gauss}(0|\theta_p,1), \tag{10.1}$$

where:
- *Region* refers to the different signal and control regions,
- *Bins* refers to the bin of the reconstruction level histogram,
- $n_{b,c}^{\text{data}}$ is the data in bin b and region c,
- $\nu_{b,c}$ is the expected total events in bin b and channel c,
- $\vec{\theta}$ are the nuisance parameters (NPs) describing systematic uncertainties [9]. The NPs are constrained with Gauss$(0|\theta_p,1)$, a Gaussian constraint for the NP $\theta_p \in \vec{\theta}$ with mean of 0 and standard deviation of 1.
- $\vec{\mu}$ are the unconstrained parameters (e.g. POIs).

The parameters $\nu_{b,c}$ can be expressed as follows:

$$\nu_{b,c}(\mu,\theta,\gamma) = \left[\sum_i \gamma_{b,c,i} \cdot \mu_i \cdot R_{b,c,i}(\theta) \cdot T_i\right] + \sum_B \gamma_{b,c}^B \times N_{b,c}^B(\theta), \tag{10.2}$$

where:
- γ factors are the bin-by-bin scale factors accounting for the MC statistical uncertainties. The background samples each have a factor $\gamma^B_{b,c}$, and for the signal each truth bin has a unique $\gamma_{b,c,t}$
- $R_{b,c,t}$ are the response matrices of the signal, calculated from the particle level and reconstruction level events
- μ_i corresponds to the signal strength of the bin T_i at particle level.

Likelihood minimization The next step in the fitting procedure is the minimization of the negative log-likelihood. This is performed using the MINUIT framework [118] which uses MIGRAD and MINOS minimization techniques. The minimization process adjusts the POIs and NPs to find the set of values that best fit the observed data. The fit yields the uncertainties on the estimated POIs, correlations among POIs and NPs.

The uncertainties on the POIs are determined by profiling the likelihood. In this approach, the likelihood is profiled over all NPs. The uncertainty on each POI is obtained by finding the parameter values that change the log-likelihood by 0.5 from the minimum value. This corresponds to a 1σ uncertainty on the POI.

10.3 Measuring normalized differential cross-section

The normalized differential cross-section is the ratio of the differential cross-section to the total cross-section, defined as $\frac{1}{\sigma_{\text{tot}}}\frac{d\sigma}{dX}$, where σ_{tot} is the total cross-section and X is the variable of interest.

The normalized differential cross-section can be measured by modifying the existing likelihood Eq. 10.1 as follows

- A new normalization factor μ_{tot} is introduced to measure the total cross-section.
- All normalization factors μ_i are replaced by $\mu_i = \mu_{\text{rel},i} \cdot \mu_{\text{tot}}$, where $\mu_{\text{rel},i}$ is the relative normalization factor for the bin i.
- One of the free parameters (μ_i) for one of the truth bin is replaced by the following formula taking into account total normalization (μ_{tot}). Generally, the last bin is chosen for this purpose.

$$\mu_{\text{rel},j} = (1 - \sum_{i,i\neq j}^{N_b} \mu_{\text{rel},i}\frac{N_i}{N})/\frac{N_j}{N} \tag{10.3}$$

where N_i is the number of events in bin i of the truth distribution. N is the total number of events, and N_b is the number of bins in the truth distribution.

After the profile likelihood fit, μ_{tot}, $\mu_{\text{rel},i}$ are obtained. The fitted number of events for other bins is calculated as $\mu_{\text{rel},i} \cdot \mu_{\text{tot}} \cdot N_i$, where for the bin j it is equal to total number of events minus the sum of the fitted number of events for other bins, as shown below,

$$\mu_{\text{rel},j} N_j = (1 - \sum \mu_{\text{rel},i} \frac{N_i}{N}) / \frac{1}{N} \tag{10.4}$$

$$\mu_{\text{rel},j} N_j = N - \sum \mu_{\text{rel},i} N_i \tag{10.5}$$

$$\mu_{\text{tot}} \mu_{\text{rel},j} N_j = \mu_{\text{tot}} N - \sum \mu_{\text{tot}} \mu_{\text{rel},i} N_i \tag{10.6}$$

10.4 Inputs for unfolding

As mentioned earlier, histogram templates are used to construct the likelihood function. For the signal template, the distribution at the reconstruction level is obtained by folding the particle-level template with the response matrix. The particle-level template represents the distribution in the fiducial phase space defined in Section 10.1. The particle-level distributions are depicted in Figure 10.2 for the single-lepton channel and in Figures 10.3 and A.8 for the dilepton channel. The bin content in bin i, denoted as T_i, serves as input for the likelihood function described in Eq. 10.2. The signal templates for different sources of systematic uncertainties are obtained using a varied response matrix.

The response matrix is a two-dimensional matrix that captures the detector response, translating the particle-level distribution to the reconstruction-level distribution. It accounts for the migration of events from one bin to another, selection efficiency, and detector acceptance. The response matrix is formulated using the migration matrix (M_{rt}), truth (N_t), and reconstructed (N_r) distributions as shown in Eq. 10.7. Its elements M_{rt} represent the probability of an event generated in bin t in the fiducial volume at particle level to be observed in bin r at the reconstruction level. The migration matrix is constructed from MC simulated events. There are four control regions in the single-lepton channel and two control regions in the dilepton channel. Therefore, four response matrices are constructed for the single lepton channel and two for the dilepton channel.

$$\text{Response, } P_{r,t} = \frac{M_{\text{r,t}} \times \epsilon_t}{f_r} = \frac{\frac{N_{r\cap t}}{\sum_r N_{r\cap t}} \times \frac{\sum_r N_{r\cap t}}{N_t}}{\frac{\sum_t N_{r\cap t}}{N_r}} = N_{r\cap t} \times \frac{N_r}{N_t \times \sum_t N_{r\cap t}}, \tag{10.7}$$

where, $M_{\mathrm{r,t}}$ is the normalized migration matrix (as shown in Figure 10.4 and Figure 10.7), ϵ_t is the efficiency of the truth events, and f_r is the acceptance of the reconstructed events.

For illustration, the normalized migration matrices for $p_{\mathrm{T}}(\gamma)$ in the $t\bar{t}\gamma$ production measurement are presented for the signal and control regions in Figure 10.4 and Figure 10.7, corresponding to the single-lepton and dilepton channels, respectively. The corresponding response matrices for $p_{\mathrm{T}}(\gamma)$ are shown in Figure 10.5 for the single-lepton channel and in Figure 10.8 for the dilepton channel. Additionally, the comparison of $p_{\mathrm{T}}(\gamma)$ in data and the MC expectation is shown for the signal and control regions in Figure 10.5 and Figure 10.8 for the single-lepton and dilepton channels, respectively. Approximately 5-7% of the events migrate to the neighboring bins. The efficiency of the events that are generated within the fiducial phase space and reconstructed and selected is about 31% for the single-lepton channel and 35% for the dilepton channel. The fraction of events that satisfy the selection criteria at reconstruction level but are not generated in the fiducial phase space is about 17% for the single-lepton channel and 19% for the dilepton channel.

The background templates are constructed using the MC simulated events by applying the signal and control region selection criteria and merging them into categories as described in Section 6.4. These background templates enter the likelihood function following Eq. 10.2. The background templates are also created for the different sources of systematic uncertainties discussed in Chapter 9.

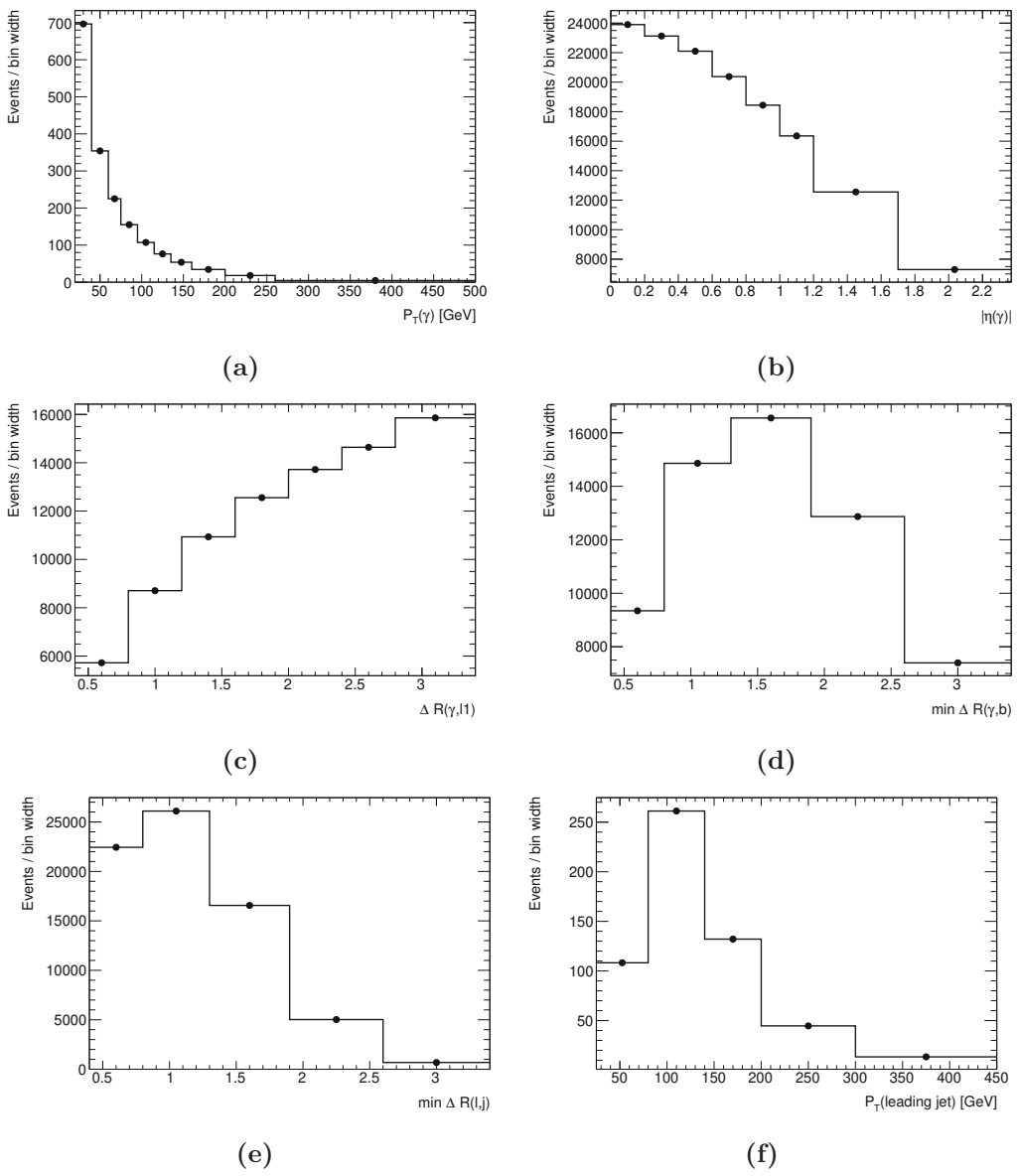

Figure 10.2: Particle level distributions of $t\bar{t}\gamma$ production as a function of (a) $p_{\mathrm{T}}(\gamma)$, (b) $|\eta|(\gamma)$, (c) $\Delta R(\gamma, \ell)$, (d) $\Delta R(\gamma, b)_{\mathrm{min}}$, (e) $\Delta R(\ell, j)_{\mathrm{min}}$, and (f) $p_{\mathrm{T}}(j_1)$ in the single-lepton channel. The number of events corresponds to the expected number of events at the particle level normalized to the luminosity of data. Overflow events are included in the last bin of the corresponding distribution. Note that values are divided by bin width.

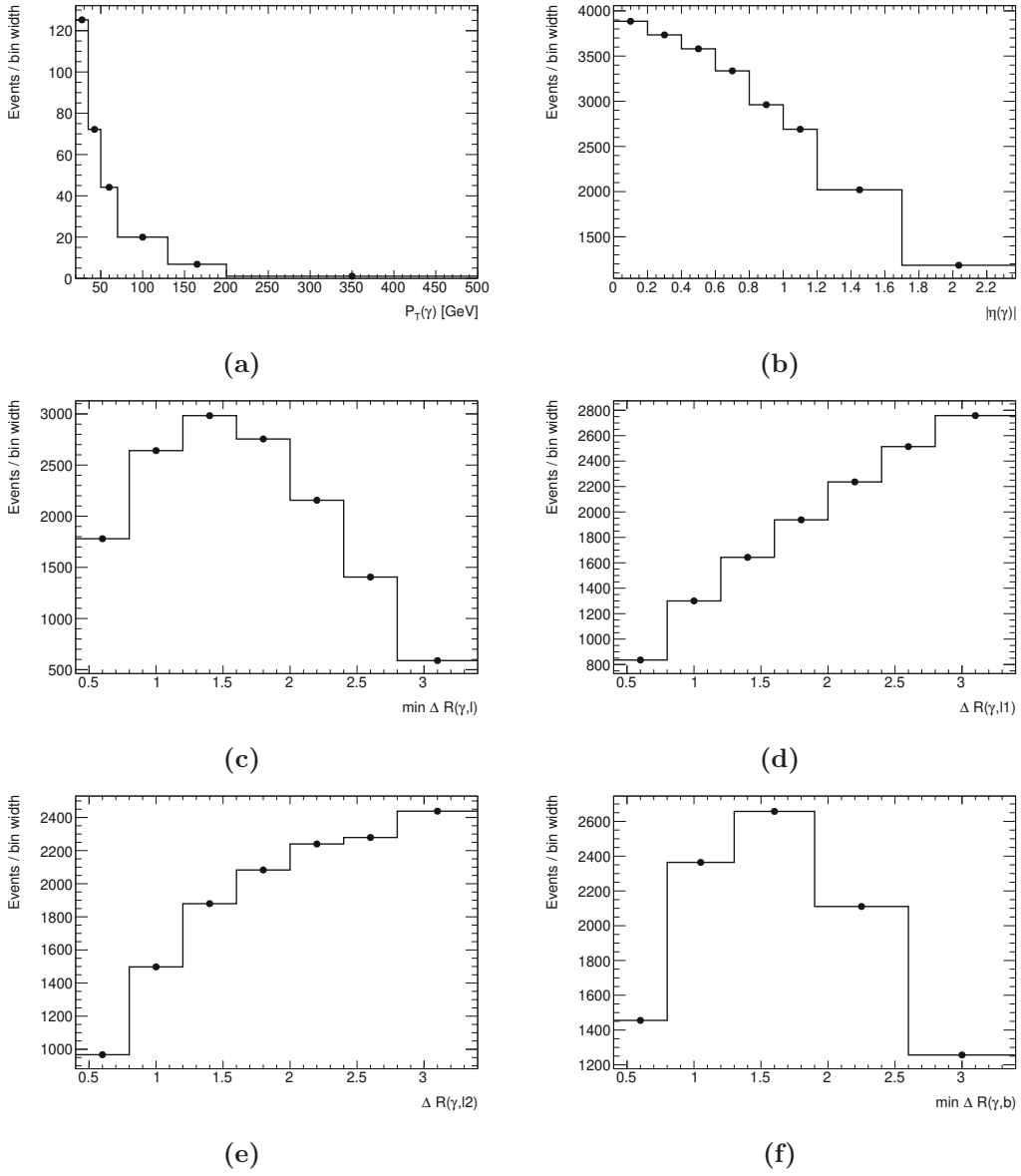

Figure 10.3: Particle level distributions of $t\bar{t}\gamma$ production as a function of (a) $p_{\mathrm{T}}(\gamma)$, (b) $|\eta|(\gamma)$, (c) $\Delta R(\gamma, \ell)_{\mathrm{min}}$, (d) $\Delta R(\gamma, \ell_1)$, (e) $\Delta R(\gamma, \ell_2)$, and (f) $\Delta R(\gamma, b)_{\mathrm{min}}$ in the dilepton channel. The number of events corresponds to the expected number of events at the particle level normalized to the luminosity of data. Overflow events are included in the last bin of the corresponding distribution. Note that values are divided by bin width.

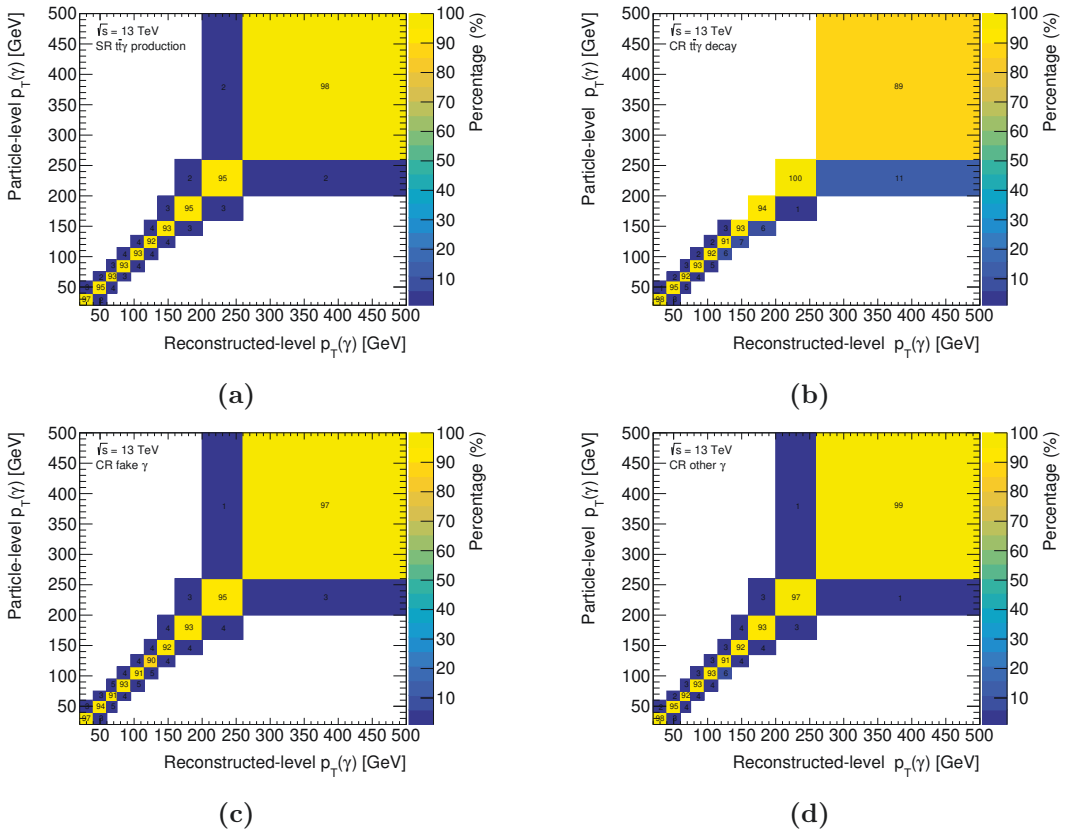

Figure 10.4: The normalized migration matrices, $M_{\mathrm{r,t}}$, representing the migration of events from particle level to four regions at the reconstruction level: (a) $t\bar{t}\gamma$ production enriched region, (b) $t\bar{t}\gamma$ decay enriched region (c) fakes enriched region, (d) prompt photon enriched region for the observable $p_{\mathrm{T}}(\gamma)$ in the single-lepton channel. The numbers correspond to the fraction of events in each bin normalized by column and shown in percentage. Around 5-7% of the events migrate to the neighboring bins. The last bin includes the overflow events.

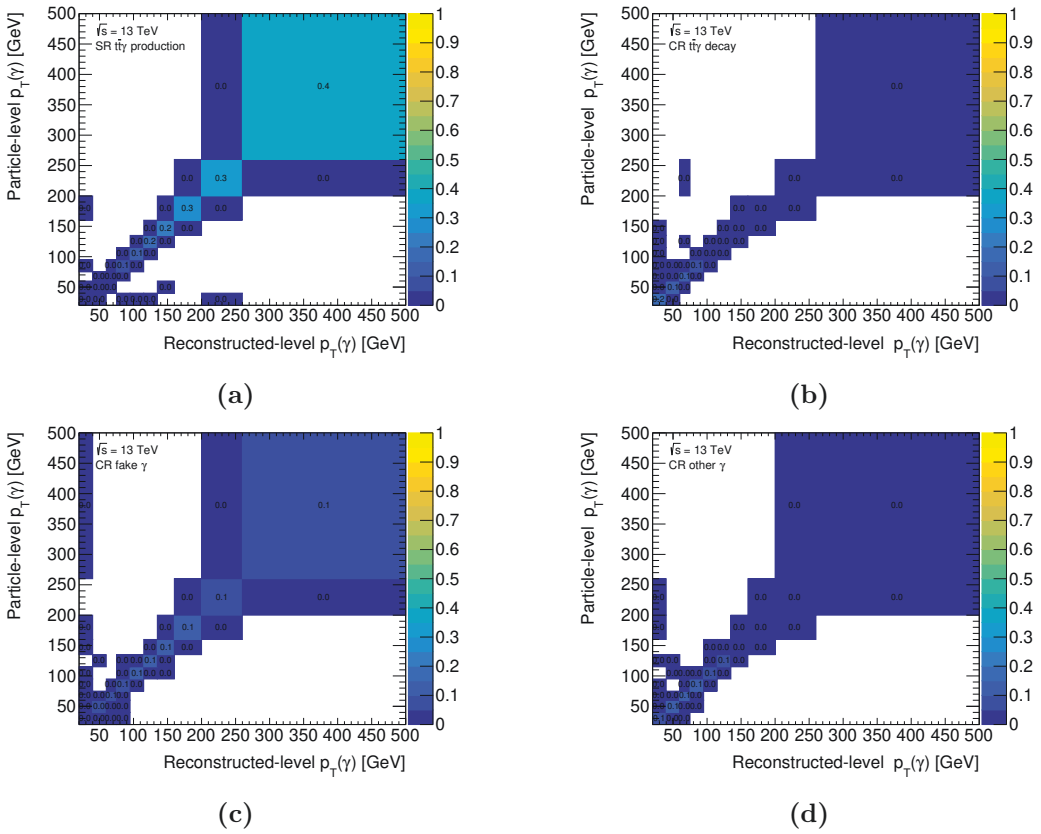

Figure 10.5: Response matrices for the observable $p_{\mathrm{T}}(\gamma)$ in the single-lepton channel, storing detector response from particle level to four regions at reconstruction level. (a-d) Response matrices for the $t\bar{t}\gamma$ production, $t\bar{t}\gamma$ decay, fakes, and prompt photon enriched regions, respectively. These matrices include the efficiency and acceptance, as well as the migration of events from particle level to reconstruction level. Numbers are rounded to one decimal place (with 0.0 indicating very small values). Bins with zero entries are not shown. The response matrices appear very diagonal, indicating minimal event migration, thus no regularization is applied in the unfolding procedure.

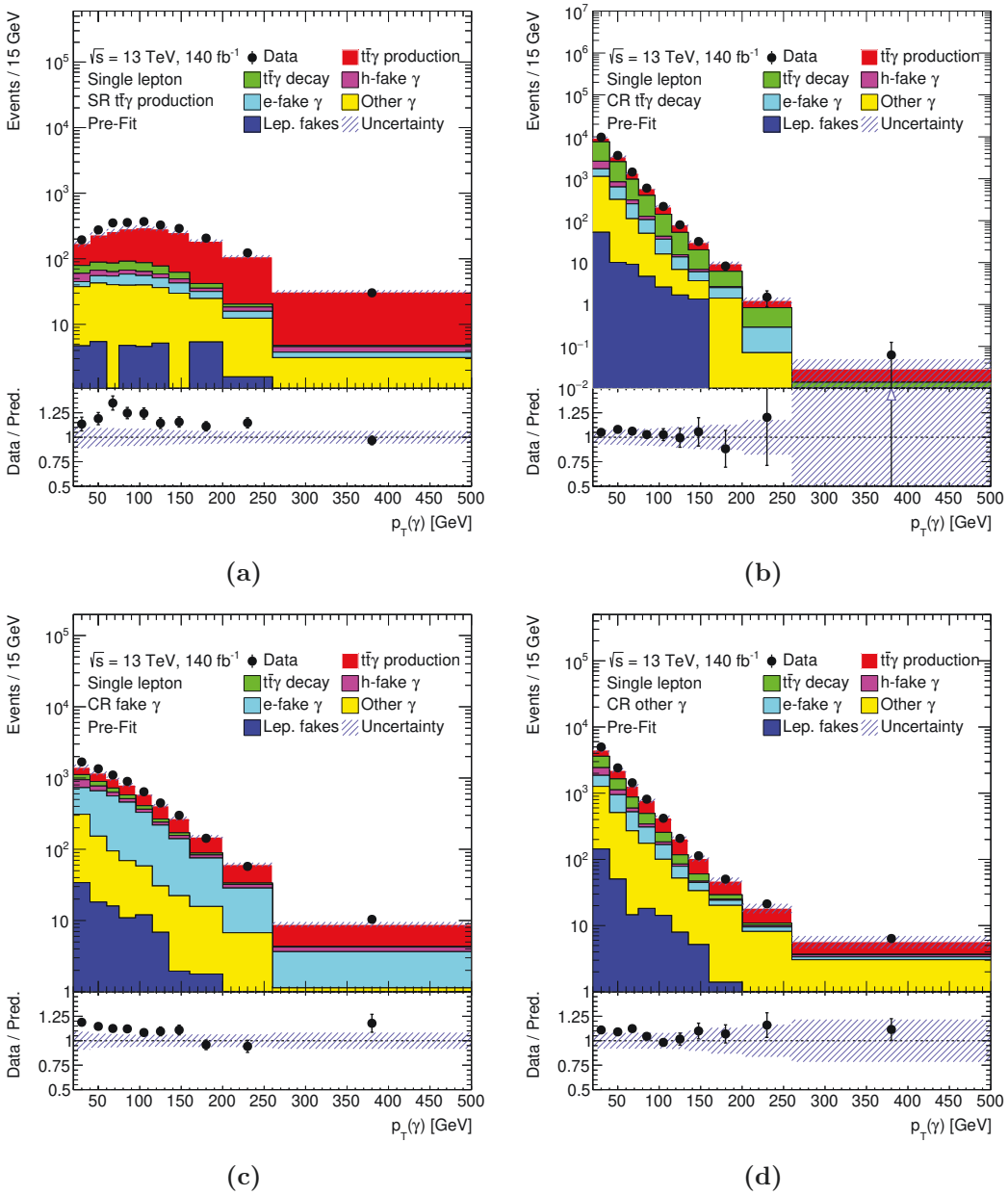

Figure 10.6: Distribution of $p_{\mathrm{T}}(\gamma)$ in the single-lepton channel for the four regions at the reconstruction level: (a) $t\bar{t}\gamma$ production SR, (b) $t\bar{t}\gamma$ decay CR, (c) fakes CR, and (d) prompt photon CR. The last bin includes the overflow events. The lower panel shows the ratio of the data to the predictions. The error bars represent the statistical uncertainty in the data. The shaded area represents the total uncertainty in the prediction.

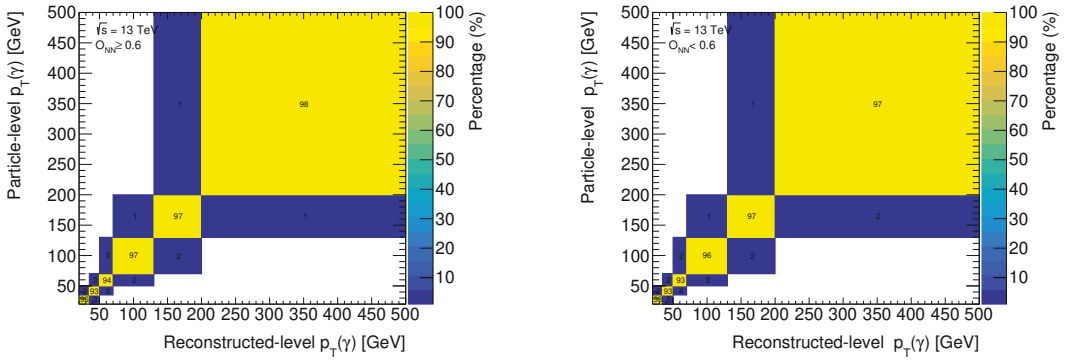

(a) **(b)**

Figure 10.7: The normalized migration matrices, $M_{\mathrm{r,t}}$ representing the migration of events from the particle level bin to the two regions at the reconstruction level: (a) $O_{\mathrm{NN}} \geq 0.6$ and (b) $O_{\mathrm{NN}} < 0.6$, for the observable $p_{\mathrm{T}}(\gamma)$ in the dilepton channel. The number corresponds to the fraction of events in each bin normalized by column and shown in percentage. Around 5% of the events migrate to the neighboring bins. The last bin includes the overflow events.

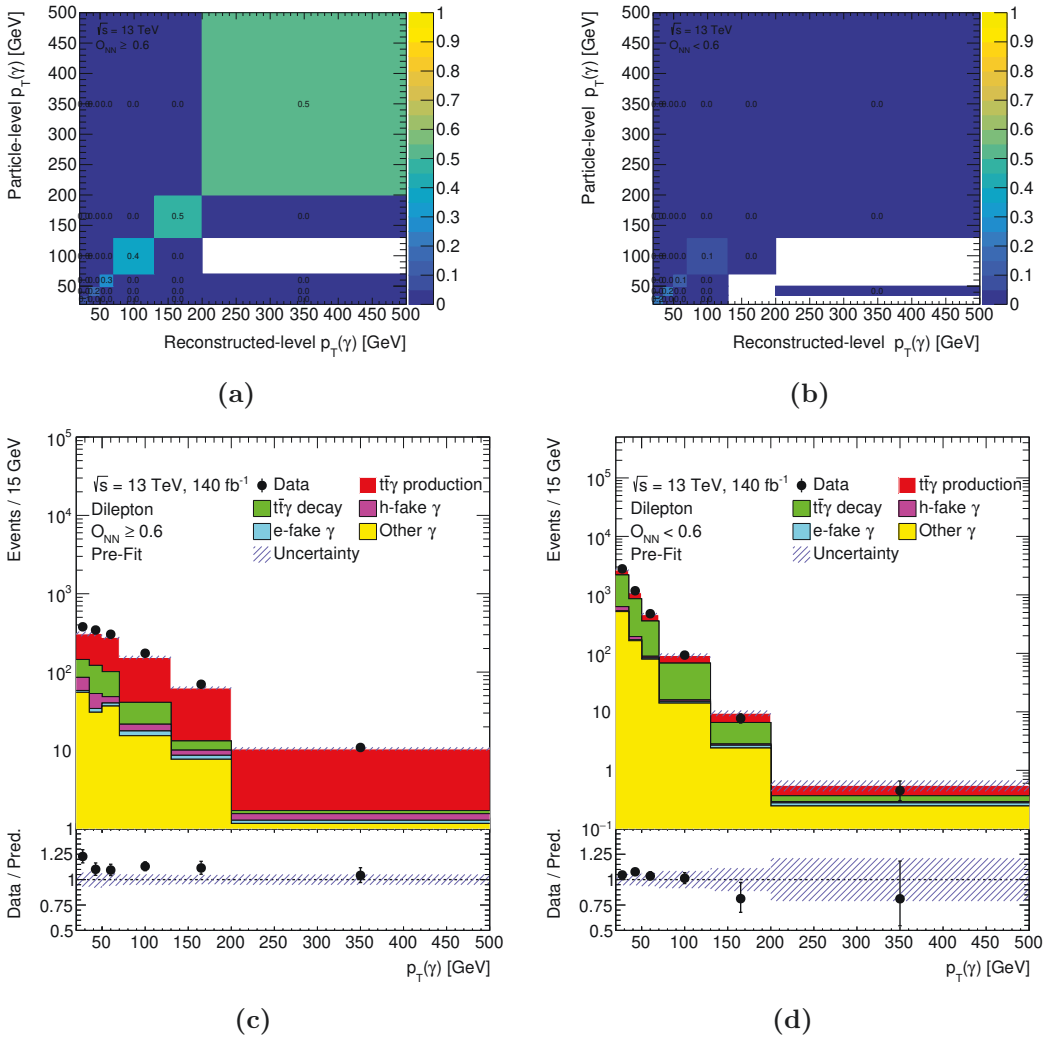

Figure 10.8: Response matrices for the observable $p_{\mathrm{T}}(\gamma)$ in the dilepton channel, representing the detector response from particle level to two regions at reconstruction level, (a) $O_{\mathrm{NN}} \geq 0.6$, (b) $O_{\mathrm{NN}} < 0.6$. These matrices include the efficiency and acceptance, as well as the migration of events from particle level to reconstruction level. Numbers are rounded to one decimal place (with 0.0 indicating very small values). Bins with zero entries are not shown. The response matrices appear very diagonal, indicating minimal event migration, thus no regularization is applied in the unfolding procedure. Subfigure (c) and (d) show the distribution of $p_{\mathrm{T}}(\gamma)$ in the dilepton channel for the two regions at the reconstruction level. The last bin includes the overflow events. The lower panel shows the ratio of the data to the predictions. The error bars represent the statistical uncertainty in the data. The shaded area represents the total uncertainty in the prediction.

10.5 Treatment of uncertainties in the fit

The signal and background templates are produced for different sources of systematic uncertainties and the difference between the nominal template and the systematic variation template is taken as a measure of the uncertainty. In the statistical model, different sources of uncertainties can be assumed as separate auxiliary measurements and can be incorporated in the likelihood function as nuisance parameters (NP). These NPs are constrained in the fit using Gaussian function where the σ is the difference between the nominal template and the systematic variation template. For every source of uncertainty, one NP is added to the fit model. Uncertainties arising from different sources are treated as independent and uncorrelated. This means that one source of uncertainty does not affect the impact of another source. The same sources of uncertainties are treated correlated across different signal and control regions. Systematic uncertainties are constrained using Gaussian constraints whereas statistical uncertainties are modeled using Poisson constraints. The uncertainties associated with the nuisance parameters are estimated from the fit using the likelihood profiling method. The uncertainties on the NP are propagated to the final result.

The treatment of the MC templates corresponding to systematic uncertainties is discussed in the following.

Smoothing The smoothing technique is used for some uncertainties to reduce the impact of statistical fluctuations in the template [119].

Symmetrization Some uncertainties have variations that result in an increase or decrease in the number of events, while others have only one available variation. For asymmetric positive and negative variations, the variation is symmetrized to allow for simpler implementation in the fit model. Uncertainties with both positive and negative variations are symmetrized in the following way:

$$\sigma_{\text{positive/negative}} = N_{\text{nominal}} \pm (N_{\text{positive variation}} - N_{\text{negative variation}})/2$$

In cases where only one variation is available, the other variation is obtained by mirroring the available one around the nominal.

Pruning Uncertainties with negligible impact are pruned from the fit model to avoid using too many nuisance parameters in the fit model to improve the stability. Very

small uncertainties are problematic as they lead to almost flat likelihood in some regions. The pruning decision is made for shape and normalization components separately. For instance, the uncertainty can have a negligible impact on the normalization but a significant impact on the shape of the variable concerned. In such cases, the component of the uncertainty affecting the shape of the distribution is kept and the component affecting the normalization is pruned. It applies to the other way around as well. For pruning based on the normalization, the integral of the template is considered and the relative difference between the nominal is calculated. If the relative difference is less than 0.1%, the uncertainty is pruned. For pruning based on the shape, the relative difference with respect to the nominal is calculated for every bin, if for any bin the difference is more than 0.1% the uncertainty is kept.

10.6 Choice of binning

The binning of the observable plays an important role in the measurement because it is not possible to measure the cross-section as a continuous function of the observable due to the finite resolution of the detector. Therefore, the bin width is chosen such that it is larger than twice the resolution of the observable. Moreover, fewer statistics in a bin can lead to large statistical uncertainty, causing the measurement to fluctuate between neighboring bins and making the result unstable and unreliable. To mitigate this, the bin width is chosen in such a way that the measured distribution has less than 10% statistical uncertainty in every bin, except for the bin in the tails. Additionally, the choice of binning should take into account the observable range of the measured quantity.

The procedure starts with a finer binned histogram at reconstruction level and starts to merge the bin from left to right till the statistical uncertainty reaches below 5-7%. This uncertainty is at the reconstruction level, while the interest is in the uncertainty in the final unfolded distribution. The algorithm is run only considering the signal region at the reconstruction level due to the complexity of the profile likelihood unfolding across multiple reconstruction regions. After determining the binning edges through the algorithm, the fit and unfolding are performed and the statistical uncertainty is checked at the unfolded distribution.

The resolution of the variables $p_{\mathrm{T}}(\gamma)$, $|\eta(\gamma)|$, $\Delta R(\gamma, \ell)$, $\Delta R(\gamma, b)_{\mathrm{min}}$, $\Delta R(\ell, j)_{\mathrm{min}}$, $\Delta\eta(\ell, \ell)$, $\Delta\phi(\ell, \ell)$, $p_{\mathrm{T}}(j_1)$, $p_{\mathrm{T}}(\ell, \ell)$ are found to be about 1-2 GeV, 0.1-0.15, 0.005-0.008, 0.014-0.020, 0.01, 0.0006, 0.0003, 10 GeV, 2-3 GeV, respectively. The optimized bin widths based on the statistical uncertainty satisfies in all cases the resolution criterion. The bin boundaries

were slightly adjusted from those obtained in the optimization procedure to have rounded bin boundaries.

This study is performed for the $t\bar{t}\gamma$ production and total $t\bar{t}\gamma$ measurements in the dilepton channel. The results are compared among the two sets and with the binning used in $t\bar{t}\gamma$ measurement performed by the CMS experiment [120]. The optimized bin boundaries are similar for several observables to those in Ref. [120] (an example shown in Figure 10.9). Testing the unfolding setup using the CMS binning revealed that the unfolded distributions met the set criteria, yielding in general similar uncertainties and migrations. Consequently, the binning of the CMS experiment was adopted, allowing a more conducive comparison in the future. For illustration, the resolution and comparison of two setups for some example variables can be found in Appendix A.1. The same binning was applied to the single-lepton channel.

The measurement of the differential crosse-sections as a function of $p_{\mathrm{T}}(\gamma)$ is performed by combining the single-lepton and dilepton fiducial phase spaces as detailed in Section 11.2. The measured cross-section is used as input for setting limits on Wilson coefficients in the context of EFT [24]. The binning for this variable was revised to improve the sensitivity of the EFT measurement, increasing the number of bins while keeping the total expected uncertainty in the tail of the distribution around 10% which is most sensitive to the EFT parameters.

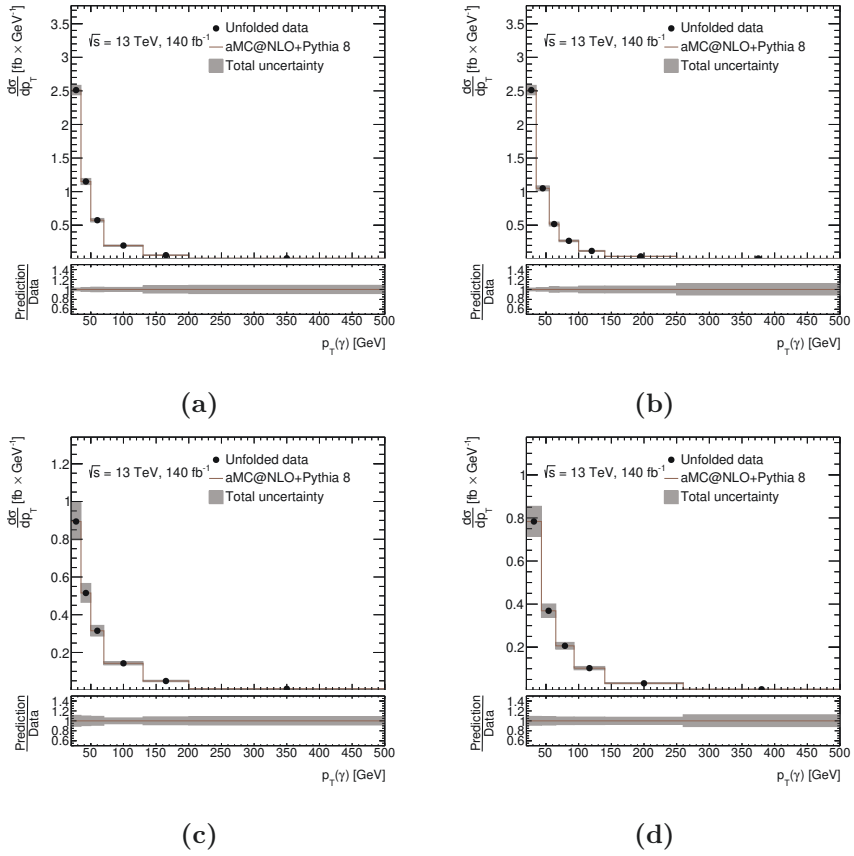

Figure 10.9: The comparison of results obtained using the CMS binning and the binning optimization procedure discussed in Section 10.6 for the $p_{\mathrm{T}}(\gamma)$ variable. The plots show unfolded distribution measured using *Asimov* data, with error bars representing the statistical uncertainty. Figures (a) and (b) show the comparison of the binning used by CMS and the binning obtained from the optimization procedure for the total $t\bar{t}\gamma$ production measurement, respectively. Figures (c) and (d) show the comparison of the binning used by CMS and the binning obtained from the optimization procedure for the $t\bar{t}\gamma$ production measurement, respectively.

10.7 Unfolding tests

This section presents various tests that have been performed before the fit is performed to the real dataset to test the robustness of the method and avoid introducing any biases in the final results. Mainly two tests are performed, referred to as closure test and stress test discussed in Section 10.7.1 and Section 10.7.2, respectively. These tests are performed on pseudo-data, which consists of the MC predicted events in the signal and control regions. The distribution of an observable in pseudo-data is constructed by summing up the MC predicted signal and background templates (at the reconstruction level) and including the data-driven estimates as well. These tests have been performed both for $t\bar{t}\gamma$ production and total $t\bar{t}\gamma$ measurements.

10.7.1 Closure Test

In the so-called closure test, the statistical model constructed in Section 10.2 is fitted to the pseudo-data. As a result, the unfolded distribution is obtained at particle level. If the unfolding procedure works as intended the distribution at particle level should match with the truth distribution from the MC simulated events. Thus, closure test validates the technical implementation of the unfolding procedure.

The results of the closure test for $t\bar{t}\gamma$ production measurement are shown in Figures 10.10 and 10.11 for single-lepton and dilepton channels respectively. For all the observables the unfolded distribution closely matches the particle-level distribution, resulting in a good closure.

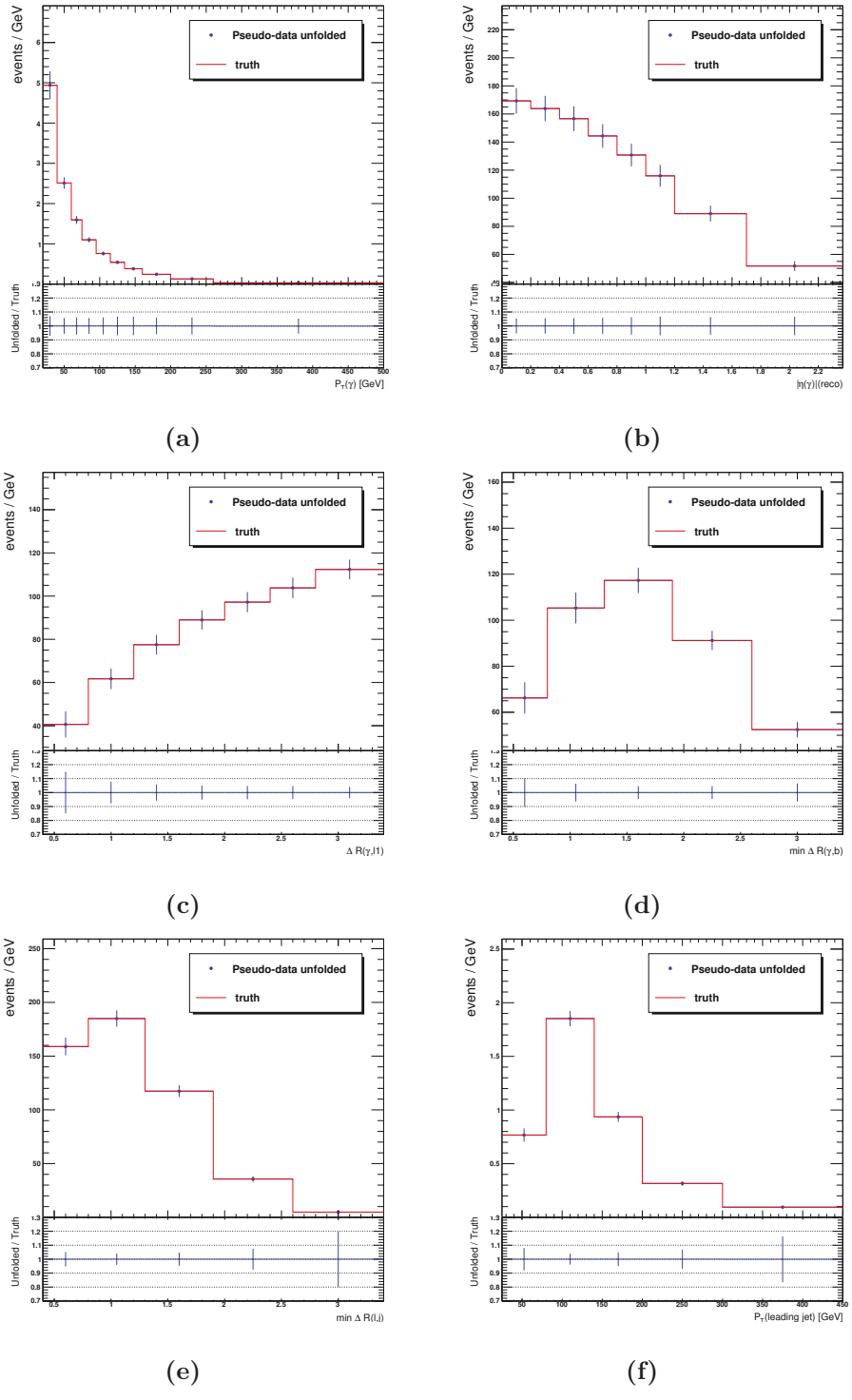

(a) **(b)** **(c)** **(d)** **(e)** **(f)**

Figure 10.10: Comparison of the unfolded pseudo-data (in blue) and the true distribution (in red) as a function $p_{\mathrm{T}}(\gamma)$ (a), $|\eta(\gamma)|$ (b), $\Delta R(\gamma, \ell)$ (c), $\Delta R(\gamma, b)_{\mathrm{min}}$ (d), $\Delta R(\ell, j)_{\mathrm{min}}$ (e) and $p_{\mathrm{T}}(j_1)$ (f) in the single-lepton channel for $t\bar{t}\gamma$ production measurement. The uncertainty bars displayed in the plots represent only the statistical error considered in the unfolding.

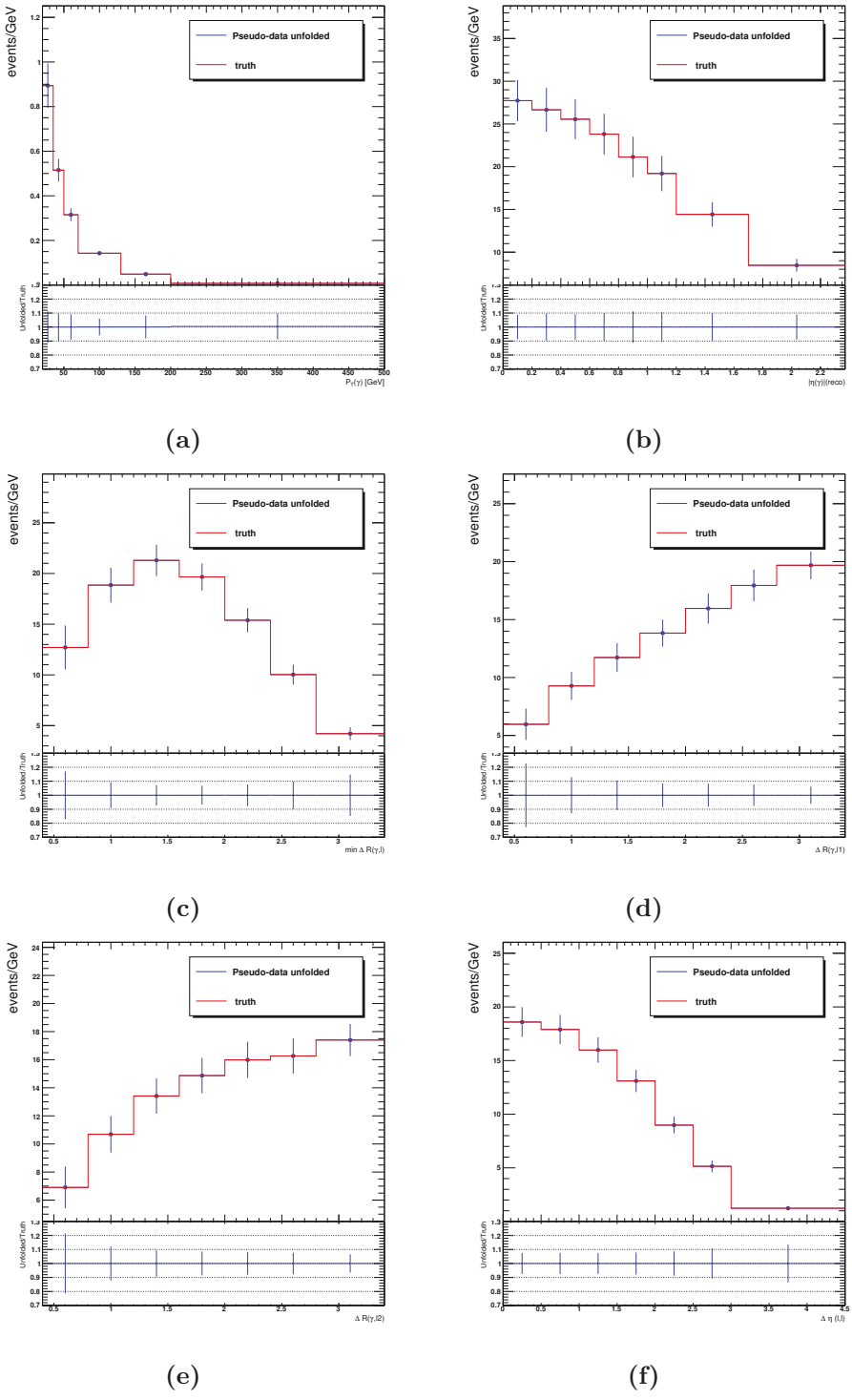

Figure 10.11: Comparison of the unfolded pseudo-data (in blue) and the true distribution (in red) as a function of $p_{\mathrm{T}}(\gamma)$ (a), $|\eta(\gamma)|$ (b), $\Delta R(\gamma,\ell)_{\mathrm{min}}$ (c), $\Delta R(\gamma,\ell_1)$ (d), $\Delta R(\gamma,\ell_2)$ (e), and $\Delta\eta(\ell,\ell)$ (f) in the dilepton channel for $t\bar{t}\gamma$ production measurement. The uncertainty bars displayed in the plots represent only the statistical error considered in the unfolding. The comparison for other observables is shown in Appendix A.2.

10.7.2 Stress Test

Recalling the profile likelihood unfolding method, the likelihood is constructed using the signal and background templates, where the signal is modeled using the truth distribution and the response matrix, and a normalization factor is assigned for each bin of the truth distribution. The detector effects are corrected using the response matrix which is derived from the MC simulated events. A question that might arise is whether the unfolding procedure is biased toward the shape of the particular MC simulations used. The stress test is performed in order to verify that the unfolding procedure is not biased by the shape of the inputs used.

In this test, both the normalization and shape of the signal template constructed using the pseudo-data are re-weighted. The unfolding procedure is then applied to the pseudo-data, and the resulting unfolded distribution is compared to the true distribution. If the unfolding procedure is unbiased with respect to the particular shape of the MC distribution, the differential cross-section should accurately describe the re-weighted signal. The signal is re-weighted to vary its shape linearly and non-linearly at truth level as described below.

Linear re-weighting A weight corresponding to a linear skewness of the shape is used. It is defined as follows for various distributions:

For the p_{T} distributions ($p_{\mathrm{T}}(\gamma)$, $p_{\mathrm{T}}(j_1)$, and $p_{\mathrm{T}}(\ell,\ell)$):

$$\text{weight} = 1 + \mathrm{Y} \times \frac{100 - i}{300} = 1 + \mathrm{Y} \times \mathrm{X}.$$

For the photon η:

$$\text{weight} = 1 + \mathrm{Y} \times \frac{1.2 - i}{2.37} = 1 + \mathrm{Y} \times \mathrm{X}.$$

For $\Delta R(\gamma,\ell)_{\mathrm{min}}$, $\Delta R(\gamma,\ell_1)$, $\Delta R(\gamma,\ell_2)$, $\Delta R(\gamma,b)_{\mathrm{min}}$, and $\Delta R(\ell,j)$:

$$\text{weight} = 1 + \mathrm{Y} \times \frac{1.8 - i}{6} = 1 + \mathrm{Y} \times \mathrm{X}.$$

For $\Delta\eta(\ell,\ell)$:

$$\text{weight} = 1 + \mathrm{Y} \times \frac{1.2 - i}{2.5} = 1 + \mathrm{Y} \times \mathrm{X}.$$

For $\Delta\phi(\ell,\ell)$:

$$\text{weight} = 1 + \text{Y} \times \frac{1.75 - i}{3.14} = 1 + \text{Y} \times \text{X}.$$

The multiplicative factor Y is -1 or 1, and i is the bin center.

Non-linear re-weighting The non-linear re-weighting function for different observables is constructed by taking the difference between data and MC at the reconstruction level:

$$\text{weight}_i = 1 + \text{Y} \times \frac{N^i_{\text{data}} - N^i_{\text{MC}}}{N^i_{\text{data}}} = 1 + Y \times \text{Obs}, \tag{10.8}$$

where i is the bin index and Y = 1, -1. The signal in the pseudo-data is re-weighted bin-by-bin using Eq. 10.8.

After unfolding the re-weighted pseudo-data, particle level distribution is obtained, referred to as *unfolded re-weighted* distribution. For comparison with the result, a new distribution is created by re-weighting the nominal particle level distribution by the same value for every bin, referred to as *re-weighted particle level* distribution. The *unfolded re-weighted* distribution is compared with *re-weighted particle level* distribution, and the results of linear and non-linear stress tests are shown in Figure 10.12 for the single-lepton channel and in Figures 10.13 and A.7 for the dilepton channel. The error bars show the statistical uncertainty after the unfolding. The *unfolded re-weighted* distribution closely matches the *re-weighted particle level* distribution for all observables, validating that the unfolding is able to retrieve the re-weighted signal from the pseudo-data.

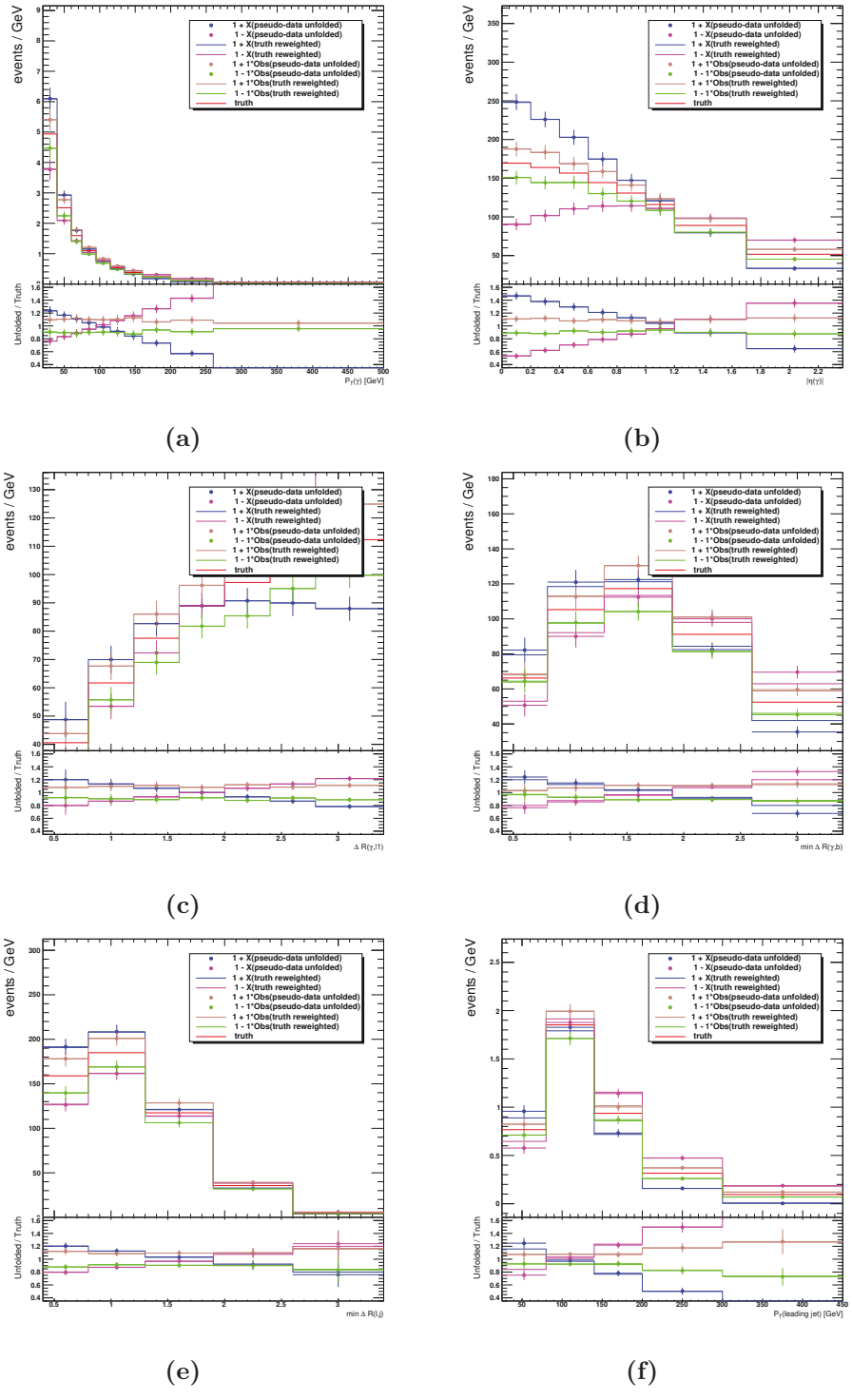

Figure 10.12: Comparison of the re-weighted unfolded pseudo-data and the re-weighted particle level distribution as a function of (a) $p_{\mathrm{T}}(\gamma)$, (b) $|\eta(\gamma)|$, (c) $\Delta R(\gamma, \ell)$, (d) $\Delta R(\gamma, b)_{\mathrm{min}}$, (e) $\Delta R(\ell, j)_{\mathrm{min}}$ and (f) $p_{\mathrm{T}}(j_1)$ in the single-lepton channel for $t\bar{t}\gamma$ production measurement. The dots are the ratio of the unfolded reweighted distributions to the nominal particle level distribution, while the solid lines are the ratio of the reweighted particle level distributions to the nominal one. X is defined in the previous section. The uncertainty bars displayed in the plots represent only the statistical error considered in the unfolding.

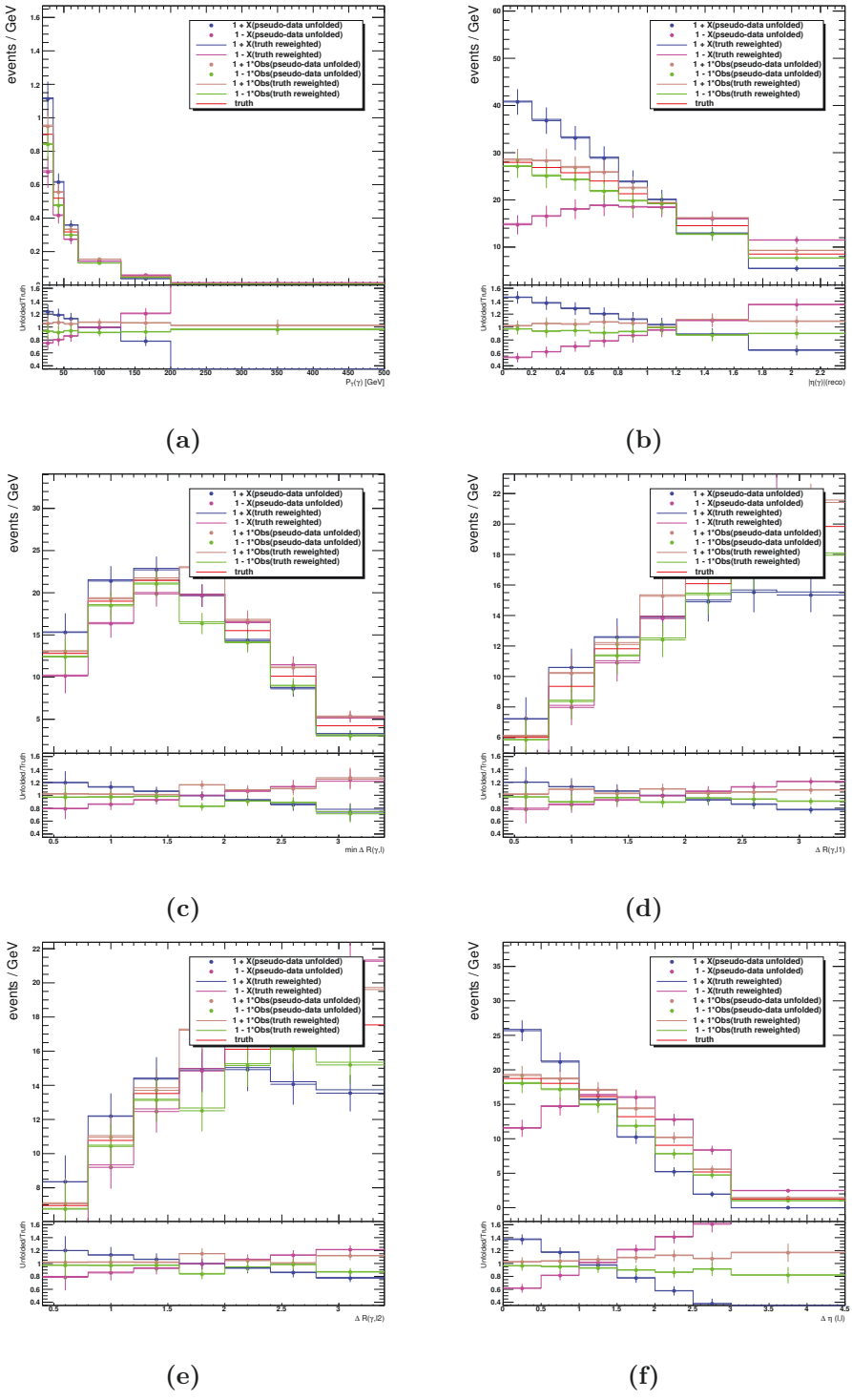

Figure 10.13: Comparison of the re-weighted unfolded pseudo-data and the re-weighted particle level distribution as a function of (a) $p_{\mathrm{T}}(\gamma)$, (b) $|\eta(\gamma)|$, (c) $\Delta R(\gamma,\ell)_{\mathrm{min}}$, (d) $\Delta R(\gamma,\ell_1)$, (e) $\Delta R(\gamma,\ell_2)$ and (f) $\Delta\eta(\ell,\ell)$ in the dilepton channel for $t\bar{t}\gamma$ production measurement. The dots are the ratio of the unfolded reweighted distributions to the nominal particle level distribution, while the solid lines are the ratio of the reweighted particle level distributions to the nominal one. X is defined in the previous section. The uncertainty bars displayed in the plots represent only the statistical error considered in the unfolding. The comparison for other observables is shown in Figure A.7.

11 Results and Interpretations

This chapter presents the results of the measurements. The measurement of the $t\bar{t}\gamma$ production differential cross-sections is detailed in Section 11.1. The combined single lepton and dilepton channel measurements of the $t\bar{t}\gamma$ production differential cross-sections are presented in Section 11.2. The total $t\bar{t}\gamma$ production and decay differential cross-sections are covered in Section 11.3. The results are compared with theoretical predictions and previous measurements in Section 11.4. For completeness, although not the work of the author, the interpretations of the results in the context of effective field theory (EFT), part of the publication [24], are discussed briefly in Section 11.5. Some of the definitions are discussed in Section 11.1 of this chapter and are not repeated in the subsequent sections.

11.1 $t\bar{t}\gamma$ production measurement

This section presents the results of the $t\bar{t}\gamma$ production cross-section measurement. Profile likelihood unfolding method is applied to measure the cross-sections from the data. The $t\bar{t}\gamma$ decay sample is simulated at LO, and a k-factor is used to scale the cross-section to NLO value. The uncertainty on the k-factor is not considered in this measurement instead the $t\bar{t}\gamma$ decay template is kept free floating in the likelihood.

Post-fit distributions For illustration, the fitted values of the signal and background normalization factors for the photon p_{T} and $|\eta|$ measurements in the single-lepton channel are displayed in Figure 11.1. In the single-lepton channel, the normalization of the $t\bar{t}\gamma$ decay varies between 0.94 and 0.96 across measurements of different observables, with a maximum uncertainty of approximately 10%. This uncertainty is consistent across the measurements of different observables. In the dilepton channel the fitted value of $t\bar{t}\gamma$ decay normalization varies between 0.92 and 1.08, but considering the uncertainty on the value they are consistent across different measurements. The post-fit distributions at the reconstruction level are shown for $|\eta(\gamma)|$ in Figure 11.2 for the single-lepton channel and for $\Delta R(\gamma, \ell)_{\mathrm{min}}$ in Figure 11.3 for the dilepton channel. A good agreement is observed

between the data and the post-fit predictions in all the regions and both channels. The post-fit distributions are consistent with the data within the post-fit uncertainties.

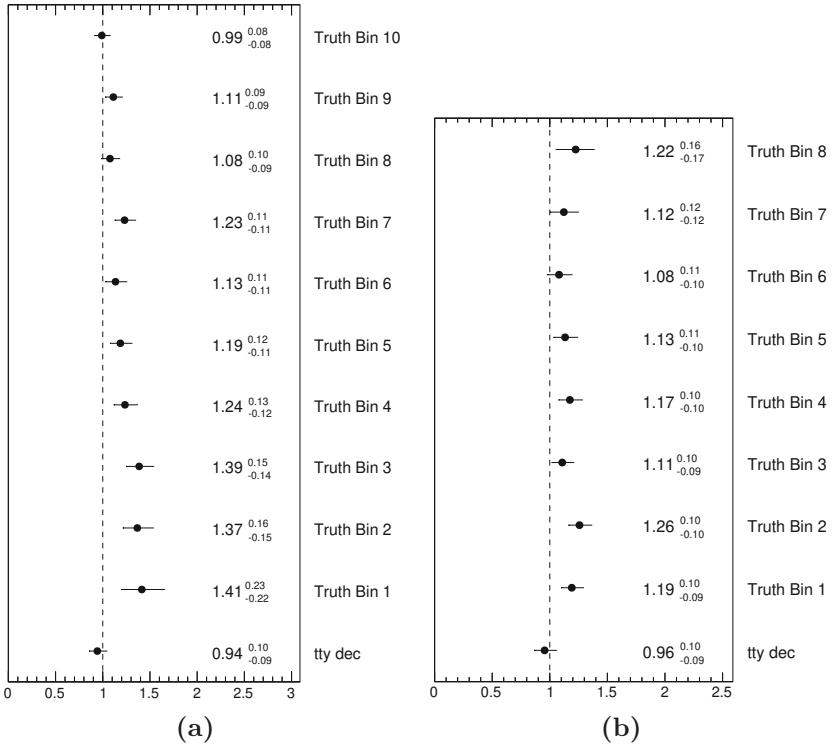

Figure 11.1: Signal strength values obtained from the fit for $t\bar{t}\gamma$ production measurement in single-lepton channel for the following observables: (a) $p_{\mathrm{T}}(\gamma)$, (b) $|\eta(\gamma|)$. The bin labeled $t\bar{t}\gamma$ dec represents the signal strength of the $t\bar{t}\gamma$ decay template, while the remaining bins are signal bins. The error bars represent the post-fit uncertainties in the signal strength which include both statistical and systematic uncertainties.

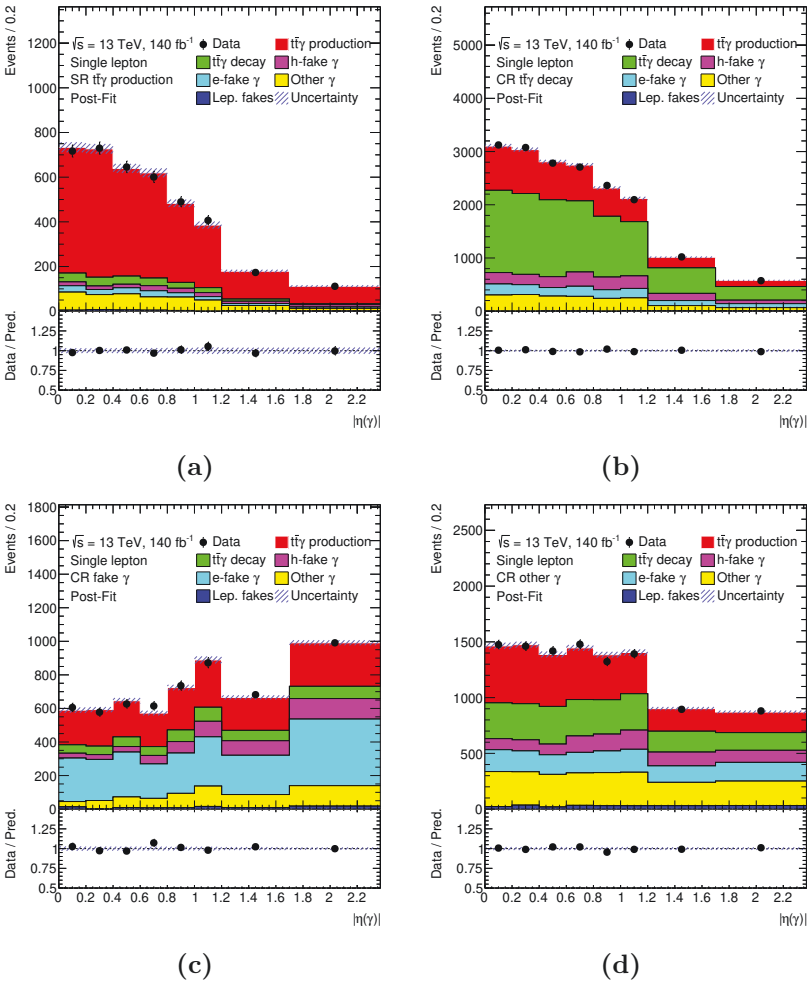

Figure 11.2: Post-fit distributions of $|\eta(\gamma)|$ in the SR and CR for $t\bar{t}\gamma$ production measurement: (a) $t\bar{t}\gamma$ production enriched region, (b) $t\bar{t}\gamma$ decay enriched region, (c) fakes enriched region, and (d) prompt photon enriched region in single-lepton channel. The lower panels show the ratio of the data to the prediction. The error bars on the data points represent the statistical uncertainties, while the shaded bands represent the statistical and systematic uncertainties of the post-fit prediction. The last bin includes overflow events.

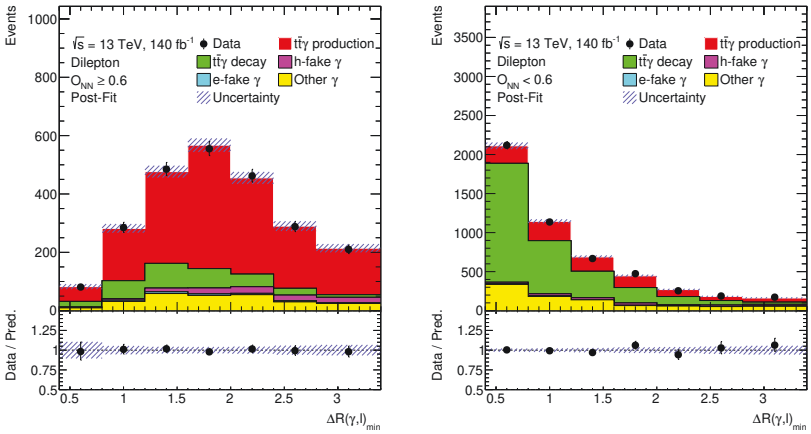

(a) **(b)**

Figure 11.3: Post-fit distributions of $\Delta R(\gamma, \ell)_{\text{min}}$ in the regions (a) $O_{NN} \geq 0.6$, (b) $O_{NN} < 0.6$ in dilepton channel. The lower panels show the ratio of the data to the prediction. The error bars on the data points represent the statistical uncertainties, while the shaded bands represent the statistical and systematic uncertainties of the post-fit prediction. The last bin includes overflow events.

As mentioned earlier the systematic uncertainties are taken into account as the nuisance parameters in the likelihood function and they are constrained using Gaussian functions (Poisson for statistical uncertainty). To study the post-fit uncertainties the *pulls* and *constraints* are investigated. The pull of a nuisance parameter is defined as the difference between the pre-fit (θ) and the post-fit ($\hat{\theta}$) values of the parameter, normalized to the pre-fit uncertainty ($\Delta\theta$), $\frac{\hat{\theta}-\theta}{\Delta\theta}$. The constraint is defined as the ratio between the post-fit and the pre-fit uncertainty of the NP. Through pulls and constraints, any possible issue in the fit can be identified. If a NP shows a large pull, that may be a hint that our estimate of the pre-fit value was not reasonable. A constrained NP indicates that the data contains enough information to improve the precision of the NP with respect to the pre-fit estimate.

The pull plot for the $t\bar{t}\gamma$ production measurement in the single-lepton channel is shown in Figure 11.3. The plot shows the pulls and constraints of the uncertainties for $p_{\text{T}}(\gamma)$ observable. Each data point represents a particular nuisance parameter. The green band shows one standard deviation range around 0, whereas the yellow band shows two standard deviation range. The pull is noticed when the black dot deviates from the center and the constraint can be noticed by looking at the uncertainty on the black dot and comparing it with the size of the green band since the pre-fit uncertainty was taken as one standard deviation (σ).

For several nuisance parameters, small pulls are observed, but all are within 1 σ. In a few cases, the pulls exceed 0.5 σ, such as for $W\gamma$ normalization, $t\bar{t}\gamma$ production ISR variation, $t\bar{t}\gamma$ production factorization scale variation, $t\bar{t}\gamma$ production parton shower uncertainty, hadron fake uncertainty, and uncalibrated light jet uncertainty. The uncertainty assigned to the uncalibrated light jets, $t\bar{t}\gamma$ production parton shower uncertainty, and $t\bar{t}\gamma$ decay parton shower uncertainty are slightly constraint. The pulls and constraints are compared across different observables and found to be consistent with each other.

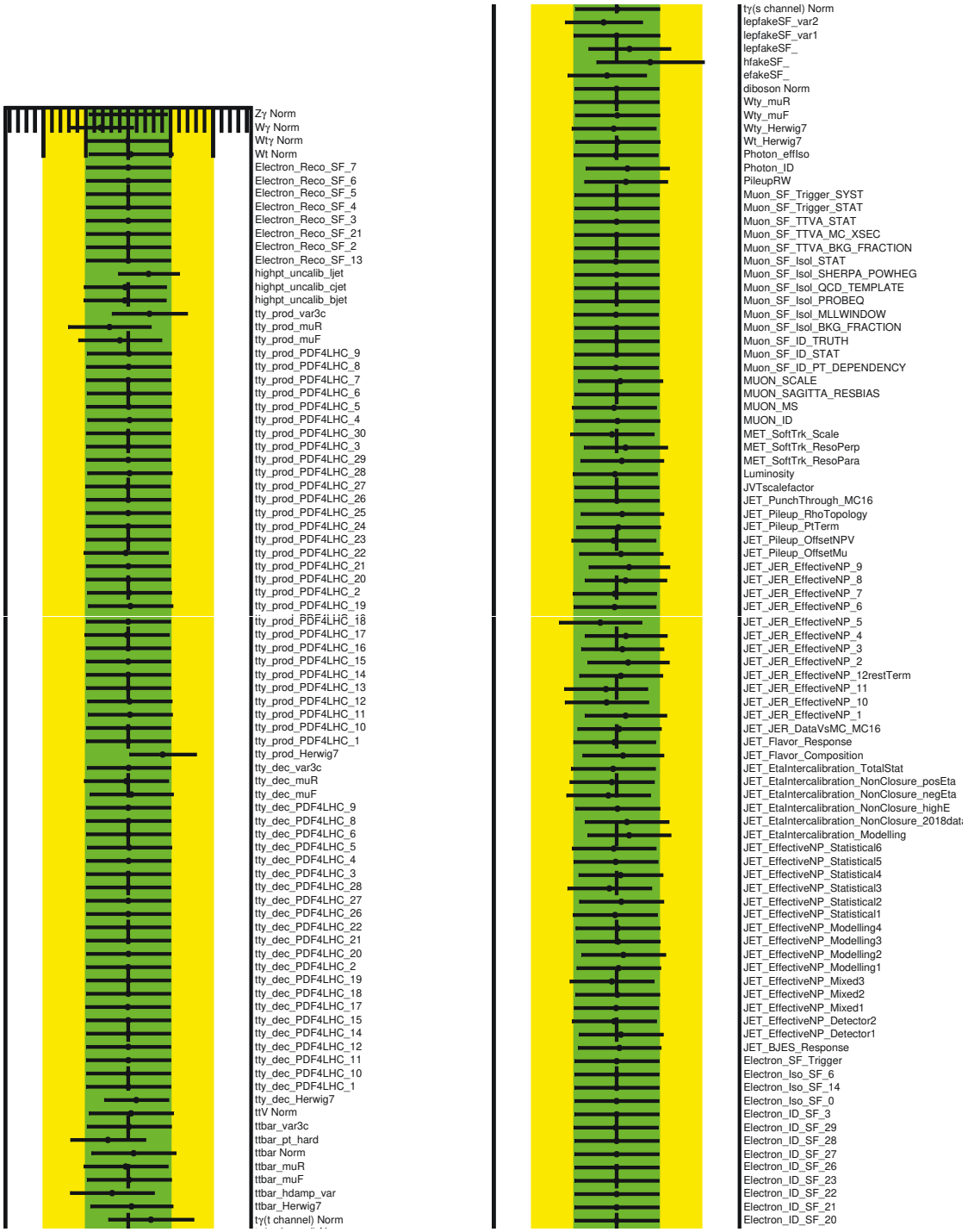
Zγ Norm
Wγ Norm
Wtγ Norm
Wt Norm
Electron_Reco_SF_7
Electron_Reco_SF_6
Electron_Reco_SF_5
Electron_Reco_SF_4
Electron_Reco_SF_3
Electron_Reco_SF_21
Electron_Reco_SF_2
Electron_Reco_SF_13
highpt_uncalib_ljet
highpt_uncalib_cjet
highpt_uncalib_bjet
tty_prod_var3c
tty_prod_muR
tty_prod_muF
tty_prod_PDF4LHC_9
tty_prod_PDF4LHC_8
tty_prod_PDF4LHC_7
tty_prod_PDF4LHC_6
tty_prod_PDF4LHC_5
tty_prod_PDF4LHC_4
tty_prod_PDF4LHC_30
tty_prod_PDF4LHC_3
tty_prod_PDF4LHC_29
tty_prod_PDF4LHC_28
tty_prod_PDF4LHC_27
tty_prod_PDF4LHC_26
tty_prod_PDF4LHC_25
tty_prod_PDF4LHC_24
tty_prod_PDF4LHC_23
tty_prod_PDF4LHC_22
tty_prod_PDF4LHC_21
tty_prod_PDF4LHC_20
tty_prod_PDF4LHC_2
tty_prod_PDF4LHC_19
tty_prod_PDF4LHC_18
tty_prod_PDF4LHC_17
tty_prod_PDF4LHC_16
tty_prod_PDF4LHC_15
tty_prod_PDF4LHC_14
tty_prod_PDF4LHC_13
tty_prod_PDF4LHC_12
tty_prod_PDF4LHC_11
tty_prod_PDF4LHC_10
tty_prod_PDF4LHC_1
tty_prod_Herwig7
tty_dec_var3c
tty_dec_muR
tty_dec_muF
tty_dec_PDF4LHC_9
tty_dec_PDF4LHC_8
tty_dec_PDF4LHC_6
tty_dec_PDF4LHC_5
tty_dec_PDF4LHC_4
tty_dec_PDF4LHC_3
tty_dec_PDF4LHC_28
tty_dec_PDF4LHC_27
tty_dec_PDF4LHC_26
tty_dec_PDF4LHC_22
tty_dec_PDF4LHC_21
tty_dec_PDF4LHC_20
tty_dec_PDF4LHC_2
tty_dec_PDF4LHC_19
tty_dec_PDF4LHC_18
tty_dec_PDF4LHC_17
tty_dec_PDF4LHC_15
tty_dec_PDF4LHC_14
tty_dec_PDF4LHC_12
tty_dec_PDF4LHC_11
tty_dec_PDF4LHC_10
tty_dec_PDF4LHC_1
tty_dec_Herwig7
ttV Norm
ttbar_var3c
ttbar_pt_hard
ttbar Norm
ttbar_muR
ttbar_muF
ttbar_hdamp_var
ttbar_Herwig7
tγ(t channel) Norm
tγ(s channel) Norm
lepfakeSF_var2
lepfakeSF_var1
lepfakeSF_
hfakeSF_
efakeSF_
diboson Norm
Wty_muR
Wty_muF
Wty_Herwig7
Wt_Herwig7
Photon_effIso
Photon_ID
PileupRW
Muon_SF_Trigger_SYST
Muon_SF_Trigger_STAT
Muon_SF_TTVA_STAT
Muon_SF_TTVA_MC_XSEC
Muon_SF_TTVA_BKG_FRACTION
Muon_SF_Isol_STAT
Muon_SF_Isol_SHERPA_POWHEG
Muon_SF_Isol_QCD_TEMPLATE
Muon_SF_Isol_PROBEQ
Muon_SF_Isol_MLLWINDOW
Muon_SF_Isol_BKG_FRACTION
Muon_SF_ID_TRUTH
Muon_SF_ID_STAT
Muon_SF_ID_PT_DEPENDENCY
MUON_SCALE
MUON_SAGITTA_RESBIAS
MUON_MS
MUON_ID
MET_SoftTrk_Scale
MET_SoftTrk_ResoPerp
MET_SoftTrk_ResoPara
Luminosity
JVTscalefactor
JET_PunchThrough_MC16
JET_Pileup_RhoTopology
JET_Pileup_PtTerm
JET_Pileup_OffsetNPV
JET_Pileup_OffsetMu
JET_JER_EffectiveNP_9
JET_JER_EffectiveNP_8
JET_JER_EffectiveNP_7
JET_JER_EffectiveNP_6
JET_JER_EffectiveNP_5
JET_JER_EffectiveNP_4
JET_JER_EffectiveNP_3
JET_JER_EffectiveNP_2
JET_JER_EffectiveNP_12restTerm
JET_JER_EffectiveNP_11
JET_JER_EffectiveNP_10
JET_JER_EffectiveNP_1
JET_JER_DataVsMC_MC16
JET_Flavor_Response
JET_Flavor_Composition
JET_EtaIntercalibration_TotalStat
JET_EtaIntercalibration_NonClosure_posEta
JET_EtaIntercalibration_NonClosure_negEta
JET_EtaIntercalibration_NonClosure_highE
JET_EtaIntercalibration_NonClosure_2018dat
JET_EtaIntercalibration_Modelling
JET_EffectiveNP_Statistical6
JET_EffectiveNP_Statistical5
JET_EffectiveNP_Statistical4
JET_EffectiveNP_Statistical3
JET_EffectiveNP_Statistical2
JET_EffectiveNP_Statistical1
JET_EffectiveNP_Modelling4
JET_EffectiveNP_Modelling3
JET_EffectiveNP_Modelling2
JET_EffectiveNP_Modelling1
JET_EffectiveNP_Mixed3
JET_EffectiveNP_Mixed2
JET_EffectiveNP_Mixed1
JET_EffectiveNP_Detector2
JET_EffectiveNP_Detector1
JET_BJES_Response
Electron_SF_Trigger
Electron_Iso_SF_6
Electron_Iso_SF_14
Electron_Iso_SF_0
Electron_ID_SF_3
Electron_ID_SF_29
Electron_ID_SF_28
Electron_ID_SF_27
Electron_ID_SF_26
Electron_ID_SF_23
Electron_ID_SF_22
Electron_ID_SF_21
Electron_ID_SF_20

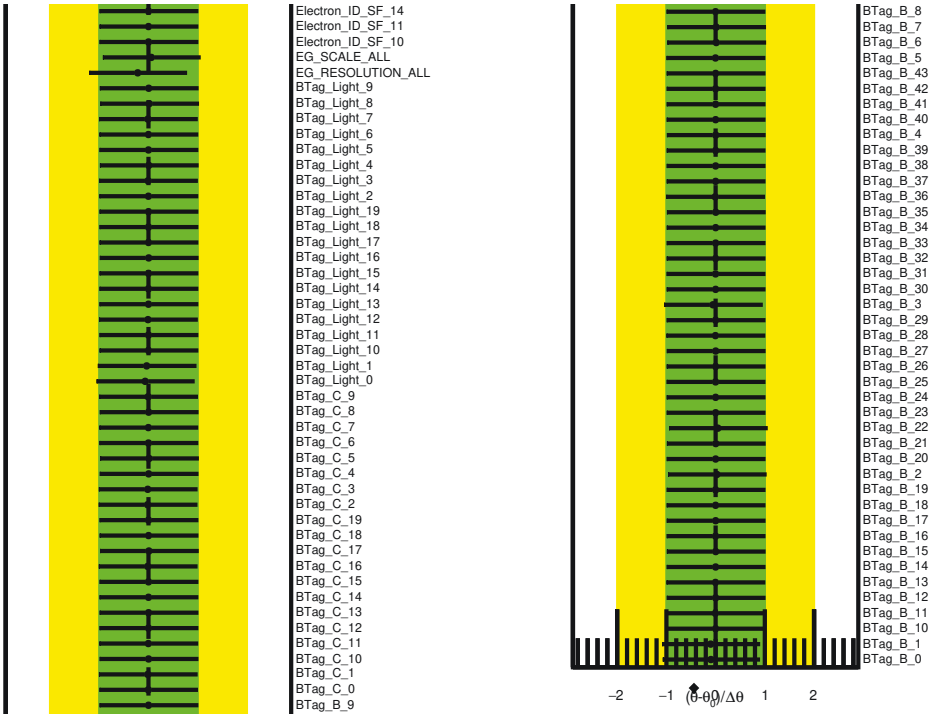

Figure 11.3: The plot shows the pulls and constraints of various uncertainties, including b-tagging (labels starting with "BTag_"), JES and JER (labels with "JET_"), electron and muon reconstruction (labels starting with "Electron_" and "Muon_"), cross-section processes (labels ending with "_Norm"), PDFs (labels with "_PDF4LHC_"), modeling (labels ending with "_Herwig7", "var3c" for ISR, "muR", "muF" for scale variations), and fake estimation (labels starting with "lepfakeSF_", "efakeSF_", "hfakeSF_").

Correlation among NPs Correlations are calculated among the signal strengths and nuisance parameters, as shown in Figure 11.4 and Figure A.11, for the single-lepton and dilepton channels, respectively (for the $p_{\mathrm{T}}(\gamma)$ measurement). In the single-lepton channel, a correlation of 57% was observed between the $t\bar{t}\gamma$ decay signal strength and the $t\bar{t}\gamma$ decay parton shower uncertainty. This effect is expected and indicates that during the fitting, both parameters tend to either increase or decrease the contribution of the $t\bar{t}\gamma$ decay template. In the dilepton channel, no large correlations are observed between the NPs and POIs.

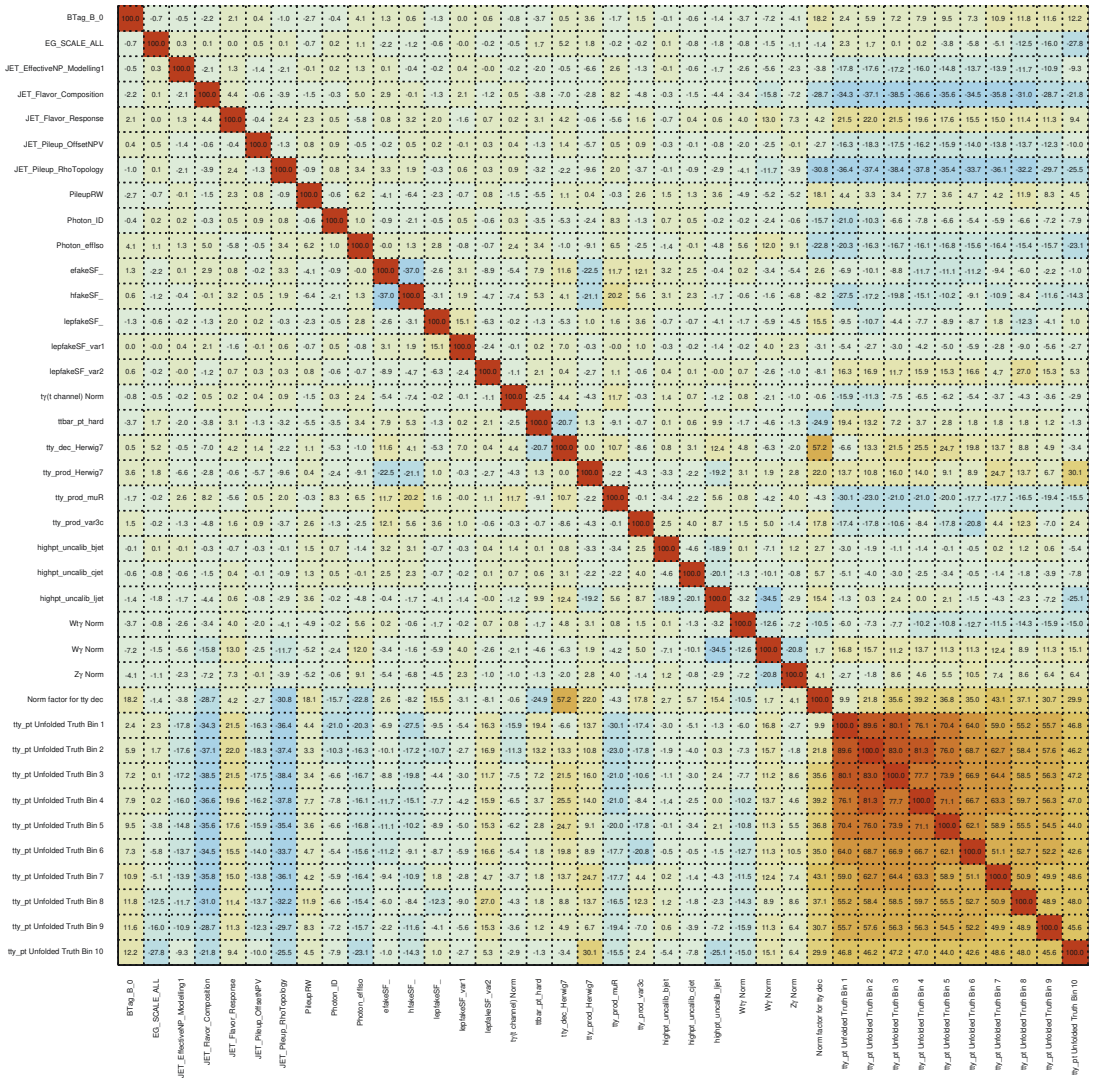

Figure 11.4: Plot showing the correlation between signal strength and nuisance parameters for the $p_{\mathrm{T}}(\gamma)$ measurement in the single-lepton channel. Only NPs with a correlation greater than 10% are shown. The NP names indicate the following uncertainties: "JET_" for JER and JES, "BTag_" for b-tagging, "_Norm" for normalization, "_muR" and "_muF" for scale, "_var3c" for ISR, "lepfakeSF_" for lepton fakes, "efakeSF_" for electron fakes, "hfakeSF_" for hadron fakes, "highpt_uncalib_" for uncalibrated jet, and "Photon_" for photon reconstruction.

Ranking of the nuisance parameters It is important to understand the impact of various uncertainties and identify which ones are most relevant. To achieve this, the impact of each NP on the signal strength (μ) is calculated. This is done by varying each NP's post-fit value by x ($\hat{\theta} + x$, where $\hat{\theta}$ is the post-fit value and x is some number), performing the fit again while keeping other NPs at their post-fit values, and measuring the change in signal strength from the nominal fit value ($\Delta\mu = \mu - \mu'$). The impact is illustrated in the ranking plots, where NPs are ranked based on their impact on the signal strength. The ranking plots for the single-lepton and dilepton channels are shown in Figure 11.5 and Figure 11.6 respectively (for the $p_{\mathrm{T}}(\gamma)$ measurement). The ranking is done for the signal strength in each bin of the $p_{\mathrm{T}}(\gamma)$ distribution.

The solid box indicates the change in signal strength from the nominal fit value ($\Delta\mu$) when the NP value is varied to $\theta = \hat{\theta} \pm \Delta\hat{\theta}$, where $\Delta\hat{\theta}$ is the post-fit uncertainty of the NP. The empty box represents the pre-fit impact, where $\Delta\hat{\theta}$ is replaced by $\Delta\theta$, the pre-fit uncertainty of the NP. The plot also shows the pulls and constraints, with the 1 σ region indicated by dotted lines.

The $t\bar{t}\gamma$ decay signal strength (indicated by "Norm factor for tty_dec") impacts the measurement and is included in the ranking plot, but only the post-fit impact is shown in this case. In the single-lepton channel, the highest-ranked uncertainties are associated with JER and JES (referred to as "JET_"), renormalization scale variation in the $t\bar{t}\gamma$ production simulation ("tty_prod_muR"), parton shower uncertainty ("tty_dec_Herwig7", "tty_prod_Herwig7"), uncertainties on hadron fake scale factors ("hfakeSF_"), and uncertainties on lepton fake estimation ("lepfakeSF_"). The $t\bar{t}\gamma$ decay signal strength also has a very high impact on the measurement. In the low p_{T} region, the uncertainties associated with JES and JER, and uncertainties on fake background have the largest impact while in the high p_{T} region, $t\bar{t}\gamma$ decay signal strength, photon related uncertainties ("EG_SCALE_") have the largest impact.

In the dilepton channel, similar sources have a significant impact on the measurement, along with cross-section uncertianty on $tW\gamma$ process ("$tW\gamma$ norm"), and photon reconstruction uncertainties ("Photon_").

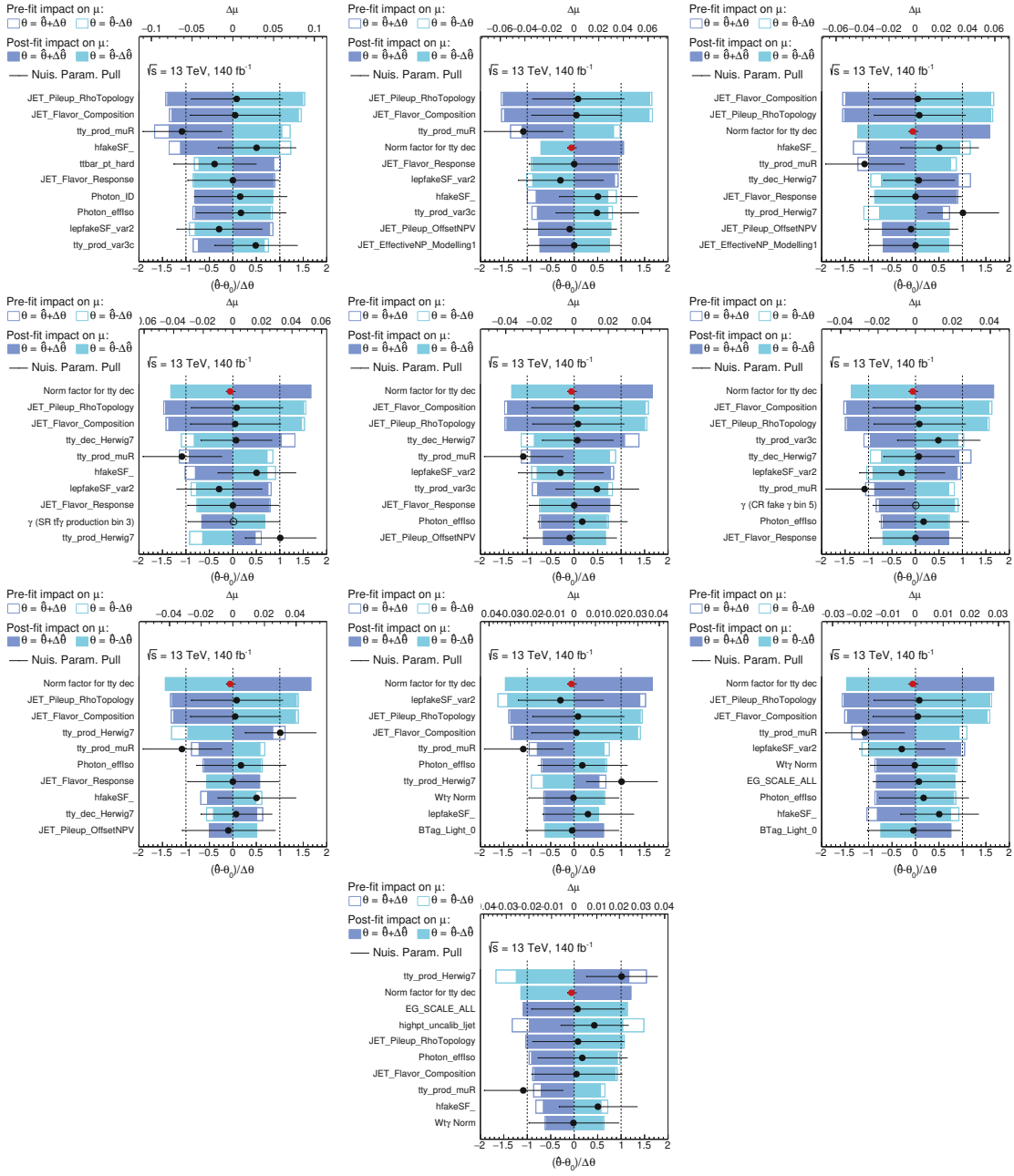

Figure 11.5: Ranking of the 10 leading systematic uncertainties included in the profile likelihood unfolding used for the $p_{\mathrm{T}}(\gamma)$ cross-section measurement in the single-lepton channel. The blue and turquoise bands represent the post-fit impact on the measured cross-section in each bin, while the outlined blue and turquoise rectangles show the pre-fit impact. The difference between these two indicates the constraint of the nuisance parameter. Most nuisance parameters are either unconstraint or only marginally constraint. The impact is overlaid with the post-fit values of the nuisance parameters (pulls), shown by the black dots. The black lines represent the post-fit uncertainties normalized to the pre-fit uncertainties. Each subfigure, corresponds to a specific bin of the $p_{\mathrm{T}}(\gamma)$ distribution, starting from bin 1 till bin 10 (from left to right and top to bottom).

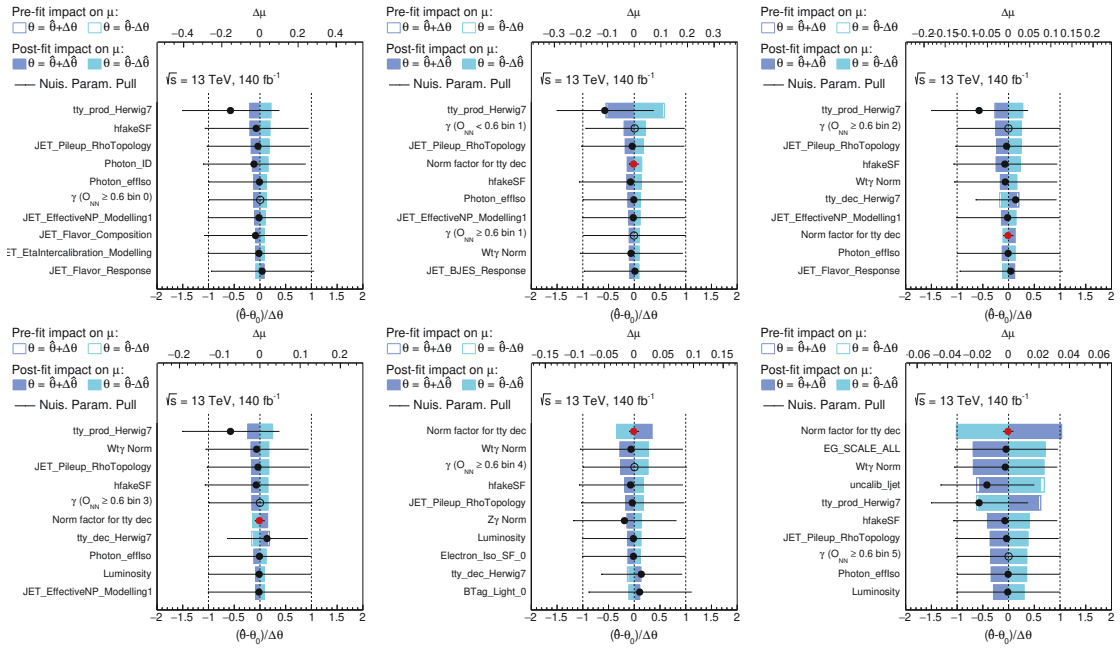

Figure 11.6: Ranking of the 10 leading systematic uncertainties included in the profile likelihood unfolding used for the $p_{\mathrm{T}}(\gamma)$ cross-section measurement in dilepton channel. The blue and turquoise bands represent the post-fit impact on the measured cross-section in each bin, while the outlined blue and turquoise rectangles show the pre-fit impact. The difference between these two indicates the constraint of the nuisance parameter. Most nuisance parameters are either unconstraint or only marginally constraint. The impact is overlaid with the post-fit values of the nuisance parameters (pulls), shown by the black dots. The black lines represent the post-fit uncertainties normalized to the pre-fit uncertainties. Each subfigure, corresponds to a specific bin of the $p_{\mathrm{T}}(\gamma)$ distribution, starting from bin 1 till bin 6 (from left to right and top to bottom).

Measured $t\bar{t}\gamma$ production cross-section Finally, from the signal strength obtained from the fit, the differential cross-section is obtained. This section presents the $t\bar{t}\gamma$ production cross-sections. The cross-section is measured as a function of $p_{\mathrm{T}}(\gamma)$, $|\eta(\gamma)|$, $\Delta R(\gamma, \ell)$, $\Delta R(\gamma, b)_{\mathrm{min}}$, $\Delta R(\ell, j)_{\mathrm{min}}$, and $p_{\mathrm{T}}(j_1)$ in the single-lepton channel. In addition, in the dilepton channel, the cross-section is measured as a function of $\Delta R(\gamma, \ell_1)$, $\Delta R(\gamma, \ell_2)$, $|\Delta\eta(\ell, \ell)|$, $|\Delta\phi(\ell, \ell)|$, and $p_{\mathrm{T}}(\ell, \ell)$. The measured cross-sections at particle level are shown in Figures 11.7 and 11.8 for the single-lepton channel. The unfolded distributions in the dilepton channel are shown in Figures 11.9, 11.10, A.12 and A.13. The normalized unfolded distributions are presented alongside the absolute differential cross-sections. The cross-section in each bin is divided by the bin width, and the normalized cross-sections are scaled to unity. The normalized cross-section highlights the shape differences between the measured data and the predictions. The uncertainty bands in the figures show both

statistical and systematic uncertainties. Additionally, a ratio plot displays the ratio of the predictions to the observed data. The final bin includes the overflow events.

The measured distributions are compared with the MadGraph5_aMC@NLO+Pythia8 and MadGraph5_aMC@NLO+Herwig7 predictions. These predictions are at NLO in QCD precision calculated using the NNPDF3.0nlo set of PDFs. There are no significant differences between the two MC predictions. In general, the measured cross-sections are higher than the MC predictions, potentially due to higher-order corrections not included in the MC prediction. A theoretical calculation shows that the $t\bar{t}\gamma$ production cross-section increases by about 15% at NNLO (with soft gluon resummation) compared to the NLO prediction [33].

The total uncertainty in the absolute cross-section measurement in the single-lepton channel ranges from 8% to 20% depending on the observable and the bin. The statistical uncertainty ranges from 3% to 10%. The largest uncertainty comes from the normalization of the background processes with prompt photons, some components of the jet energy scale (JES) uncertainty, and $t\bar{t}\gamma$ modeling uncertainties.

The total uncertainty in the dilepton channel ranges from 8% to 20% (some cases up to 30% in the tails of the distributions) depending on the observables and the bin. The dominant source is the statistical uncertainty of the data. In the case of the normalized cross-section measurement, the total uncertainty is within 10% for most of the observables and bins owing to the large cancellation of the systematic uncertainties.

χ^2 and p-values The compatibility between the measured cross-sections and the MC predictions is quantified by calculating the χ^2/ndf and p-values. The χ^2/ndf represents the goodness of fit, showing how well the theoretical predictions describe the experimental results. The χ^2/ndf is calculated as follows:

$$\chi^2 = \sum_{i,j} \left(\sigma_i^{\text{obs}} - \sigma_i^{\text{pred}}\right) C_{ij}^{-1} \left(\sigma_j^{\text{obs}} - \sigma_j^{\text{pred}}\right), \tag{11.1}$$

where σ_i^{obs} and σ_i^{pred} are the measured and predicted cross-sections, respectively, and C_{ij} is the covariance matrix, i, j are the bin indices.

The covariance matrix is calculated using the uncertainty sources as follows:

$$C_{ij} = \sum_{k,l} \sigma_i^k \hat{\rho}_{kl} \sigma_j^l, \tag{11.2}$$

where σ_i^k is the uncertainty in the i-th bin due to the k-th source of uncertainty, and $\hat{\rho}_{kl}$ is the correlation coefficient between the k-th and l-th sources of uncertainty.

The p-value is calculated using the χ^2 value and the number of degrees of freedom. The p-value represents the probability of observing a χ^2 statistic at least as extreme as the observed value under the null hypothesis that the model predictions are correct. χ^2/ndf and p-values between the measured absolute and normalized cross-sections of $t\bar{t}\gamma$ production and the MadGraph5_aMC@NLO simulations interfaced with Pythia 8 and Herwig 7 are shown in Table 11.1 and discussed in the following.

The $p_{\mathrm{T}}(\gamma)$ observable is sensitive to the coupling between the top quark and the photon. Any change in the coupling will be reflected in the $p_{\mathrm{T}}(\gamma)$ distribution. The cross-section is measured from 20 to 500 GeV where the p_{T} above 500 GeV events are included in the last bin. The measured absolute cross-section is higher than the MC prediction in the low p_{T} regions. However, for p_{T} values above 150 GeV, the prediction aligns with the measurement within the uncertainties. The uncertainty in the absolute cross-section measurement ranges from 10% to 16% in the single-lepton channel and from 10% to 13% in the dilepton channel. In the normalized cross-section, the uncertainty is below 10%. However, there is a slight discrepancy observed between the data and the prediction. For the absolute cross-section measurement, a χ^2/ndf of 12.3/10 and a p-value of 0.26 are observed with the Pythia8 prediction, indicating that the measurement is consistent with the prediction. However, for the normalized cross-section, the p-value is less than 0.01, indicating a slight disagreement between the data and the prediction.

The pseudo rapidity of the photon $|\eta(\gamma)|$ is also sensitive to the coupling between the top quark and the photon. The distribution is symmetric around 0 and falls off towards larger $|\eta(\gamma)|$ values. The measured cross-section is higher than the MC prediction where the normalized cross-section shows a good shape agreement with the prediction both in single-lepton and dilepton channels. The uncertainty on the absolute cross-section is about 9-15% in the single-lepton channel and about 10-12% in the dilepton channel. For both absolute and normalized cross-sections, the p-values are above 0.18, indicating a good agreement between the data and the prediction.

The other observables cannot be compared across channels due to the different event topologies. The $\Delta R(\gamma, \ell)$ distribution measures the separation between the photon and the lepton. The uncertainty on the absolute cross-section is about 10-20% in the single-lepton channel. Similarly, the measured cross-section is larger than the prediction across bins. The normalized distribution shows good shape agreement. In the dilepton channel, for the observables, $\Delta R(\gamma, \ell_1)$, $\Delta R(\gamma, \ell_2)$, and $\Delta R(\gamma, \ell)_{\mathrm{min}}$, the measured cross-section aligns with

the prediction in low ΔR bins. However, a higher cross-section is observed in the higher ΔR bins. In the case of normalized cross-section, there is a slight shape disagreement observed.

The $\Delta R(\gamma, b)_{\text{min}}$ distribution measures the separation between the photon and the closest b-jet. The distribution increases slowly, peaks around 1.5 and falls off with increasing ΔR. Similar to the $\Delta R(\gamma, \ell)$ distribution, the measured cross-section is higher than the prediction in the high ΔR bins. In the dilepton channel, the measured cross-section is higher than the MC prediction across all bins. The normalised cross-section shows a good shape agreement with the MC prediction in both channels.

The $\Delta R(\ell, j)_{\text{min}}$ distribution is the separation between the lepton and the closest jet. The distribution peaks around 1.2 and falls off with increasing ΔR. The measured cross-section is higher than the MC prediction across all bins in both channels. The normalized cross-section shows a good shape agreement.

The $p_{\text{T}}(j_1)$ distribution represents the transverse momentum of the leading jet. The cross-section increases with increasing p_{T} peaks around 100 GeV and falls off steeply with increasing p_{T}. In both channels, the measured cross-section is higher than the MC prediction in high p_{T} jets. The normalized cross-section shows a good shape agreement with the MC prediction.

The $|\Delta\eta(\ell, \ell)|$ and $\Delta\phi(\ell, \ell)$ distributions correspond to the separation between the two leptons in η and ϕ, and are sensitive to the spin correlation between the two top quarks. In the absolute cross-section, the measured cross-section is higher than the MC prediction across all bins of $|\Delta\eta(\ell, \ell)|$ while in $\Delta\phi(\ell, \ell)$ the measured cross-section is higher than the MC prediction in the low $\Delta\phi$ bins but the high $\Delta\phi$ bins show a good agreement. While $|\Delta\eta(\ell, \ell)|$ shows a good shape agreement in the normalized cross-section, $\Delta\phi(\ell, \ell)$ shows a slight shape disagreement. This is also observed in $t\bar{t}$ production measurements in dilepton channel [121].

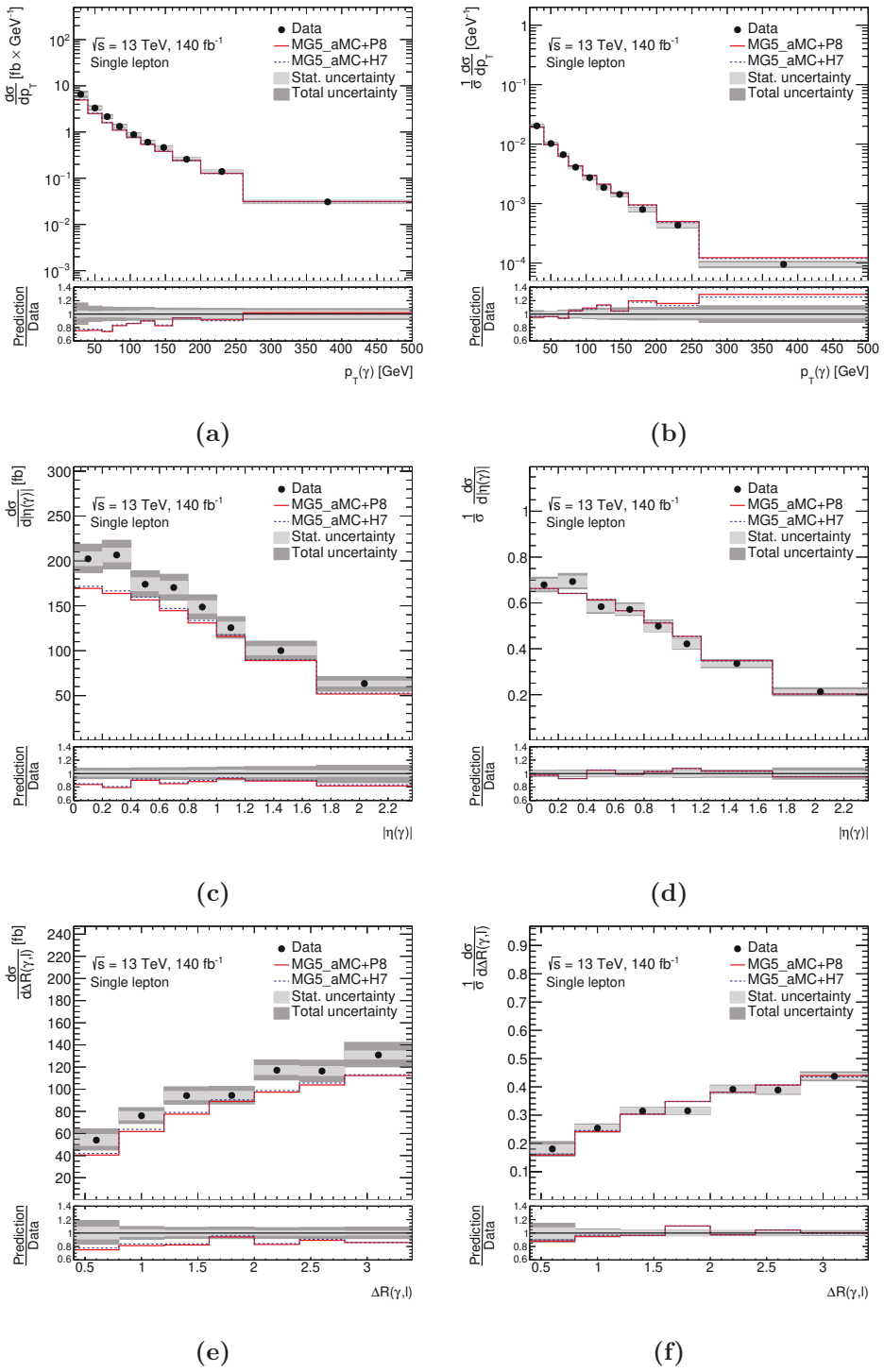

Figure 11.7: Absolute (left) and normalized (right) differential cross-sections of $t\bar{t}\gamma$ production in the single-lepton fiducial phase space at particle level as a function of $p_{\mathrm{T}}(\gamma)$ (a, b), $|\eta(\gamma)|$ (c, d), $\Delta R(\gamma, \ell)$ (e, f). Data are compared with MadGraph5_aMC@NLO simulation interfaced with Pythia8 and Herwig7. The last bin includes overflow events.

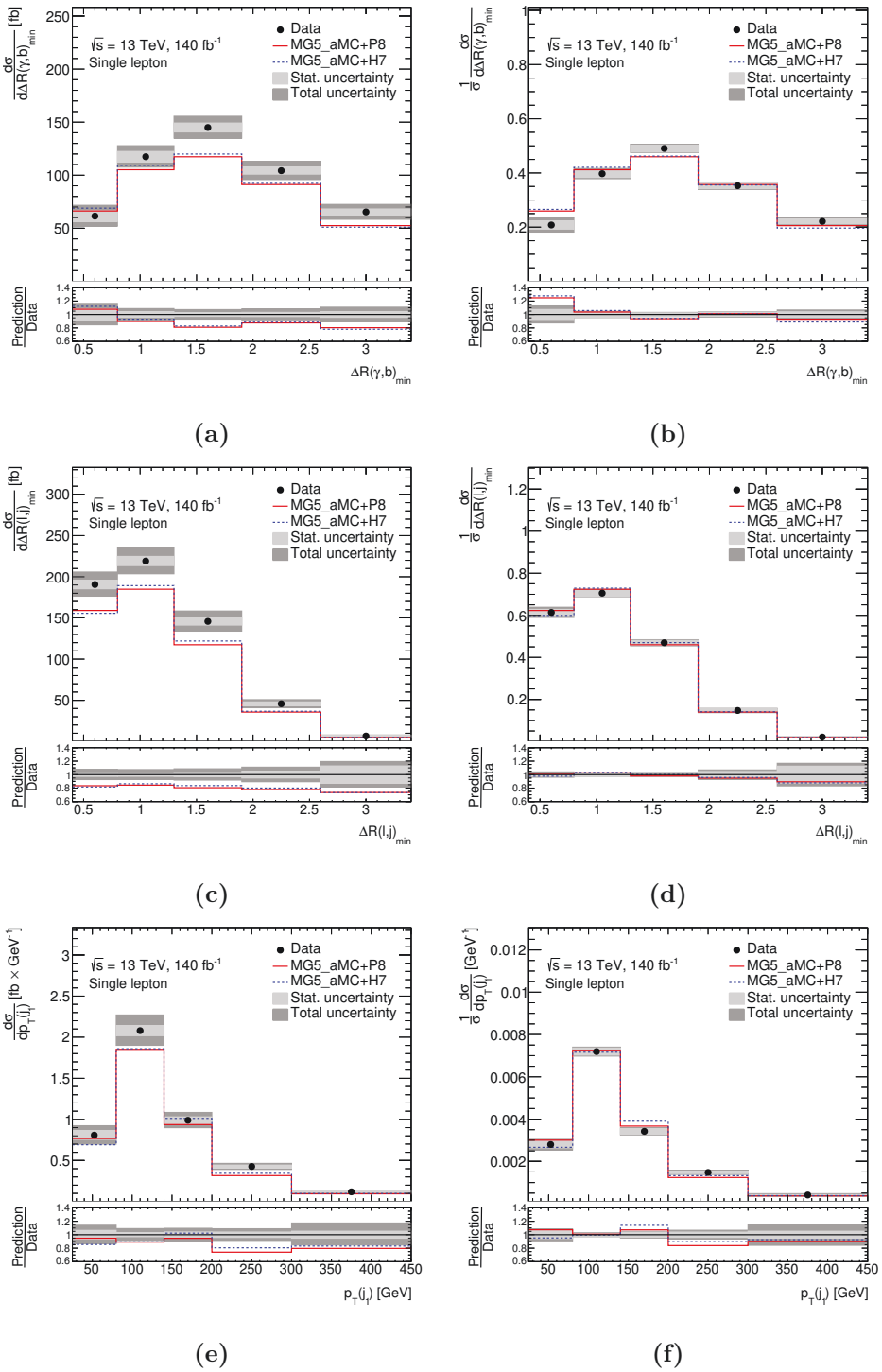

Figure 11.8: Absolute (left) and normalized (right) differential cross-sections of $t\bar{t}\gamma$ production in the single-lepton fiducial phase space at particle level as a function of $\Delta R(\gamma, b)$ (a, b), $\Delta R(\ell, j)$min (c, d), and $p_{\mathrm{T}}(j_1)$ (e, f). Data are compared with MadGraph5_aMC@NLO simulation interfaced with Pythia8 and Herwig7. The last bin includes overflow events.

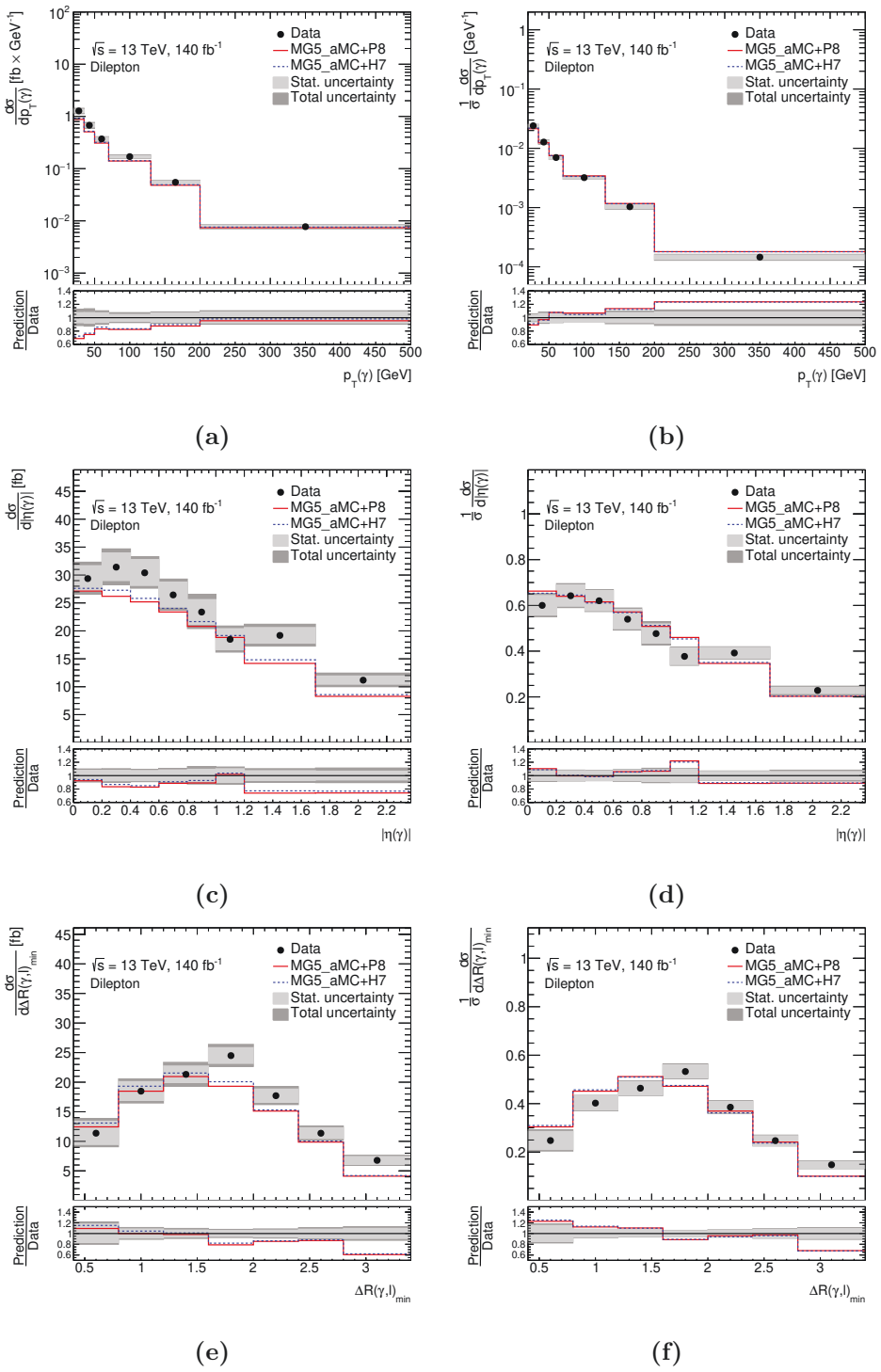

Figure 11.9: Absolute (left) and normalized (right) differential cross-sections of $t\bar{t}\gamma$ production in the dilepton fiducial phase space at particle level as a function of $p_{\mathrm{T}}(\gamma)$ (a, b), $|\eta(\gamma)|$ (c, d), $\Delta R(\gamma, \ell)_{\mathrm{min}}$ (e, f). Data are compared with MadGraph5_aMC@NLO simulation interfaced with Pythia8 and Herwig7. The last bin includes overflow events.

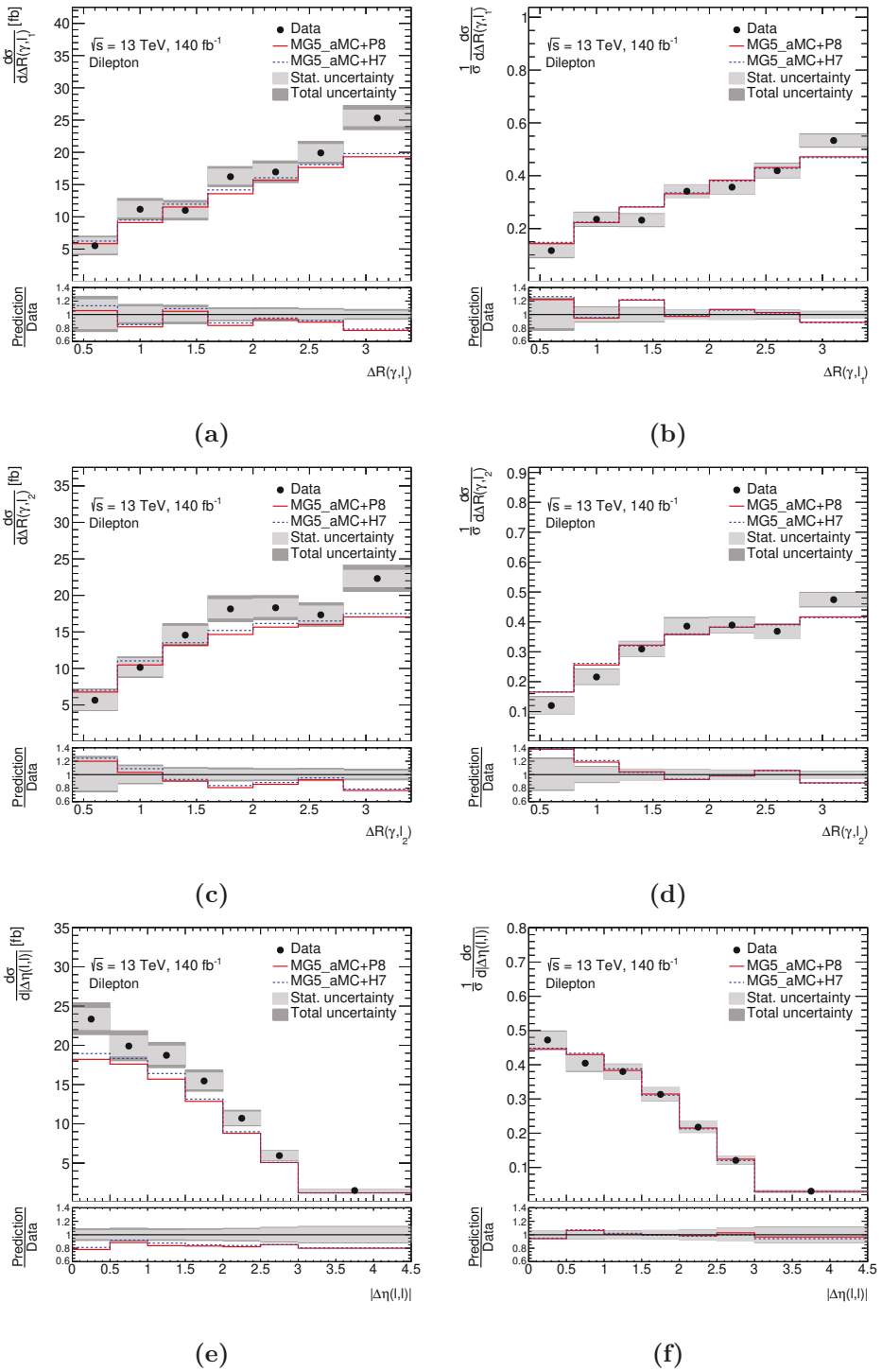

Figure 11.10: Absolute (left) and normalized (right) differential cross-sections of $t\bar{t}\gamma$ production in the dilepton fiducial phase space at particle level as a function of $\Delta R(\gamma, \ell_1)$ (a, b), $\Delta R(\gamma, \ell_2)$ (c, d), and $|\Delta\eta(\ell, \ell)|$ (e, f). Data are compared with MadGraph5_aMC@NLO simulation interfaced with Pythia8 and Herwig7. The last bin includes overflow events.

Table 11.1: χ^2/ndf and p-values between the measured absolute and normalised cross-sections of $t\bar{t}\gamma$ production and the NLO MadGraph5_aMC@NLO simulations interfaced with Pythia 8 and Herwig 7.

	Absolute cross-sections				Normalised cross-sections			
	MG5_aMC@NLO+Pythia 8		MG5_aMC@NLO+Herwig 7		MG5_aMC@NLO+Pythia 8		MG5_aMC@NLO+Herwig 7	
Variables	χ^2/ndf	p-value	χ^2/ndf	p-value	χ^2/ndf	p-value	χ^2/ndf	p-value
Single-lepton channel								
p_{T} (γ)	11.7/10	0.31	10.4/10	0.40	43.9/9	< 0.01	32.1/9	< 0.01
$\lvert\eta\rvert(\gamma)$	11.8/8	0.16	11.1/8	0.20	8.1/7	0.33	8.1/7	0.32
$\Delta R(\gamma, \ell)$	10.5/7	0.16	9.9/7	0.19	8.8/6	0.19	8.8/6	0.19
$\Delta R(\gamma, b)_{min}$	12.5/5	0.03	12.3/5	0.03	7.6/4	0.11	9.0/4	0.06
$\Delta R(\ell, j)_{min}$	6.3/5	0.28	6.6/5	0.25	1.5/4	0.83	2.5/4	0.65
$p_{\mathrm{T}}(j_1)$	12.6/5	0.03	10.8/5	0.06	8.2/4	0.08	9.7/4	0.05
Dilepton channel								
p_{T} (γ)	8.6/6	0.20	7.2/6	0.31	6.5/5	0.26	5.9/5	0.32
$\lvert\eta\rvert(\gamma)$	12.1/8	0.15	9.9/8	0.27	9.2/7	0.24	7.9/7	0.34
$\Delta R(\gamma, \ell)_{min}$	17.2/7	0.02	16.5/7	0.02	14.2/6	0.03	14.4/6	0.03
$\Delta R(\gamma, b)_{min}$	7.8/5	0.17	5.0/5	0.42	1.4/4	0.84	0.8/4	0.93
$\Delta R(\ell, j)_{min}$	9.3/5	0.10	6.4/5	0.27	5.4/4	0.25	3.7/4	0.45
$p_{\mathrm{T}}(j_1)$	10.5/5	0.06	5.0/5	0.42	7.8/4	0.10	3.6/4	0.46
$\Delta R(\gamma, \ell_1)$	14.8/7	0.04	13.8/7	0.06	10.0/6	0.13	10.4/6	0.11
$\Delta R(\gamma, \ell_2)$	13.1/7	0.07	12.3/7	0.09	9.7/6	0.14	10.3/6	0.11
$\lvert\Delta\eta(\ell, \ell)\rvert$	10.0/7	0.19	8.5/7	0.29	1.9/6	0.93	2.1/6	0.91
$\Delta\phi(\ell, \ell)$	14.6/8	0.07	15.6/8	0.05	15.4/7	0.03	17.1/7	0.02
$p_{\mathrm{T}}(\ell, \ell)$	13.4/6	0.04	9.8/6	0.13	9.9/5	0.08	7.8/5	0.17

11.2 $t\bar{t}\gamma$ production measurement combining channels

The differential cross-section is also measured by combining the single-lepton and dilepton channels. This increases the statistics of the sample and slightly reduces the statistical uncertainties, the impact is very small due to the relatively small number of events in the dilepton compared to the single-lepton channel. The unfolded differential cross-sections are measured in a combined phase space at the particle level by taking the union of the phase spaces of the single-lepton and dilepton channels. The measurement is performed only for $p_{\mathrm{T}}(\gamma)$ and $|\eta(\gamma)|$ observables. This is because other observables do not correspond between the two channels due to their shape difference because of event topologies.

The analysis strategy remains the same as in the $t\bar{t}\gamma$ production measurement discussed in the previous section. The only changes affect the signal template at the particle level and the response matrices. The signal template at the particle level is constructed by combining the events from the single-lepton and dilepton channels and requiring the fiducial phase space selection for the combined phase space. The response matrices are constructed using the same method. The migration of events between the channels is properly taken into account. This includes cases where a dilepton event at the particle level is selected as a single-lepton event if one of the leptons is not reconstructed or fails the lepton selection. The particle level distributions are shown in Figure 11.11. The response matrices are constructed for six regions at the reconstruction level, four in single lepton channel and two in dilepton channel, they are shown in Figure A.9 for the $p_{\mathrm{T}}(\gamma)$ observable.

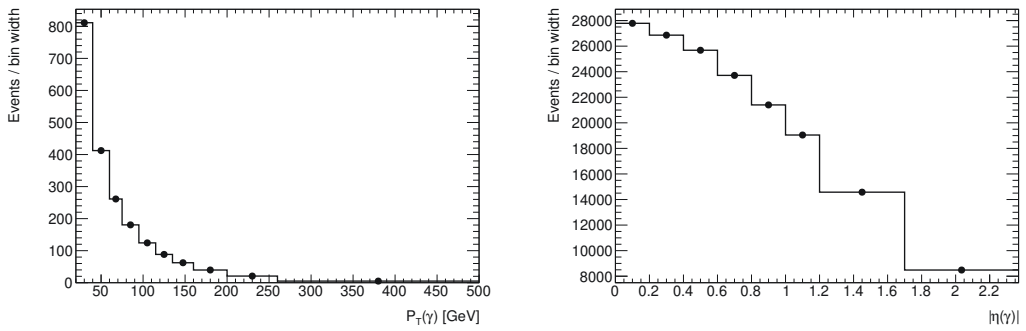

(a) **(b)**

Figure 11.11: Particle-level distributions of $t\bar{t}\gamma$ production of $p_{\mathrm{T}}(\gamma)$ (a) and $|\eta(\gamma)|$ (b) in the combined fiducial phase space at particle level in the single-lepton and dilepton channels. The number of events corresponds to the expected number of events at particle level normalised to the luminosity of data. Overflow events are included in the last bin of the corresponding distribution. Note that values are divided by bin width.

The profile likelihood unfolding is performed on the data simultaneously in six regions. As expected from the measurements in the individual channels, the uncertainties with the largest impact comes from the JES related uncertainties, parton shower uncertainties in the $t\bar{t}\gamma$ production and $t\bar{t}\gamma$ decay simulation, $tW\gamma$ cross-section uncertainty, fake photon (e-fake, h-fake) scale factor uncertainties, photon identification scale factor uncertainties, and lepton fake estimation uncertainties, which are the dominant sources of systematic uncertainties in both channels.

Impact of a group of uncertainties To better visualize how different categories of uncertainties affect the measurement, the sources are grouped into several categories, and the impact of each group on the signal strength is calculated. The uncertainties are categorized as follows: $t\bar{t}\gamma$ production modeling, $t\bar{t}\gamma$ decay modeling, jet and b-jet tagging, photon-related uncertainties, background uncertainties including normalization uncertainties and data-driven uncertainties, statistical uncertainties, and other experimental uncertainties.

The impact is calculated as follows: the nominal fit results in a signal strength uncertainty $\Delta\mu$. The fit is then repeated, excluding the sources of uncertainty in a specific category. The impact of that category is determined as the square root of the difference between the total uncertainty, $\Delta\mu$, and the uncertainty obtained after removing the sources of the category, $\Delta\mu'$: $\sqrt{(\Delta\mu)^2 - (\Delta\mu')^2}$.

When splitting all nuisance parameters into groups, the quadrature sum of the uncertainty contributions from all groups will generally differ from the total signal strength uncertainty due to the missing correlations of the nuisance parameters between the different groups. The impact of the categories of uncertainties is shown in Figure 11.13 for absolute cross-section measurement for $p_{\mathrm{T}}(\gamma)$ and $|\eta(\gamma)|$ observables. In the low p_{T} region, jet-related uncertainties and b-tagging uncertainties are the dominant sources. In the high p_{T} region, along with those uncertainties, signal modeling and photon-related uncertainties have a significant impact. For the $|\eta(\gamma)|$ observable, jet-related and b-tagging uncertainties are the dominant sources across all bins. The background category, which includes normalization uncertainties and data-driven uncertainties, is a relevant contribution in the $|\eta(\gamma)| > 1.8$ region.

The absolute and normalized differential cross-sections at particle level as a function of the photon p_{T} and $|\eta(\gamma)|$ are shown in Figure 11.12. The measured cross-sections are compared with the NLO MadGraph5_aMC@NLO simulations interfaced with Pythia 8 and Herwig 7. The predictions are calculated at the matrix element level with NLO

in QCD accuracy calculated using the MadGraph5_aMC@NLO generator with the NNPDF3.0nlo set of PDFs. For $p_{\mathrm{T}}(\gamma)$ distribution, the measured absolute cross-section is higher than the prediction in the low p_{T} region, while in the high p_{T} region, the prediction agrees within the uncertainties. The uncertainty is about 6-12%. For the normalized cross-section, the uncertainty is about 5-9% and a slight shape disagreement is observed.

For absolute cross-section as a function of $|\eta(\gamma)|$, the data shows a higher cross-section than the prediction across all the bins. The uncertainty is about 6-10%. For the normalized cross-section, the uncertainty is about 4-6% and the data agrees very well with the prediction.

The compatibility between the measured cross-section and the MC prediction is quantified by calculating the χ^2/ndf and p-values mentioned in Section 11.1. The χ^2/ndf and p-values between the measured absolute and normalised cross-sections of $t\bar{t}\gamma$ production and the NLO MadGraph5_aMC@NLO simulations interfaced with Pythia 8 and Herwig 7 are shown in Table 11.2. The higher p-values are observed indicating that the data is in good agreement with the prediction.

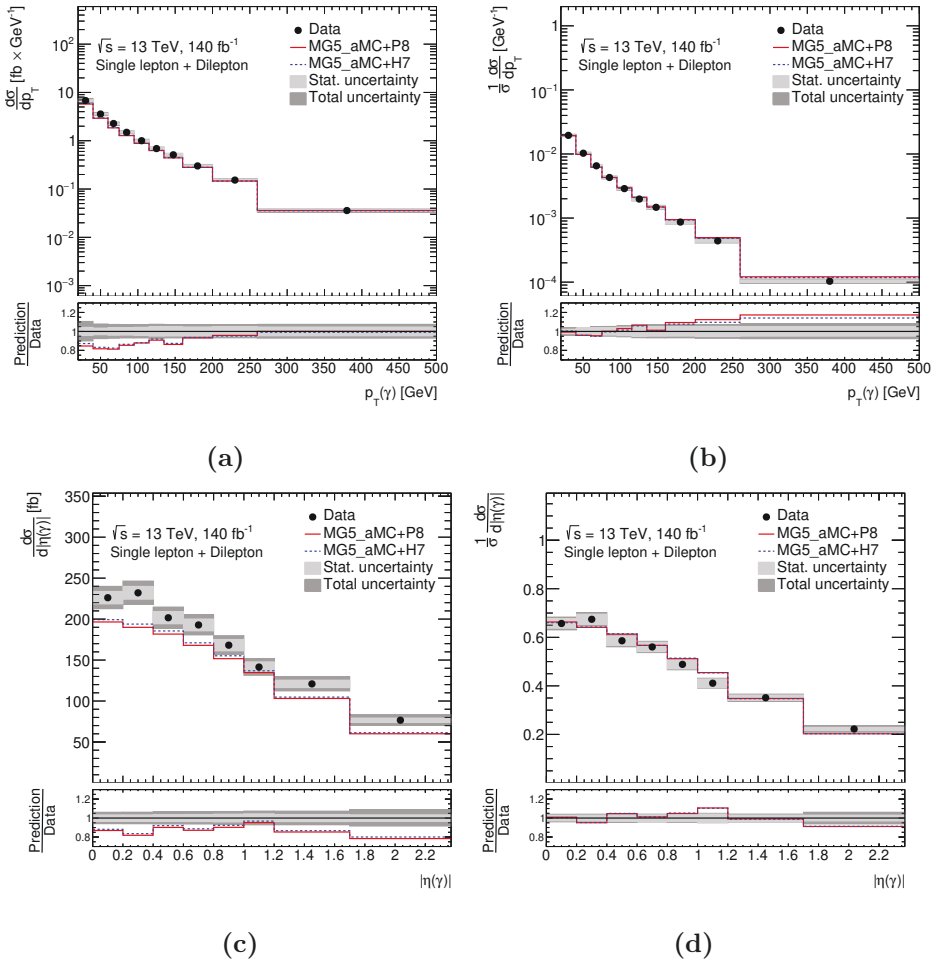

Figure 11.12: Abolute (left) and normalized (right) differential cross-section for the $t\bar{t}\gamma$ production measured in a combined single-lepton and dilepton fiducial phase space as a function of the photon p_{T} (a, b), and photon $|\eta|$ (c, d). Data are compared with the MadGraph5_aMC@NLO simulation interfaced with Pythia 8 and Herwig 7. The lower parts of each plot show the ratio of the prediction to the data. The last bin includes the overflow events.

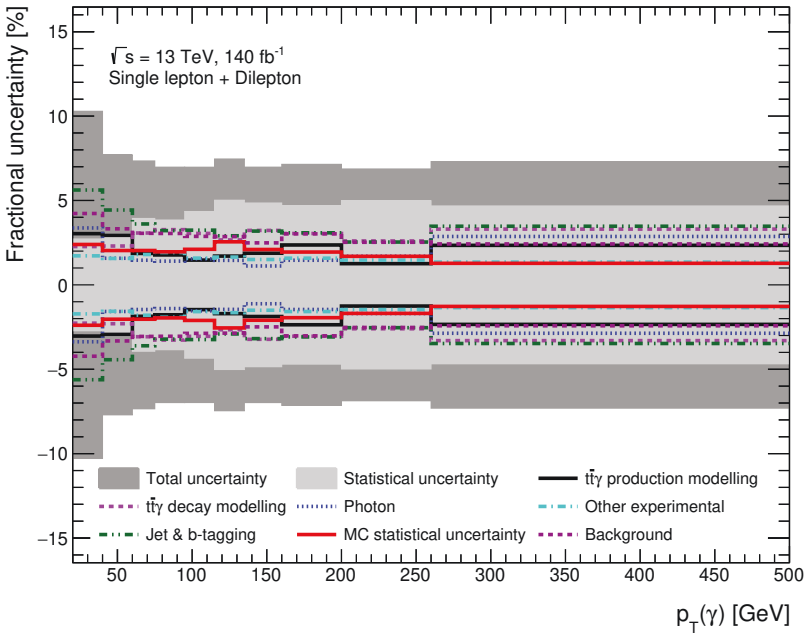

(a)

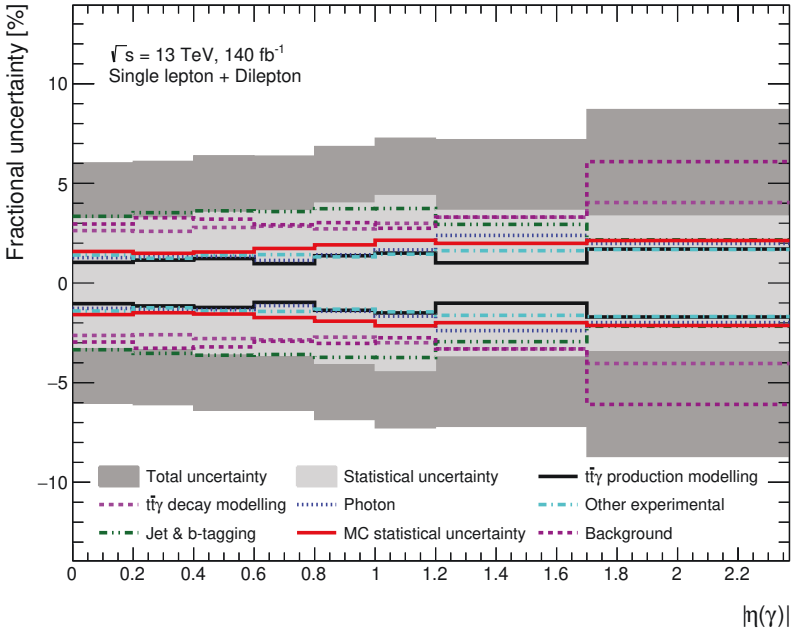

(b)

Figure 11.13: The decomposed systematic uncertainties for absolute differential cross-sections as a function of (a) $p_{\mathrm{T}}(\gamma)$ and (b) $|\eta(\gamma)|$ in the combined single-lepton and dilepton channel for $t\bar{t}\gamma$ production measurement.

Table 11.2: χ^2/ndf and p-values between the measured absolute and normalised cross-sections of $t\bar{t}\gamma$ production and the NLO MadGraph5_aMC@NLO simulations interfaced with Pythia 8 and Herwig 7.

	Absolute cross-sections				Normalised cross-sections			
	MG5_aMC@NLO+Pythia 8		MG5_aMC@NLO+Herwig 7		MG5_aMC@NLO+Pythia 8		MG5_aMC@NLO+Herwig 7	
Variables	χ^2/ndf	p-value	χ^2/ndf	p-value	χ^2/ndf	p-value	χ^2/ndf	p-value
Single-lepton and dilepton combined								
p_{T} (γ)	10.7/10	0.38	9.3/10	0.50	11.6/9	0.23	8.6/9	0.47
$\lvert\eta\rvert$(γ)	15.8/8	0.04	14.2/8	0.08	10.2/7	0.18	10.0/7	0.19

11.3 Inclusive $t\bar{t}\gamma$ production and decay measurement

This section presents the results of the measurement of the total $t\bar{t}\gamma$ production and decay process. Unlike the $t\bar{t}\gamma$ production process, photons originating from the top quark decay products are considered as signal. This means that photons can originate from the charged leptons, W bosons, or quarks before they form hadrons. Photons originating from hadron decay are not considered as mentioned in the fiducial phase space definition Section 10.1.

The analysis strategy is similar to the $t\bar{t}\gamma$ production process, the changes come in constructing the signal template, which is now constructed by summing up the $t\bar{t}\gamma$ production template and $t\bar{t}\gamma$ decay template. The migration and response matrices are also constructed using $t\bar{t}\gamma$ production and $t\bar{t}\gamma$ decay events.

The distributions at particle level are shown in Figures 11.14 and A.14 for the single-lepton and dilepton channels, respectively. The migration matrices for the $p_{\mathrm{T}}(\gamma)$ distribution are shown in Figures A.15 and A.16 for the single-lepton and dilepton channels, respectively. Approximately 5% of the events migrate from one bin to the neighboring bin.

The $p_{\mathrm{T}}(\gamma)$ distribution in data is compared with the expected MC in the single-lepton and dilepton channels in Figures A.17 and A.18 respectively. The signal template at the reconstruction level is obtained by folding the truth distribution with the response matrix. The distribution at the reconstruction level is compared with the one created by folding and there are no discrepancies observed. This validates the correctness of the response matrix construction. The likelihood is obtained using the signal template at particle level, the response matrices, and the background templates at reconstruction level (as described in Section 10.2). Before the profile likelihood unfolding is performed on the real data to measure the differential cross-section, the fit is performed on the pseudo-data to check the behavior of the nuisance parameters in the fit. Additionally, unfolding tests, including closure tests and stress tests as introduced in Section 10.7, are performed to validate the technical implementation of the unfolding method and to ensure it is unbiased with respect to the inputs used.

After validating the statistical model with pseudo-data, the model is fit with the real data. The resulting post-fit distributions shown for $p_{\mathrm{T}}(\gamma)$ measurement in Figure 11.15 for the single-lepton channel and in Figure 11.16 for the dilepton channel. The post-fit values of the nuisance parameters are well within one standard deviation of the pre-fit uncertainties. Most of the nuisance parameters are either unconstraint or only marginally constraint. The $t\bar{t}\gamma$ decay cross-section uncertainty is constraint by about 50%, largely due to an initially assigned 20% cross-section uncertainty. This reduction in post-fit uncertainty is

observed in both channels. The correlations among the nuisance parameters and the signal strengths are shown in Figures A.19 and A.20 for the $p_{\mathrm{T}}(\gamma)$ measurement in the single-lepton and dilepton channels, respectively. The ranking of the nuisance parameters based on pre-fit and post-fit impact is shown in Figures 11.17 and 11.18 for $p_{\mathrm{T}}(\gamma)$ measurement in the single-lepton and dilepton channels, respectively. The uncertainties that impact the measurement most are $t\bar{t}\gamma$ decay cross-section uncertainty, jet pileup uncertainty, jet flavor composition uncertainty, $t\bar{t}\gamma$ decay parton shower uncertainty, $t\bar{t}\gamma$ production parton shower uncertainty, and uncertainties related to fake lepton estimation.

The measured differential cross-sections at particle level are shown in Figures 11.19 and 11.20 in the single-lepton channel, and in Figures 11.21, 11.22, A.21 and A.22 in the dilepton channel. The normalized cross-sections are shown side by side. The measured cross-sections are compared with the simulation of $t\bar{t}\gamma$ process performed at the LO in QCD. These MC samples are generated using MadGraph5_aMC@NLO interfaced with NNPDF2.3LO PDF set and interfaced with Pythia 8 or Herwig 7 for parton showering. These events were generated as a doubly resonant $2 \to 7$ process. The diagrams where the photon is radiated from the initial state, from the intermediate top quarks, b-quarks, the intermediate W bosons, and from the decay products of the W bosons, were included. These samples are scaled to NLO prediction using the K-factors derived in [20].

In the single-lepton channel, the measured cross-section is slightly higher than the MC prediction whereas in the dilepton channel the measurement aligns with the MC prediction within uncertainty. The shapes of ΔR and $|\eta|$ distributions are well described by the MC prediction while the description of the p_{T} distributions by the LO simulation is poor. As seen in the $t\bar{t}\gamma$ production measurement, the $\Delta\phi(\ell,\ell)$ distribution shows a shape discrepancy between data and MC.

The compatibility between the measured data and the MC prediction is quantified using the χ^2/ndf and p-values, which are shown in Table 11.3. On average p-values corresponding to the LO $2 \to 7$ simulation are lower than those for the MadGraph5_aMC@NLO simulation showing a somewhat poorer description of the data provided by the LO simulation.

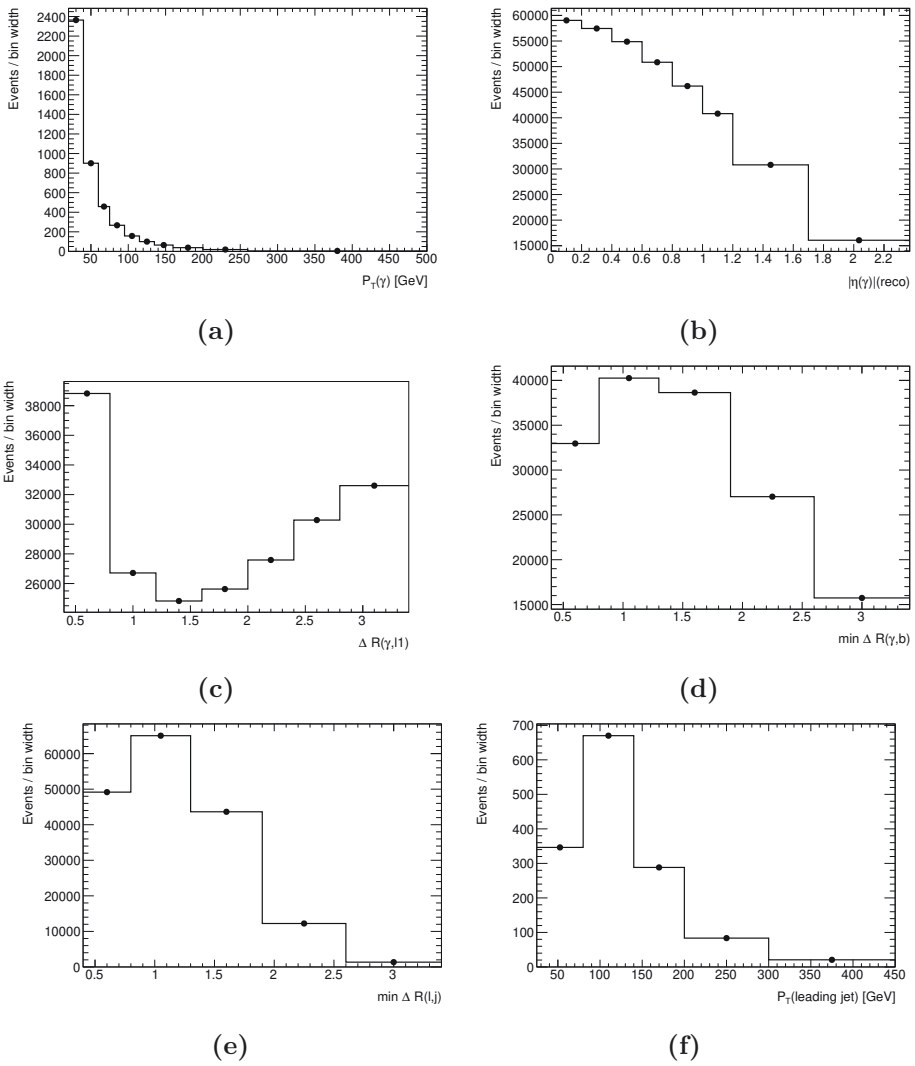

Figure 11.14: Particle level distributions of total $t\bar{t}\gamma$ production and decay as a function of $p_{\mathrm{T}}(\gamma)$ (a), $|\eta|(\gamma)$ (b), $\Delta R(\gamma, \ell)$ (c), $\Delta R(\gamma, b)_{\mathrm{min}}$ (d), $\Delta R(\ell, j)_{\mathrm{min}}$ (e), and $p_{\mathrm{T}}(j_1)$ (f) in the single-lepton channel. The number of events corresponds to the expected number of events at the particle level normalized to the luminosity of data. Overflow events are included in the last bin of the corresponding distribution. Note that values are divided by bin width.

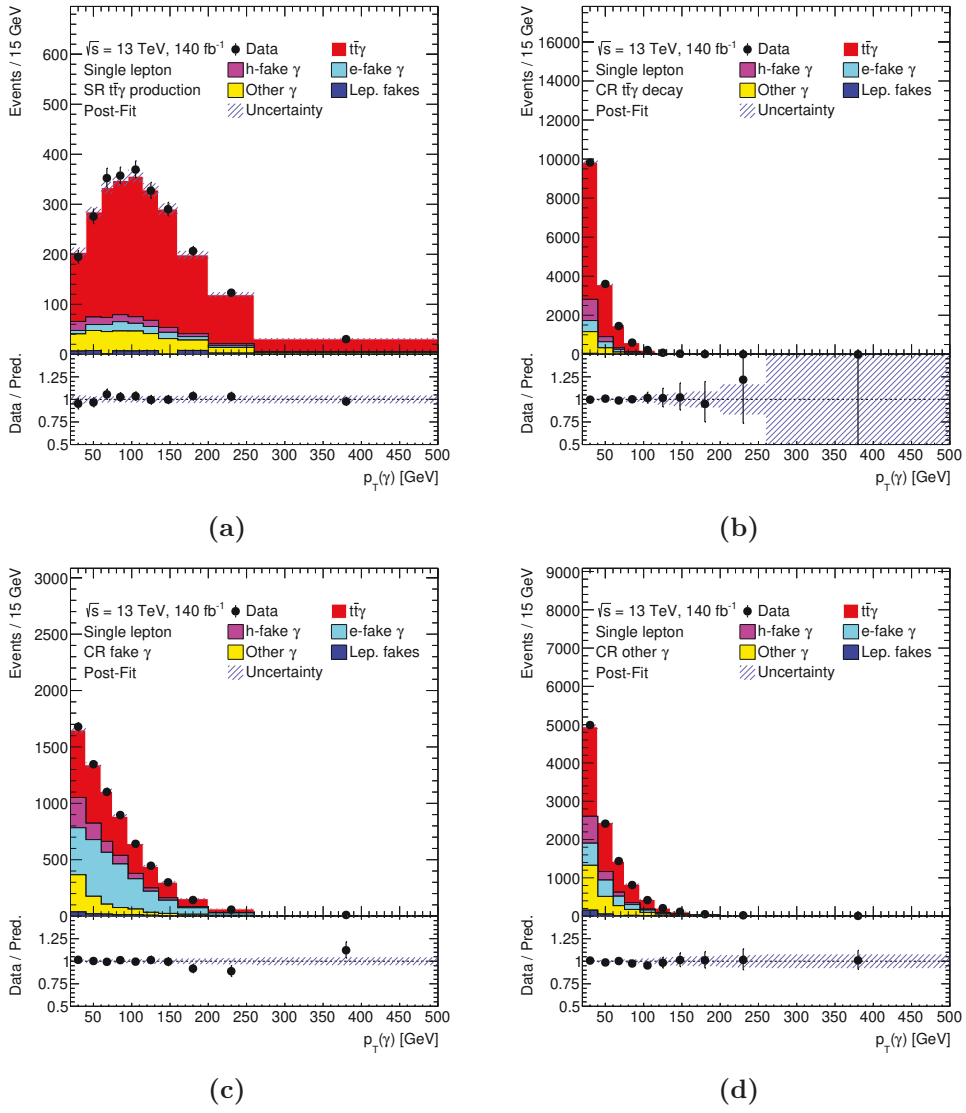

Figure 11.15: Post-fit distributions of $p_{\mathrm{T}}(\gamma)$ in the SR and CRs: (a) $t\bar{t}\gamma$ production enriched region, (b) $t\bar{t}\gamma$ decay enriched region, (c) fakes enriched region, and (d) prompt photon enriched region in single lepton channel. The lower panels show the ratio of the data to the prediction. The error bars on the data points represent the statistical uncertainties, while the shaded bands represent the statistical and systematic uncertainties of the post-fit prediction. The last bin includes overflow events.

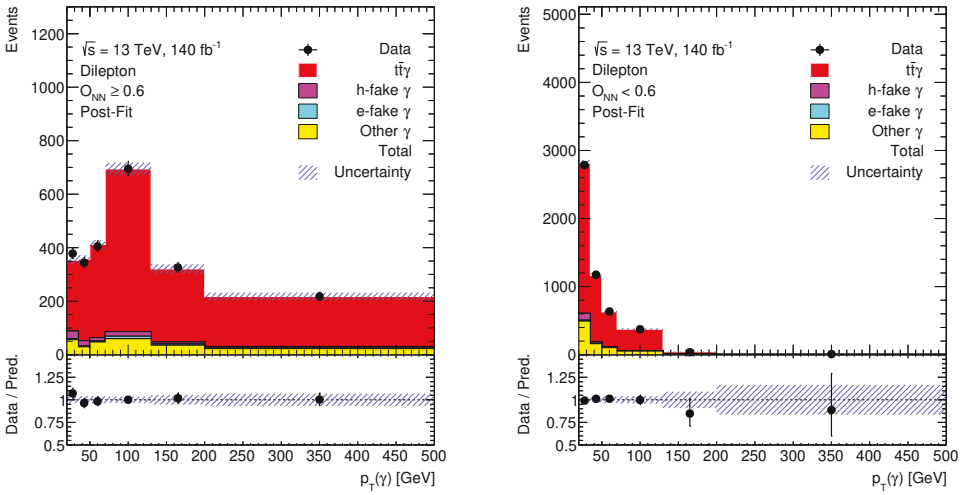

(a) **(b)**

Figure 11.16: Post-fit distributions of $p_{\mathrm{T}}(\gamma)$ in the regions (a) $O_{NN} >= 0.6$, (b) $O_{NN} < 0.6$ in dilepton channel. The lower panels show the ratio of the data to the prediction. The error bars on the data points represent the statistical uncertainties, while the shaded bands represent the statistical and systematic uncertainties of the post-fit prediction. The last bin includes overflow events.

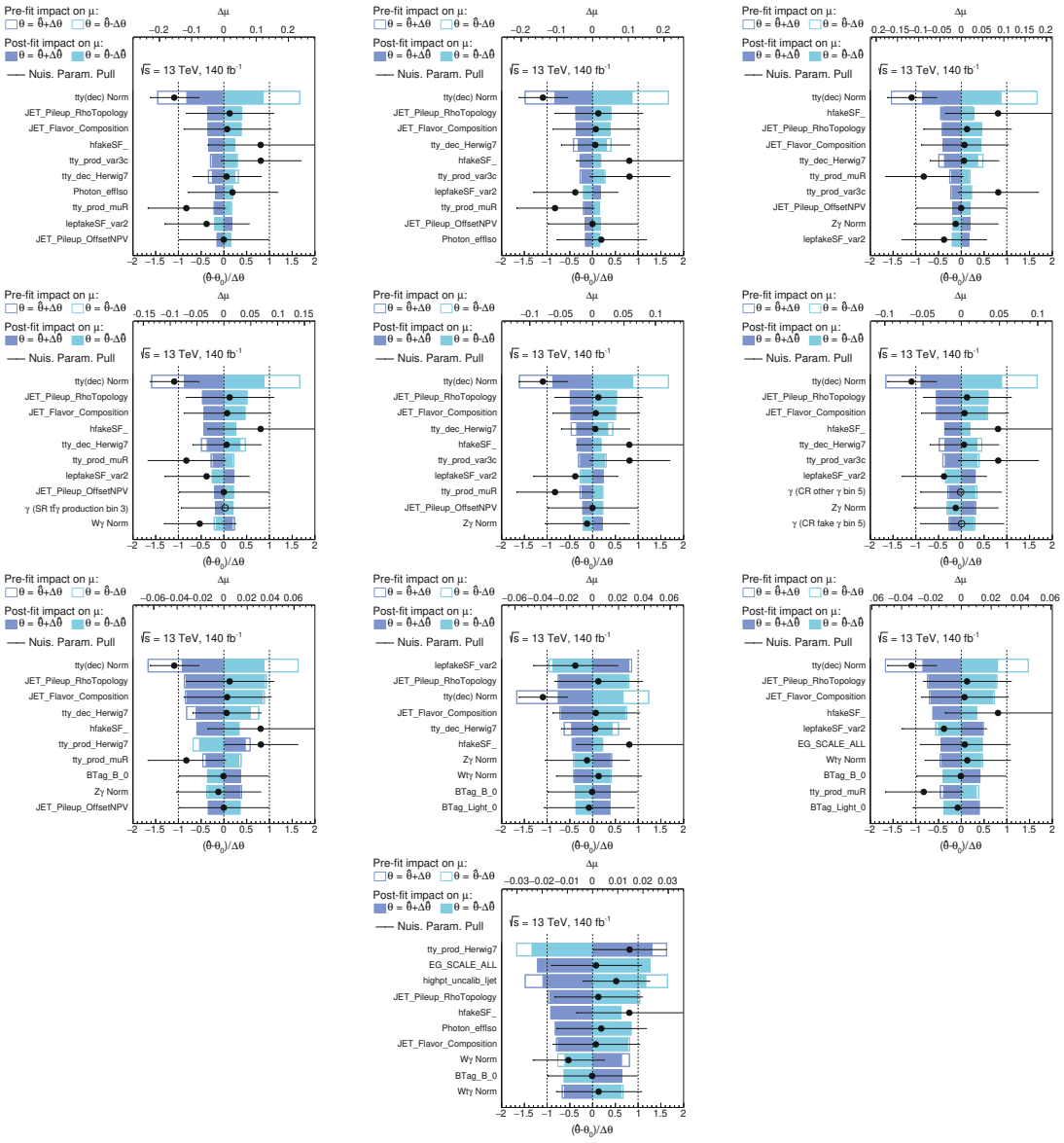

Figure 11.17: Ranking of the 10 leading systematic uncertainties included in the profile likelihood unfolding used for the $p_{\mathrm{T}}(\gamma)$ cross-section measurement in single-lepton channel. The blue and turquoise bands represent the post-fit impact on the measured cross-section in each bin, while the outlined blue and turquoise rectangles show the pre-fit impact. The difference between these two indicates the constraint of the nuisance parameter due to correlations in the fit. Most nuisance parameters are either unconstraint or only marginally constraint. The impact is overlaid with the post-fit values of the nuisance parameters (pulls), shown by the black dots. The black lines represent the post-fit uncertainties normalized to the pre-fit uncertainties. Each subfigure, corresponds to a specific bin of the $p_{\mathrm{T}}(\gamma)$ distribution, starting from bin 1 till bin 10 (from left to right and top to bottom).

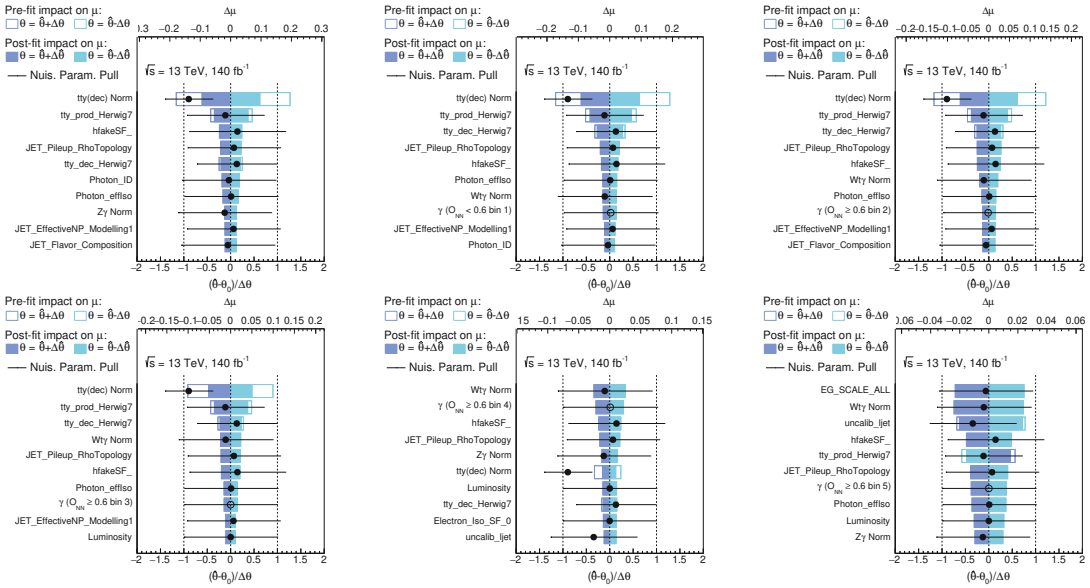

Figure 11.18: The ranking of systematic uncertainties included in the profile likelihood unfolding used for the $p_{\mathrm{T}}(\gamma)$ cross-section measurement in dilepton channel is shown. The blue and turquoise bands represent the post-fit impact on the fit result, while the outlined blue and turquoise rectangles show the pre-fit impact. The difference between these two indicates the constraint of the nuisance parameter due to correlations in the fit. Most nuisance parameters are either unconstraint or only marginally constraint. The impact is overlaid with the post-fit values of the nuisance parameters (pulls), shown by the black dots. The black lines represent the post-fit uncertainties normalized to the pre-fit uncertainties. Each subfigure, corresponds to a specific bin of the $p_{\mathrm{T}}(\gamma)$ distribution, starting from bin 1 till bin 6 (from left to right and top to bottom).

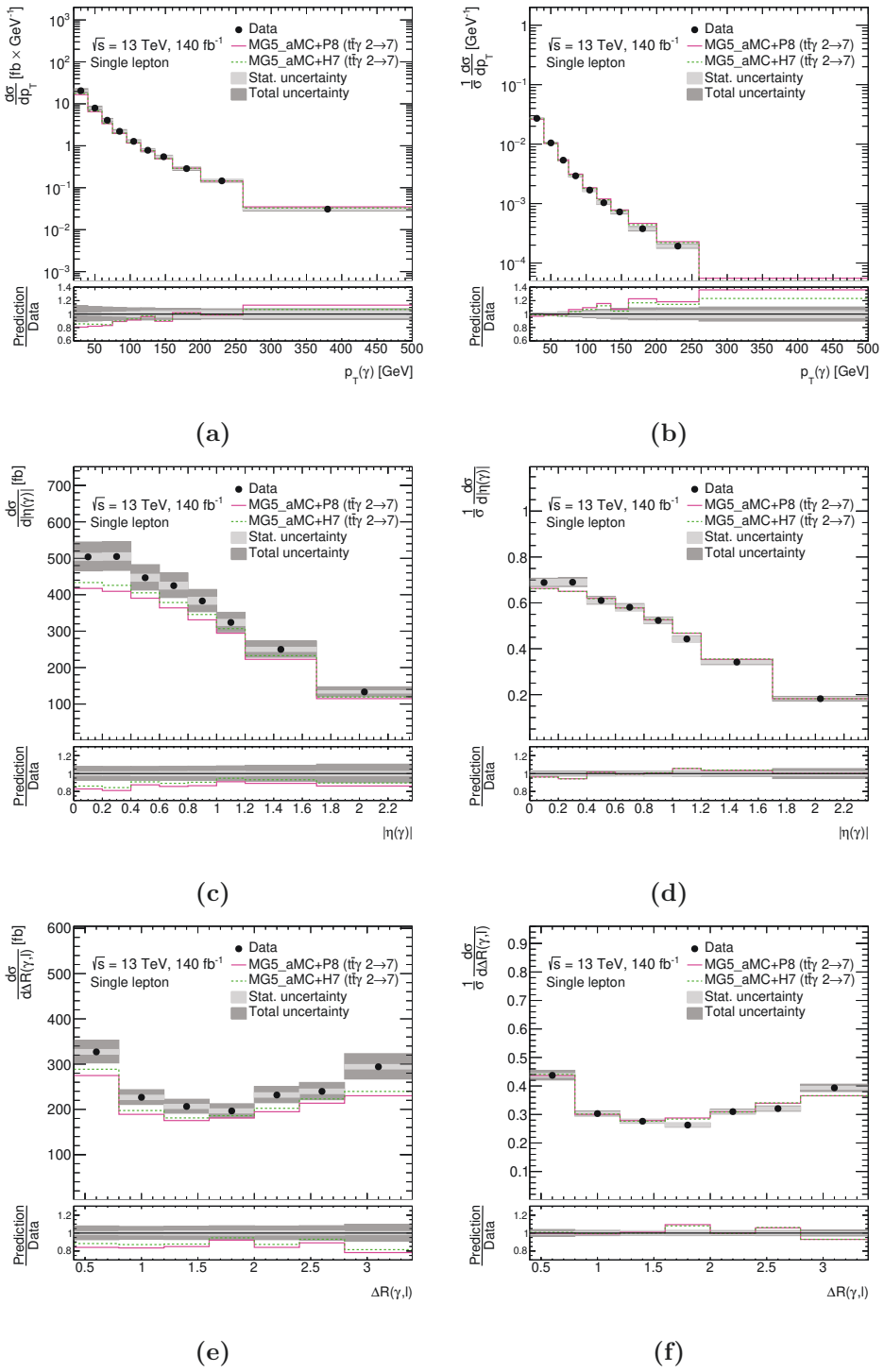

Figure 11.19: Absolute (left) and normalized (right) differential cross-sections of total $t\bar{t}\gamma$ production and decay in the single-lepton fiducial phase space at particle level as a function of $p_{\mathrm{T}}(\gamma)$ (a, b), $|\eta(\gamma)|$ (c, d), $\Delta R(\gamma, \ell)$ (e, f). Data are compared with LO $2 \to 7$ MadGraph5_aMC@NLO simulation interfaced with Pythia 8 and Herwig 7. The last bin includes overflow events.

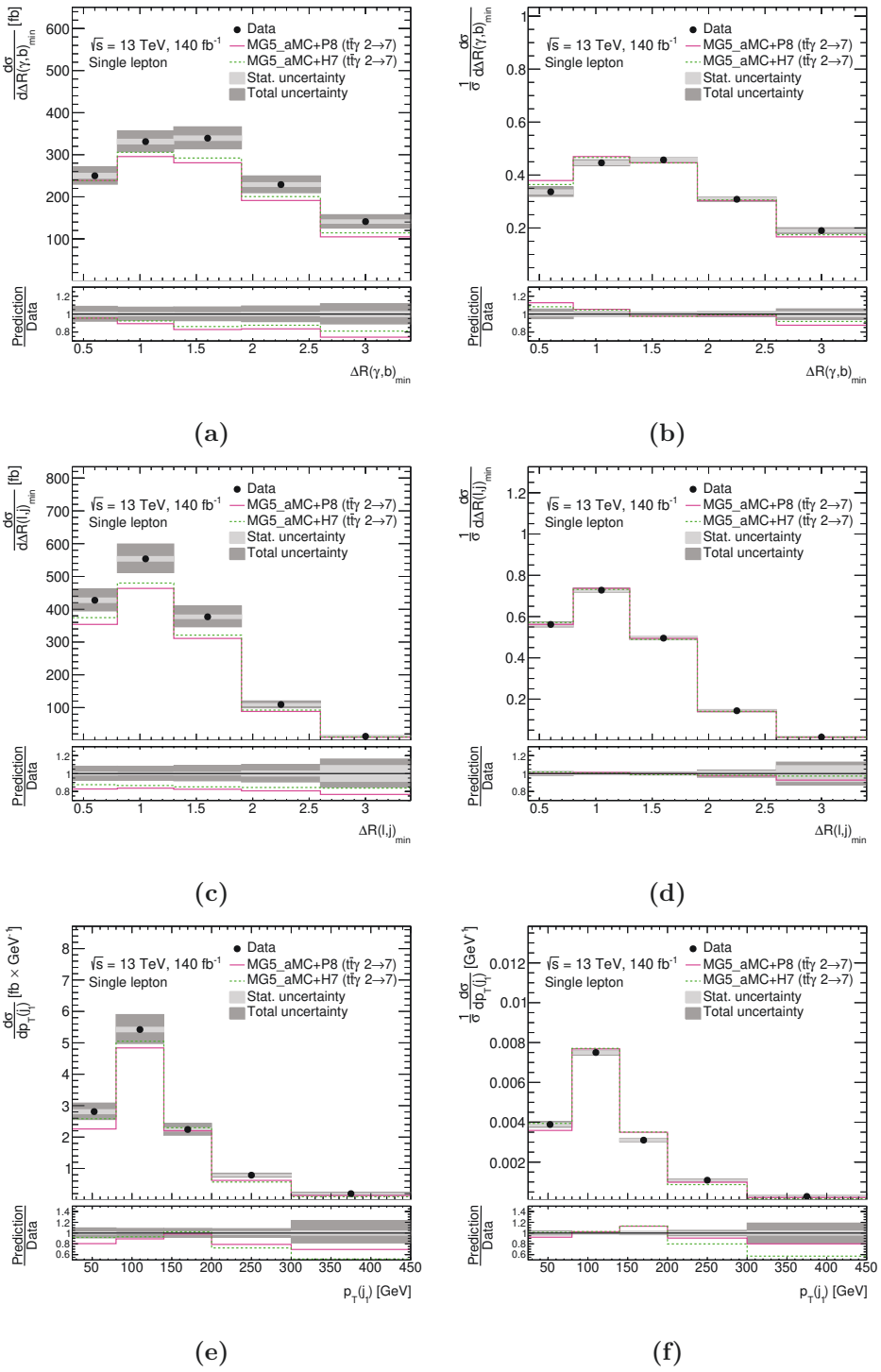

Figure 11.20: Absolute (left) and normalized (right) differential cross-sections of total $t\bar{t}\gamma$ production and decay in the single-lepton fiducial phase space at particle level as a function of $\Delta R(\gamma, b)$ (a, b), $\Delta R(\ell, j)$min (c, d), and $p_{\mathrm{T}}(j_1)$ (e, f). Data are compared with LO $2 \to 7$ MadGraph5_aMC@NLO simulation interfaced with Pythia 8 and Herwig 7. The last bin includes overflow events.

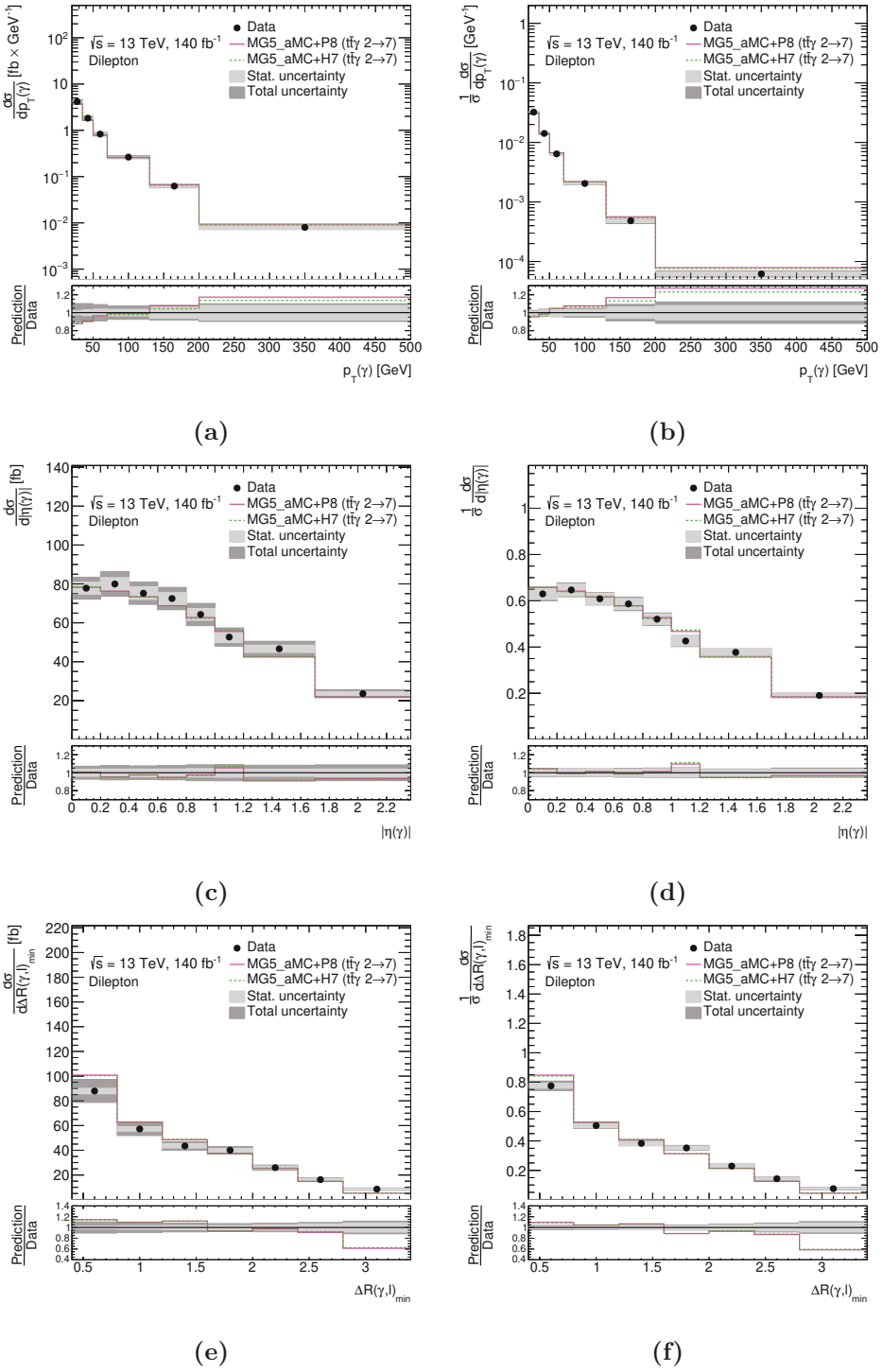

Figure 11.21: Absolute (left) and normalized (right) differential cross-sections of total $t\bar{t}\gamma$ production and decay in the dilepton fiducial phase space at particle level as a function of $p_{\mathrm{T}}(\gamma)$ (a, b), $|\eta(\gamma)|$ (c, d), $\Delta R(\gamma, \ell)_{\mathrm{min}}$ (e, f). Data are compared with LO $2 \to 7$ MadGraph5_aMC@NLO simulation interfaced with Pythia 8 and Herwig 7. The last bin includes overflow events.

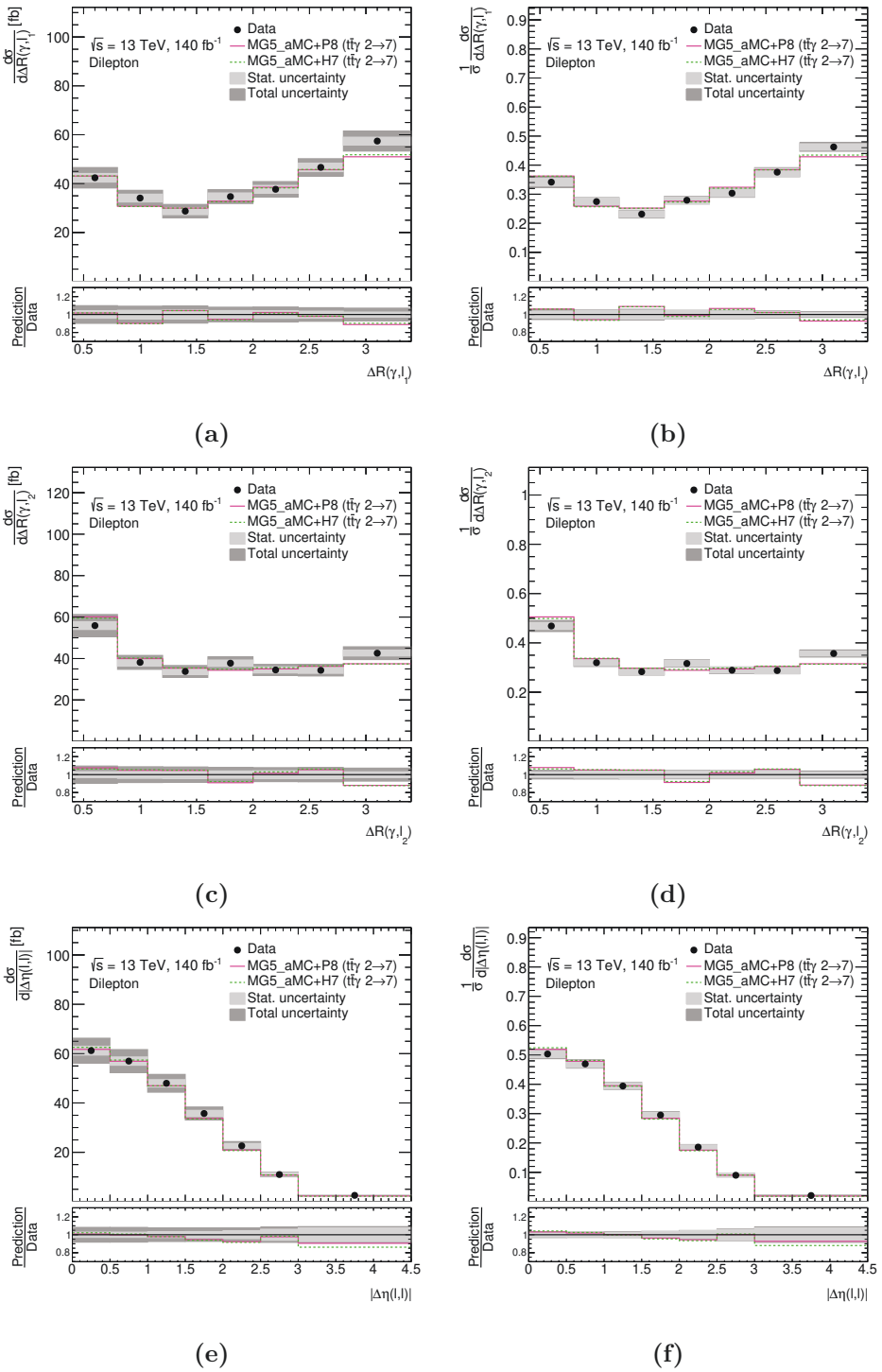

Figure 11.22: Absolute (left) and normalized (right) differential cross-sections of total $t\bar{t}\gamma$ production and decay in the dilepton fiducial phase space at particle level as a function of $\Delta R(\gamma, \ell_1)$ (a, b), $\Delta R(\gamma, \ell_2)$ (c, d), and $|\Delta\eta(\ell, \ell)|$ (e, f). Data are compared with LO $2 \to 7$ MadGraph5_aMC@NLO simulation interfaced with Pythia 8 and Herwig 7. The last bin includes overflow events.

Table 11.3: χ^2/ndf and p-values between the measured absolute and normalised cross-sections of the total $t\bar{t}\gamma$ production and decay process and the LO $2 \to 7$ MadGraph5_aMC@NLO simulation interfaced with Pythia 8 and Herwig 7.

	Absolute cross-sections				Normalised cross-sections			
	MG5_aMC@NLO+Pythia 8		MG5_aMC@NLO+Herwig 7		MG5_aMC@NLO+Pythia 8		MG5_aMC@NLO+Herwig 7	
Variables	χ^2/ndf	p-value	χ^2/ndf	p-value	χ^2/ndf	p-value	χ^2/ndf	p-value
Single-lepton channel								
p_{T} (γ)	12.6/10	0.25	8.5/10	0.58	21.2/9	0.01	12.1/9	0.21
$\lvert\eta\rvert(\gamma)$	13.5/8	0.10	13.3/8	0.10	12.0/7	0.10	12.9/7	0.08
$\Delta R(\gamma,\ell)$	15.3/7	0.03	14.0/7	0.05	13.8/6	0.03	18.6/6	< 0.01
$\Delta R(\gamma,b)_{\mathrm{min}}$	8.9/5	0.11	6.2/5	0.29	9.3/4	0.05	6.0/4	0.20
$\Delta R(\ell,j)_{\mathrm{min}}$	4.9/5	0.43	3.1/5	0.68	0.8/4	0.93	0.8/4	0.94
$p_{\mathrm{T}}(j_1)$	25.4/5	< 0.01	43.0/5	< 0.01	27.2/4	< 0.01	45.0/4	< 0.01
Dilepton channel								
p_{T} (γ)	7.6/6	0.27	4.9/6	0.56	6.7/5	0.24	4.7/5	0.45
$\lvert\eta\rvert(\gamma)$	5.2/8	0.73	6.0/8	0.64	5.4/7	0.61	6.3/7	0.50
$\Delta R(\gamma,\ell)_{\mathrm{min}}$	23.6/7	< 0.01	22.8/7	< 0.01	20.1/6	< 0.01	19.6/6	< 0.01
$\Delta R(\gamma,\ell_1)$	10.1/7	0.18	8.8/7	0.27	9.8/6	0.13	8.5/6	0.21
$\Delta R(\gamma,\ell_2)$	14.8/7	0.04	15.1/7	0.03	14.3/6	0.03	14.7/6	0.02
$\lvert\Delta\eta(\ell,\ell)\rvert$	3.9/7	0.79	6.7/7	0.46	3.1/6	0.80	5.5/6	0.48
$\Delta\phi(\ell,\ell)$	35.4/8	< 0.01	37.8/8	< 0.01	35.3/7	< 0.01	37.5/7	< 0.01
$p_{\mathrm{T}}(\ell,\ell)$	6.7/6	0.35	12.9/6	0.04	5.9/5	0.32	11.5/5	0.04
$\Delta R(\gamma,b)_{\mathrm{min}}$	1.8/5	0.87	3.7/5	0.59	1.8/4	0.77	3.7/4	0.45
$\Delta R(\ell,j)_{\mathrm{min}}$	6.1/5	0.30	9.2/5	0.10	10.0/4	0.04	12.8/4	0.01
$p_{\mathrm{T}}(j_1)$	10.8/5	0.05	19.2/5	< 0.01	9.8/4	0.04	17.6/4	< 0.01

11.4 Comparison to previous measurements

Only the total $t\bar{t}\gamma$ production and decay cross-section can be compared with other experiments because the $t\bar{t}\gamma$ production cross-section is measured for the first time in this work. The total $t\bar{t}\gamma$ production and decay cross-section is compared with the ATLAS measurement at $\sqrt{s} = 13$ TeV [20] performed with 36 fb^{-1} of data in the single-lepton and dilepton channels, and the CMS measurement at $\sqrt{s} = 13$ TeV [120] with 138 fb^{-1} in the dilepton channel. The previous ATLAS analysis only measured the normalized differential cross-section, while CMS measured both absolute and normalized differential cross-sections.

Both measurements compare the results with the LO $2 \to 7$ MadGraph5_aMC@NLO prediction interfaced with Pythia 8 and Herwig 7. These measurements cannot be directly compared due to different fiducial phase space definitions, but the agreement with the SM prediction can be qualitatively compared. In general, similar agreement and trends are observed between measurement and prediction across all observables when compared with CMS results. This is especially noticeable in the normalized differential cross-sections; the shape agreement/disagreement has a similar trend for $\Delta R(\gamma, \ell)_{\text{min}}$, $\Delta R(\gamma, \ell_1)$, $\Delta R(\gamma, \ell_2)$, $\Delta R(\ell, j)_{\text{min}}$, $\Delta\phi(\ell, \ell)$, and $p_{\text{T}}(j_1)$. The trend in $\Delta\phi(\ell, \ell)$ distribution is also seen in both ATLAS measurements.

It is important to mention that the different fiducial phase space definitions used in these measurements may impact the observed trends, especially for observables that depend on kinematic selection criteria.

11.5 EFT interpretations

As introduced in Section 2.3, the $t\bar{t}\gamma$ differential cross-section measured in this thesis is used to set limits on the Wilson coefficients of the dimension-six operators as detailed in Ref. [24]. While these EFT interpretations are not part of the author's work, a brief overview of the results, taken from Ref. [24], is provided here for completeness.

The operators that modify the top quark and photon vertex are C_{tW} and C_{tB}, which are dimension-six operators. The photon p_{T} spectrum is the most sensitive observable to these Wilson coefficients. Figure 11.23 shows how the photon p_{T} spectrum changes with the Wilson coefficients.

Using the measured p_{T} distribution Figure 11.12(a), the limits on the Wilson coefficients are obtained with the EFTFitter tool [122]. The fit to the measured cross-section is performed simultaneously, keeping the real and imaginary parts of the Wilson coefficients

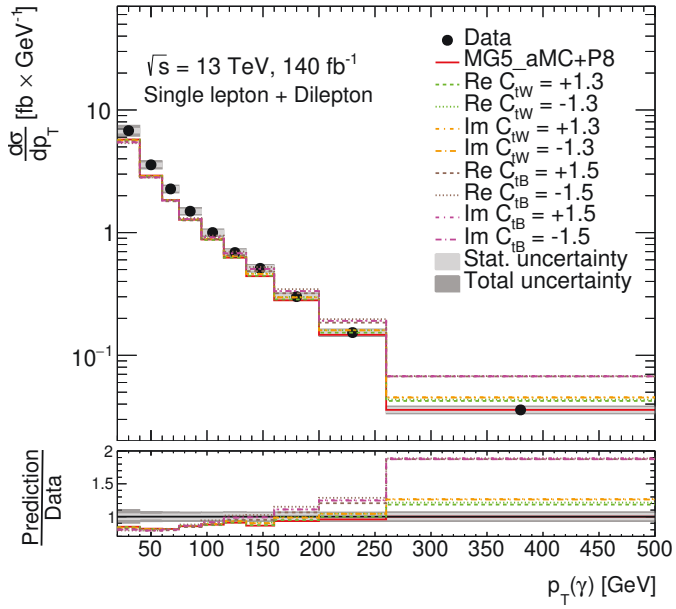

Figure 11.23: Comparison of the photon p_{T} distribution from the measurement in combined single-lepton and dilepton channels with the SM prediction and for different values of the Wilson coefficients.

freely floating. The best-fit value and the 68% and 95% credible intervals are obtained. These values and boundaries are projected in a plane to obtain marginalized limits and are shown in Figure 11.24. The best-fit value agrees well with the SM prediction and a limit is set on the Wilson coefficients.

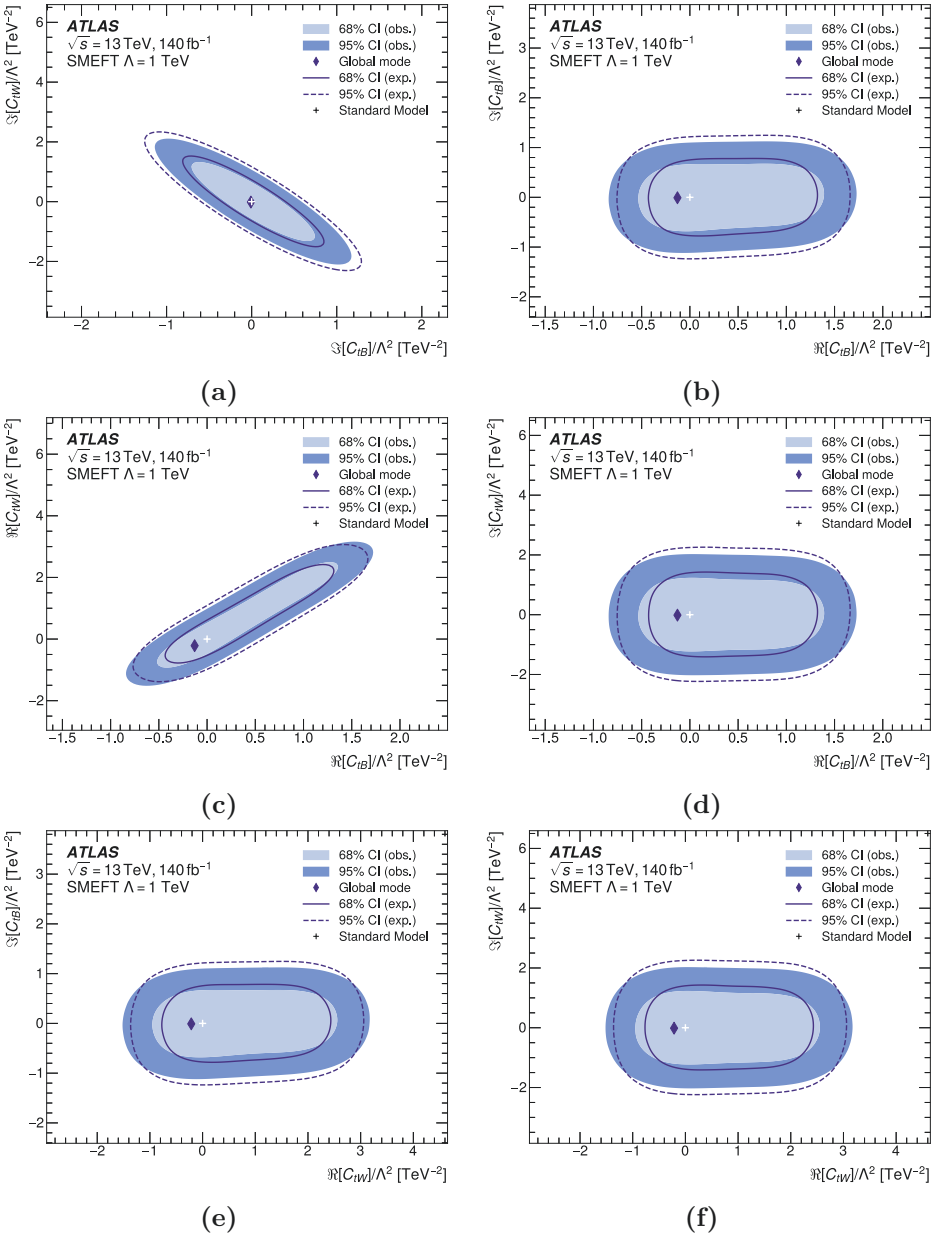

Figure 11.24: The 2D posterior marginalized posteriors of the Wilson coefficients indicating the 68% and 95% credible intervals. The limits are extracted using the measured photon p_{T} distribution Figure 11.12(a). The plots show the marginalized limits on the Wilson coefficients: (a) C_{tB}^{Im} vs. C_{tW}^{Im}, (b) C_{tB}^{Re} vs. C_{tB}^{Im}, (c) C_{tB}^{Re} vs. C_{tW}^{Re}, (d) C_{tB}^{Re} vs. C_{tW}^{Im}, (e) C_{tW}^{Re} vs. C_{tB}^{Im}, and (f) C_{tW}^{Re} vs. C_{tW}^{Im}, taken from [24].

12 Summary

In this thesis, a measurement of the differential cross-sections of the $t\bar{t}\gamma$ process was presented using proton-proton collision data at a center-of-mass energy of 13 TeV collected by the ATLAS detector during Run 2 operation (2015-2018). The top quark and photon coupling was probed through the $t\bar{t}\gamma$ process and tested against the predictions of the Standard Model. A total of 140.1 fb^{-1} of integrated luminosity was analyzed, and the events were categorized into single-lepton and dilepton channels based on the decay products of the top quarks. To enhance sensitivity to the top quark and photon coupling, a dedicated measurement focused on separating $t\bar{t}\gamma$ production from $t\bar{t}\gamma$ decay was performed for the first time.

Data-driven techniques were employed to estimate backgrounds from misidentified electrons as photons, and from non-prompt leptons. The electron-fake photon background was estimated using a tag-and-probe method in a $Z \to ee$ control region, while the non-prompt lepton background was estimated using matrix method.

The differential cross-section of the $t\bar{t}\gamma$ production process was measured as a function of various observables related to the kinematic properties of the photon, the angular separation between the photon and the leptons, the kinematic properties of the jet, and the separation between the leptons. The measurement was performed at particle level within a fiducial phase space volume defined to closely match the detector acceptance. To correct detector effects, a profile likelihood unfolding method was implemented. This involved constructing response matrices that captured the migration of events from the particle level to the reconstruction level. The results were compared to theoretical predictions obtained from MadGraph5_aMC@NLO simulations interfaced with Pythia8 and Herwig7 parton showering.

Overall, the measured cross-sections were found to be in good agreement with the theoretical predictions within the uncertainties of the measurement. The dominant source of uncertainty in the single-lepton channel came from the normalization of the background processes with prompt photon emission, jet energy scale uncertainties, and $t\bar{t}\gamma$ modeling

uncertainties. In the dilepton channel, the statistical uncertainty of the data was the dominant source.

This measurement shows a slightly higher cross-section than the theoretical prediction in the low photon p_{T} region, potentially due to higher-order corrections not included in the simulation. Additionally, the inclusive $t\bar{t}\gamma$ process, taking into account photon radiation from both $t\bar{t}\gamma$ production and decay products of the top quark, was measured, providing a complete picture of photon radiation in this process. The normalized cross-sections, which emphasize shape differences between data and predictions, are also presented, showing good agreement across most observables.

The precision of the current measurement is limited by several factors. The reliance on LO simulations for the $t\bar{t}\gamma$ decay process introduces a significant uncertainty. Future analyses would benefit from dedicated next-to-leading order simulations of the $t\bar{t}\gamma$ decay process to reduce these uncertainties. Additionally, experimental uncertainties related to jet, b-tagging, and photon reconstruction contribute significantly to the total uncertainty. Better modeling of the electron-fake photon and hadron-fake photon backgrounds would also improve the precision of the measurement. Larger datasets, anticipated from future LHC runs, will also improve statistical precision, particularly in the dilepton channel. The inclusion of the fully hadronic $t\bar{t}$ decay channel, which currently presents challenges due to large QCD multijet backgrounds, could provide substantial gains in sensitivity if these backgrounds can be effectively mitigated with improved detector performance and object reconstruction algorithms in future analyses.

This work is summarized in the publication [24]. The results of this thesis contribute to our understanding of the top quark and its interactions, confirming the predictions of the Standard Model with good precision. This measurement sets the stage for future analyses with larger datasets, which could delve deeper into the top quark and photon coupling, further characterizing this interaction and potentially uncovering new physics beyond the Standard Model.

A Appendix

A.1 Additional material for the binning optimization study

This section presents the study on the choice of binning for the differential cross-section measurements. The choice of binning depends on several factors, such as the detector resolution and the available events in that bin. The study is performed for the $t\bar{t}\gamma$ production and total $t\bar{t}\gamma$ production and decay measurements. In the following plots the resolution of the observables is shown in the first row. The unfolded results (using *Asimov* data) for the tested binning obtained from the optimization procedure and final binning (adapted from binning used in [120]) are shown in the second and third rows. The uncertainty band shows only statistical uncertainty. The migration matrix showing the fraction of events that migrate from particle level to the signal region at reconstruction level for the tested and final binning is shown in the last row. In both cases, the migration of events from one bin to another is very small.

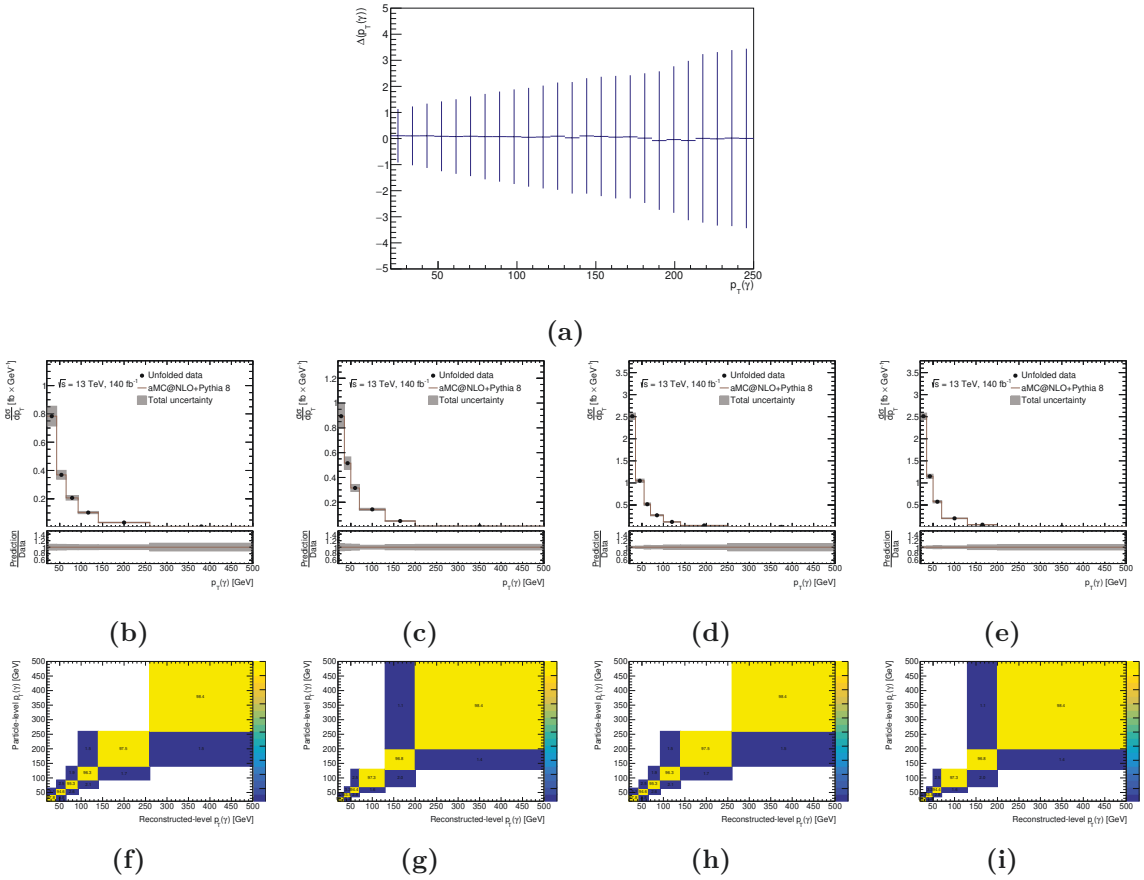

Figure A.1: (a) Resolution of the photon p_{T} observable is represented by the error bars. The y-axis is the mean of the distribution of the difference between the photon p_{T} at reconstruction and at truth level, and the error bars represent one standard deviation around that mean. Unfolded results with the tested binning (b) and final binning (c) for $t\bar{t}\gamma$ production measurement and unfolded results with the tested (d) and final (e) binning for total $t\bar{t}\gamma$ measurement, The error bar in (b), (c), (d), (e) represents statistical uncertainty only. Plots (f)- (i) represent the migration matrix in the SR for above cases.

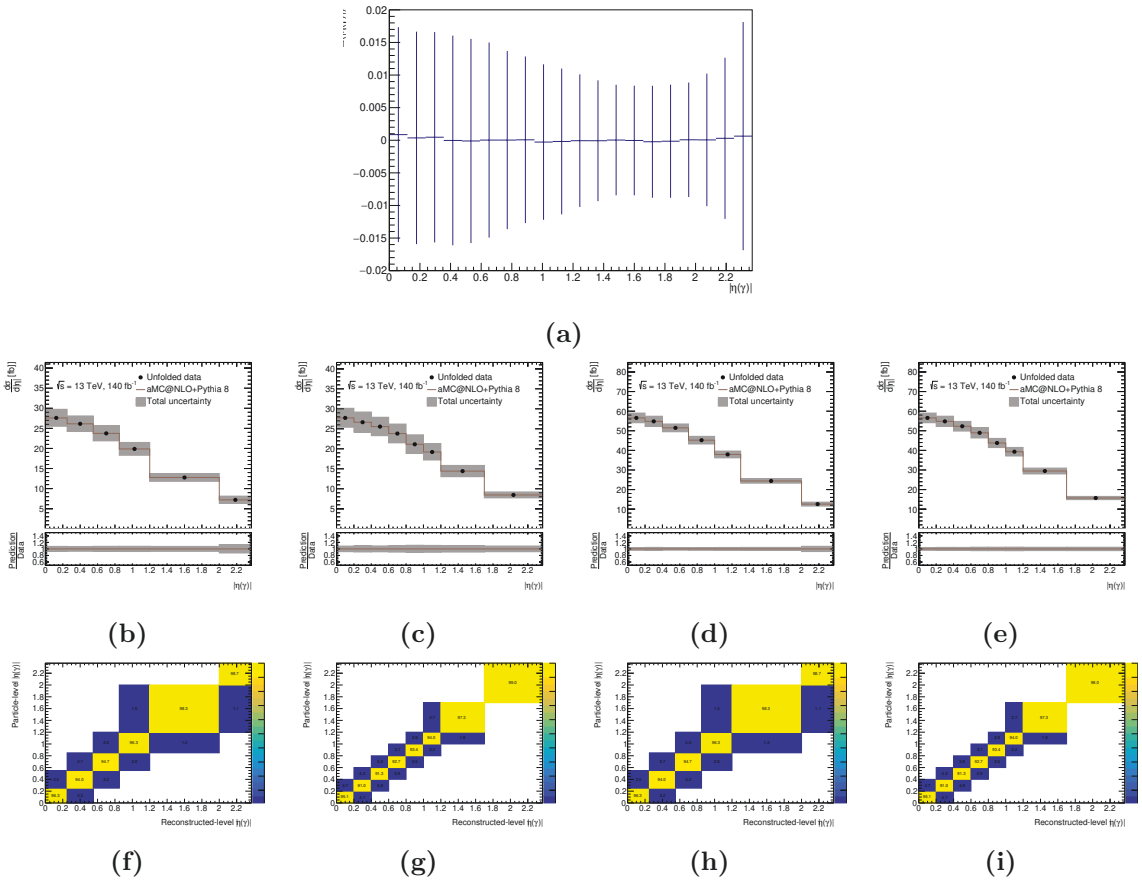

Figure A.2: (a) Resolution of the photon $|\eta(\gamma)|$ observable is represented by the error bars. The y-axis is the mean of the distribution of the difference between the $|\eta(\gamma)|$ at reconstruction and truth level, and the error bars represent one standard deviation around that mean. Unfolded results with the tested binning (b) and final binning (c) for $t\bar{t}\gamma$ production measurement and unfolded results with the tested (d) and final (e) binning for total $t\bar{t}\gamma$ measurement, The error bar in (b), (c), (d), (e) represents statistical uncertainty only. The error bar in (b), (c), (d), (e) represents statistical uncertainty only. Plots (f)- (i) represent the migration matrix in the SR for above cases.

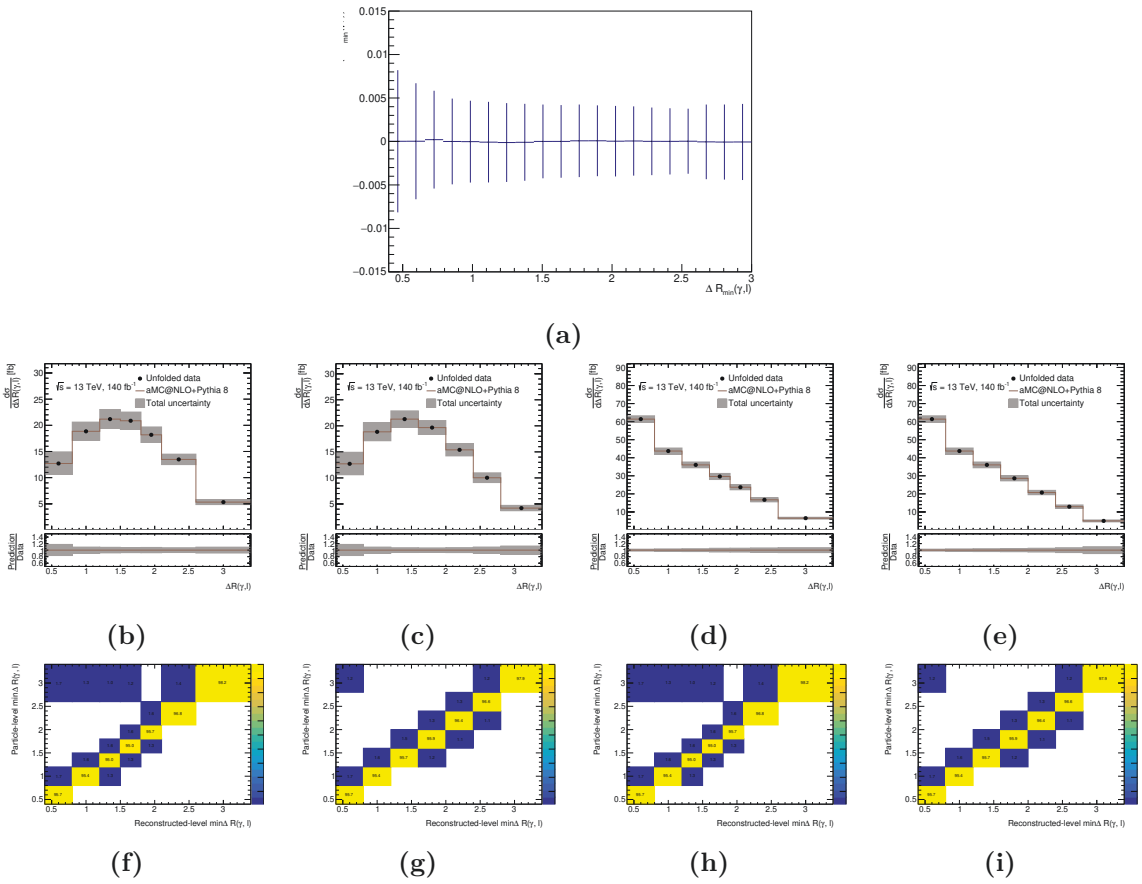

Figure A.3: (a) Resolution of the photon $\Delta R_{min}(\gamma, \ell)$ observable is represented by the error bars. The y-axis is the mean of the distribution of the difference between the $\Delta R(\gamma, \ell)_{\text{min}}$ at reconstruction and truth level, and the error bars represent one standard deviation around that mean. Unfolded results with the tested binning (b) and final binning (c) for $t\bar{t}\gamma$ production measurement and unfolded results with the tested (d) and final (e) binning for total $t\bar{t}\gamma$ measurement, The error bar in (b), (c), (d), (e) represents statistical uncertainty only. The error bar in (b), (c), (d), (e) represents statistical uncertainty only. Plots (f)- (i) represent the migration matrix in the SR for above cases.

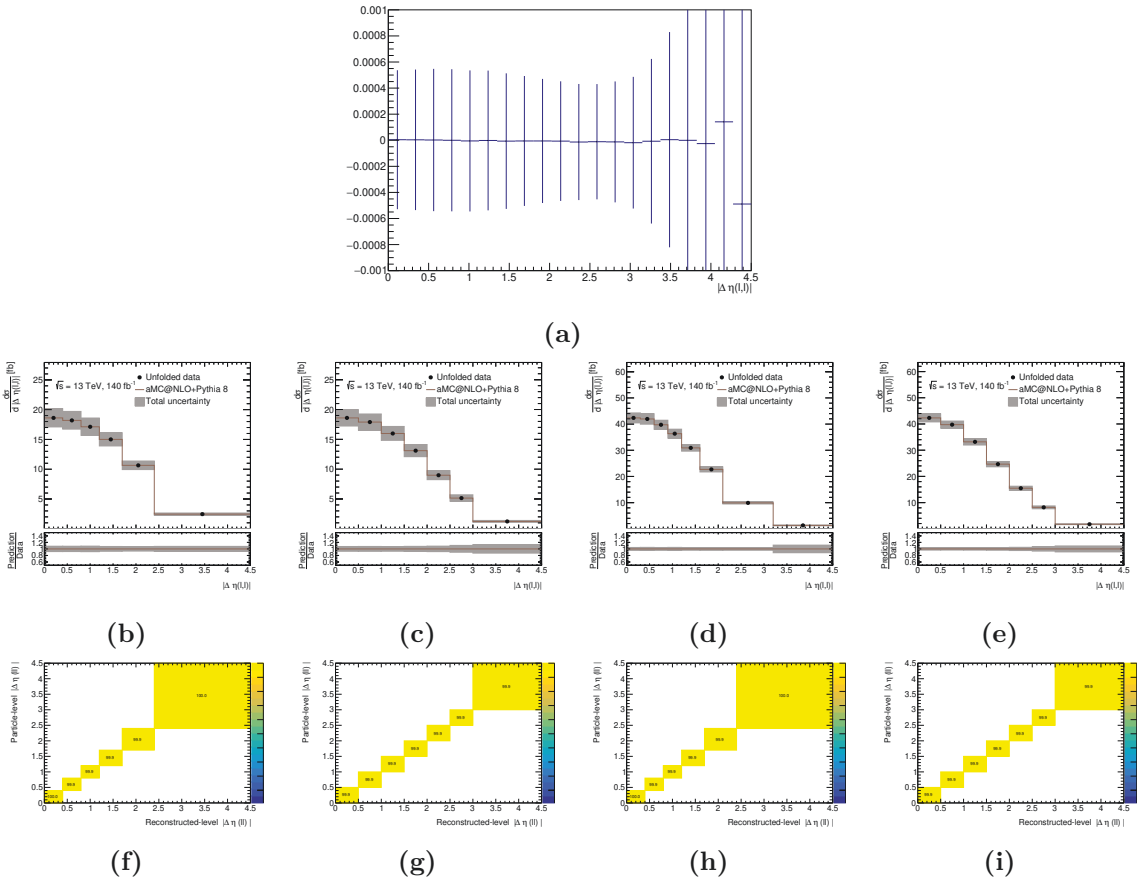

Figure A.4: (a) Resolution of the photon $|\Delta\eta(\ell,\ell)|$ observable is represented by the error bars. The y-axis is the mean of the distribution of the difference between the $|\Delta\eta(\ell,\ell)|$ at reconstruction and truth level, and the error bars represent one standard deviation around that mean. Unfolded results with the tested binning (b) and final binning (c) for $t\bar{t}\gamma$ production measurement and unfolded results with the tested (d) and final (e) binning for total $t\bar{t}\gamma$ measurement, The error bar in (b), (c), (d), (e) represents statistical uncertainty only. The error bar in (b), (c), (d), (e) represents statistical uncertainty only. Plots (f)- (i) represent the migration matrix in the SR for above cases.

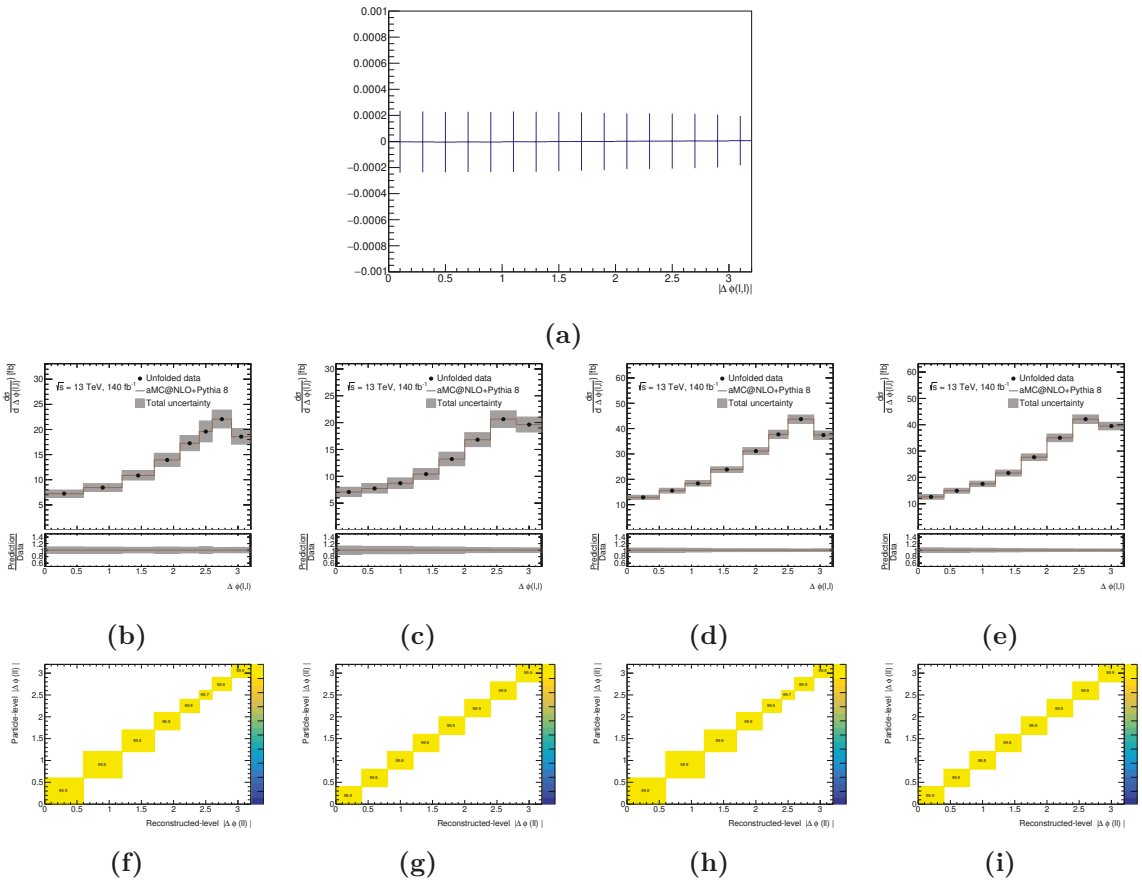

Figure A.5: (a) Resolution of the photon $\Delta\phi(\ell,\ell)$ observable is represented by the error bars. The y-axis is the mean of the distribution of the difference between the $\Delta\phi(\ell,\ell)$ at reconstruction and truth level, and the error bars represent one standard deviation around that mean. Unfolded results with the tested binning (b) and final binning (c) for $t\bar{t}\gamma$ production measurement and unfolded results with the tested (d) and final (e) binning for total $t\bar{t}\gamma$ measurement, The error bar in (b), (c), (d), (e) represents statistical uncertainty only. The error bar in (b), (c), (d), (e) represents statistical uncertainty only. Plots (f)- (i) represent the migration matrix in the SR for above cases.

A.2 Additional material for the unfolding tests

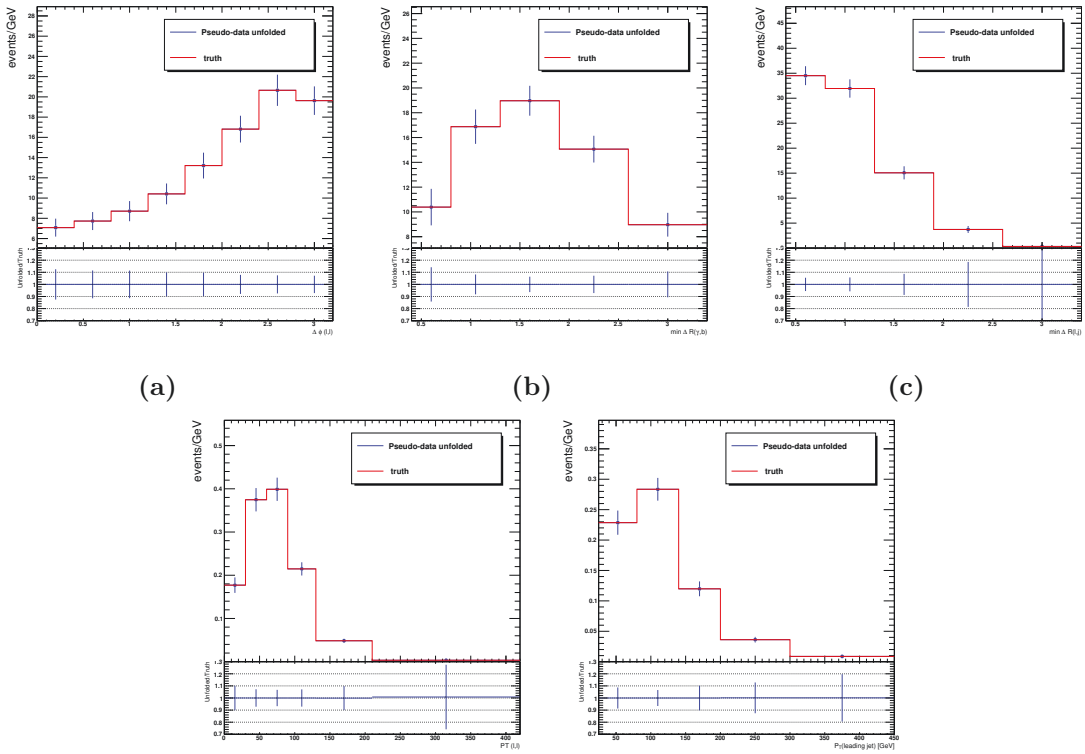

Figure A.6: Comparison of the unfolded pseudo-data (in blue) and the true distribution (in red) as a function of (a) $\Delta\phi(\ell,\ell)$, (b) $\Delta R(\gamma,b)_{\text{min}}$, (c) $\Delta R(\ell,j)_{\text{min}}$, (d) $p_T(\ell,\ell)$, and (e) $p_T(j_1)$ in the dilepton channel for $t\bar{t}\gamma$ production measurement. The uncertainty bars displayed in the plots represent only the statistical error considered in the unfolding.

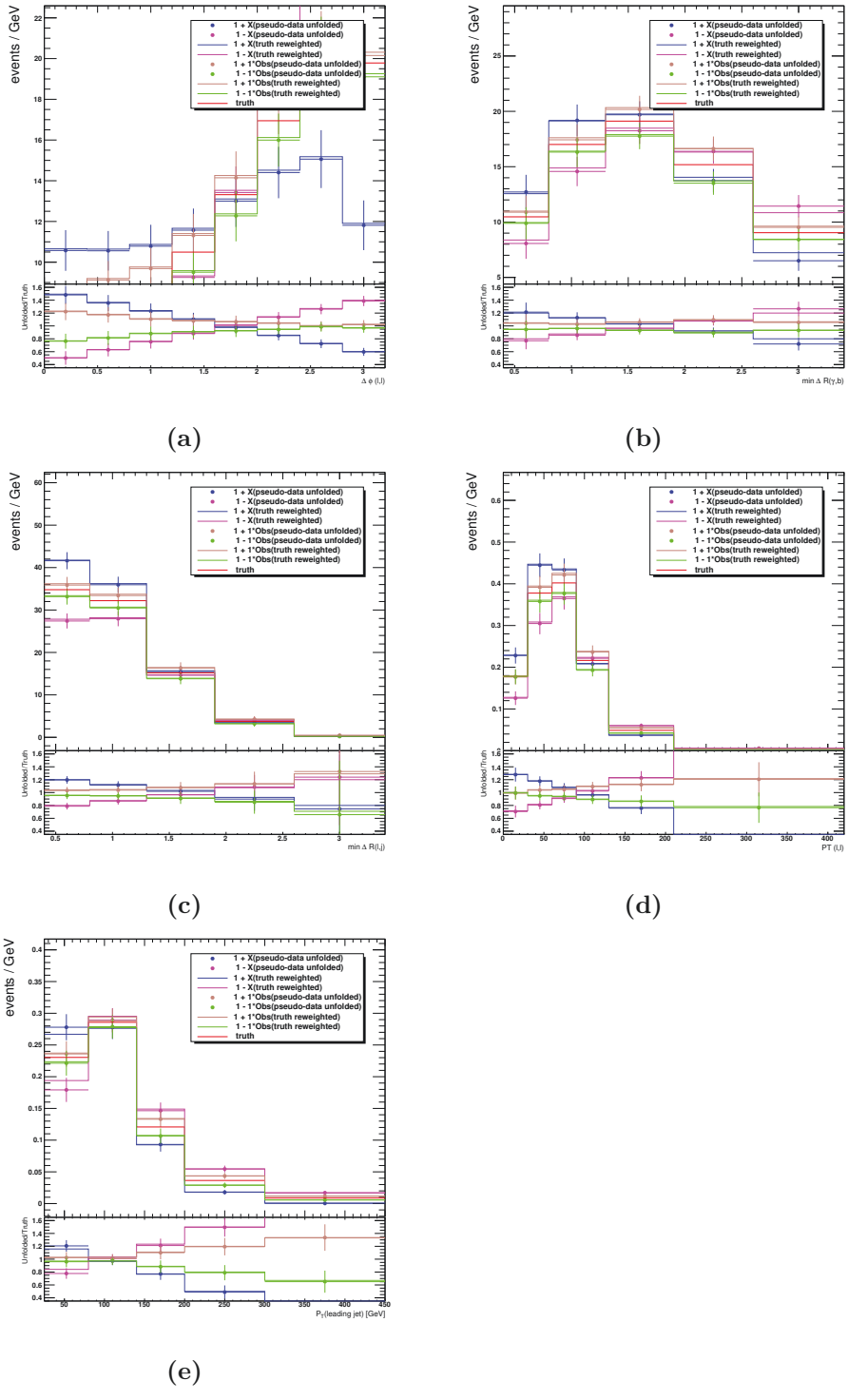

(a) **(b)** **(c)** **(d)** **(e)**

Figure A.7: Comparison of the re-weighted unfolded pseudo-data and the re-weighted particle level distribution as a function of (a) $\Delta\phi(\ell,\ell)$, (b) $\Delta R(\gamma,b)_{\text{min}}$, (c) $\Delta R(\ell,j)_{\text{min}}$, (d) $p_T(\ell,\ell)$, and (e) $p_T(j_1)$ in the dilepton channel for $t\bar{t}\gamma$ production measurement. The dots are the ratio of the unfolded reweighted distributions to the nominal particle level distribution, while the solid lines are the ratio of the reweighted particle level distributions to the nominal one. X is defined in the previous section. The uncertainty bars displayed in the plots represent only the statistical error considered in the unfolding.

A.3 Additional material for the $t\bar{t}\gamma$ production measurement

A.3.1 Particle-level distributions in the dilepton channel

This section presents the particle-level distributions of the $t\bar{t}\gamma$ production in the dilepton channel. The particle-level distributions are used as inputs to the unfolding procedure to measure the differential cross-sections.

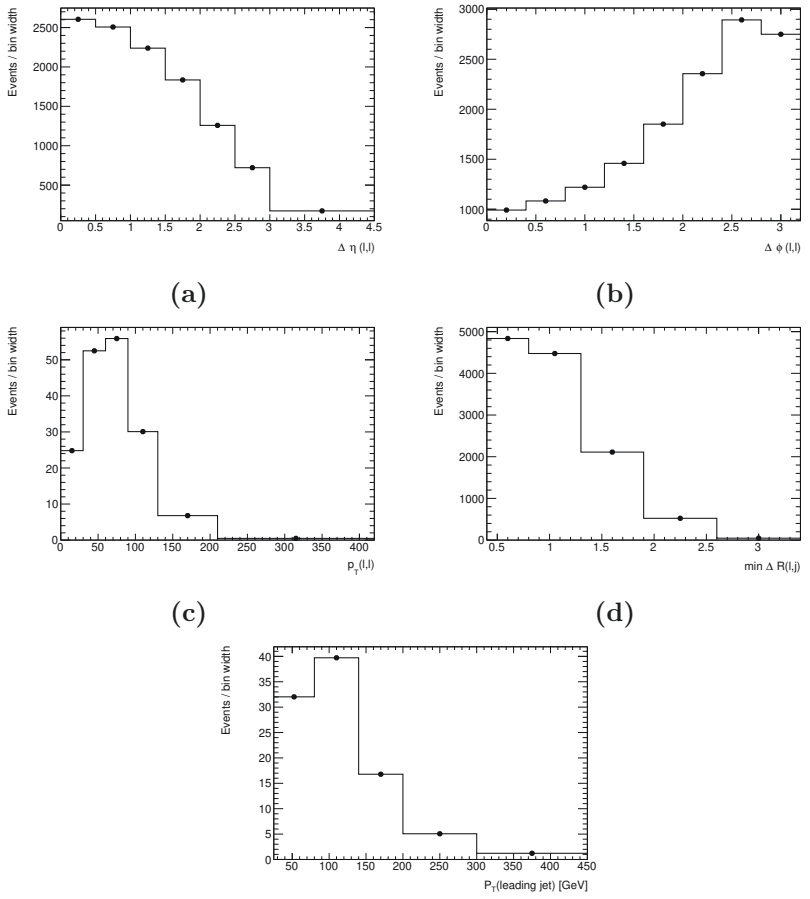

Figure A.8: Particle level distributions of $t\bar{t}\gamma$ production as a function of (a) $\Delta\eta(\ell,\ell)$, (b) $\Delta\phi(\ell,\ell)$, (c) $p_{\mathrm{T}}(\ell,\ell)$, (d) $\Delta R(\ell,j)_{\mathrm{min}}$, and (e) $p_{\mathrm{T}}(j_1)$ in the dilepton channel. The number of events corresponds to the expected number of events at the particle level normalized to the luminosity of data. Overflow events are included in the last bin of the corresponding distribution. Note that values are divided by bin width.

A.3.2 Response matrices in the combined channel

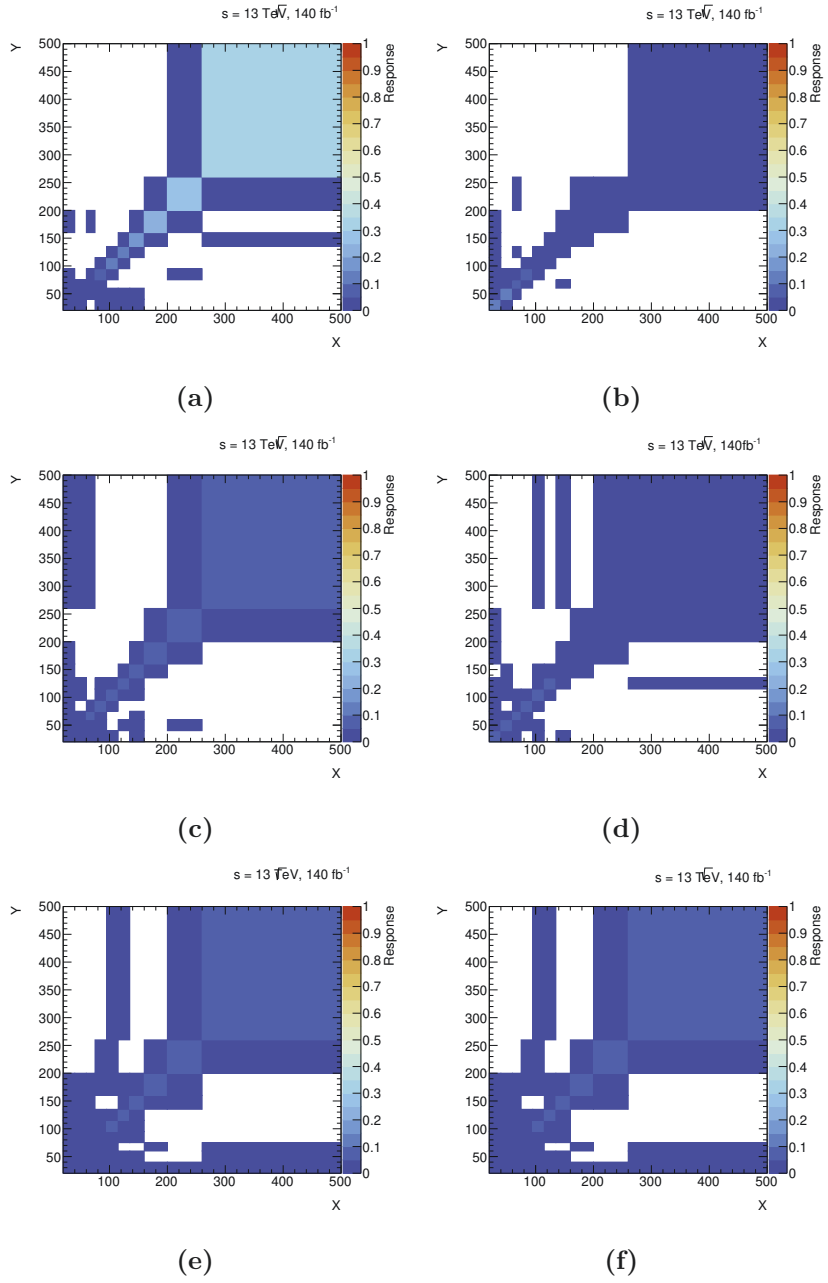

Figure A.9: Response matrices for the observable $p_{\mathrm{T}}(\gamma)$ for the combined single-lepton and dilepton measurement, split across six regions determined by the NN output. (a-d) Response matrices for the $t\bar{t}\gamma$ production SR, $t\bar{t}\gamma$ decay CR, fakes CR, prompt photon CR in the single-lepton channel and (e-f) for the dilepton channel for $O_{\mathrm{NN}} \geq 0.6$, $O_{\mathrm{NN}} < 0.6$ regions, respectively.

A.3.3 Ranking of systematic uncertainties in the combined channel

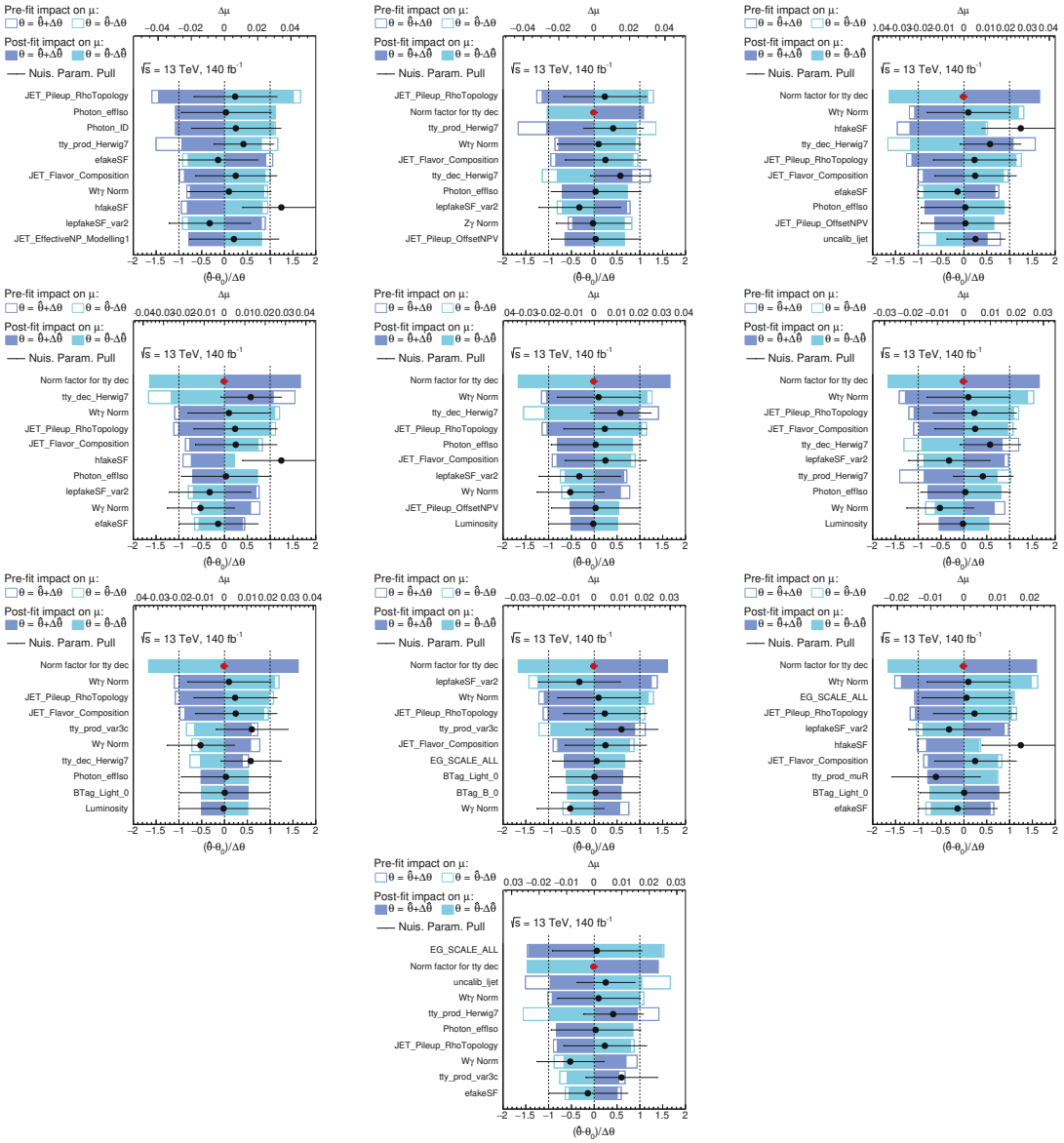

Figure A.10: Ranking of the 10 leading systematic uncertainties included in the profile likelihood unfolding used for the $p_{\mathrm{T}}(\gamma)$ cross-section measurement in the combined single-lepton and dilepton channel. The blue and turquoise bands represent the post-fit impact on the measured cross-section in each bin, while the outlined blue and turquoise rectangles show the pre-fit impact. The difference between these two indicates the constraint of the nuisance parameter. Most nuisance parameters are either unconstraint or only marginally constraint. The impact is overlaid with the post-fit values of the nuisance parameters (pulls), shown by the black dots. The black lines represent the post-fit uncertainties normalized to the pre-fit uncertainties. Each subfigure, corresponds to a specific bin of the $p_{\mathrm{T}}(\gamma)$ distribution, starting from bin 1 till bin 10 (from left to right and top to bottom).

A.3.4 Correlations among signal strength and nuisance parameters

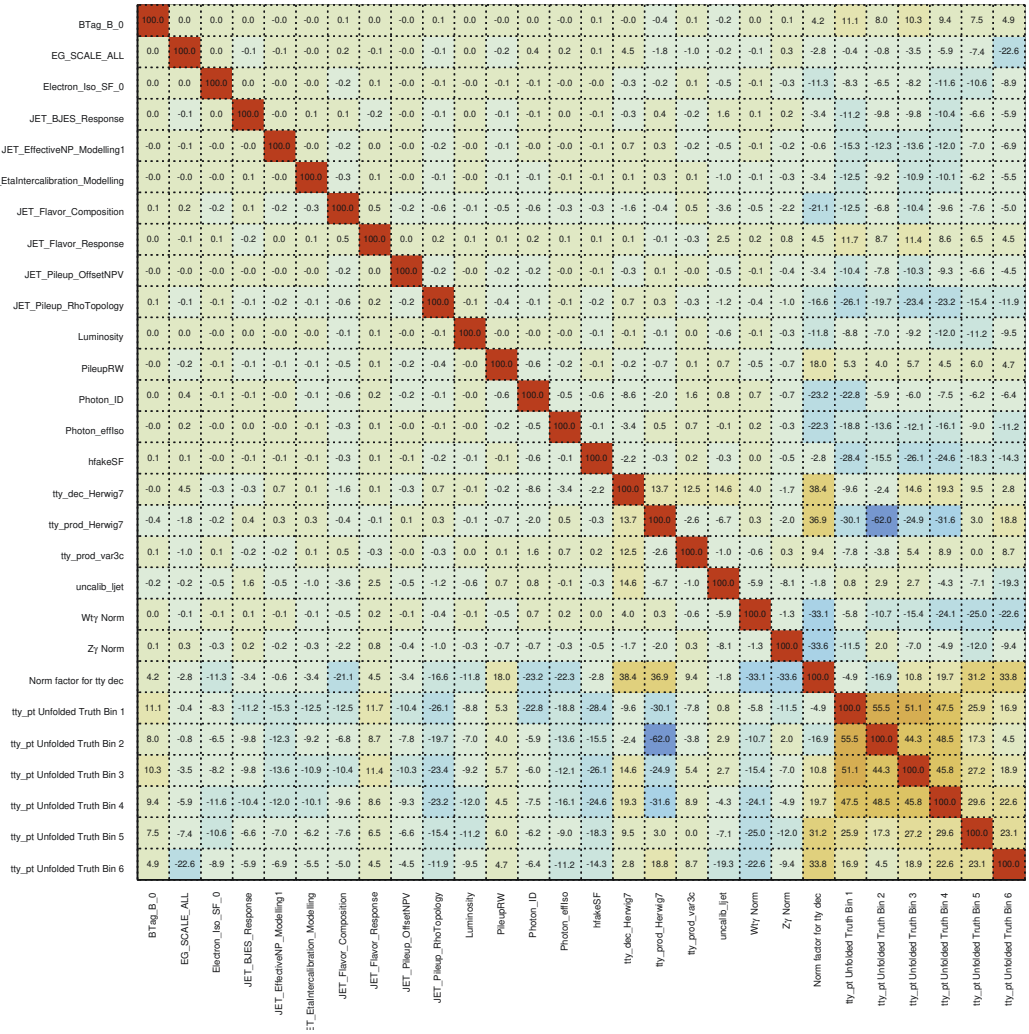

Figure A.11: Plot showing the correlation between signal strength and nuisance parameters for the $p_{\mathrm{T}}(\gamma)$ measurement in the dilepton channel. Only NPs with a correlation greater than 10% are shown. The NP names indicate the following uncertainties: "JET_" for JER and JES, "BTag_" for b-tagging, "_Norm" for normalization, "_muR" and "_muF" for scale, "_var3c" for ISR, "lepfakeSF_" for lepton fakes, "efakeSF_" for electron fakes, "hfakeSF_" for hadron fakes, "highpt_uncalib_" for uncalibrated jet, and "Photon_" for photon reconstruction.

A.3.5 Differential cross-sections

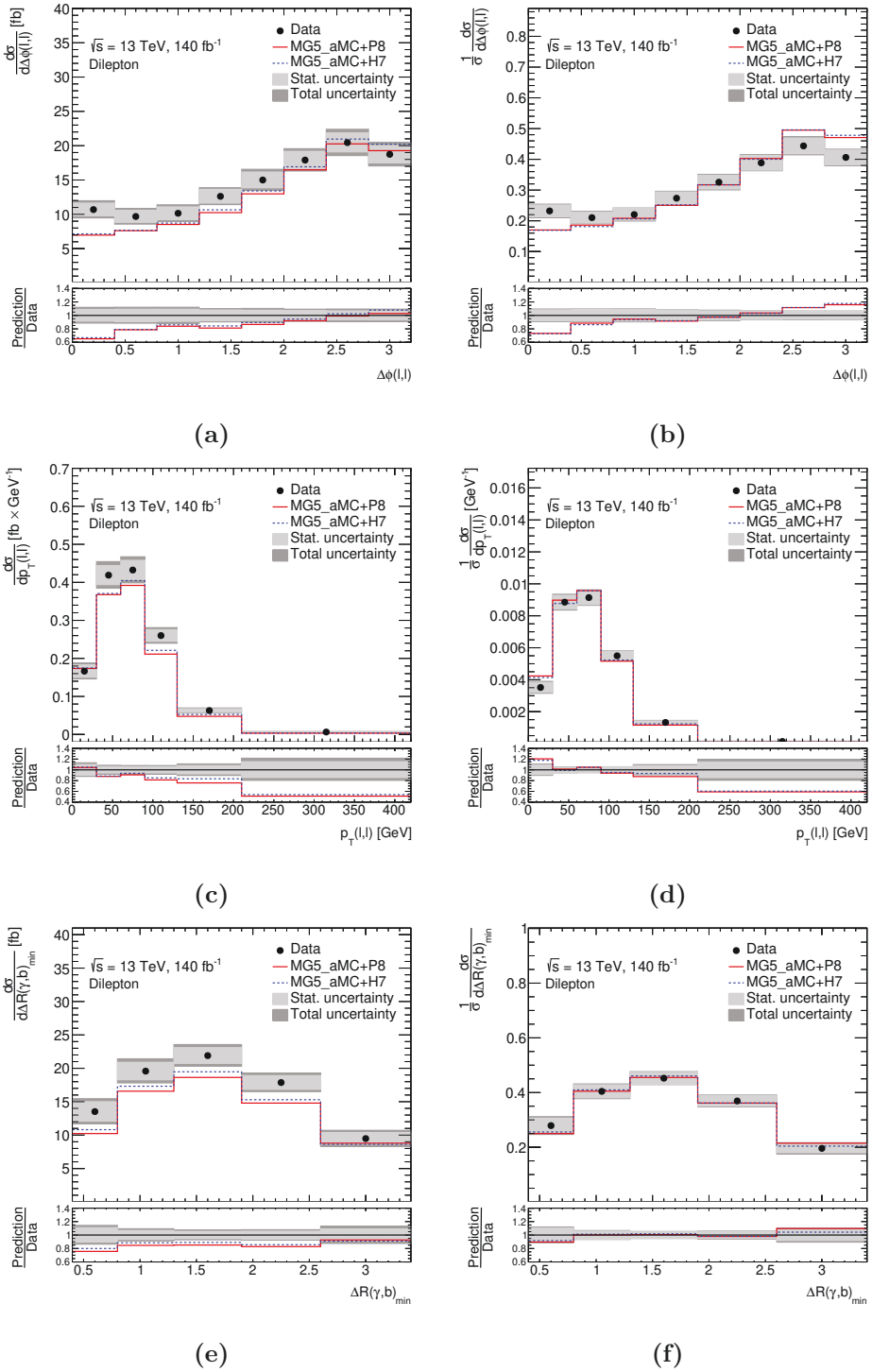

Figure A.12: Absolute (left) and normalized (right) differential cross-sections of $t\bar{t}\gamma$ production in dilepton fiducial phase space as a function of $\Delta\phi_{\ell,\ell}$ (a, b), $p_{\mathrm{T}}(\ell,\ell)$ (c, d) and $\Delta R(\gamma,b)_{\mathrm{min}}$ (e, f). Data are compared with MadGraph5_aMC@NLO simulation interfaced with Pythia8 and Herwig7. The last bin includes overflow events.

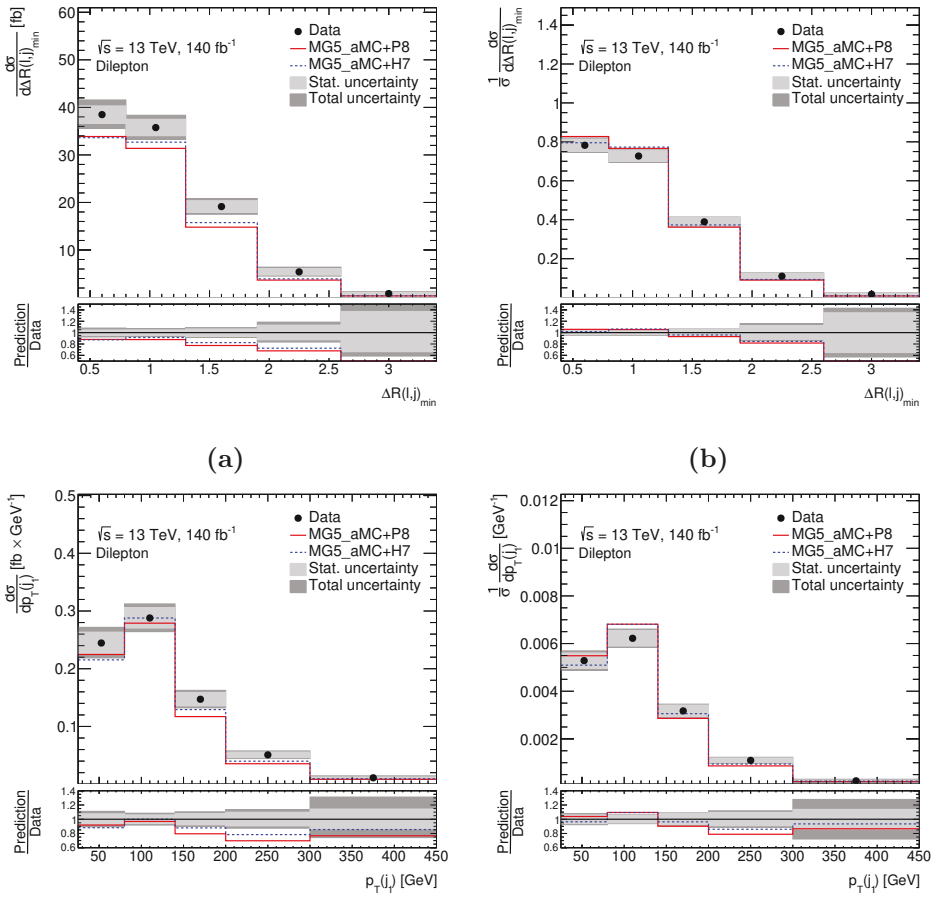

Figure A.13: Absolute (left) and normalized (right) differential cross-sections of $t\bar{t}\gamma$ production in dilepton fiducial phase space as a function of $\Delta R(\ell, j)_{\text{min}}$ (a, b), $p_{\text{T}}(j_1)$ (c, d). Data are compared with MadGraph5_aMC@NLO simulation interfaced with Pythia8 and Herwig7. The last bin includes overflow events.

A.4 Additional material for the total $t\bar{t}\gamma$ prodcution and decay measurement

A.4.1 Particle-level distributions in the dilepton channel

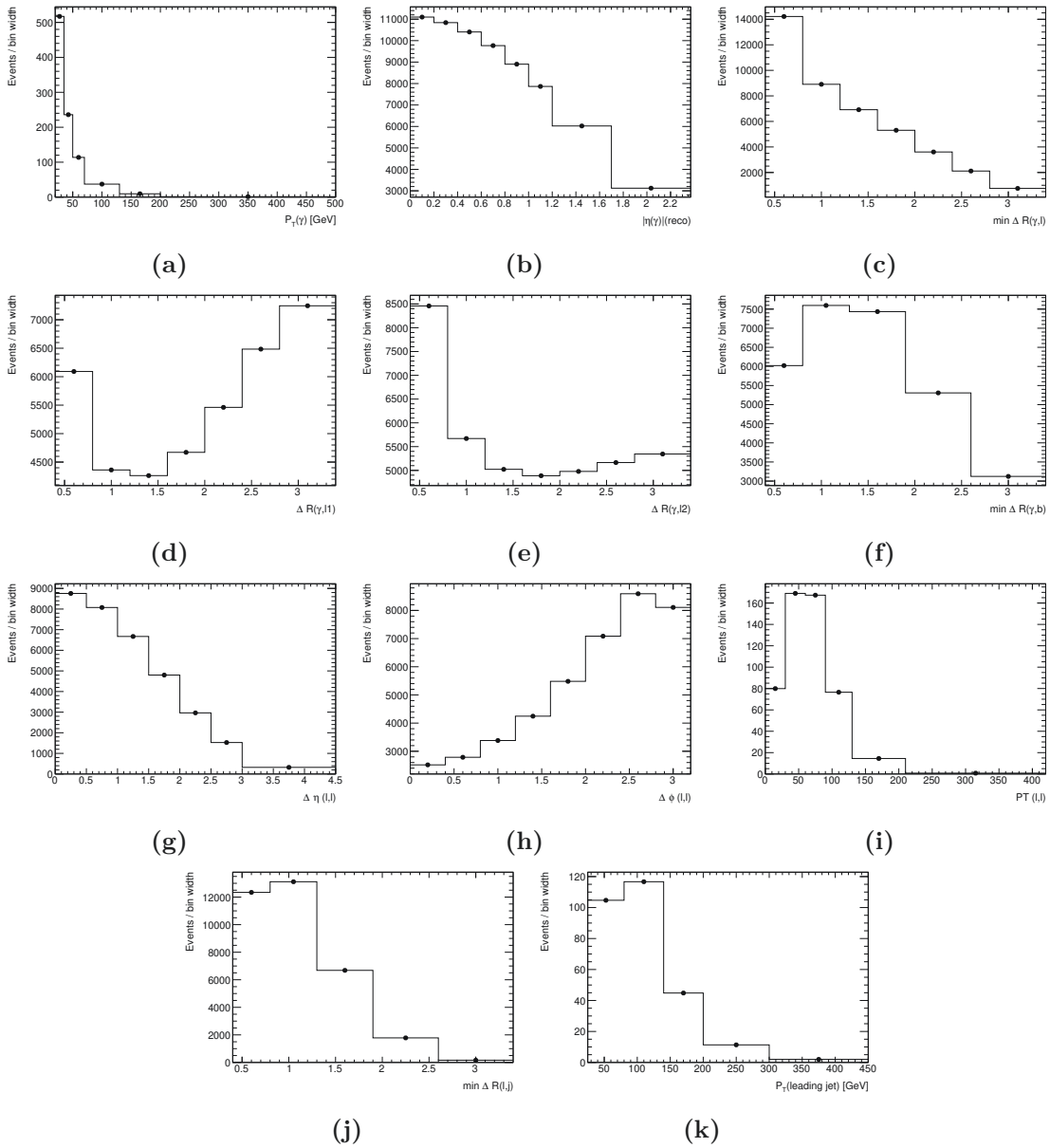

Figure A.14: Particle level distributions of total $t\bar{t}\gamma$ production and decay as a function of (a) $p_{\mathrm{T}}(\gamma)$, (b) $\eta(\gamma)$, (c) $\Delta R(\gamma,\ell)_{\mathrm{min}}$, (d) $\Delta R(\gamma,\ell_1)$, (e) $\Delta R(\gamma,\ell_2)$, (f) $\Delta R(\gamma,b)_{\mathrm{min}}$, (g) $|\Delta\eta(\ell,\ell)|$, (h) $\Delta\phi(\ell,\ell)$, (i) $p_{\mathrm{T}}(\ell,\ell)$, (j) $\Delta R(\ell,j)_{\mathrm{min}}$, and (k) $p_{\mathrm{T}}(j_1)$ in the dilepton channel. The number of events corresponds to the expected number of events at the particle level normalized to the luminosity of data. Overflow events are included in the last bin of the corresponding distribution. Note that values are divided by bin width.

A.4.2 Migration and response matrices

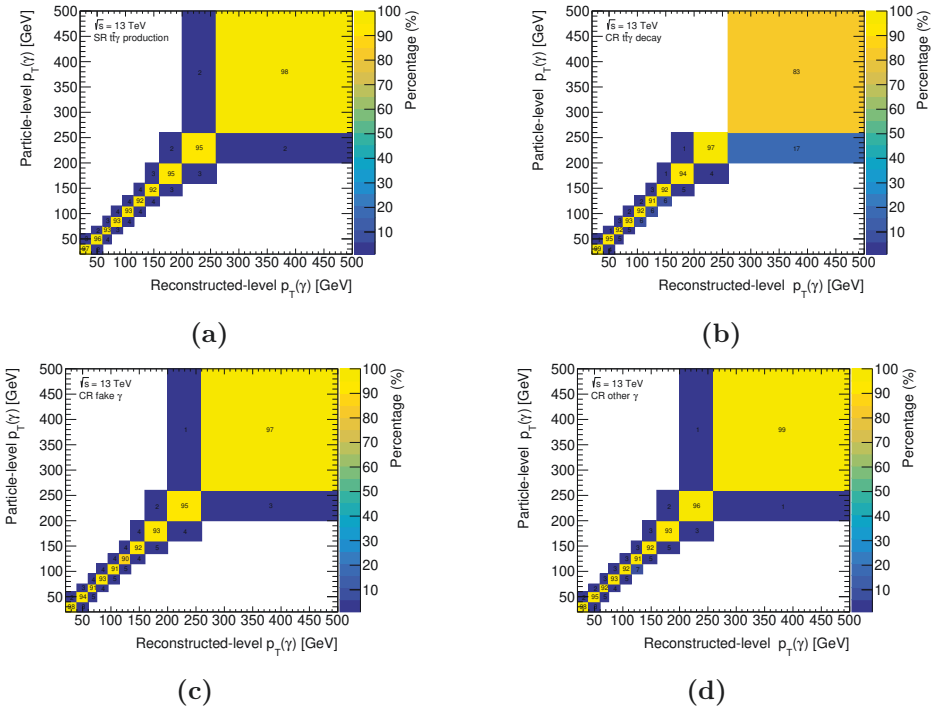

Figure A.15: The normalized migration matrices, $M_{\mathrm{r,t}}$, representing the migration of events from particle level to four regions at the reconstruction level: (a) $t\bar{t}\gamma$ production enriched region, (b) $t\bar{t}\gamma$ decay enriched region (c) fakes enriched region, (d) prompt photon enriched region for the observable $p_{\mathrm{T}}(\gamma)$ in single-lepton channel for total $t\bar{t}\gamma$ production and decay measurement.

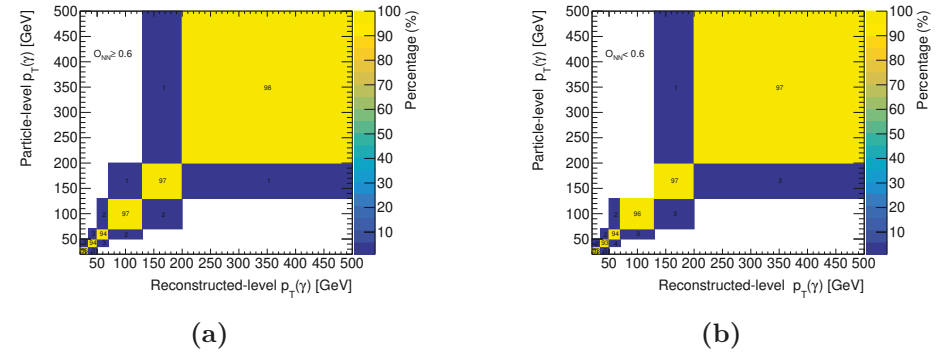

Figure A.16: The normalized migration matrices, $M_{\mathrm{r,t}}$ representing the migration of events from the particle level bin to the two regions at the reconstruction level: (a) $O_{\mathrm{NN}} \geq 0.6$ and (b) $O_{\mathrm{NN}} < 0.6$, for the observable $p_{\mathrm{T}}(\gamma)$ in the dilepton channel for total $t\bar{t}\gamma$ production and decay measurement.

A.4.3 Data-MC comparisons

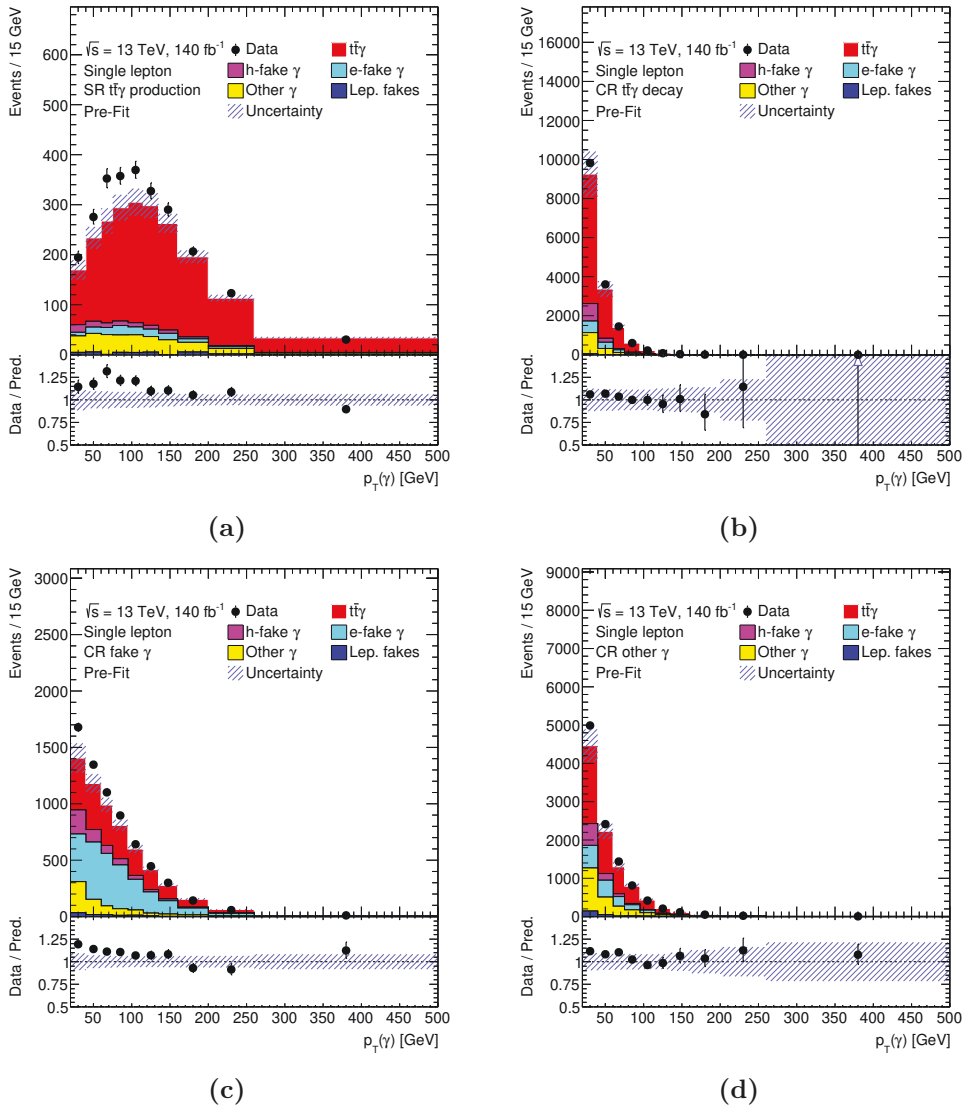

Figure A.17: Distribution of $p_{\mathrm{T}}(\gamma)$ in the single-lepton channel for the four regions at the reconstruction level: (a) $t\bar{t}\gamma$ production SR, (b) $t\bar{t}\gamma$ decay CR, (c) fakes CR, and (d) prompt photon CR. The last bin includes overflow events. The lower panel shows the ratio of the data to the predictions. The error bars represent the statistical uncertainty in the data. The shaded area represents the total uncertainty in the prediction.

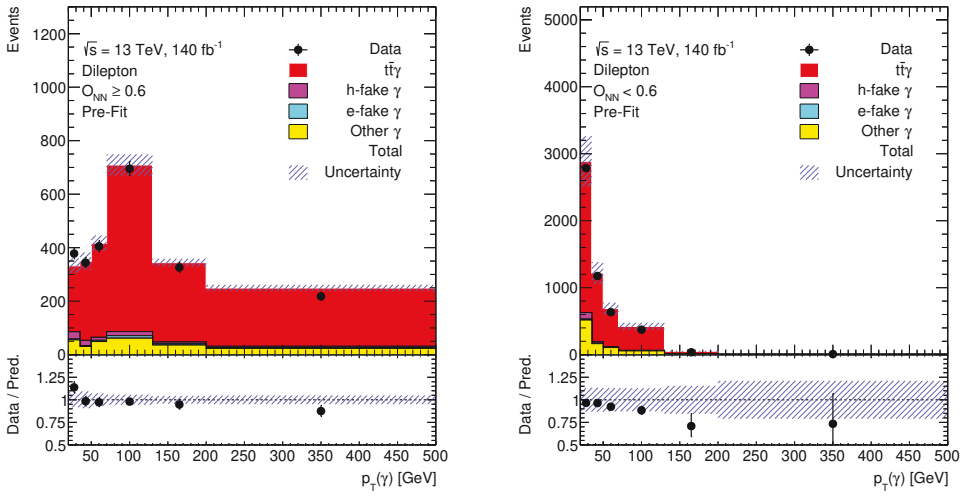

(a) **(b)**

Figure A.18: Distribution of $p_{\mathrm{T}}(\gamma)$ in the dilepton channel for the two regions at the reconstruction level, $O_{\mathrm{NN}} \geq 0.6$ and $O_{\mathrm{NN}} < 0.6$. The last bin includes overflow events. The lower panel shows the ratio of the data to the predictions. The error bars represent the statistical uncertainty in the data. The shaded area represents the total uncertainty in the prediction. The last bin includes overflow events.

A.4.4 Correlations among signal strength and nuisance parameters

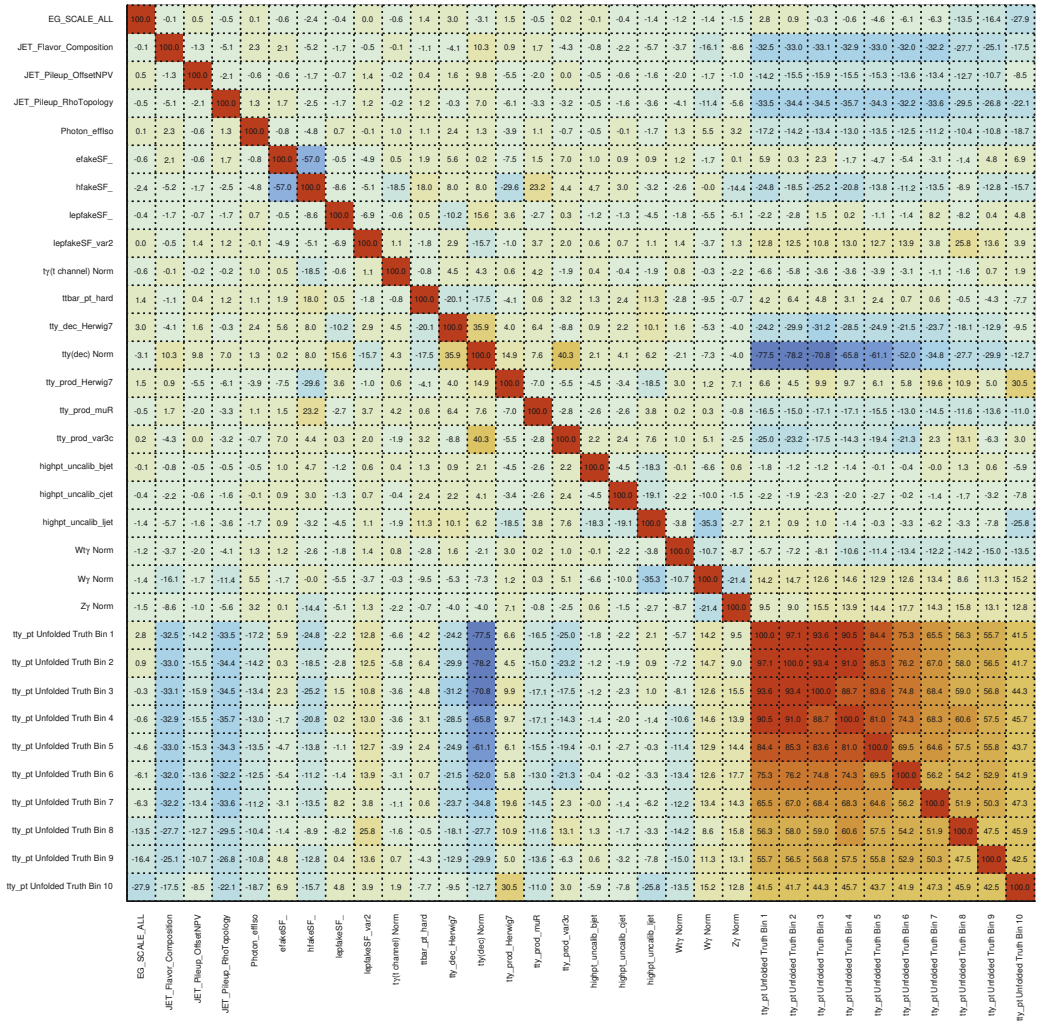

Figure A.19: Plot showing the correlation between signal strength and nuisance parameters for total $t\bar{t}\gamma$ production and decay measurement as a function of $p_{\mathrm{T}}(\gamma)$ in the single-lepton channel. Only NPs with a correlation greater than 10% are shown. The NP names indicate the following uncertainties: "JET_" for JER and JES, "BTag_" for b-tagging, "_Norm" for normalization, "_muR" and "_muF" for scale, "_var3c" for ISR, "lepfakeSF_" for lepton fakes, "efakeSF_" for electron fakes, "hfakeSF_" for hadron fakes, "highpt_uncalib_" for uncalibrated jet, and "Photon_" for photon reconstruction.

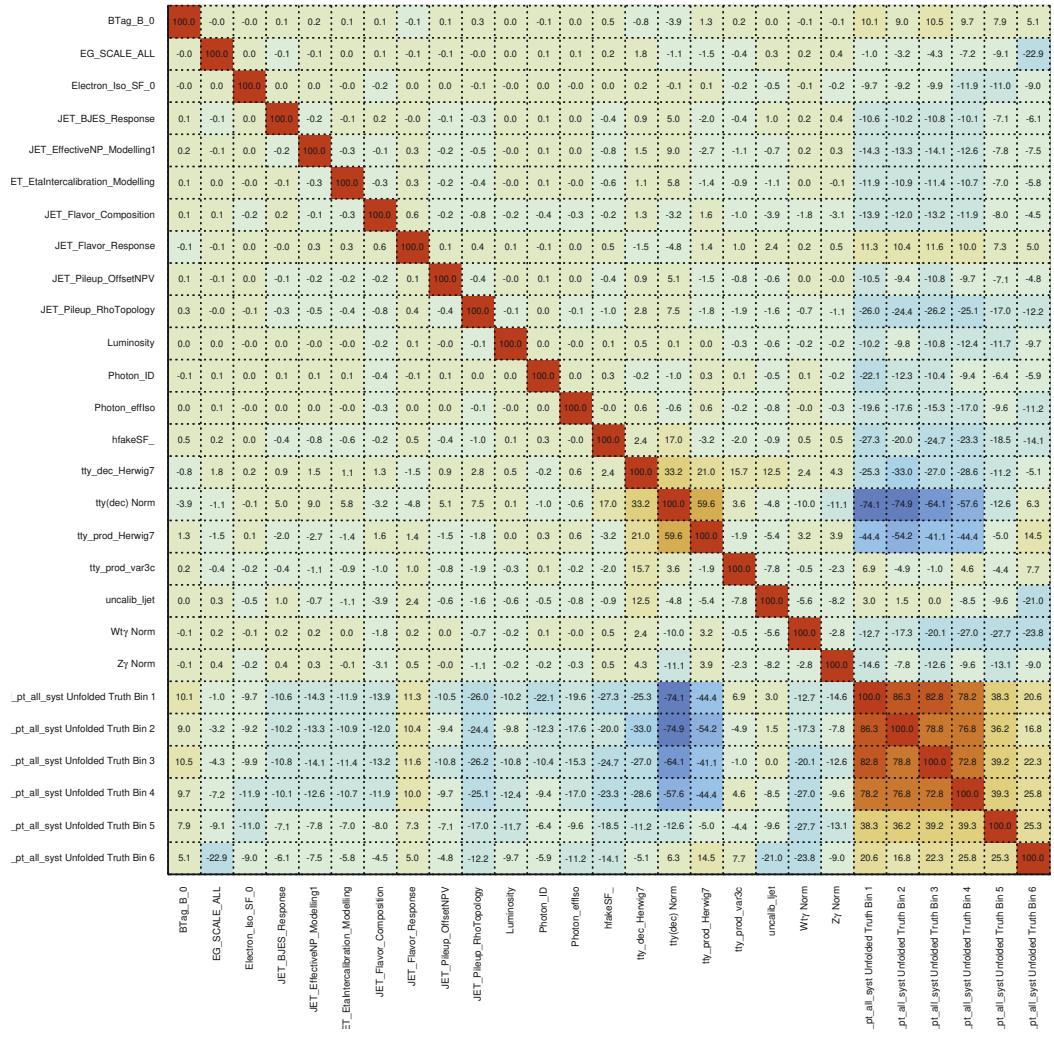

Figure A.20: Plot showing the correlation between signal strength and nuisance parameters for total $t\bar{t}\gamma$ production and decay measurement as a function of $p_{\mathrm{T}}(\gamma)$ in the dilepton channel. Only NPs with a correlation greater than 10% are shown. The NP names indicate the following uncertainties: "JET_" for JER and JES, "BTag_" for b-tagging, "_Norm" for normalization, "_muR" and "_muF" for scale, "_var3c" for ISR, "lepfakeSF_" for lepton fakes, "efakeSF_" for electron fakes, "hfakeSF_" for hadron fakes, "highpt_uncalib_" for uncalibrated jet, and "Photon_" for photon reconstruction.

A.4.5 Differential cross-sections

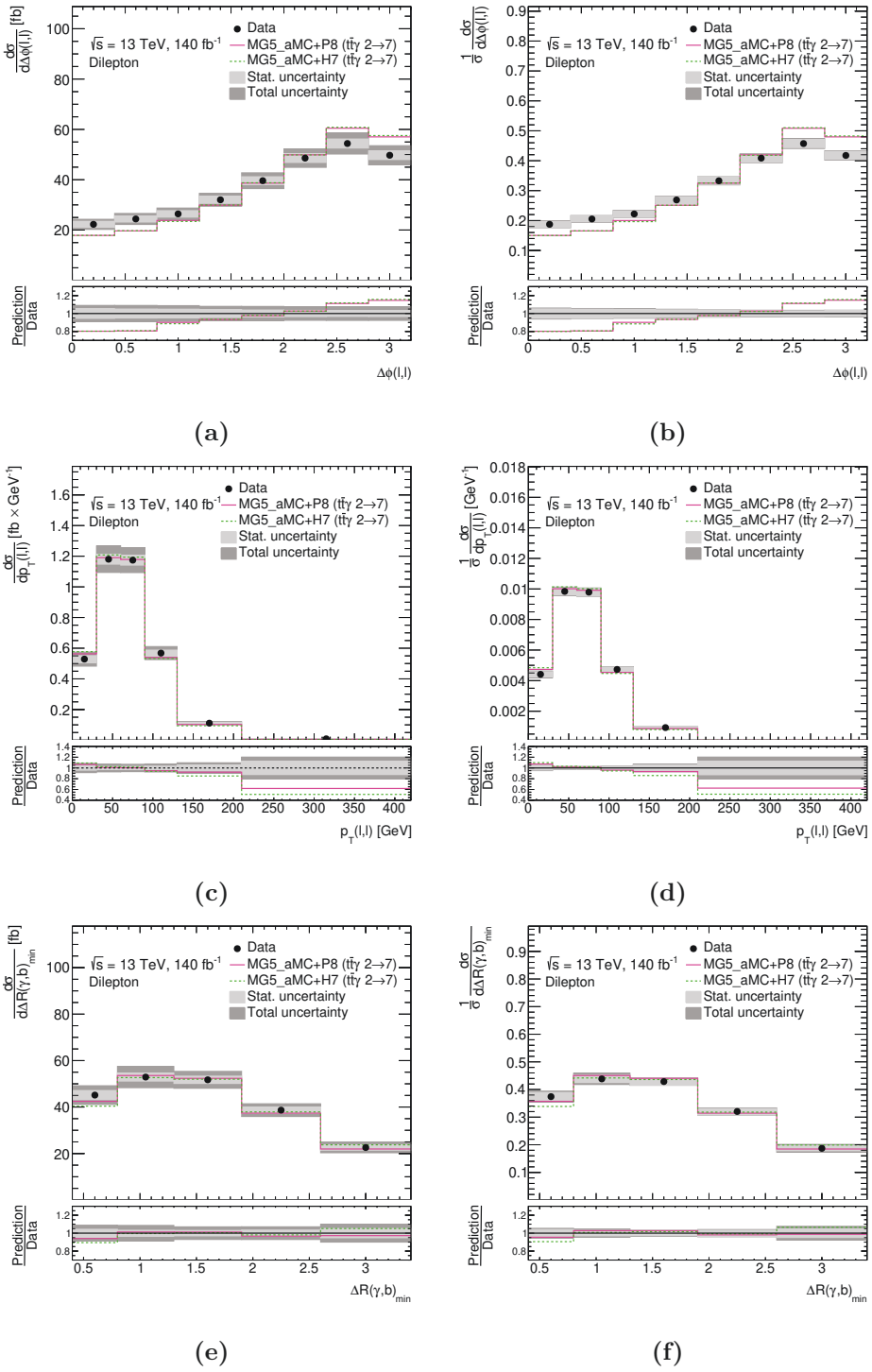

Figure A.21: Absolute (left) and normalized (right) differential cross-sections of total $t\bar{t}\gamma$ production and decay in the dilepton fiducial phase space at particle level as a function of $|\Delta\phi(\ell,\ell)|$ (a, b), $p_{\mathrm{T}}(\ell,\ell)$ (c, d), and $\Delta R(\gamma,b)_{\mathrm{min}}$ (e, f). Data are compared with LO $2 \to 7$ MadGraph5_aMC@NLO simulation interfaced with Pythia 8 and Herwig 7. The last bin includes overflow events.

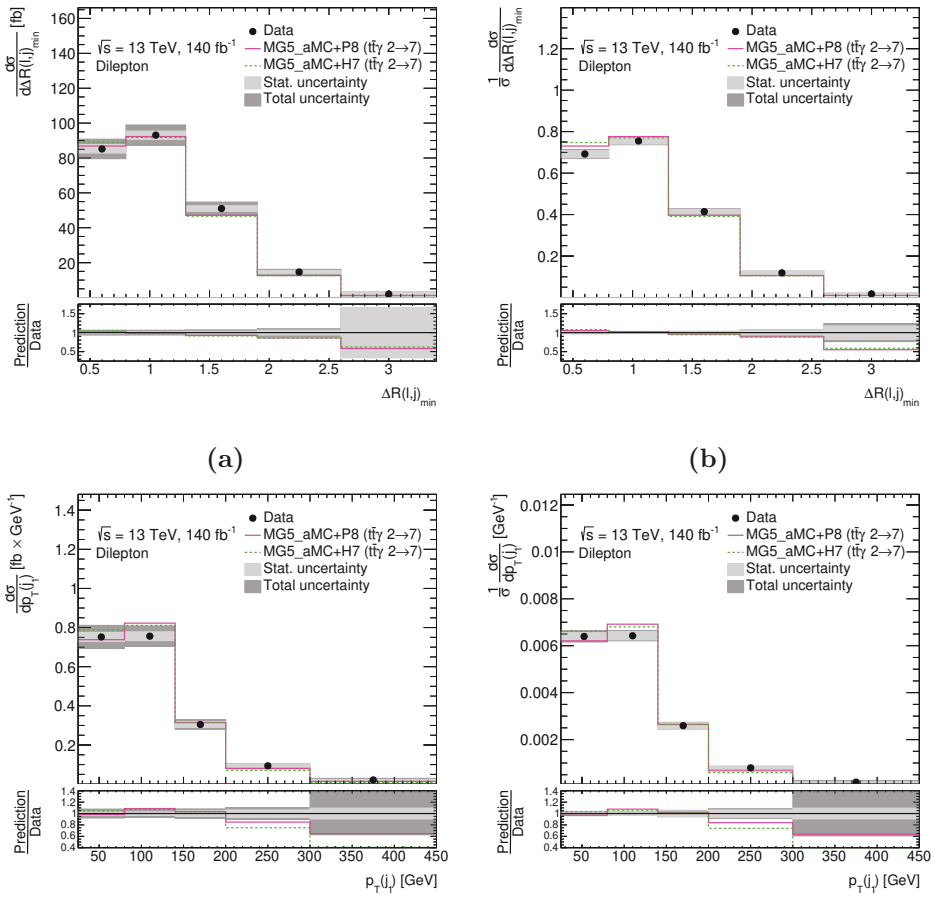

Figure A.22: Absolute (left) and normalized (right) differential cross-sections of total $t\bar{t}\gamma$ production and decay in the dilepton fiducial phase space at particle level as a function of $\Delta R(\ell, j)_{\text{min}}$ (a, b), and $p_{\text{T}}(j_1)$ (c, d). Data are compared with LO $2 \to 7$ MadGraph5_aMC@NLO simulation interfaced with Pythia 8 and Herwig 7. The last bin includes overflow events.

A.4.6 Grouped impact of systematic uncertainties

This section presents the grouped impact of systematic uncertainties for the total $t\bar{t}\gamma$ production and decay measurement in the single-lepton and dilepton channels. Both in single-lepton and dilepton channel $t\bar{t}\gamma$ decay normalization uncertainty is the dominant source of uncertainty. In single-lepton channel uncertainties related to jet, $t\bar{t}\gamma$ production modelling are the dominant sources of uncertainty. In dilepton channel, uncertainties related $t\bar{t}\gamma$ production modelling, jet related uncertainties and the statistical uncertainty are the dominant sources of uncertainty.

This section presents the grouped impact of systematic uncertainties on the total $t\bar{t}\gamma$ production and decay measurement, in the single-lepton and dilepton channels. Across both channels, the uncertainties associated with the $t\bar{t}\gamma$ decay modeling is the dominant contributor. In the single-lepton channel, uncertainties from jet-related measurements and the modeling of $t\bar{t}\gamma$ production also play substantial roles. The dilepton channel is primarily affected by uncertainties related to statistics, the modeling of $t\bar{t}\gamma$ production, and jet-related measurements.

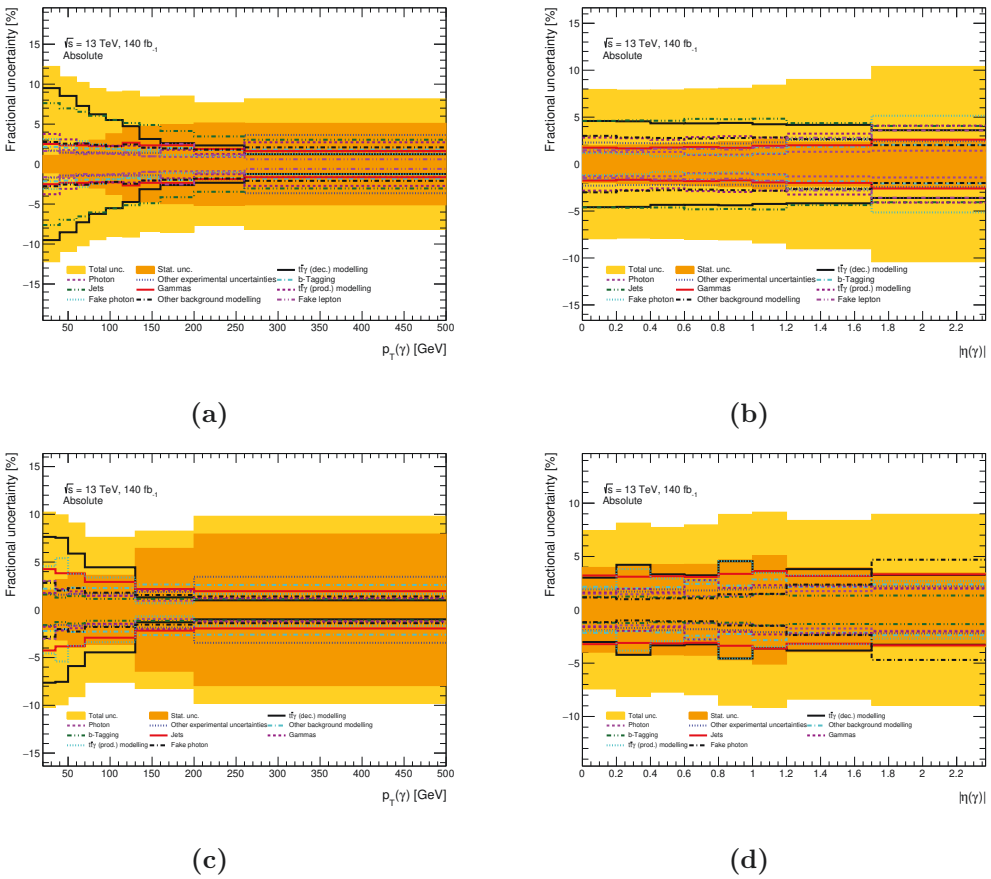

Figure A.23: The decomposed systematic uncertainties for absolute differential cross-sections as a function of $p_{\mathrm{T}}(\gamma)$ and $|\eta(\gamma)|$ in the single-lepton (a, b) and dilepton (c, d) channel for total $t\bar{t}\gamma$ production and decay measurement.

Bibliography

[1] Wikimedia Foundation, *Satellite Image of Earth*, https://upload.wikimedia.org/wikipedia/commons/0/00/Standard_Model_of_Elementary_Particles.svg, Accessed: 4 May 2024, 2021.

[2] E. Noether, *Invariante Variationsprobleme*, ger, Nachrichten von der Gesellschaft der Wissenschaften zu Göttingen, Mathematisch-Physikalische Klasse **1918** (1918), p. 235, URL: http://eudml.org/doc/59024.

[3] A. Quadt, *Top quark physics at hadron colliders*, Eur. Phys. J. C **48** (2006), p. 835, DOI: 10.1140/epjc/s2006-02631-6.

[4] L. Canetti, M. Drewes and M. Shaposhnikov, *Matter and Antimatter in the Universe*, New J. Phys. **14** (2012), p. 095012, DOI: 10.1088/1367-2630/14/9/095012.

[5] G. F. Giudice, *Naturally Speaking: The Naturalness Criterion and Physics at the LHC* (2008), ed. by G. Kane and A. Pierce, p. 155, DOI: 10.1142/9789812779762_0010.

[6] R. D. Peccei, *The Strong CP problem and axions*, Lect. Notes Phys. **741** (2008), ed. by M. Kuster, G. Raffelt and B. Beltran, p. 3, DOI: 10.1007/978-3-540-73518-2_1.

[7] A. Hayrapetyan et al., *Combination of measurements of the top quark mass from data collected by the ATLAS and CMS experiments at* $\sqrt{s} = 7$ *and* 8 TeV (2023), arXiv: 2402.08713 [hep-ex].

[8] C. Patrignani et al., *Review of Particle Physics*, Chin. Phys. C **40** (2016), p. 100001, DOI: 10.1088/1674-1137/40/10/100001.

[9] D. Chang, W.-F. Chang and E. Ma, *Alternative interpretation of the Tevatron top events*, Phys. Rev. D **59** (1999), p. 091503, DOI: 10.1103/PhysRevD.59.091503.

[10] D. Chang, W.-F. Chang and E. Ma, *Fitting precision electroweak data with exotic heavy quarks*, Phys. Rev. D **61** (2000), p. 037301, DOI: 10.1103/PhysRevD.61.037301.

[11] G. Aad et al., *Measurement of the top quark charge in pp collisions at* $\sqrt{s} = 7$ *TeV with the ATLAS detector*, JHEP **11** (2013), p. 031, DOI: 10.1007/JHEP11(2013)031.

[12] *Constraints on the Top-Quark Charge from Top-Pair Events* (2012).

[13] A. O. Bouzas and F. Larios, *Electromagnetic dipole moments of the Top quark*, Phys. Rev. D **87** (2013), p. 074015, DOI: 10.1103/PhysRevD.87.074015.

[14] J. A. Aguilar-Saavedra, *A Minimal set of top anomalous couplings*, Nucl. Phys. B **812** (2009), p. 181, DOI: 10.1016/j.nuclphysb.2008.12.012.

[15] O. Bessidskaia Bylund et al., *Probing top quark neutral couplings in the Standard Model Effective Field Theory at NLO in QCD*, JHEP **05** (2016), p. 052, DOI: 10.1007/JHEP05(2016)052.

[16] T. Aaltonen et al., *Evidence for $t\bar{t}\gamma$ Production and Measurement of $\sigma_t\bar{t}\gamma/\sigma_t\bar{t}$*, Phys. Rev. D **84** (2011), p. 031104, DOI: 10.1103/PhysRevD.84.031104.

[17] G. Aad et al., *Observation of top-quark pair production in association with a photon and measurement of the $t\bar{t}\gamma$ production cross section in pp collisions at $\sqrt{s} = 7$ TeV using the ATLAS detector*, Phys. Rev. D **91** (2015), p. 072007, DOI: 10.1103/PhysRevD.91.072007.

[18] M. Aaboud et al., *Measurement of the $t\bar{t}\gamma$ production cross section in proton-proton collisions at $\sqrt{s} = 8$ TeV with the ATLAS detector*, JHEP **11** (2017), p. 086, DOI: 10.1007/JHEP11(2017)086.

[19] A. M. Sirunyan et al., *Measurement of the semileptonic $\mathrm{t\bar{t}} + \gamma$ production cross section in pp collisions at $\sqrt{s} = 8$ TeV*, JHEP **10** (2017), p. 006, DOI: 10.1007/JHEP10(2017)006.

[20] M. Aaboud et al., *Measurements of inclusive and differential fiducial cross-sections of $t\bar{t}\gamma$ production in leptonic final states at $\sqrt{s} = 13$ TeV in ATLAS*, Eur. Phys. J. C **79** (2019), p. 382, DOI: 10.1140/epjc/s10052-019-6849-6.

[21] G. Aad et al., *Measurements of inclusive and differential cross-sections of combined $t\bar{t}\gamma$ and $tW\gamma$ production in the eμ channel at 13 TeV with the ATLAS detector*, JHEP **09** (2020), p. 049, DOI: 10.1007/JHEP09(2020)049.

[22] A. Tumasyan et al., *Measurement of the inclusive and differential $\mathrm{t\bar{t}}\gamma$ cross sections in the single-lepton channel and EFT interpretation at $\sqrt{s} = 13$ TeV*, JHEP **12** (2021), p. 180, DOI: 10.1007/JHEP12(2021)180.

[23] A. Tumasyan et al., *Measurement of the inclusive and differential $\mathrm{t\bar{t}}\gamma$ cross sections in the dilepton channel and effective field theory interpretation in proton-proton collisions at $\sqrt{s}$ =13 TeV*, JHEP **05** (2022), p. 091, DOI: 10.1007/JHEP05(2022)091.

[24] ATLAS Collaboration, *Measurements of inclusive and differential cross-sections of $t\bar{t}\gamma$ production in pp collisions at $\sqrt{s}$ = 13 TeV with the ATLAS detector*, Journal of High Energy Physics **2024** (2024), DOI: 10.1007/JHEP10(2024)191.

[25] G. Aad et al., *Measurement of the charge asymmetry in top-quark pair production in association with a photon with the ATLAS experiment*, Phys. Lett. B **843** (2023), p. 137848, DOI: 10.1016/j.physletb.2023.137848.

[26] P.-F. Duan et al., *QCD corrections to associated production of $t\bar{t}\gamma$ at hadron colliders*, Phys. Rev. D **80** (1 2009), p. 014022, DOI: 10.1103/PhysRevD.80.014022.

[27] P.-F. Duan et al., *Next-to-leading order QCD corrections to $t\bar{t}\gamma$ production at the 7 TeV LHC*, Chin. Phys. Lett. **28** (2011), p. 111401, DOI: 10.1088/0256-307X/28/11/111401.

[28] P.-F. Duan et al., *Electroweak corrections to top quark pair production in association with a hard photon at hadron colliders*, Physics Letters B **766** (2017), p. 102, DOI: https://doi.org/10.1016/j.physletb.2016.12.061.

[29] A. Kardos and Z. Trócsányi, *Hadroproduction of t anti-t pair in association with an isolated photon at NLO accuracy matched with parton shower*, JHEP **05** (2015), p. 090, DOI: 10.1007/JHEP05(2015)090.

[30] K. Melnikov, M. Schulze and A. Scharf, *QCD corrections to top quark pair production in association with a photon at hadron colliders*, Phys. Rev. D **83** (7 2011), p. 074013, DOI: 10.1103/PhysRevD.83.074013.

[31] G. Bevilacqua et al., *Hard Photons in Hadroproduction of Top Quarks with Realistic Final States*, JHEP **10** (2018), p. 158, DOI: 10.1007/JHEP10(2018)158.

[32] G. Bevilacqua et al., *Off-shell vs on-shell modelling of top quarks in photon associated production*, JHEP **03** (2020), p. 154, DOI: 10.1007/JHEP03(2020)154.

[33] N. Kidonakis and A. Tonero, *Higher-order corrections in $tt^{-}\gamma$ cross sections*, Phys. Rev. D **107** (2023), p. 034013, DOI: 10.1103/PhysRevD.107.034013.

[34] *LHC Machine*, JINST **3** (2008), ed. by L. Evans and P. Bryant, S08001, DOI: 10.1088/1748-0221/3/08/S08001.

[35] G. Aad et al., *The ATLAS Experiment at the CERN Large Hadron Collider*, JINST **3** (2008), S08003, DOI: 10.1088/1748-0221/3/08/S08003.

[36] *Electron and photon reconstruction and performance in ATLAS using a dynamical, topological cell clustering-based approach* (2017).

[37] G. Aad et al., *Topological cell clustering in the ATLAS calorimeters and its performance in LHC Run 1*, Eur. Phys. J. C **77** (2017), p. 490, DOI: 10.1140/epjc/s10052-017-5004-5.

[38] T. Cornelissen et al., *Concepts, Design and Implementation of the ATLAS New Tracking (NEWT)* (2007), ed. by A. Salzburger.

[39] R. Fruhwirth, *Application of Kalman filtering to track and vertex fitting*, Nucl. Instrum. Meth. A **262** (1987), p. 444, DOI: 10.1016/0168-9002(87)90887-4.

[40] T. G. Cornelissen et al., *The global chi**2 track fitter in ATLAS*, J. Phys. Conf. Ser. **119** (2008), ed. by R. Sobie, R. Tafirout and J. Thomson, p. 032013, DOI: 10.1088/1742-6596/119/3/032013.

[41] *Improved electron reconstruction in ATLAS using the Gaussian Sum Filter-based model for bremsstrahlung* (2012).

[42] G. Aad et al., *Muon reconstruction and identification efficiency in ATLAS using the full Run 2 pp collision data set at* $\sqrt{s} = 13$ *TeV*, Eur. Phys. J. C **81** (2021), p. 578, DOI: 10.1140/epjc/s10052-021-09233-2.

[43] J. Illingworth and J. Kittler, *A survey of the hough transform*, Computer Vision, Graphics, and Image Processing **44** (1988), p. 87, DOI: https://doi.org/10.1016/S0734-189X(88)80033-1.

[44] M. Cacciari, G. P. Salam and G. Soyez, *The anti-*k_t *jet clustering algorithm*, JHEP **04** (2008), p. 063, DOI: 10.1088/1126-6708/2008/04/063.

[45] M. Cacciari, G. P. Salam and G. Soyez, *FastJet User Manual*, Eur. Phys. J. C **72** (2012), p. 1896, DOI: 10.1140/epjc/s10052-012-1896-2.

[46] M. Aaboud et al., *Jet reconstruction and performance using particle flow with the ATLAS Detector*, Eur. Phys. J. C **77** (2017), p. 466, DOI: 10.1140/epjc/s10052-017-5031-2.

[47] M. Aaboud et al., *Jet energy scale measurements and their systematic uncertainties in proton-proton collisions at* $\sqrt{s} = 13$ *TeV with the ATLAS detector*, Phys. Rev. D **96** (2017), p. 072002, DOI: 10.1103/PhysRevD.96.072002.

[48] G. Aad et al., *ATLAS flavour-tagging algorithms for the LHC Run 2 pp collision dataset*, Eur. Phys. J. C **83** (2023), p. 681, DOI: 10.1140/epjc/s10052-023-11699-1.

[49] E_T^{miss} *performance in the ATLAS detector using 2015-2016 LHC pp collisions* (2018).

[50] R. Brun and F. Rademakers, *ROOT: An Object-Oriented Data Analysis Framework*, Accessed: 2024-05-28, CERN, 1997, URL: https://root.cern/.

[51] I. Kitware, *CMake: Cross-Platform Make*, Accessed: 2024-05-28, 2024, URL: https://cmake.org/.

[52] A. Collaboration, *Athena*, https://gitlab.cern.ch/atlas/athena, Accessed: 2024-05-28, 2024.

[53] W. Fernando, *Overview and status of ATLAS Pixel Detector*, Nuclear Instruments and Methods in Physics Research Section A: Accelerators, Spectrometers, Detectors and Associated Equipment **596** (2008), Proceedings of the 8th International Conference on Large Scale Applications and Radiation Hardness of Semiconductor Detectors, p. 58, DOI: https://doi.org/10.1016/j.nima.2008.07.113.

[54] M. E. Stramaglia, *DAQ hardware and software development for the ATLAS Pixel Detector*, Nucl. Instrum. Meth. A **824** (2016), ed. by M. G. Bisogni et al., p. 53, DOI: 10.1016/j.nima.2015.11.104.

[55] C. P. Bee et al., *The raw event format in the ATLAS Trigger & DAQ* (1998).

[56] C. P. Bee et al., *The raw event format in the ATLAS Trigger & DAQ*, tech. rep., Geneva: CERN, 2016, URL: https://cds.cern.ch/record/683741.

[57] L. Franconi, *Insertable B-Layer integration in the ATLAS experiment and development of future 3D silicon pixel sensors*, PhD thesis, Oslo U., 2018.

[58] C. Bierlich et al., *A comprehensive guide to the physics and usage of PYTHIA 8.3*, SciPost Phys. Codeb. **2022** (2022), p. 8, DOI: 10.21468/SciPostPhysCodeb.8.

[59] J. F. Owens, A. Accardi and W. Melnitchouk, *Global parton distributions with nuclear and finite-Q^2 corrections*, Phys. Rev. D **87** (2013), p. 094012, DOI: 10.1103/PhysRevD.87.094012.

[60] J. Alwall et al., *The automated computation of tree-level and next-to-leading order differential cross sections, and their matching to parton shower simulations*, JHEP **07** (2014), p. 079, DOI: 10.1007/JHEP07(2014)079.

[61] S. Frixione, P. Nason and C. Oleari, *Matching NLO QCD computations with parton shower simulations: the POWHEG method*, JHEP **11** (2007), p. 070, DOI: 10.1088/1126-6708/2007/11/070.

[62] E. Bothmann et al., *Event Generation with Sherpa 2.2*, SciPost Phys. **7** (2019), p. 034, DOI: 10.21468/SciPostPhys.7.3.034.

[63] T. Sjöstrand, S. Mrenna and P. Skands, *A brief introduction to PYTHIA 8.1*, Comput. Phys. Commun. **178** (2008), p. 852, DOI: 10.1016/j.cpc.2008.01.036.

[64] J. Bellm et al., *Herwig 7.0/Herwig++ 3.0 release note*, Eur. Phys. J. C **76** (2016), p. 196, DOI: 10.1140/epjc/s10052-016-4018-8.

[65] G. Aad et al., *Luminosity determination in pp collisions at $\sqrt{s} = 13$ TeV using the ATLAS detector at the LHC*, Eur. Phys. J. C **83** (2023), p. 982, DOI: 10.1140/epjc/s10052-023-11747-w.

[66] *ATLAS data quality operations and performance for 2015–2018 data-taking*, Journal of Instrumentation **15** (2020), P04003, DOI: 10.1088/1748-0221/15/04/p04003.

[67] G. Aad et al., *The ATLAS Simulation Infrastructure*, Eur. Phys. J. C **70** (2010), p. 823, DOI: 10.1140/epjc/s10052-010-1429-9.

[68] S. Agostinelli et al., *GEANT4–a simulation toolkit*, Nucl. Instrum. Meth. A **506** (2003), p. 250, DOI: 10.1016/S0168-9002(03)01368-8.

[69] T. Sjöstrand et al., *An introduction to PYTHIA 8.2*, Comput. Phys. Commun. **191** (2015), p. 159, DOI: 10.1016/j.cpc.2015.01.024.

[70] *The Pythia 8 A3 tune description of ATLAS minimum bias and inelastic measurements incorporating the Donnachie-Landshoff diffractive model* (2016).

[71] J. Pumplin et al., *New generation of parton distributions with uncertainties from global QCD analysis*, JHEP **07** (2002), p. 012, DOI: 10.1088/1126-6708/2002/07/012.

[72] The NNPDF Collaboration, R. D. Ball et al., *Parton distributions for the LHC run II*, JHEP **04** (2015), p. 040, DOI: 10.1007/JHEP04(2015)040.

[73] ATLAS Collaboration, *ATLAS Pythia 8 tunes to 7 TeV data* (2014), URL: https://cds.cern.ch/record/1966419.

[74] S. Frixione et al., *Angular correlations of lepton pairs from vector boson and top quark decays in Monte Carlo simulations*, JHEP **04** (2007), p. 081, DOI: 10.1088/1126-6708/2007/04/081.

[75] P. Artoisenet et al., *Automatic spin-entangled decays of heavy resonances in Monte Carlo simulations*, JHEP **03** (2013), p. 015, DOI: 10.1007/JHEP03(2013)015.

[76] D. J. Lange, *The EvtGen particle decay simulation package*, Nucl. Instrum. Meth. A **462** (2001), p. 152, DOI: 10.1016/S0168-9002(01)00089-4.

[77] S. Frixione, *Isolated photons in perturbative QCD*, Phys. Lett. B **429** (1998), p. 369, DOI: 10.1016/S0370-2693(98)00454-7.

[78] ATLAS Collaboration, *Measurements of inclusive and differential fiducial cross-sections of $t\bar{t}\gamma$ production in leptonic final states at $\sqrt{s} = 13$ TeV in ATLAS*, Eur. Phys. J. C **79** (2019), p. 382, DOI: 10.1140/epjc/s10052-019-6849-6.

[79] K. Melnikov, M. Schulze and A. Scharf, *QCD corrections to top quark pair production in association with a photon at hadron colliders*, Phys. Rev. D **83** (2011), p. 074013, DOI: 10.1103/PhysRevD.83.074013.

[80] T. Gleisberg et al., *Event generation with SHERPA 1.1*, JHEP **02** (2009), p. 007, DOI: 10.1088/1126-6708/2009/02/007.

[81] S. Höche et al., *QCD matrix elements and truncated showers*, JHEP **05** (2009), p. 053, DOI: 10.1088/1126-6708/2009/05/053.

[82] T. Gleisberg and S. Höche, *Comix, a new matrix element generator*, JHEP **12** (2008), p. 039, DOI: 10.1088/1126-6708/2008/12/039.

[83] S. Schumann and F. Krauss, *A parton shower algorithm based on Catani–Seymour dipole factorisation*, JHEP **03** (2008), p. 038, DOI: 10.1088/1126-6708/2008/03/038.

[84] S. Höche et al., *A critical appraisal of NLO+PS matching methods*, JHEP **09** (2012), p. 049, DOI: 10.1007/JHEP09(2012)049.

[85] S. Catani et al., *QCD Matrix Elements + Parton Showers*, JHEP **11** (2001), p. 063, DOI: 10.1088/1126-6708/2001/11/063.

[86] S. Höche et al., *QCD matrix elements + parton showers. The NLO case*, JHEP **04** (2013), p. 027, DOI: 10.1007/JHEP04(2013)027.

[87] F. Cascioli, P. Maierhöfer and S. Pozzorini, *Scattering Amplitudes with Open Loops*, Phys. Rev. Lett. **108** (2012), p. 111601, DOI: 10.1103/PhysRevLett.108.111601.

[88] A. Denner, S. Dittmaier and L. Hofer, *Collier: A fortran-based complex one-loop library in extended regularizations*, Comput. Phys. Commun. **212** (2017), p. 220, DOI: 10.1016/j.cpc.2016.10.013.

[89] P. Nason, *A new method for combining NLO QCD with shower Monte Carlo algorithms*, JHEP **11** (2004), p. 040, DOI: 10.1088/1126-6708/2004/11/040.

[90] S. Alioli et al., *A general framework for implementing NLO calculations in shower Monte Carlo programs: the POWHEG BOX*, JHEP **06** (2010), p. 043, DOI: 10.1007/JHEP06(2010)043.

[91] M. Czakon and A. Mitov, *Top++: A program for the calculation of the top-pair cross-section at hadron colliders*, Comput. Phys. Commun. **185** (2014), p. 2930, DOI: 10.1016/j.cpc.2014.06.021.

[92] N. Kidonakis, *Next-to-next-to-leading logarithm resummation for s-channel single top quark production*, Phys. Rev. **D81** (2010), p. 054028, DOI: 10.1103/PhysRevD.81.054028.

[93] N. Kidonakis, *Two-loop soft anomalous dimensions for single top quark associated production with a W^- or H^-*, Phys. Rev. D **82** (2010), p. 054018, DOI: 10.1103/PhysRevD.82.054018.

[94] N. Kidonakis, *Next-to-next-to-leading-order collinear and soft gluon corrections for t-channel single top quark production*, Phys. Rev. **D83** (2011), p. 091503, DOI: 10.1103/PhysRevD.83.091503.

[95] ATLAS Collaboration, *Measurement of $W^{\pm}$ and Z Boson Production Cross Sections in pp Collisions at $\sqrt{s} = 13$ TeV with the ATLAS Detector* (2015), URL: https://cds.cern.ch/record/2045487.

[96] J. M. Campbell and R. K. Ellis, *Update on vector boson pair production at hadron colliders*, Phys. Rev. D **60** (1999), p. 113006, DOI: 10.1103/PhysRevD.60.113006.

[97] D. de Florian et al., *Handbook of LHC Higgs Cross Sections: 4. Deciphering the Nature of the Higgs Sector* (2016), DOI: 10.23731/CYRM-2017-002.

[98] M. Aaboud et al., *Electron reconstruction and identification in the ATLAS experiment using the 2015 and 2016 LHC proton-proton collision data at $\sqrt{s} = 13$ TeV*, Eur. Phys. J. C **79** (2019), p. 639, DOI: 10.1140/epjc/s10052-019-7140-6.

[99] G. Aad et al., *Muon reconstruction performance of the ATLAS detector in proton–proton collision data at $\sqrt{s}$ =13 TeV*, Eur. Phys. J. C **76** (2016), p. 292, DOI: 10.1140/epjc/s10052-016-4120-y.

[100] M. Aaboud et al., *Measurement of the photon identification efficiencies with the ATLAS detector using LHC Run 2 data collected in 2015 and 2016*, Eur. Phys. J. C **79** (2019), p. 205, DOI: 10.1140/epjc/s10052-019-6650-6.

[101] *Tagging and suppression of pileup jets with the ATLAS detector*, tech. rep., All figures including auxiliary figures are available at https://atlas.web.cern.ch/Atlas/GROUPS/PHYSICS/CON CONF-2014-018, Geneva: CERN, 2014, URL: https://cds.cern.ch/record/1700870.

[102] G. Aad et al., *Performance of electron and photon triggers in ATLAS during LHC Run 2*, Eur. Phys. J. C **80** (2020), p. 47, DOI: 10.1140/epjc/s10052-019-7500-2.

[103] G. Aad et al., *Performance of the ATLAS muon triggers in Run 2*, JINST **15** (2020), P09015, DOI: 10.1088/1748-0221/15/09/p09015.

[104] *Measurement of $\sigma B(W \to e\nu)$ and $\sigma B(Z^0 \to e^+e^-)$ in $\overline{p}p$ collisions at $\sqrt{s} = 1800$ GeV*, Phys. Rev. D **44** (1 1991), p. 29, DOI: 10.1103/PhysRevD.44.29.

[105] M. Aaboud et al., *Measurement of the photon identification efficiencies with the ATLAS detector using LHC Run-1 data*, Eur. Phys. J. C **76** (2016), p. 666, DOI: 10.1140/epjc/s10052-016-4507-9.

[106] G. Aad et al., *Electron and photon performance measurements with the ATLAS detector using the 2015–2017 LHC proton-proton collision data*, JINST **14** (2019), P12006, DOI: 10.1088/1748-0221/14/12/P12006.

[107] G. Aad et al., *Jet energy scale and resolution measured in proton–proton collisions at* $\sqrt{s} = 13$ *TeV with the ATLAS detector*, Eur. Phys. J. C **81** (2021), p. 689, DOI: 10.1140/epjc/s10052-021-09402-3.

[108] *Tagging and suppression of pileup jets* (2014).

[109] G. Aad et al., *ATLAS b-jet identification performance and efficiency measurement with* $t\bar{t}$ *events in pp collisions at* $\sqrt{s} = 13$ *TeV*, Eur. Phys. J. C **79** (2019), p. 970, DOI: 10.1140/epjc/s10052-019-7450-8.

[110] *Eigenvector recomposition: a new method to correlate flavor-tagging systematic uncertainties across analyses* (2022).

[111] *Optimisation and performance studies of the ATLAS b-tagging algorithms for the 2017-18 LHC run* (2017).

[112] J. Butterworth et al., *PDF4LHC recommendations for LHC Run II*, J. Phys. G **43** (2016), p. 023001, DOI: 10.1088/0954-3899/43/2/023001.

[113] G. Aad et al., *Measurement of the* $t\bar{t}$ *production cross-section in the lepton+jets channel at* $\sqrt{s} = 13$ *TeV with the ATLAS experiment*, Phys. Lett. B **810** (2020), p. 135797, DOI: 10.1016/j.physletb.2020.135797.

[114] M. Cacciari, G. P. Salam and G. Soyez, *The catchment area of jets*, JHEP **04** (2008), p. 005, DOI: 10.1088/1126-6708/2008/04/005.

[115] G. Cowan et al., *Asymptotic formulae for likelihood-based tests of new physics*, **C 71** (2011), 1554, Erratum: **C 73** (2013) 2501, DOI: 10.1140/epjc/s10052-011-1554-0,10.1140/epjc/s10052-013-2501-z.

[116] K. Cranmer et al., *HistFactory: A tool for creating statistical models for use with RooFit and RooStats* (2012).

[117] W. Verkerke and D. P. Kirkby, *The RooFit toolkit for data modeling*, eConf **C0303241** (2003), ed. by L. Lyons and M. Karagoz, MOLT007, arXiv: physics/0306116.

[118] F. James and M. Winkler, *MINUIT User's Guide* (2004).

[119] *1974 CERN School of Computing, Godoysund, Norway, 11-24 Aug 1974: Proceedings*, CERN Yellow Reports: School Proceedings, 1974, DOI: 10.5170/CERN-1974-023.

[120] CMS Collaboration, *Measurement of the Inclusive and Differential* $\mathrm{t\bar{t}}\gamma$ *Cross Sections in the Dilepton Channel and Effective Field Theory Interpretation in Proton-Proton Collisions at* $\sqrt{s} = 13$ *TeV.* Journal of High Energy Physics (2022), p. 91, DOI: 10.1007/JHEP05(2022)091.

[121] G. Aad et al., *Inclusive and differential cross-sections for dilepton* $t\bar{t}$ *production measured in* $\sqrt{s} = 13$ *TeV pp collisions with the ATLAS detector*, JHEP **07** (2023), p. 141, DOI: 10.1007/JHEP07(2023)141.

[122] N. Castro et al., *EFTfitter—A tool for interpreting measurements in the context of effective field theories*, Eur. Phys. J. C **76** (2016), p. 432, DOI: 10.1140/epjc/s10052-016-4280-9.

Acknowledgements

This thesis represents the culmination of a journey made possible by the invaluable help and support of numerous individuals. To my colleagues, collaborators, friends, and family, and to all those who have inspired and guided me along this path, I express my deepest gratitude.

I want to deeply thank Prof. Ivor Fleck for believing in me and giving me the chance to explore this fascinating research area. His guidance, constant support, and patience were essential for my growth as a physicist. He gave me the freedom and time to really dive deep into the subject and develop a strong understanding.

I am profoundly grateful to Dr. Carmen Diez Pardos for her exceptional mentorship. Her guidance at every step, coupled with her patient instruction, has been instrumental in shaping me as a researcher. The lessons learned during our time together have equipped me with the skills and perspective needed to excel in this field. I am particularly thankful for her willingness to take the lead when I encountered challenges, offering invaluable support and direction.

I extend my sincere thanks to Dr. Oldrich Kepka for his supervision during my time at CERN. His guidance in computing techniques proved incredibly valuable, and our discussions on various topics were always stimulating and insightful.

To my collaborators in Goettingen, Andreas Kirchoff and Dr. Elizaveta Shabalina, I express my gratitude for the engaging discussions and collaborative spirit that enriched this research endeavor. I would like to acknowledge the unwavering support provided by my colleagues at the ATLAS collaboration throughout this process, particularly the technical assistance received during the physics analysis. My heartfelt thanks go to Arpan, Amartya, Diptaparna, and Jan for the deep and thought-provoking discussions on a wide range of topics that challenged my understanding and prompted me to revisit and relearn many aspects of my research. I extend my appreciation to all my fellow PhD students and colleagues at Siegen for fostering a friendly and supportive environment. Their willingness to offer help, engage in numerous discussions, and endure countless debates has made this experience both productive and enjoyable.